# UNIVERSITY OF ZULULAND

# Synthesis of Cadmium, Lead and Iron Sulfide Thin Films and Nanoparticles

By

**Sixberth Mlowe**

201200104

B. Sc. (Hons), M.Sc. (University of Dar es Salaam, TZ)

**THESIS**

**Submitted in Fulfilment of the Requirements for the Degree**

**DOCTOR OF PHILOSOPHY IN CHEMISTRY**

**Faculty of Science and Agriculture**

**University of Zululand**

**Supervisor: Prof. Neerish Revaprasadu**

Department of Chemistry, University of Zululand,

Private Bag X1001, KwaDlangezwa 3886,

South Africa.

11 April 2016

## DECLARATION

I hereby declare that the work described in this thesis entitled "**Synthesis of Cadmium, Lead and Iron Sulfide Thin Films and Nanoparticles**" is my own work and has not been submitted in any form for another degree or qualification of the University of Zululand or any other University/Institution of tertiary education. Information derived from the published or unpublished work of others has been acknowledged in the text and a list of references is given.

Name: Sixberth Mlowe

Signature..... Date.....

## CERTIFICATION BY SUPERVISOR

This is to certify that this work was carried out by Mr. Sixberth Mlowe in the Department of Chemistry, University of Zululand and is approved for submission in fulfilment of the requirements for the degree of Doctor of Philosophy in Chemistry.

.....

Supervisor

N. Revaprasadu (PhD)

Professor of Inorganic Chemistry

Department of Chemistry, University of Zululand,

KwaDlangezwa, South Africa

## Dedication

This work is dedicated to Almighty God and my entire family.

## ACKNOWLEDGEMENTS

I express, in a very special way my profound gratitude to my supervisor Prof. Neerish Revaprasadu for his immense guidance, encouragement, commitment and support throughout my PhD programme. I also thank the love and hospitality of his wife Shaneera and their kids Manav, Mahee and Aryana. I gratefully acknowledge the financial support from NRF/DST South Africa through SARChi granted to Prof. N. Revaprasadu and NRF Innovation, which enabled me to pursue this study smoothly.

My special thanks to Prof. Paul O'Brien of the Schools of Chemistry and Materials Science of the University of Manchester for a visit to his research laboratory, Dr. Azad M. Malik and Dr. David Lewis for their assistances, useful advice and suggestions. Dr. James Raftery, Dr. Christopher Wilkins, Dr. Alan Harvey, Gary Harrison, Dr. Nicky Savjani, Dr. Claire Lydon, Dr. Paul McNaughter, Christine Taylor, Dr. Masood Akhtar, Emmanuel Ezenwa (housemate), Edward Lewis and Robert Page for their help and support during my stay in Manchester.

I also thank Prof. Shivram Garje of the University of Mumbai (India) for inviting me to visit his inorganic research laboratory. Many thanks to his staff colleagues and postgraduate research students; Amol Pawar, Jagruti Shurose, Sonali Parkar, Amey, Vipuli and Swaleha for their warm hospitality, love and constant care during my stay in Mumbai. Dr. Bonex Mwakikunga is also thanked for setting and conducting gas sensing measurements at the CSIR, Pretoria.

I am equally thankful to the staff of the Chemistry Department of the University of Zululand; Prof. Motaung, Dr. Segapelo, Dr. Raj Pullabhotla, Dr. Mavundla, Sibusiso Buthelezi, Zibane Welcome and my colleagues Rekha Dunpall, Masikane Siphamandla, Fr. Charles Gervas, Malik Dilshad, Mzimela Zimele, Sandile, Sibusisiwe Lukhele, Nobuhle Hadebe, Lethu Nene, former postdocs and students and research visitors for assistance, care and useful discussions during my programme. I also thank all people who made any contribution, however small, to the completion of this work.

**TABLE OF CONTENTS**

**Content** **Page**

## ABSTRACT

The usefulness and application of semiconductor nanomaterials continue to expand the frontier of research in bringing their benefits via technological applications. Several synthetic methods for the preparation of semiconductor nanoparticles have been established. The design and development of a simple technique that is able to fabricate very pure, high quality and tunable morphology thin films and nanoparticles is therefore important and pressing. In this research project, Cadmium Sulfide, Lead Sulfide and Iron Sulfide nanoparticles and thin films were selected and synthesized because of their unique properties and applications. The use of single source precursors for the fabrication of these nanomaterials has been used by several routes such as hot injection, chemical vapour deposition and pyrolysis methods.

Therefore, in this study, the synthesis of nine (9) heterocyclic dithiocarbamate metal complexes namely; *bis*(piperidinedithiocarbamato)cadmium(II) (**1**), *bis*(tetrahydroquinolinedithiocarbamato)cadmium(II) (**2**) and the pyridine adduct of *bis*(piperidinedithiocarbamato)cadmium(II) (**3**), *bis*-(piperidinedithiocarbamato)lead(II) (**4**) and *bis*-(tetrahydroquinolinedithiocarbamato)lead(II) (**5**), *tris*-(piperidinedithiocarbamato)iron(III) (**6**) and *tris*-(tetrahydroquinolinedithiocarbamato)iron(III) (**7**), *bis*-(piperidinedithiocarbamato)iron(II) (**8**) and *bis-(*tetrahydroquinolinedithiocarbamato)iron(II) (**9**) are presented. Single crystal structures of four single source precursors (**1**), (**3**), (**6**) and (**7**) have been elucidated in this study. These complexes have been used as single-source precursors (SSPs) for the fabrication of cadmium sulfide (CdS), lead sulfide (PbS) and iron sulfide (FeS) thin films by aerosol-assisted chemical vapour deposition (AACVD) and spin coating methods for PbS. Also, nanoparticles of similar metal sulfide were made by the hot injection and pyrolysis routes. Various parameters such as temperature, solvent and time were used to ascertain their properties.

The morphological, structural, optical properties and composition of the as-synthesized materials were found to depend on the reaction conditions used during the synthesis. The synthesized CdS thin films and nanoparticles were found to exhibit blue shifted optical properties, which were size and morphological dependent. Their morphologies and structural properties were investigated using different electron microscopy and

diffraction techniques. Similarly, PbS thin films deposited were studied and their optical and structural properties show formation of high quality nanomaterials which are also temperature dependent. Optical properties of the deposited PbS thin films show blue shift compared to the bulk PbS. Best morphologies of PbS films deposited by spin coating method highlighted the usefulness of this route. Iron sulfide thin films deposited by AACVD method show that variation of parameters could result in the formation of high quality nanostructures. Furthermore, optically active greigite and pyrrhotite-iron sulfide nanoparticles were prepared by simply varying the temperature of the hot solvent. Pyrrhotite-$Fe_{1-X}S$ sensor device showed interesting performance when tested for humidity and different nitrogenous gases such $NO_2$ and $NH_3$. The gas sensors further revealed that stoichiometric structure of iron sulfide nanostructures have significant effect on the end-user device performance.

**List of Figures** **Page**

**List of Tables**

**List of abbreviations**

| | |
|---|---|
| HDA | Hexadecylamine |
| TOPO | Tri-octlyphosphine oxide |
| TOP | Tri-octlyphosphine |
| CdS | Cadmium sulfide |
| EG | Ethylene glycol |
| $(CH_3)_2Cd$ | Dimethylcadmium |
| $Cd(CH_3COO)_2$ | Cadmium acetate |
| $Pb(CH_3COO)_2$ | Lead acetate |
| S | Sulfur |
| PbS | Lead sulfide |
| FeS | Iron sulfide |
| DTC | Dithiocarbamate |
| Phen | Phenanthroline |
| Pip | Piperidine |
| Py | Pyridine |
| THQ | tetrahydroquinoline |

**Techniques and methods**

| | |
|---|---|
| TEM | Transmission electron microscopy |
| XRD | Powder X-ray diffraction |
| FTIR | Fourier transform infrared spectroscopy |
| AFM | Atomic force microscopy |
| XPS | X-ray photoelectron spectroscopy |
| NMR | Nuclear magnetic resonance |
| EDX | Energy dispersive X-ray spectroscopy |
| SEM | Scanning electron microscopy |
| AACVD | Aerosol-assisted chemical vapour deposition |
| SSP | Single source precursor |

**Symbols and constants**

| | |
|---|---|
| λ | Wavelength |
| θ | Theta |
| Å | Angstroms |
| nm | nanometre |
| eV | electron volts |
| CB | conduction band |
| VB | valence band |

# CHAPTER ONE

# INTRODUCTION AND LITERATURE REVIEW

## 1.1. General Introduction

Nanoscience is a multi-displinary field that cuts across chemistry, physics, engineering and biological sciences. In the nanoscale regime neither quantum chemistry nor classical laws of physics hold. In materials where strong chemical bonding is present, delocalization of valence electrons can be extensive, and the degree of delocalization can vary with the size of the system. This effect, together with structural changes with size variation, can lead to different chemical and physical properties, depending on size. Indeed, it has now been demonstrated that a multitude of properties depend on the size of such nanoscale particles, these include magnetic properties, optical properties, melting points, specific heats and surface reactivity.

Nanoparticles have been known as suitable systems for studying the shift from the molecular to the macrocrystalline level and have been extensively studied in recent years. These particles have dimensions in the range of 1–20 nm. Current interest in these materials can be traced to the work by Louis Brus in the mid-1980s in which he pointed out that the band gap of a simple direct-band-gap semiconductor such as CdS should be dependent on its size once its dimensions were smaller than the Bohr radius [1]. The optical spectra of many nanocrystalline semiconductors show a blue shift in the absorption edge as the particle size decreases. The charge carriers in these nanoparticles are restricted in three dimensions and, as the dimensions of the nanoparticle become similar to the excitonic radius, quantum size effects occur [2]. The electron–hole pairs are so close together that the Coulomb interaction between the electron and hole cannot be ignored and they assume a state of higher kinetic energy than in a bulk solid. The effect causes the continuous band of the solid to split into distinct, quantized, levels and the “band gap” to increase. The shift in the absorption edge for II–VI semiconductors such as CdSe and CdS can be a large portion of the bulk band gap and

for CdSe can result in alteration across a major fraction of the visible spectrum. For example the band gap in CdSe can be tuned from 1.7 eV (deep red) to 2.4 eV (green) by reducing the particle size diameter from 200 to 20 Å [3]. Furthermore, the size- and shape-dependent properties of nanomaterials raising expectations for a better performance generally are a consequence of quantum confinement within the particle [2]. The precise controlled synthesis of the size, shape, chemical composition, crystal structure, and surface chemistry of nanomaterials allows obtaining their unique properties, which have become one of the most challenging issues faced by material scientists.

Research into new synthetic routes for semiconductor nanocrystallites has received increased attention because modern devices and applications are improved through the use of such materials [4]. Theoretical models predicting the optical properties of semiconductor nanoparticles are available [5- 6], but the properties of nanoparticles obtained by any new synthetic route are hard to predict. High purity, monodispersity and the ability to control the surface derivatization are the requirements for this system. Several synthetic methods for the preparation of semiconductor nanoparticles have been reported [7-9]. The best synthetic route should produce nanoparticles which are pure, crystalline, reasonably monodisperse and have a surface which is independently derivatized [10].

The usefulness and application of semiconductor nanoparticles continue to expand the frontier of research in bringing their benefits via technological applications. In this research project, we selected to synthesize cadmium sulfide, lead sulfide and iron sulfide nanoparticles and thin films because of their unique properties and applications. The use of single source precursors for the fabrication of nanomaterials has been used to produce binary metal sulfide nanomaterials by several routes such as hot injection, chemical vapour deposition just to

mention a few. Hence a comprehensive literature review is important to detail the efforts made so far.

## 1.2. Literature Review

The development of reliable and reproducible methods for producing large amounts of uniformly sized inorganic nanocrystals has been a major aspiration in materials chemistry research over several years. In the case of semiconductors, the most successful preparations involve growth in solution from molecular precursors [11], a powerful method for the preparation of semiconductor nanoparticles extended by Bawendi group [12]. In this method, a volatile metal alkyl e.g. $[Cd(CH_3)_2]$ and a chalcogen source were injected into hot tri-n-octylphosphine oxide (TOPO) (120 – 300 $^oC$), resulting in TOPO capped nanocrystallites CdE (E = S, Se, Te). One of the limitations of this method is the use of the metal alkyl $[Cd(CH_3)_2]$ which is extremely toxic, pyrophoric, expensive, unstable at room temperature, and explosive at elevated temperature, releasing large amount of gas. Due to these reasons, the $Cd(CH_3)_2$-related schemes require special equipment and reaction conditions and are not suited for large scale synthesis.

Several efforts have been made to overcome the use of metal alkyl as a precursor. For instance, Peng [13] reported a reproducible one-pot synthesis, termed green chemistry approach for synthesising high quality semiconductor nanocrystals by replacing alkyl metal with cadmium oxide. The reaction conditions were mild and simple without using glovebox. Another approach for overcoming this problem has been the solution phase thermal decomposition, which involves the use of single source precursors (SSPs) in a high boiling solvent [Figure 1.1]. Mostly, this solvent promotes decomposition and acts as a capping agent for the nanoparticles [10,14]. Trindade and O'Brien [15,16] investigated cadmium dithio and

diselenocarbamate complexes as precursors for the preparations of TOPO capped II-VI materials. Several other classes of SSPs for the preparation of semiconductor nanoparticles have also been reported. These include xanthates [17,18], thiourea [19,20] and thiosemicarbazone [21, 22] complexes.

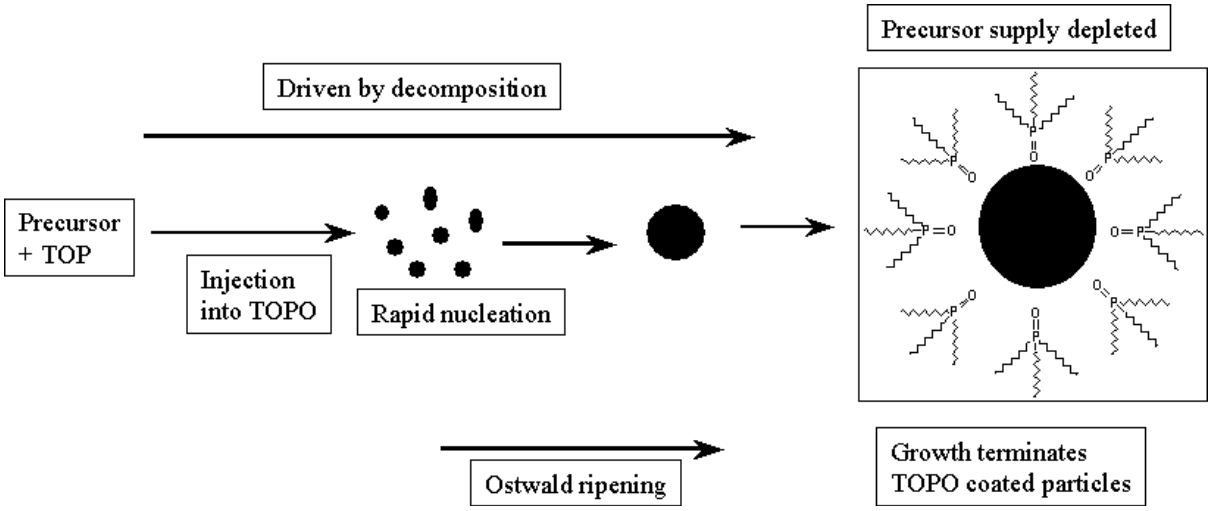


**Figure 1.1.** General scheme for the growth of nanoparticle via thermal decomposition of SSPs.

The use of SSPs provides a number of advantages over other routes. For example, the existence of preformed bonds leads to material with fewer defects and/or better stoichiometry. Several of the SSPs are also air-stable and are therefore easier to handle and characterise. Interestingly, the use of SSPs is motivated by their potential to trim down the environmental impact of material processing, thus investigation of new routes of preparing SSPs are now gaining momentum. The use of SSPs has solved problems of using hazardous compounds such as dimethylcadmium. The SSP is also required to have low degree of toxicity for easy use and storage, be easily synthesised in quantities of at least several grams and more importantly, is its purity; to prevent contamination of the nanoparticles and other undesirable side products [10, 14].

Recently, Revaprasadu and co-workers revisited the use of thiocarbamate precursors for nanoparticle synthesis. They reported a series of heterocyclic metal dithiocarbamate complexes as effective SSPs for the preparations of cadmium sulfide and lead sulfide nanoparticles [23-25]. Cadmium and lead piperidine/tetraisoquinoline dithiocarbamate complexes were thermally decomposed in various capping agents (hexadecylamine, trioctylphosphine oxide, oleylamine and decylamine) resulting in nanoparticles with different shapes and morphology. A combination of shapes ranging from spherical, cubes, rods, bipods and tripods were obtained by varying the reaction parameters such as precursor concentration, temperature and nature of the capping agent. This method enjoys robust potential advantages of mildness, safety and simplified one pot synthesis. Apart from using coordinating solvents, solid state thermal decomposition has also been reported as an efficient method of making metal sulfide nanoparticles [22,26,27], where a SSP is heated up to a specific temperature for a given period of time without the presence of any surfactants or solvents.

### 1.3. Cadmium Sulfide (CdS)

Cadmium sulfide is a direct band gap semiconductor with $E_g$ = 2.42 eV at room temperature. Cadmium sulfide (CdS) exists in two natural forms: greenockite and hawleyite, which differ in their crystal structures. Greenockite forms hexagonal crystals with the wurtzite structure, hawleyite has the cubic (zinc blende) structure (Figure. 1.2) [28]. Crystalline cadmium sulfide (CdS) semiconductor nanoparticles as a typical and important II-VI group of semiconductors have attracted extensive investigation due to their unique optical, chemical and electrical properties and the intriguing prospects for the development of photovoltaic solar cells and light emitting diodes (LEDs) [29-34], gas sensors [35-37], and photocatalysts [38-40]. The uniqueness about these semiconducting nanocrystals is that they exhibit distinct size, shape and composition dependent physical and chemical properties [41]. Cadmium sulfide is particularly attractive system to demonstrate the size-dependence of the

band gap, which can be tuned between 4.5 and 2.5 eV. As an inspiring and interesting example, Figure 1.3 shows the optical fluorescence of CdSe/CdS core-shell nanocrystals in the size range of 1.7 – 6.0 nm.

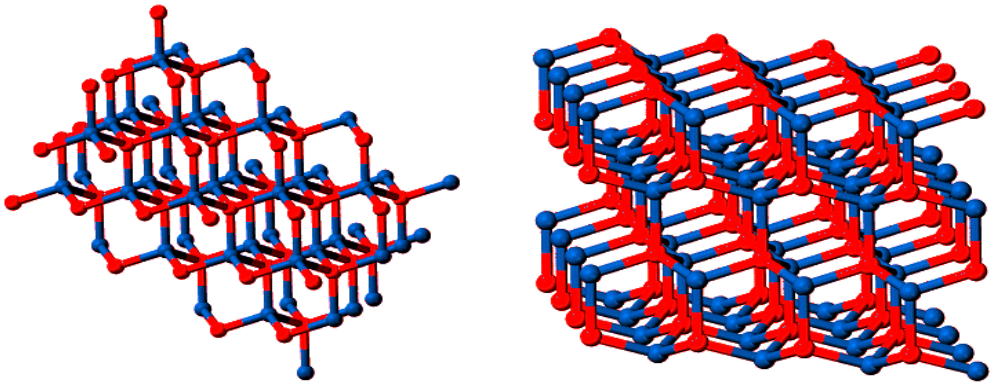

(a) (b)

**Figure 1.2.** Crystal structures of (a) Hawleyite (cubic) and (b) Greenockite (hexagonal) of CdS semiconductor [28].

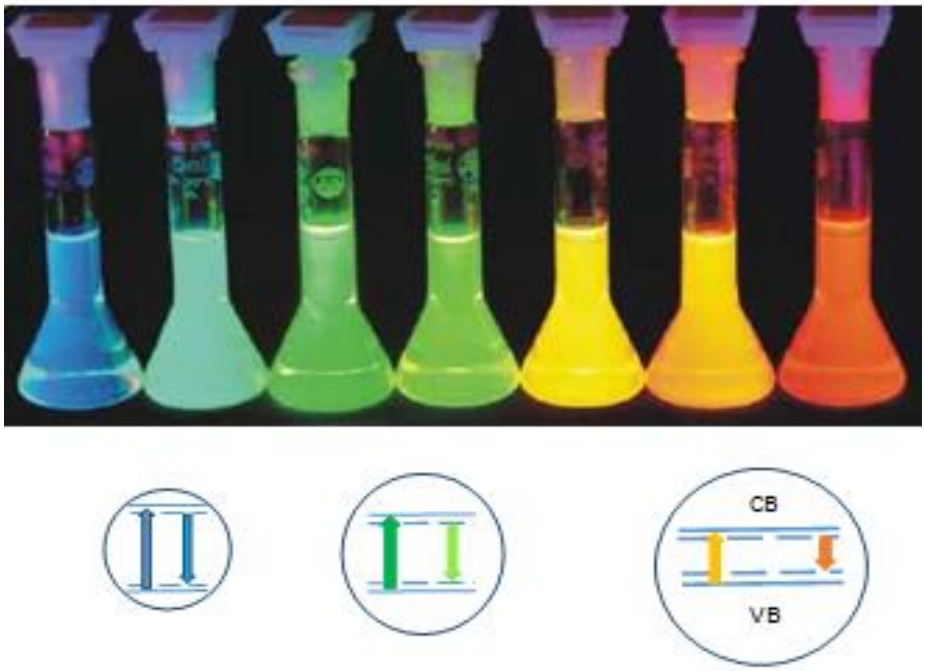


**Figure 1.3.** Fluorescence of CdSe/CdS core-shell nanoparticles in a size range increasing from 1.7 nm with blue fluorescence at the left to *ca.* 6 nm with red fluorescence at the right (upper panel: Figure courtesy of H. Weller, University of Hamburg) and schematic representation of the absorption and emission across the size-dependent band gap (lower panel) [41]. Smaller particles have a wider band gap.

### 1.3.1. Synthesis of CdS nanomaterials

The development of general and facile synthetic approaches that yield nanocrystals with precise control over not only the size and shape but also the chemical composition is highly desirable for both fundamental study and practical applications. Since Murray *et al*. [12] reported the synthesis of cadmium chalcogenides using the thermolysis method, there has been significant advances in the synthesis of chalcogenide nanoparticles, and such strategies have also been employed for the synthesis of cadmium sulfide nanoparticles. CdS nanoparticles were prepared by the reaction of metal salts with an appropriate sulfiding agents under thermolysis conditions. Synthesis of CdS NPs of 5-10 nm has been carried out by the reaction of cadmium stearate with sulfur in the presence of tetralin [42]. Several other synthetic methods for the preparation of CdS semiconductor nanoparticles have been reported. To mention a few, the wet chemical (hydrothermal) method [43], an alternative approach to the use of high temperature solvents, and microwave irradiation (MWI) [44] method, which have also attracted research interest. The latter method, which provides the significant enhancement in reaction rates, is one of the simple, energy efficient and fast methods. For example, Nirmal *et al.* [45] recently reported the synthesis of monodispersed CdS nanocrystals by the microwave irradiation using new single molecular precursor cadmium pyrrolidine dithiocarbamate complex as SSP and HDA was used as a capping agent. Microwave irradiation has both thermal and non-thermal effects on chemical reaction; these effects are as a result of microwave dielectric heating and the inherent property of the microwave radiation respectively [46,47].

#### 1.3.1.1. Single source precursor (SSP) route

Thermal decomposition of SSPs method has also been considered as a convenient and effective way to produce size- and shape-controlled CdS NPs [48]. The size and shape as well as the chemical composition of metal sulfides can be easily controlled by simply adjusting the experimental conditions [49]. Following the success of the use of dithio-/diseleno-carbamato complexes in CVD experiments, O'Brien and co-workers have used similar complexes and extensively investigated the synthesis of metal chalcogenide nanoparticles. The process involves dissolution of a TOP solution of the precursor in a suitable high boiling coordinating solvent usually at temperatures above 200 °C [50,51]. Comparative study between the pattern of thermal decomposition and morphology of resulting nanoparticles from dithiourea, xanthates and thiosemicarbazide has been done [17,20,21,52]. Revaprasadu *et al.* have recently reported the synthesis of CdS nanoparticles in various coordinating solvents in the shapes of rod, bipods and tripods when HDA was employed whereas TOPO gave spherical shaped CdS nanoparticles [23]. A decomposition mechanism for dithiocarbamate II-IV metal complexes has been studied by O'Brien *et al.* [53] and Wold *et al.* [54], which shows the clean elimination of the particles from the complexes.

Furthermore, nitrogen donor adducts of dithiocarbamate complexes have also been widely used in the preparation of semiconductor nanoparticles of transition metal sulfide. Four coordinated complexes of cadmium metal are known to expand their coordination number by adding neutral nitrogen containing ligands (Lewis base) [55,56]. Physical properties and single crystal X-ray structural studies on numerous cadmium and zinc complexes comprising dithiocarbamate and nitrogen containing ligands such as pyridine, 2,2'-bipyridine, 1,10-phenanthroline have been reported [57-61]. These five and six

coordinated complexes showed increased electron density on metal centres. Thermal properties of these adducts experienced increased volatility upon introduction of the Lewis base ligands containing nitrogen, which is described as the effect caused by the lone pair of electron into the d-orbital of metal ion [61]. Studies on the effect of pyridine and other nitrogen donor ligands in the heterocyclic cadmium dithiocarbamate complexes have recently been reported. Srinivasan and Thirumaran [59] have investigated the influence of pyridine as a ligand in the precursor for CdS nanomaterials fabrication. Also, Onwudiwe *et al.* [62] synthesized HDA capped CdS nanoparticles by thermal decomposition of the 2,2'-bipyridine and 1,10-phenanthroline adduct of cadmium ethyl phenyl dithiocarbamate complexes. In both studies, the effect of nitrogen containing ligands in the precursor affected the axial growth of CdS nanoparticles [63].

Many techniques such as spray pyrolysis [64], chemical bath deposition [65], sol-gel [66], and metal-organic chemical vapour deposition (MOCVD) [67-71], have been used to deposit phase pure films of CdS. The nature, morphology and composition of the final product can be affected by the single source precursor used to deposit the materials [72,73]. Various single-source precursors have been used for the preparation of CdS thin films deposition by a number of chemical vapour deposition (CVD) methods [74,75]. O'Brien and co-workers have reported a number of dithiocarbamatocadmium(II) complexes as single source precursors for CdS thin films using low pressure metal-organic chemical vapour deposition (LP-MOCVD) [61,69]. Aerosol-assisted chemical vapour deposition (AACVD) has been used to deposit a wide range of metal chalcogenide thin films [76-78]. Ehsan *et al.* used *bis*(*N*,*N*-dicyclohexyldithiocarbamato)pyridinecadmium(II) to deposit greenockite CdS thin films which proved to be suitable for application in photoelectrochemical (PEC) cells [79]. Various classes of single source precursors have been identified and developed

including dialkyldithiocarbamates [61,69], xanthates [78], N-alkyl thiourea [79], and dithioimidodiphosphinates [80,81], for the preparation of CdS thin films and nanoparticles.

## 1.4. Lead Sulfide (PbS)

PbS, being an important IV-VI semiconductor, has attracted considerable attention in the field of materials science due to its intrinsic small band gap energy (0.41 eV) and a large exciton Bohr radius (18 nm) [82]. The latter property is potentially useful for making devices that require small band gap semiconductors, optical absorption and emission in the red and near-infrared region of the electromagnetic spectrum. Such devices include infrared detectors, light emitting diodes and solar absorbers [83-85]. They also allow quantum size confinement effect to be clearly evident even for relatively larger particle crystallites [86]. In addition, the exceptional third order nonlinear optical properties of PbS demonstrate their promising application in the high-speed optical switches [87].

### 1.4.1. Synthesis of PbS nanomaterials

Currently there is an interest in devising novel and mild methods for the synthesis of PbS nanoparticles with controllable morphologies and sizes [26, 88-90]. This not only provides an alternative in tailoring the optical, electronic, physical and chemical properties of this material, but is also crucial to develop building blocks in constructing future nanoscale electronic and optoelectronic devices using the so called bottom-up approach. The rapid hot injection of precursor(s) into hot coordinating solvents remains the most common method with definite control of size and reproducibility. In this method, the lead precursor and sulfur source are injected into hot coordinating solvents at temperatures ranging from 120 – 300 $^{o}$C [91-95]. In most cases, long chain phosphines or amine based solvents are used as capping

groups. The average size and the size distribution of the particles are controlled essentially by the temperature at which the synthesis is undertaken, with larger particles being obtained at higher temperatures. The shape control of the as-synthesized nanoparticles has been depicted by the type of the ligands used [94].

### 1.4.2. Single source precursor route

Another route developed for the shape-controlled synthesis of PbS nanoparticles is the use of single-source precursors (SSPs). One of the earliest reports was the deposition of well-defined cubes of PbS from decomposition of diethyldithiocarbamate complexes [88]. Cheon and co-workers [96,97] have envisaged the factors underlying the control of shape and morphology of PbS nanoparticles from a single source precursor. By varying the ratio and injection temperature, the shape of the resulting particles evolved from rods to multirods to cubes. Many precursors have been used to deposit PbS and PbSe. Decomposition of lead hexadecylxanthate in trioctylamine has been reported to yield ultra narrow rods [98]. Also Vittal *et al.* synthesised spherical and dendrite PbS particles by employing a Lewis-base catalysed approach to decompose metal alkyl xanthates by using alkyl amines as solvents to promote decomposition as well as capping ligand for the particles formed [18].

Meanwhile, lead dithiocarbamate complexes have received little attention as potential precursors for the production of PbS nanomaterials. There are few reports on their syntheses and thermal behaviour [99]. Trindade *et al*. reported the synthesis and characterization of lead dithiocarbamate complexes, and their use as single molecule precursor to produce cubic PbS nanocrystalline particles by thermolysis in TOPO [88]. The optical and morphological properties of the nanocrystals were strongly dependent on the temperature of the reaction than the chemical nature of the precursor. Likewise, the work of Plante [100] justified the

effect of the precursor concentration and the choice of suitable solvent on the final morphology of the PbS nanoparticles, because it was observed that the degree of branching increased as the concentration of the precursor increased. Revaprasadu *et al.* have recently reported the use of the heterocyclic lead piperidine/tetraisoquinoline dithiocarbamates as SSPs for PbS nanoparticles [24]. The complexes were thermolysed in hexadecylamine (HDA), oleylamine (OM) and decylamine (DA) to give PbS particles with varying shapes.

Aerosol assisted chemical vapour deposition (AACVD), a sub-class of CVD, allows the use of a wide range of precursors to deposit multi-component layers of inorganic nanocrystal thin films. The particle size and morphology of the films can be controlled by the choice of a suitable solvent and deposition temperature among other parameters [101]. Several studies on the deposition of lead sulfide thin films using single source precursors have been reported. O'Brien group has extensively studied the deposition of PbS thin films by aerosol assisted chemical vapour deposition (AACVD) using alkyldithiocarbamato and dichalcogenoimidodiphosphinato lead complexes [102-104]. In one of the studies [102], it was found that the length of alkyl chain had an effect on the crystallinity of the deposited PbS thin films. It was also observed that, the longer the chain the more crystalline and uniform films were obtained. Clark *et al.* also generated PbS nanocubes by AACVD using a series of xanthate lead(II) complexes on various substrates (glass, Mo-coated glass and Si) when decomposed under an autogenerated pressure at 350 °C [105].

Furthermore, PbS nanocrystals can be fabricated using an in-situ synthetic route, where semiconductor nanocrystals are grown within the polymer matrix [106-110]. This method, where a solution of both precursor and polymer are spin coated to form a matrix, which when heated the growth of an inorganic semiconductor nanostructure within the

polymer matrix occurs [106-109]. The advantage of this method includes improved contact between adjacent nanostructures leading to improved charge separation and transport [111,112]. This method involves no additional ligands, is simple, and is possible for large scale processing [110,113,114]. Several single source precursors have recently been used to deposit PbS thin films by spin coating method, including lead(II) dithiocarbamates and xanthates of different alkyl chains lengths (butyl, hexyl and octyl) [115].

## 1.5. Iron sulfide (FeS)

Iron chalcogenides are of particular interest because of their remarkable magnetic, semiconducting, and structural properties [116,117]. Consequently, they have been targeted for potential use in biomedical applications, including protein immobilization and separation [118], catalysis [119] and ultrahigh-density magnetic storage [120] to mention a few. Iron sulfide nanoparticles are a class of materials with many different forms which are summarized in Table 1.1, showing structure type (crystal class), space group and unit cell parameters (Å), with only pyrite and troilite being the truly energetically stable phases [121].

**Table 1.1.** Iron sulfides and their properties [121,122].

| Composition mineral | Crystal structure type and structural data | Electrical and magnetic properties | Thermal stability | Natural occurrence |
|---|---|---|---|---|
| $FeS_2$ pyrite | Pyrite-type (cubic) Pa3; a = 5.42 | Semiconductor diamagnetic | <742 $^oC$ | The most abundant sulfide in many massive. Bedded or vein type ores. |
| $FeS_2$ marcasite | Marcasite-type (orthorhombic) Pnnm; a = 4.44, b = 5.41, c = 3.38 | Semiconductor diamagnetic | Metastab-le | Occurs as a primary mineral in certain sediments and lower temperature hydrothermal deposits. |
| $Fe_3S_4$ greigite | Spinel-type (cubic) Fd3m; a = 9.88 | Metallic conductor ferromagnetic | Metastab-le (~180-200 $^oC$) | A very rare mineral reported from recent sediments and low temperature hydrothermal deposits. |
| $Fe_{1+X}S$ (x ≈ 0.03-0.10) cubic FeS (synthetic) | Sphalerite-type (cubic) F43m; a = 5.42 | Paramagnetic (above 234K) | Metastab-le | Known only from synthetic studies at present and formed as a layer on sulfudized iron surfaces |
| FeS troilite | NiAs-type (distorted super-structure) | Metallic conductor antiferromagne | <138 $^oC$ | Found in iron meteorites and lunar rocks. |

| | | | | |
|---|---|---|---|---|
| | (hexagonal). P62c; a = 5.97, c = 11.75 | tic | | |
| $Fe_7S_8$ Monoclinic pyrrhotite | NiAs-type; superstructure (mono). F2/d; a = 11.90; b = 6.86; c = 22.79; β = 90º26’ | Metallic conductor ferromagnetic | ~254 ºC metastab -le | As an important mineral in the sulfide ores of magmatic origin. |

Iron sulfide materials contain complex solid phase structures and various properties that are of crucial ingredient in recent investigations [121,122]. Although the iron-sulfur system is a binary system, its phase relationships are complicated due to the different valency states taken by sulfur (disulfide, mono sulfide) and iron (ferric, ferrous) [123]. Because of the complex structure of iron sulfide compound, a small variation in stoichiometry can lead to huge changes in their properties. The composition and structure of Fe-S system is best described in the context of the phase relations (in terms of temperature-composition relations) in the iron-sulfur system (Figure 1.4). Iron sulfides exhibit a wide range of properties, from the semiconducting nanomagnetic pyrite ($FeS_2$) to ferromagnetic $Fe_3S_4$ [124]. The magnetic and electrical properties of iron sulfides are dependent on the stoichiometric ratio between iron and sulfur as well as their crystallinity [125,126]. Their complex structure and valence state contribute to their particular properties [127].

Iron sulfide nanocrystals are promising materials for light harvesting in photovoltaic and photocatalytic applications [128]. When the size of the grains is considerably larger,

quantum-confinement effects seem inexistent. Iron sulfide nanocrystals display an absorption in the visible and near-infrared spectral range. The pyrite ($FeS_2$) class shows an onset of the absorption at 0.9 eV corresponding to the indirect band gap found in bulk crystals of 0.8–1.2 eV [129,130], and the direct band gap at 2.62 eV [131]. Because of its high absorption coefficient (~$10^5$ $M^{-1}$ $cm^{-1}$) and low toxicity, pyrite is a potential semiconductor as an absorber material in the thin film solar cells [132,133].

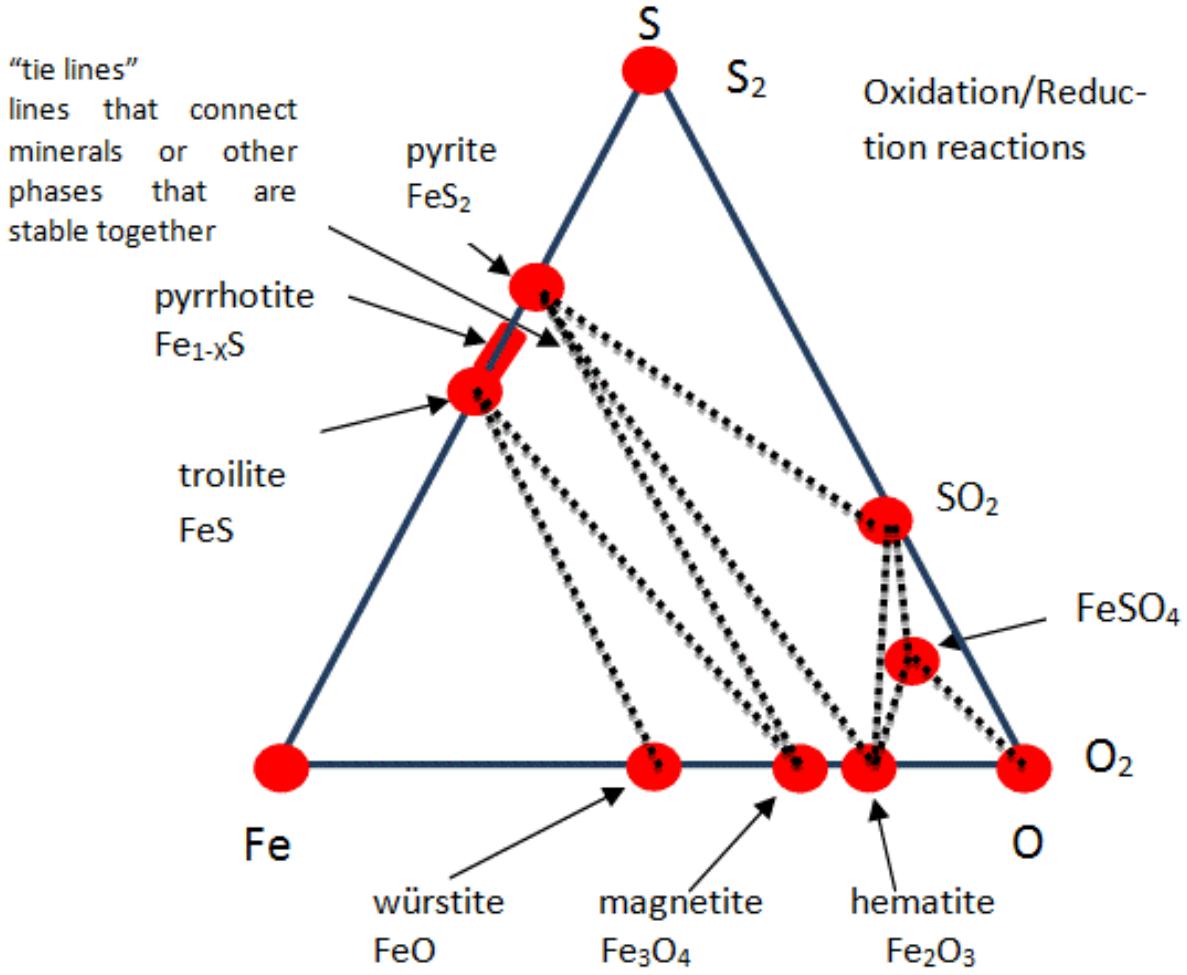


**Figure 1.4.** Phase relations in the iron-sulfur system [121,122].

### 1.5.1. Synthesis of iron sulfide nanomaterials

Up to now, several methods have been developed to synthesize iron sulfide nanoparticles, including microwave-assisted preparation [134], hydro/solvothermal process

[135], and thermal decomposition of a single source molecular precursor [136]. Low temperature methods like hot injection and hydro/ solvothermal processes have been explored recently to synthesize iron sulfide particles for sol-gel processing of low-cost, flexible large area devices [137-139]. Recently, it has been demonstrated that monodispersed pyrite microspherolites can be obtained via a microwave- assisted hydrothermal process in the presence of polyvinylpyrrolidone (PVP) [137]. Feng *et al.* prepared uniform $Fe_3S_4$ flower-like particles by hydrothermal reaction using L-cysteine as a source of sulfur and as a coordinating ligand [140].

### 1.5.2. Single source precursor route

Several single source precursors have been used to grow iron sulfide nanoparticles. Very recently, O'Brien and co-workers have used symmetrical and unsymmetrical dithiocarbamate complexes of iron(III) with the general formula $[Fe(S_2CNRR')_3]$ as single source precursors to synthesize iron sulfide nanocrystals by thermolysis in oleylamine, hexadecylamine and octadecene at different temperatures [141]. Shen et al have also reported the thermal decomposition of iron-diethyldithiocarbamate in solution phase using oleylamine and oleic acid as capping agents [142]. As a result, iron sulfide nanoparticles ($Fe_3S_4$ and $Fe_7S_8$) exhibited strong magnetic and electronic properties. The chemical composition of iron sulfide nanocrystals can also be controlled by changing the sort of precursor (ferrous ion with different valences in a single-source precursor). For example, $Fe(DDTC)_3$ (Fe with oxidation state of +3) as precursor, when the reaction was carried out in the mixture of oleylamine (OM) and octadecene (ODE), $Fe_3S_4$ nanoparticles were obtained. When $Fe(DDTC)_2$(phen) (Fe with an oxidation state of +2) was present as precursor under the same reaction condition of OM and ODE, $Fe_7S_8$ hexagonal nanoplates were obtained [143]. More

recently, Han and Gao prepared the $Fe_3S_4$ and $Fe_7S_8$ nanosheets using SSP approach based on the thermo-decomposition process [144]. They found that the reaction temperatures play a critical role in controlling the chemical compositions, morphologies, crystalline structures and the magnetic properties of the resultant iron sulfide nanosheets. However, the effects of the different sorts of solvents as well as their compositions on the phase, shapes and the formation mechanisms of the resultant iron sulfides have not been systematically clarified.

### 1.5.3. Iron sulfide thin films

Various binary and ternary chalcogenide films have been synthesized by AACVD-based methods. Single-source metal-organic compounds are still the most common precursor chemicals for chalcogenide films in aerosol-assisted chemical vapour deposition (AACVD). The deposition temperatures of the chalcogenide compounds range from 200 to 500 °C. Temperatures above 500 °C may cause the formation of oxide composition in the films [145]. However, in some cases, $H_2S$ gas is used to avoid the oxidation and enhance the sulfidizing reaction [145,146]. The morphology and orientations of the deposited films are dependent on the precursor solution and the processing parameters [147]. Varying and unique surface morphology of the films can be obtained by changing the solvent of the precursor [148,149]. Using AACVD, highly oriented crystalline films can be synthesized [150-152] even on amorphous substrates [153].

The AACVD method involves the atomization of a precursor solution into fine, sub-micrometer-sized aerosol droplets which are delivered to a heated reaction zone and undergo evaporation, decomposition, and homogeneous and/or heterogeneous chemical reactions to form the desired products (Figure 1.5). As a variant of conventional CVD processes, AACVD addresses the availability and delivery problems of the chemical precursors. A wide range of

precursors can be used since volatility is no longer crucial, offering more possibilities to produce high-quality CVD products at low cost. Some variants of AACVD have also been developed, such as AA combustion (C) CVD, electrostatic spray-assisted vapor deposition (ESAVD), and electrostatic-assisted aerosol jet deposition (EAAJD). These variants provide additional flexibility and capability to the AACVD-based processes. AACVD-based processes have attracted increasing interest in most of the CVD-related areas, and have been widely used to synthesize various films, coatings, powders, composites, nanotubes and nanowires.

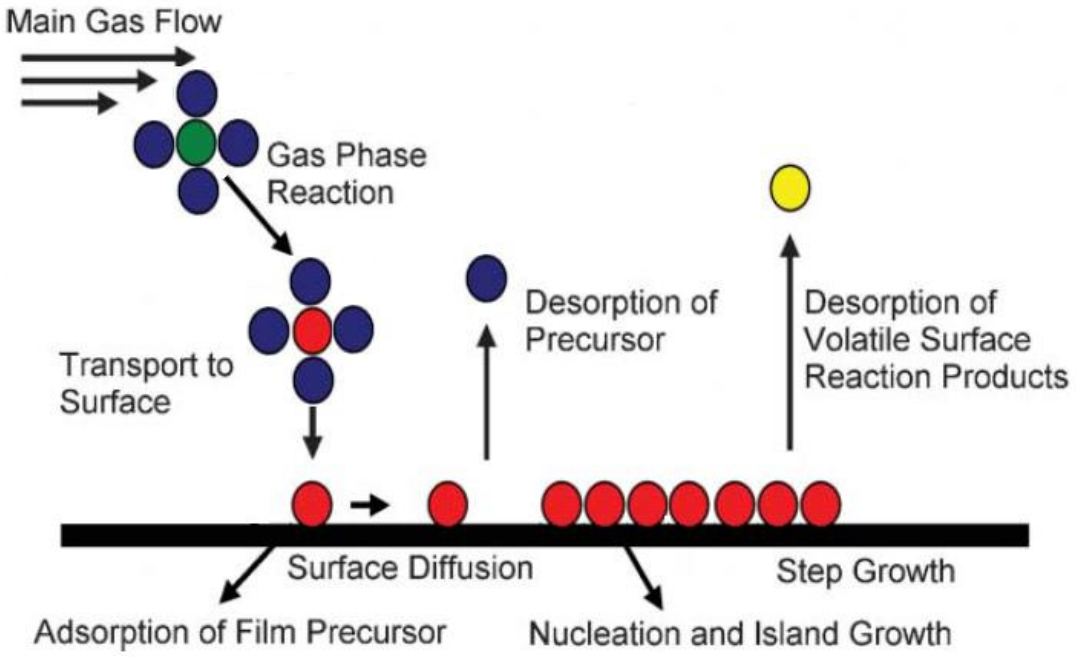


**Figure 1.5.** A schematic mechanism for the deposition of thin films and powders during AACVD process.

Iron sulfide thin films have been prepared by atmospheric or low-pressure metal–organic chemical vapor deposition (AP or LP MOCVD; $FeS_2$) [154-157]. Schleigh and Chang [154] deposited $FeS_2$ thin films using iron pentacarbonyl [$Fe(CO)_5$], hydrogen sulfide, and *tert*-butyl sulfide as precursors by LPCVD. There have been a very limited number of iron complexes employed as single-source precursors for the deposition of iron sulfide as

$Fe_{1+x}S$, $FeS_2$, and $Fe_{1+x}S$ thin films, which include dithiocarbamato complexes $[Fe(S_2CNRR')_3]$ (R, R' = Et, Et,[1] Me, $^{i}$Pr) [158] and the sulfur-bridged binuclear iron carbonyl complex $[Fe_2(CO)_6(m\text{-}S_2)]$ [159]. Recently, the O'Brien group used a series of iron(III) thiobiurets complexes as single source precursors for the synthesis of iron sulfide thin films by the aerosol assisted chemical vapour deposition (AACVD) method [160]. Different iron sulfide phases, including FeS hexagonal troilite, cubic pyrite ($FeS_2$) and tetragonal pyrrhotite ($Fe_{1+x}S$), were deposited depending on the nature of precursor and the deposition temperature. The unsymmetrical $[Fe(S_2CNEt^{i}Pr)_3]$, $[Fe(S_2CNEtMe)_3]$ and symmetrical $[Fe(S_2CN(Hex)_2)_3]$, $[Fe(S_2CN(Et)_2)_3]$ tris(dialkyldithiocarbamato)iron(III) complexes have also been used as single source precursors for the deposition of iron sulfide thin films by AACVD method [161]. The iron sulfide thin films deposited had mixed phases (pyrite and marcasite) at all deposition temperatures except the complex $[Fe(S_2CN(Et)_2)_3]$ which deposited pyrite and pyrrhotite at 400 °C. The symmetrical complex $[Fe(S_2CN(Hex)_2)_3]$, with longer alkyl groups produced a mixture of pyrite and pyrrhotite phases at 350 and 450 °C but pyrite and mackinawite at 400 °C whereas the complex $[Fe(S_2CN(Et)_2)_3]$ with shorter alkyl groups deposited a mixture of pyrite and marcasite at 350 °C but a pure pyrrhotite phase at 400 and 450 °C.

### 1.5.4. Magnetic properties of nanoparticles

The magnetic properties of nanoparticles are influenced by many parameters including their size, shape, chemical composition, crystal structure and interparticle interactions [162]. In bulk/giant magnetic materials, their intrinsic magnetic properties including saturation magnetization, coercive force and curie temperature depend only on their chemical and crystallographic structure but in nanoparticles these properties become

influenced by the finite size and surface effects. The evolution of nanoparticles has provided the opportunity to study magnetic properties from the bulk to the atomic scale. Hence novel properties including superparamagnetism, high magnetic coercivity and quantum tunnelling are sometimes exhibited by these magnetic nanoparticles.

Magnetism is as a result of magnetic moments associated with individual electrons. Magnetic moments originate from two main sources: orbital motion and electron spin. The net magnetic moment is the sum of these moments from all electrons. The magnetic property of a material depends on the response of electrons and magnetic dipoles to an applied magnetic field and these are classified into diamagnetic, paramagnetic, antiferromagnetic, and ferromagnetic materials.

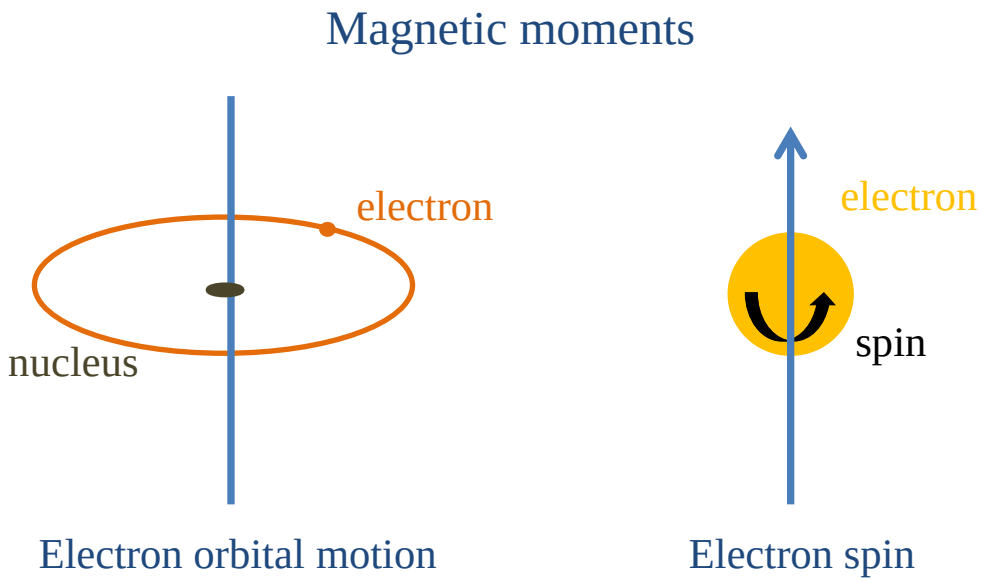


**Figure 1.6.** Magnetic moments arising from electron orbital motion (left) and electron spin (right) [163].

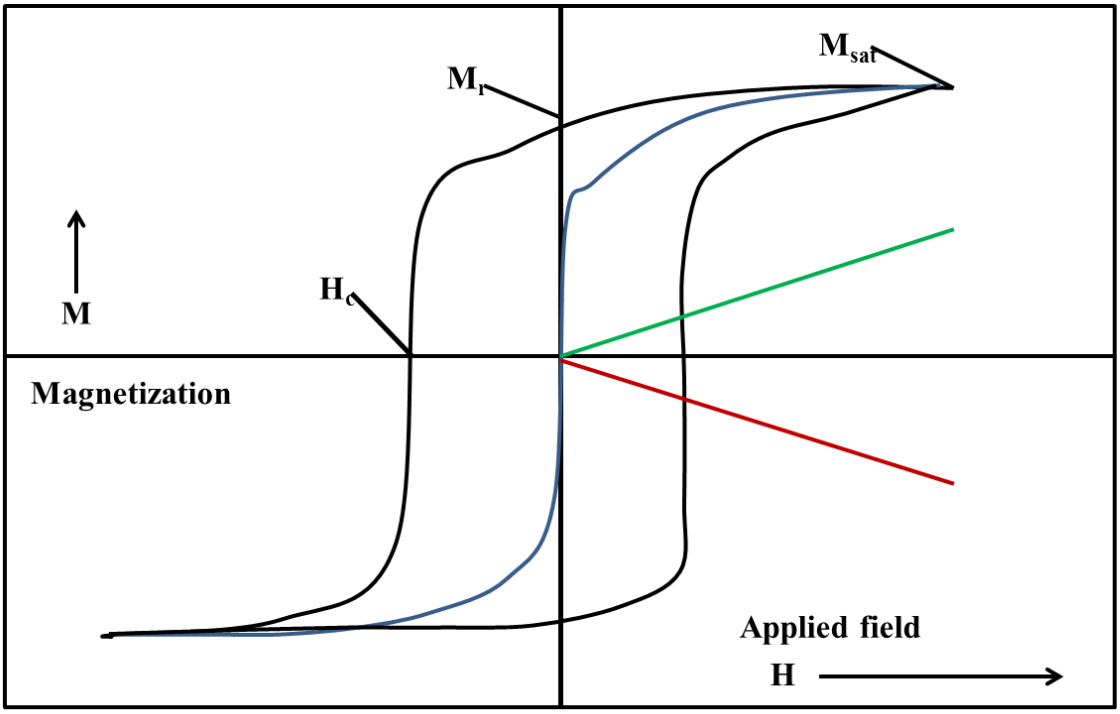


**Figure 1.7.** Hysteresis loops for the different types of magnetic materials [164].

Nanoparticles are said to be in a state of superparamagnetism when the magnetization of the nanoparticles is a single giant magnetic moment in each particle instead of individual atomic moment [165]. This behaviour can be explained in terms of magnetic anisotropy which is defined as the dependence of magnetic properties on a preferred direction. Superparamagnetic materials have a high saturation magnetization but zero coercivity and remanence. This unique property makes it possible for controlling their movement when placed in an external magnetic field. Thus they find numerous applications in biomedicine [166].

## 1.6. Applications of semiconductor nanocrystals

Semiconductor nanocrystals of metal sulfide have potential applications in a number of fields such as solar energy, sensor, biomedicine, electronics, information storage and environmental applications. Some of these applications are discussed in the following subsections.

### 1.6.1. Photovoltaics

The use of fossil fuel is much more limited and causes environmentally highly problematic emission of pollutants. Solar energy, on the other hand is most abundant and does not itself cause any pollution. Thus, highly attractive alternative technologies have been developed to replace fossil fuels. Using solar energy is well established as a form of electrical energy. It can be generated in photovoltaic (PV) cells. Established technology uses various forms of silicon, but economically more competitive materials have been well investigated including polymers and oxides of cheap elements to replace silicon and other expensive solid state semiconductors [167]. Significant efforts have been made to overcome solar energy conversions efficiencies, such as stacked multi-junction systems where by stacks of cells are wired up in series to optimize energy conversion efficiencies [168]. Also, photonic engineering method has been proposed that works with a single absorber material [169].

### 1.6.2. Sensor technology

Sensor technology has made tremendous progress in recent years. A multitude of nanobased sensor materials such as semiconductors is deposited on selected areas of a chip or on a nano-cantilevers and serves to analyse gas mixtures by measuring solubility, vapour pressure, melting point or reaction of the components [170]. Other sensors are functionalized by biomolecules which allow a selective trapping of biomolecules, viruses or cells via

molecular recognition [171]. Such a complex miniaturised sensor, which is often termed lab-on-a-chip, requires a high degree of inter-displinary cooperation among chemists, biochemists, physists, materials scientists and engineers.

### 1.6.3. Photocatalysts and environmental technologies

Nanomaterials have been explored greatly with regard to their potential use in solving environmental problems. Nanoporous aluminosilicates have been used as adsorbents to bind radionuclide and poisonous transition metal ions for removal from waste [172,173]. These materials are also known for their high sorption capacity and tuneable selectivity. Some gold nanoparticles have been reported to be used for the degradation of toilet odours [174]. Zinc oxide has been reported to be used as a photocatalyst for the degradation of chlorinated phenols [175]. It is not far that, the walls of the swimming pools will be coated by an ultra-thin layer of photocatalytically active materials. Activation of oxygen leads to the formation of hydroxyl radicals which are strong antibacterial agents and can degrade many organic compounds.

### 1.6.4. Applications in medicine

Nanoparticles offer some attractive possibilities in biomedicine. They are smaller than or of comparable size to a cell (10 – 100 μm) or a virus (20 – 450 nm). They can therefore move more or less freely within an organism. They may be coated to make them compatible with, mimic or bind to a biological entity of interest. Ferromagnetic nanoparticles have also been developed and are further optimized in view of applications for targeted delivery of therapeutics drugs, genes or radionuclides [176]. Artificially induced hyperthermia is one of the possible techniques which involve dispersing magnetic particles throughout the target

tissue and then applying an alternating magnetic field of sufficient strength and frequency [177]. Also magnetic nanoparticles have been applied in contrast enhancement agents for magnetic resonance imaging [178].

## 1.7. Statement of the research problem

There have been great developments of reliable and reproducible methods for producing large amounts of uniformly sized inorganic nanocrystals as a major aspiration in materials chemistry research over several past years. In the case of semiconductors, one of the most reported and cited approach for the preparation of semiconductor nanoparticles has been the hot injection route reported by Bawendi group [12]. The method suffers from the use of volatile metal alkyl [$Cd(CH_3)_2$], a limitation towards further extension of this approach. The use of single source precursors for the synthesis of semiconductor nanomaterials solves this problem. Several classes of SSPs for the preparation of semiconductor nanoparticles have also been reported. These include xanthates [17,18], dithiocarbamates [15], thiourea [19,20] and thiosemicarbazide [21, 22] complexes.

This work seeks to expand the work on the utilization of heterocyclic dithiocarbamates metal complexes as single source precursors for the synthesis of binary cadmium, lead and iron sulfide materials for electronic applications.

## 1.8. Scope of the work

This work focuses on the synthesis of heterocyclic dithiocarbamate complexes of cadmium, lead and iron that are suitable as single source precursors for the synthesis of cadmium sulfide, lead sulfide and iron sulfide nanomaterials. The work includes the production of

cadmium sulfide nanoparticles and thin films, lead sulfide thin films and iron sulfide thin films and nanoparticles synthesized by hot injection and chemical deposition methods.

## 1.9. Objectives

The main objective was to synthesize heterocyclic metal (Cd, Pb and Fe) dithiocarbamate complexes as single source precursors for the preparation of nanoparticles and thin films.

The specific objectives of this project were:

1. To synthesize and characterize heterocyclic metal (Cd, Pb and Fe) dithiocarbamate complexes

2. To synthesize and characterize cadmium sulfide nanomaterials

3. To synthesize and characterize lead sulfide thin films

4. To synthesize and characterize iron sulfide nanoparticles and thin films

5. To establish and study the gas sensing application of iron sulfide nanoparticles.

## 1.10. Thesis layout

This thesis is composed of six chapters

| |
|---|
| 1. Chapter one is an introduction and literature review summarizing the scientific knowledge related to the subjects mentioned in this thesis |
| 2. Chapter two details the synthesis, results and discussion of piperidine and tetrahydroquinoline cadmium complexes and their cadmium sulfide thin films |

| |
|---|
| and nanoparticles |
| 3. Chapter three. This is based on the synthesis results obtained of lead sulfide thin films deposited by AACVD and spin coating of lead dithiocarbamate complexes |
| 4. Chapter four gives the details of the synthesis and characterization of iron sulfide thin films obtained by AACVD of its dithiocarbamate complex |
| 5. Chapter five extends the use of iron dithiocarbamate complexes to synthesize iron sulfide nanoparticles and their use for gas sensing applications |
| 6. Chapter six summarizes the results obtained from this project, challenges and recommendations for future work. |

## 1.11. References


1. L. E. Brus, J. Chem. Phys. 1984, 80, 4403
2. W. J. Parak, L. Manna, F. C. Simmel, D. Gerion and P. Alivisatos, Nanoparticles: From Theory to Application. 2004. Wiley- VCH, Weinheim, Germany. Pg. 1
3. A. P. Alivasatos, Sci. 1996, 27, 933
4. N. Chestnoy T. D. Harris, R. Hull and L. E. Brus, J. Phys. Chem. 1986, 90, 3393
5. L. E. Brus, J. Chem. Phys. 1983, 79, 5560
6. Y. Wang and N. Herron, J. Phys. Chem. 1991, 95, 525
7. H. Weller, Adv. Mater. 1993, 5, 88
8. J. H. Fendler and F. C. Meldrum, Adv. Mater. 1995, 95, 607
9. A. Hagfeldt and M. Gratzel, Chem. Rev. 1995, 95, 49
10. M. A. Malik and P. O'Brien, Top Organomet. Chem. 2005, 9, 173
11. J. G. Brennan, T. Siegrist, P. J. Carroll, S. M. Stuczynski, P. Reynders, L. E. Brus and M. L. Steigerwald, Chem. Mater. 1990, 2, 403
12. C. B. Murray, D. J. Norris and M. G. Bawendi, J. Am. Chem. Soc. 1993, 115, 8706
13. Z. A. Peng and X. Peng, J. Am. Chem. Soc. 2001, 123, 183
14. D. Fan, M. Afzaal, M. A. Malik, C. Q. Nguyen, P. O'Brien and J. P. Thomas, Coord. Chem. Rev. 2007, 251, 1878
15. T. Trindade and P. O'Brien, Adv. Mater. 1996, 8, 161
16. T. Trindade, P. O'Brien and X. Zhang, Chem. Mater. 1997, 9, 523
17. P. S. Nair, T. Radhakrishnan, N. Revaprasadu, G. A. Kolawole and P. O'Brien, J. Mater. Chem. 2002, 12, 2722
18. Z. Zhihua, S. H. Lee, J. J. Vittal and W. S. Chin, J. Phys. Chem. B. 2006, 110, 6649

19. M. J. Moloto, N. Revaprasadu, P. O'Brien and M. A. Malik, J. Mater. Sci: Mater. Electronics. 2004, 15, 313.
20. P. S. Nair and G. D. Scholes, J. Mater. Chem. 2006, 16, 467.
21. P. S. Nair, T. Radhakrishnan, N. Revaprasadu, G. A. Kolawole and P. O'Brien, Chem. Commun. 2002, 564.
22. M. Salavati-Niasari, A. Sobhani and F. Davar, J. Alloy. Compd. 2010, 507, 77.
23. D. L. Nyamen, R. S. V. Pullabhotla, A. A. Nejo, P. Ndifon and N. Revaprasadu, New J. Chem. 2011, 35, 1133.
24. D. L. Nyamen, A. A. Nejo, P. Ndifon and N. Revaprasadu, Dalton Trans. 2012, 41, 8297.
25. T. Mthethwa, R. S. V. Pullabhotla, P. S. Mdluli, J. Wesley-Smith and N. Revaprasadu, Polyhedron. 2009, 28(14), 2977.
26. G. Krauter, P. Favreau and W. S. Rees, Chem. Mater. 1994, 6, 543.
27. P. Boudjouk, B. R. Jarabek, D. L. Simonson, D. J. Seidler, D. G. Grier, G. J. McCarthy and L. P. Keller, Chem. Mater. 1998, 10, 2358.
28. A. F. Wells, Structural Inorganic Chemistry. 5$^{th}$ Edition, Oxford Science Publications, 1984. ISBN 0-19-855370-6.
29. L. X. Reynolds, T. Lutz, S. Dowland, A. MacLachlan, S. King and S. A. Haque, Nanoscale, 2012, 4, 1561-1564.
30. P –F. Yin, T. Ling, Y–R. Lu, Z. –W Xu, S-Z. Qiao and X–W. Du, Adv. Mater. 2014, 27, 740-745.
31. F. Cao, H. Wang, Z. Xia, X. Dai, S. Cong, C. Dong, B. Sun, Y. Lou, Y. Sun, J. Zhao and G. Zou, Mater. Chem. Phys. 2015, 149-150, 124-128.

32. S. Nizamoglu, E. Mutlugun, O. Akyuz, N. K. Perkgoz, H. V. Demir, L. Liebscher, S. Sapra, N. Gaponik and A. Eychmüller, New J. Phys. 2008, 10, 023026.
33. J. I. Wong, N. Mishra, G. Xing, M. Li, S. Chakrabortty, T. C. Sum, Y. Shi, Y. Chan and H. Y. Yang, ACS Nano, 2014, 8, 2873-2879.
34. E. V. Kolobkova, D. S. Kukushkin, N. V. Nikonorov, A. I. Sidorov and T. A. Shakhverdov, Glass Phys. Chem. 2015, 41, 104.
35. X. Fu, J. Liu, Y. Wan, X. Zhang, F. Meng and J. Liu, J. Mater. Chem. 2012, 22, 17782-17791.
36. S. T. Navale, A. T. Mane, M. A. Chougule, N. M. Shinde, J. Kim and V. B. Patil, RSC Adv. 2014, 4, 44547-44554.
37. L. Maserati, I. Moreels, M. Prato, R. Krahne, L. Manna and Y. Zhang, ACS Appl. Mater. Interfaces, 2014, 6, 9517-9523.
38. Y. Zhang, N. Zhang, Z–R. Tang, Y–J. Xu, Chem. Sci. 2012, 3, 2812.
39. A. Girbeti, B. Fabbri, A. Gaiardo, V. Guidi and C. Malagù, Appl. Phys. Lett. 2014, 104, 222102.
40. J. Xiong, W. Wu, Y. Liu, L. Shen and L. Wu, J. Nanopart. Res. 2015, 17, 55.
41. E. Roduner, Chem. Soc. Rev., 2006, 35, 583.
42. U. K. Gautam, R. Seshadri and C. N. R. Rao, Chem. Phys. Lett. 2003, 375, 560
43. B. L. Cushing, V. L. Kolesnichenko and C. J. O'Connor, Chem. Rev. 2004, 104, 3893.
44. N. Pradhan and S. Efrima, J. Am. Chem. Soc. 2003, 125, 2050.
45. R. M. Nirmal, K. Pandian and Sirakumar K, Appl. Surf. Sci. 2011, 257, 2745.
46. A. de Hoz, A. D. Ortiz and A. Moreno, Chem. Soc. Rev. 2005, 34, 164.
47. S. A. Galema, Chem. Soc. Rev. 1997, 26, 233.

48. B. Ludolph, M. A. Malik, P. O'Brien and N. Revaprasadu, Chem. Commun. 1998, 1849.
49. S. Shen, Y. Zhang, L. Peng, B. Xu, Y. Du, M. Deng, H. Xub and Q. Wang, Cryst. Eng. Comm. 2011, 13, 4572.
50. M. A. Malik, P. O'Brien and N. Revaprasadu, Chem. Mater. 2002, 14, 2004
51. N. Revaprasadu, M. A. Malik, P. O'Brien and G. Wakefield, J. Mater. Res. 1999, 14, 3237.
52. P. S. Nair, T. Radhakrishnan, N. Revaprasadu, G. A. Kolawole and P. O'Brien, Polyhedron 2003, 22, 3129.
53. M. Chunggaz, M. A. Malik and P. O'Brien, J. Mater. Chem. 1999, 9, 2433.
54. R. D. Pike, H. Cui, R. Kershaw, K. Dwight , A. Wold, T. N. Blanton, A. A. Wernberg and H. J. Gysling, Thin Solid Films. 1993, 224, 221.
55. G. Hogarth, Prog. Inorg. Chem. 2005, 53, 71.
56. E. R. T. Tiekink, I. Haiduc, Prog. Inorg. Chem. 2005, 54, 127.
57. P. Popluakhin and E. R. T. Tiekink, Acta Cryst. 2008, E64, m1176.
58. P. A. Ajibade and D. C. Onwudiwe, J. Mol. Struct. 2013, 1034, 249.
59. N. Srinivasan and S. Thirumaran, Superlattice Microst. 2012, 51, 912.
60. P. V. Subha, P. Valarmathi, N. Srinivasan, S. Thirumaran and K. Saminathan, Polyhedron. 2010, 29, 1078.
61. M. Chunggaze, M. A. Malik and P. O'Brien, Adv. Mater. Opt. Electron. 1997, 7, 311.
62. C. D. Onwudiwe, C. A. Strydom and O. S. Oluwafemi, New J. Chem. 2013, 37, 834.
63. P. Yan, Y. Xie, Y. Qian and X. Liu, Chem. Commun. 1999, 1293.

64. H.H. Afifi, S.A. Mahmoud, A. Ashour, Thin Solid Films. 263 (1995) 248.

65. P. Nèmec, I. Nèmec, Y. Nahalkova, F. Trojaner, P. Maly, Thin Solid Films. 403-404 (2002) 9.

66. W. Tang, D.C. Cameron, Thin Solid Films. 280 (1996) 221.

67. D. Barreca, A. Gasparotto, C. Maragno, E. Tondello, C. Sada, Chem. Vap. Deposition. 10 (2004) 229.

68. M. B. Hursthouse, M. A. Malik, M. Motevalli and P. O'Brien, Organomet. 10 (1991) 730.

69. D. M. Frigo, O. F. Z. Khan and P. O'Brien, J. Cryst. Growth. 96 (1989) 989.

70. C. Byrom, M. A. Malik, P. O'Brien, A. J. P. White and D. J. Williams, Polyhedron. 19 (2000) 211.

71. K. Ramasamy, M.A. Malik, P. O'Brien and J. Raftery, Dalton Trans. 39 (2010) 1460.

72. F. Maury, Chem. Vap. Deposition. 2 (1996) 113.

73. A. N. Gleizes, Chem. Vap. Deposition. 6 (2000) 115.

74. D. Barreca, A. Gasparotto, C. Maragno, R. Seraglia, E. Tondello, A. Venzo, V. Krishnan and H. Bertagnolli, Appl. Organometal. Chem. 2005, 19, 59.

75. K. S. Youn, K. H. Yu, J. S. Song and I. H. Choi, J. Korean Phys. Soc. 2005, 47(1), 89.

76. K. Ramasamy, M. A. Malik, M. Helliwell, J. Raftery and P. O'Brien, Chem. Mater. 2011, 23, 1471.

77. D. Oyetunde, M. Afzaal, M. A. Vincent, I. H. Hillier and P. O'Brien, Inorg. Chem. 2011, 50, 2052.

78. I. D. Rojas-Montoya, A. Santana-Silva, V. García-Montalvo, M-Á. Muñoz-Hernández and M. Rivera. New J. Chem. 2014. DOI: 10.1039/C4NJ00482E

79. M. A. Ehsan, H. N. Ming, M. Misran, Z. Arifin, E. R. T. Tiekink, A. P. Safwan, M. Ebadi, W. J. Basirun and M. Mazhar, Chem. Vap. Deposition. 2012, 18, 191.
80. A. Bayer, D. S. Boyle, M. R. Heinrich, P. O'Brien, D. J. Otway and O. Robbe, Green Chem. 2000, 79.
81. S. Thirumaran, K. Ramalingam, G. Bocelli, and L. Righi, Polyhedron. 2009, 28, 263.
82. J. L. Machol, W. F. Wise and R. C. Patel, Phys. Rev. B. 1993, 48, 2819
83. L. Bakueva, I. Gorelikov and S. Musikhin, Adv. Mater. 2004, 16, 926
84. T. K. Chaudhuri and S. Chatteries, Proc. Int. Conf. Thermoelectr. 1992, 11, 40
85. P. Yang, C. F. Song, K. M. Lu, X. Yin, G. J. Zhou, D. Xu and D. R. Yuan, Chem. Phys. Lett. 2001, 345, 429.
86. A. K. Dutta T. Ho, L. Zhang and P. Stroeve, Chem. Mater. 2000, 12, 1042.
87. V. L. Colvin, M. C. Schlamp and A. P. Alivisatos, Nature. 1994, 370, 354.
88. T. Trindade, P. O'Brien, X. Zhang and M. Motevalli, J. Mater. Chem. 1997, 7(6), 1011.
89. D. Yu, D. Wang and S. Zhang, J. Cryst. Growth. 2003, 249, 195.
90. D. Wang, D. Yu and M. Shao, J. Cryst. Growth. 2003, 257, 384.
91. M. A. Hines and G. D. Scholes, Adv. Mater. 2003, 15, 1844.
92. J. Joo, B. H. Na, T. Y. Yu, J. H. Yu, Y. W. Kim, F. Wu, J. Z. Zhang and T. Hyeon, J. Am. Chem. Soc. 2003, 125, 11100.
93. H. J. Warner, E. Thomson, R. A. Watt, N. R. Heckenberg and H. Rubinsztein-Dunlop, Nanotechnology 2005, 16, 175.
94. H. J. Warner and H. Cao, Nanotechnology 2008, 19, 305605.

95. K. Ramasamy, A. O. Nejo, N. Ziqubu, P. V. S. R. Rajasekhar, A. A. Nejo, N. Revaprasadu and P. O'Brien, Eur. J. Inorg. Chem, 2011, 5196.

96. S. M. Lee, Y. W. Jun, S. N. Cho and J. Cheon, J. Am. Chem. Soc. 2002, 124, 11244.

97. S. M. Lee, S. N. Cho and J. Cheon, Adv. Mater. 2003, 15, 441.

98. S. Acharya, U. J. Gautam, T. Sasaki, Y. Bando, Y. Golan and K. Ariga, J. Am. Chem. Soc. 2008, 10, 4594.

99. P. O'Brien and T. Trindade, Adv. Mat. Chem. Vap. Dep. 1997, 3, 75.

100. J. PlanteI, T. W. Zeid, P. Yang and T. Mokari, J. Mater. Chem. 2010, 20, 6612.

101. M. A. Ehsan, H. N. Ming, M. Misran, Z. Arifin, E. R. T. Tiekink, A. P. Safwan, M. Ebadi, W. J. Basirun and M. Mazhar, Chem. Vap. Deposition. 2012, 18, 191.

102. J. Akhtar, M. A. Malik, P. O'Brien and M. Helliwell. J. Mater. Chem, 2010, 20, 6116.

103. M Afzaal, K. Ellwood, N. L. Pickett, P. O'Brien, J. Raftery and J. Waters. J. Mater. Chem. 2004, 14, 1310.

104. J. Akhtar, M. Afzaal, M. A. Vincent, N. A. Burton, I. H. Hillier and P. O'Brien, Chem. Commun. 2011, 47, 1991–1993.

105. J. M. Clark, G. Kociok-Köhn, N. J. Harnett, M. S. Hill, R. Hill, K. C. Molloy, H. Saponia, D. Stanton and A. Sudlow. Dalton Trans. 2011, 40, 6893.

106. S. Dowland, T. Lutz, A. Ward, S. P. King, A. Sudlow, M. S. Hill, K. C. Molloy, S. A. Haque, Adv. Mater. 2011, 23, 2739.

107. H. C. Leventis, S. P. King, A. Sudlow, M. S. Hill, K. C. Molloy and S. A. Haque, Nano Lett. 2010, 10, 1253.

108. T. Rath and G. Trimmel, Hybrid Mater. 2014, 1, 15.

109. T. Rath, M. Edler, W. Haas, A. Fischereder, S. Moscher, A. Schenk, R. Trattnig, M. Sezen, G. Mauthner, A. Pein, D. Meischler, K. Bartl, R. Saf, N. Bansal, S. A. Haque, F. Hofer, E. J. W. List and G. Trimmel, Adv. Energy Mater. 2011, 1, 1046.

110. C. Fradler, T. Rath, S. Dunst, I. Letofsky-Papst, R. Saf, B. Kunert, F. Hofer, R. Resel, and G. Trimmel, Sol. Energy Mater. Sol. C 2014, 124, 117.

111. N. Bansal, F. T. F. O'Mahony, T. Lutz and S. A. Haque, Adv. Energy Mater. 2013, 3, 986.

112. L. X. Reynolds, T. Lutz, S. Dowland, A. MacLachlan, S. King and S. A. Haque, Nanoscale. 2012, 4, 1561.

113. F. C. Krebs, S. A. Gevorgyan, and J. Alstrup, J. Mater. Chem. 2009, 19, 5442.

114. M. Pagliaro, R. Ciriminna and G. Palmisano, ChemSusChem. 2008, 1, 880.

115. E. A. Lewis, P. D. McNaughter, Z. Yin, Y. Chen, J. R. Brent, S. A. Saah, J. Raftery, J. A. M. Awudza, M. A. Malik, P. O'Brien, and S. J. Haigh, 2015, 27 (6), 2127. DOI: 10.1021/cm504765z.

116. K. B. Tang, Y. T. Qian, J. H. Zeng and X. G. Yang, Adv. Mater. 2003, 15, 448.

117. I. J. Ferrer, F. Caballero, H. C. Delas and C. Sarchez, Solid State Commun. 1994, 89, 349.

118. J. M. Perez, F. J. Simeone, A. Tsourkas, L. Josephson and R. Weissleder, Nano Lett. 2004, 4, 119.

119. A. K. Dutta, K. S. Maji, N. D. Srivastava, A. Mondal, P. Biswas, P. Paul and B. Adhikary, Appl. Mater. Interfaces. 2012, 4, 1919.

120. H. Zeng, J. Li, J. P. Liu, Z. L. Wang and S. H. Sun, Nature. 2002, 420, 395.

121. D. J. Vaughan and J. R. Craig, (1978). Mineral Chemistry of Metal Sulfides. Cambridge University Press, Cambridge. UK.

122. S. A. Kissin and S. D. Scott, Econ. Geol. 1982, 77, 1739-1754.

123. R. E. Krupp, Eur. J. Mineral. 1994, 6, 265.

124. H. Wang and I. Salveson, Phase Transit. 2005, 78, 547.

125. D. Rickard and G W Luther, Chem. Rev. 2007, 107, 514.

126. W. Han and M Y Gao, Cryst. Growth Des. 2008, 8, 1023.

127. D. W. Wang, Q. H. Wang and T. M. Wang, CrystEngComm. 2010, 12, 755.

128. W. Li, M. Döblinger, A. Vaneski, A. L. Rogach, F. Jäckel and J. Feldmann. J. Mater. Chem. 2011, 21, 17946.

129. J. P. Wilcoxon, P. P. Newcomer and G. A. Samara, Solid State Commun. 1996, 98, 581.

130. I. J. Ferrer, D. M. Nevskaia, C. de las Heras and C. Sanchez, Solid State Commun. 1990, 74, 913.

131. A. K. Abass, Z. A. Ahmed and R. E. Tahir, Phys. Status Solidi A, 1986, 97, 243.

132. H. A. Macpherson and C. R. Stoldt, ACS Nano, 2012, 6 (10), 8940.

133. A. Kirkeminde, R. Scott and S. Ren, Nanoscale, 2012,4, 7649.

134. E. J. Kim and B. Batchelor, Mater. Res. Bull. 2009, 44, 1553.

135. X. H. Chen, and R. Fan, Chem. Mater. 2001, 13, 802.

136. C. Wadia, Y. Wu, S. Gul, S. K. Volkman, J. H. Guo and A. P. Alivisatos, Chem. Mater. 2009, 21, 2568.

137. Q. Z. Yao, M. L. Li, G. T. Zhou, T. X. Qu, C. F. Mu and S. Q. Fu, CrystEngComm. 2011, 13, 5936.

138. Q. H. Wang, D. W. Wang and T. M. Wang, CrystEngComm. 2010, 12, 3797.

139. Q. H. Wang, D. W. Wang and T. M. Wang, CrystEngComm. 2010, 12, 755.

140. W. H. Feng, Z. Liang, S. Weidong, S. Shuyan, L. Yonngqian, W. Song and Z. Hongjie, Dalton Trans. 2009, 9246.

141. M. Akhtar, J. Akhter, M. Malik, P. O'Brien, F. Tuna, J. Raftery and M. Helliwell, J. Mater. Chem. 2011, 21, 9737.

142. S. Shen, Y. Zhang, L. Peng, B. Xu, Y. Du, M. Deng, H. Xu and Q. Wang, CrystENgComm. 2011, 13, 4572.

143. Y. Zhang, Y. Du, H. Xu and Q. Wang, CrystEngComm. 2010, 12, 3658.

144. W. Han and M. Y. Gao. Cryst. Growth Des. 2008, 8, 1023

145. G. Barone, T. G. Hibbert, M. F. Mahon, K. C. Molloy, L. S. Price, I. P. Parkin, A. M. E. Hardy, M. N. Field, J. Mater. Chem. 2001, 11, 464.

146. I. P. Parkin, L. S. Price, T. G. Hibbert, K. C. Molloy, J. Mater. Chem. 2001, 11, 1486.

147. J. H. Park, M. Afzaal, M. Kemmler, P. O'Brien, D. J. Otway, J. Raftery, J. Waters, J. Mater. Chem. 2003, 13, 1942.

148. C. J. Carmalt, S. A. O'Neill, I. P. Parkin, E. S. Peters, J. Mater. Chem. 2004, 14, 830.

149. E. S. Peters, C. J. Carmalt, I. P. Parkin, D. A. Tocher, Eur. J. Inorg. Chem. 2005, 4179.

150. M. H. C. Jin, K. K. Banger, J. D. Harris, A. F. Hepp, Mater. Sci. Eng. B 2005, 116, 395.

151. M. Kemmler, M. Lazeel, P. O'Brien, D. J. Otway, J. H. Park, J. Mater. Sci.: Mater. Electron. 2002, 13, 531.

152. M. Nyman, M. J. Hampden-Smith, E. N. Duesler, Chem. Vap. Deposition 1996, 2, 171.

153. G. A. Horley, M. R. Lazell, P. O'Brien, Chem. Vap. Deposition 1999, 5, 203.

154. D. M. Schleigh and H. S. W. Chang, J. Cryst. Growth. 1991, 112, 737.

155. B. Thomas, C. Hoepfner, K. Ellmer, S. Fiechter and H. Tributsch, J. Cryst. Growth. 1995, 146, 630.

156. B. Thomas, T. Cibik, C. Hoepfner, D. Diesner, G. Ehlers, S. Fiechter, K. Ellmer, J. Mater. Sci. 1998, 9, 61.

157. B. Meester, L. Reijnen, A. Goossens and J. Schoonman, J. de Physique (Paris). 1999, 9, 613.

158. P. O'Brien, D. J. Otway and J. H. Park, Mater. Res Soc. 2000, 606, 133.

159. S. G. Shyu, J. S. Wu, C. C. Wu, S. H. Chuang and K. M. Chi, Inorg. Chim. Acta. 2002, 334, 276.

160. K. Ramasamy, M. A. Malik, M. Helliwell, F. Tuna and P. O'Brien, Inorg. Chem. 2010, 49, 8495.

161. M. Akhtar, A. L. Abdelhady, M. A. Malik and P. O'Brien, J. Cryst. Growth 2012, 346, 106–112.

162. Y. A. Koksharov, Magnetism of Nanoparticles: Effects of size, shape and interactions. In Magnetic Nanoparticles, 1st Edtion; S. P. Gubin. Wiley-VCH, Berlin, Germany. 2009; 228-229.

163. D. C. William and D. G. Rethwisch, Wiley: Fundamentals of Materials Science and Engennering, 5th Edition SI Version, 2012.

164. M. Arruebo, R. Ferńandez-pacheco, M. R. Ibarra and J. Santamaría. Nanotoday. 2007, 2, 22.

165. A. H. Lu, E. L. Salabas and F. Schüth. Angew. Chem. Int. Ed. 2007, 46, 1222.

166. N. K. Devaraj, B. H. Ong and M. Matsumoto. Syn. React. Inorg. Met. Org. Nano-met. Chem. 2008, 38, 208.

167. P. V. Kamat, J. Phys. Chem. C. 2007, 111, 2834.

168. M. S. Dresselhaus and I. L. Thomas, Nature. 2001, 414, 332.

169. Z. Yu, S. Sandhu and S. Fan, Nano Lett. 2014, 14, 66.

170. C. S. S R. Kumar, Nanomaterials for biosensors, Vol. 8, 2007, Wiley-VCH Verlag GmbH and Co., Weinheim, Germany

171. R. H. Griffin, O. Mozenson, M. A. Beking, M. C. DeRosa, G. Lopinski and N. G. Tarr, Nuclear Science: IEEE Transactions, 2014, 61, 1112.

172. S. A. El-Safty, A. Shahat and M. R. Awual, J. Colloid Interface Sci. 2011, 359, 9.

173. S. A. El-Safty, A. Shahat and M. Ismael, J. Hazard Mater. 2012, 201-202, 23.

174. D. T. Thompson, Gold Bulletin, 2001, 34(2), 56.

175. I. Udom, P. D. Myers, M. K. Ram, A. F. Hepp, E. Archibong, E. K. Stefanakos and D. Y. Goswami, Am. J. Analyt. Chem. 2014, 5, 743.

176. Q. A. Pankhurst, J. Conolly, S. K. Jones and J. Dobson, J. Phys. D: Appl. Phys. 2003, 36, R167.

177. Y-S. C S. Savitha, S. S. C-K Hsu and F-H. Lin, J. Colloid and Interface Science 2011, 363, 314.

178. R. S. Chaughule, S. Purushotham and R. V. Ramanujan, Proc. Natl. Acad. Sci. India. Sect. A. Phys Sci. DOI: 10.1007/s40010-012-0038-4.

# CHAPTER TWO

# SYNTHESIS OF CADMIUM SULFIDE NANOPARTICLES AND THIN FILMS USING SINGLE SOURCE PRECURSORS

## 2.1. Introduction

Dithiocarbamates (DTCs) are versatile chelating ligands which form stable complexes with transition metals as well as the majority of main group, lanthanide and actinide metals [1]. Cadmium complexes of alkyl DTCs, with varying chain lengths, have been extensively reported [2-8]. These complexes have been used as single source precursors (SSPs) for the deposition of high quality cadmium sulfide (CdS) thin films and nanomaterials. Recently, the Revaprasadu group reported the use of heterocyclic DTC complexes of cadmium for shape controlled CdS nanostructures through the hot injection route [9-11].

Intensive studies on numerous Cd and Zn-DTC complexes and their adducts of pyridine, 2,2′-bipyridine and 1,10-phenanthroline ligands, have been reported [12-17]. These five to six-coordinate adducts showed increased electron density at the metal centre, seemingly due to back donation of electrons from the N atom. Furthermore, they are relatively more volatile, due to the incorporation of nitrogen-containing Lewis base ligands [18]. Studies on the effect of these nitrogen-containing Lewis base ligands in heterocyclic Cd-DTC complexes on the properties of CdS nanoparticles have recently been reported. Srinivasan and Thirumaran have investigated the influence of pyridine as a ligand in the precursor for the synthesis of CdS nanoparticles [19]. Onwudiwe *et al*. synthesized CdS nanoparticles by thermolysis of the 2,2′-bipyridine and 1,10-phenanthroline adduct of cadmium ethyl phenyl dithiocarbamate complexes in hexadecylamine (HDA) [20]. In both studies, the incorporation of nitrogen-donor ligands in the precursor enhances the axial growth direction of CdS nanoparticles [21].

The use of SSPs can potentially provide several key advantages over other routes due to the existence of preformed bonds which can lead to a material with fewer defects and better stoichiometry [22]. In addition to DTC-type complexes, other SSPs have been exploited in the deposition of CdS thin films, using various chemical vapour deposition (CVD) methods [22-25]. O'Brien and co-workers have deposited CdS thin films using a number of Cd-DTC complexes as SSPs, through low pressure metal-organic chemical vapour deposition (LP-MOCVD) technique [18, 26]. Aerosol-assisted chemical vapour deposition (AACVD) remains to be the most exploited and

relatively mild/soft CVD technique [27]; a wide range of metal chalcogenide thin films have been deposited using this method [28,29].

Furthermore, several adducts of cadmium dithiocarbamate complexes have been reported for a couple of years, their capabilities as SSPs for AACVD studies, have not been investigated thoroughly [15-17]. Ehsan *et al.* used *bis*(*N*,*N*-dicyclohexyldithiocarbamato)pyridinecadmium(II) to deposit greenockite CdS thin films, which proved to be suitable for application in photoelectrochemical cells [31]. CdS thin films, in general, possess good electrical and optical properties, including wide band gaps (ca. 2.4 eV) making it an ideal material for solar cell device fabrication [31,32]. Hence, research in this context is of great importance.

In the light of this short literature review, an opportunity has been identified pertaining the synthesis of heterocyclic-based Cd-DTC complexes, then subsequently using them as SSPs to deposit CdS thin films through an AACVD technique. The complexes, *bis*(piperidinedithiocarbamato)cadmium(II) (**1**), *bis*(tetrahydroquinolinedithiocarbamato)cadmium(II) (**2**) and the pyridine adduct of *bis*(piperidinedithiocarbamato)cadmium(II) (**3**), were prepared for this purpose. The complexes have been used as single source precursors to evaluate their potential for the deposition CdS thin films at different reaction temperatures. A pyridine adduct (**3**) has also been used to synthesize CdS nanoparticles by hot injection method.

## 2.2. Experimental

### 2.2.1. Materials and methods

Cadmium chloride 99 %, acetonitrile, 1,2,3,4, tetrahydroquinoline 98 % (Aldrich) and piperidine 99 % (Sigma-Aldrich), petroleum ether, methanol 99.5 %, dichloromethane, carbon disulfide 99.5 %, chloroform, sodium hydroxide 98 %, hexadecylamine (HDA) 98 %, pyridine, tri-n-octylphosphine (TOP) 90 %, toluene and acetone (Merck) were used as purchased without any further purification.

### 2.2.2. Synthesis of ligands

Carbon disulfide (0.1 mol, 6.0 mL) was added in small portions to an equimolar solution mixture of sodium hydroxide (4.0 g, 0.1 mol) in the corresponding amine

(piperidine or tetrahydroquinoline, 0.1 mol), while being cooled in an ice bath at 0-5 °C. After 15 min of addition, a precipitate was formed. This was filtered off, dried in open air and then recrystallised in a mixture of acetone/petroleum ether. The crystalline, white-coloured material was filtered off, washed with chloroform and vacuum dried.

$NaS_2C(NC_5H_{10})$, yield: 90 %. $^1$H NMR (400 MHz, $D_2O$): δ 1.41 (m, 2H, 3-$CH_2$), 1.53 (t, 2H, 4-$CH_2$), 4.28 (t, 2H, 2-$CH_2$). IR ($\nu_{max}$ in cm$^{-1}$, ATR): 967, $\nu$(C=S); 1468, $\nu$(C=N). Anal. Calc. for $C_6H_{12}NS_2ONa$ (%): C, 35.8; H, 6.01; N, 6.96. Found (%): C, 35.9; H, 6.13; N, 6.98.
$NaS_2C(NC_9H_{10})$, Yield: 61 %. $^1$H NMR (400 MHz, $CD_3OD$): δ 2.07 (m, 2H, 3-CH2), 2.73 (t, 2H, 4-CH2), 4.58 (t, 2H, 2-CH2), 7.08–7.85 (m, 4H, Ar–H). IR ($\nu_{max}$ in cm$^{-1}$, ATR): $\nu_{(O-H)}$: 3250, $\nu_{(C=S)}$: 968, $\nu_{(C=N)}$: 1481. Anal. Calc. for $C_{10}H_{10}NS_2Na.2H_2O$: C, 44.93; H, 5.28; N, 5.24. Found: C, 45.43; H, 5.09; N, 5.25.

### 2.2.3. Synthesis of complexes (1), (2) and (3)

A solution of cadmium chloride (5.0 mmol) in distilled water (25.0 mL) was added drop-wise to the solution of the appropriate dithiocarbamate ligand (10.0 mmol). The reaction mixture was stirred for 1 h, and the white (1) and yellow (**2**) precipitates formed were filtered, washed with excess distilled water and vacuum dried overnight.

#### *2.2.3.1. Bis(piperidinedithiocarbamato)cadmium(II) complex (1)*

[Cd(pip-dtc)$_2$], **(1)** (pip = piperidinyl, dtc = dithiocarbamato), Yield: 86%. $^1$H NMR δ ppm (400 MHz, DMSO): 4.13 (t, 8H, 2-$CH_2$), 1.73 (t, 4H, 3-CH2), 1.63 (m, 8H, 3-CH2), IR (cm$^{-1}$, ATR): 967, $\nu$(C═S); 1485, $\nu$(C═N); 388, $\nu$(Cd–S). Anal. calc. for $C_{12}H_{20}N_2S_4Cd$: C, 33.29; H, 4.66; N, 6.47. Found: C, 33.47; H, 4.55; N, 6.43%. M.p. 331 °C.

#### *2.2.3.2. Bis(tetrahydroquinolinedithiocarbamato)cadmium(II) complex (2)*

[Cd(thq-dtc)$_2$], **(2)** (thq = tetrahydroquinoline, dtc = dithiocarbamato), Yield: 69%. $^1$H NMR δ ppm (400 MHz, DMSO): 1.99 (m, 4H, 3-$CH_2$), 2.71 (t, 4H, 4-$CH_2$), 4.24 (t, 4H, 2-$CH_2$), 7.18–7.86 (m, 8H, Ar–H). IR (cm$^{-1}$, ATR): 972, $\nu$(C═S); 1492, $\nu$(C═N); 397, $\nu$(Cd–S). Anal. calc. for $C_{20}H_{20}N_2S_4Cd$: C, 45.40; H, 3.81; N, 5.29. Found: C, 44.88; H, 3.61; N, 4.95%. M.p. 320 °C.

#### *2.2.3.3. Bis(piperidinedithiocarbamato)pyridinecadmium(II) complex (3)*

Complex (**1**) (1.0 mmol) was dissolved in pyridine (25 mL). The light yellow solution obtained was filtered into a beaker and the pyridine was allowed to evaporate at room temperature. After 2 days, the colourless crystals which had formed were isolated by filtration, washed with hexane and vacuum dried.

$[Cd(S_2C(NC_5H_{10}))_2(NC_5H_5)]$, yield: 97%. IR ($\nu_{max}$ in $cm^{-1}$, ATR): 989, $\nu$(C=S); 1544, $\nu$(C=N); 402, $\nu$(Cd–S). Anal. Calc. for $C_{17}H_{25}N_3S_4Cd$ (%): C, 39.87; H, 4.92; N, 8.21. Found (%): C, 39.08; H, 4.32; N, 7.69.

### 2.2.4. Synthesis of CdS nanoparticles

In a typical reaction, 6 mL of a capping agent was heated in a three necked flask, and then purged with $N_2$ throughout the reaction. A mixture of complex (**3**) (0.5 g) dispersed in TOP (6 mL), was injected into the preheated HDA. The reaction mixture was stirred for a further hour at a desired temperature, and then cooled to room temperature. Methanol (45 mL) was added to induce flocculation; yellow-coloured sediments were separated by centrifugation, washed twice with methanol and redispersed in toluene for further characterisation. Only complex (**3**) was used; complexes (**1**) and (**2**) have already been reported for HDA-capped CdS nanoparticles [10].

### 2.2.5. Aerosol assisted chemical vapour deposition of CdS thin films

In a typical deposition, a solution of a complex (0.2 g) dissolved in an appropriate organic solvent (20 mL) is made in a two-necked 100 mL round-bottom flask, equipped with a carrier gas (argon) inlet. Complexes (**1**) and (**2**) were dissolved in acetonitrile, and complex (**3**) was dissolved in chloroform. The other joint of the flask was connected to the reactor tube, through a piece of reinforced tubing. Seven microscope glass substrates (*ca.* 1 x 2 cm) were placed inside the reactor tube, which is placed in a Carbolite furnace. The reaction flask was semi-submerged in a water bath, slightly above the piezoelectric modulator, Pifco ultrasonic humidifier Model No. 1077. The generated aerosol droplets from the precursor solution was transferred into the hot-wall zone of the reactor by a carrier gas, at a desired flow rate controlled by a Platon flow gauge. The schematic diagram of the AACVD setup is provided in

Figure 2.1. The aerosols adsorb on to the glass substrates prior to undergoing thermal decomposition to afford deposited thin films. Deposition temperatures were varied between 350-450 °C.

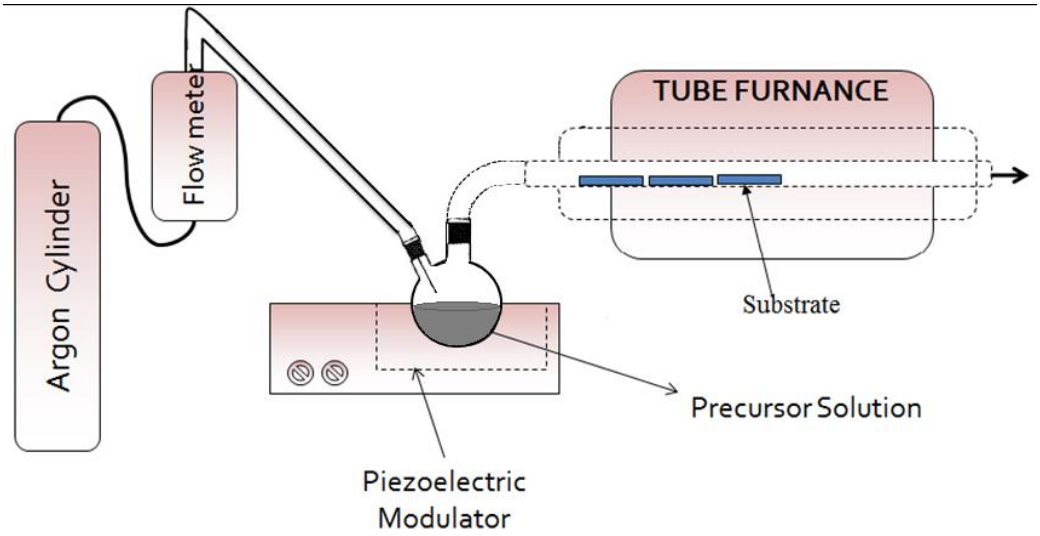


**Figure 2.1.** A schematic diagram of the AACVD apparatus.

### 2.2.6. Characterization techniques

#### *2.2.6.1. Perkin-Elmer automated model 2400 series II CHNS/O analyser*

Elemental (C, H, N) microanalysis provides a highly sensitive analysis of a sample's atomic composition. The analyses were performed on a Perkin-Elmer 2400 series II CHNS/O analyser.

#### *2.2.6.2. Infra-red analysis (IR)*

Infra-red spectra were recorded on a Bruker FT-IR Tensor 27 spectrophotometer, equipped with a standard ATR crystal cell detector. Analyses were performed in the wavenumber range of 200 – 4000 $cm^{-1}$.

#### *2.2.6.3. Thermogravimetric analyses (TGA)*

Thermogravimetric analyses were carried out at 20 °C/min heating rate from 30 °C to 700 °C under $N_2$ gas flow rate of 10 mL/min, using a Perkin Elmer Pyris 6 TGA equipped with a closed perforated ceramic pan.

### *2.2.6.4. $^{1}H$ Nuclear Magnetic Resonance (NMR)*

The $^{1}H$ NMR spectra of both the ligands and Cd(II) complexes were obtained using a Bruker advance III 400 MHz spectrophotometer equipped with trimethylsilane as an internal standard reference. The instrument is housed at the University of KwaZulu-Natal, South Africa.

### *2.2.6.5. Single crystal X-ray crystallography*

Single crystal X-ray diffraction data for complexes were collected on a Bruker APEX diffractometer, using graphite monochromated Cu-$K_\alpha$ radiation ($\lambda$ = 1.54178 Å). The structures were resolved by direct methods, and refined by full-matrix least squares on $F^2$. All non-H atoms were refined anisotropically. Hydrogen atoms were included in calculated positions, assigned isotropic thermal parameters and allowed to ride on their parent carbon atoms. All calculations were carried out using the SHELXTL software suite [33].

### *2.2.6.6. Optical measurements*

For CdS thin films, a Perkin Elmer Lambda 1050 UV/Vis/NIR spectrophotometer was used to carry out UV-Vis absorption measurements while photoluminescence properties were measured using an Edinburgh Instruments FLS900 spectrofluorimeter. For CdS nanoparticles, optical absorption measurements were carried out on a Varian Cary 50 UV-Visible spectrophotometer using quartz cuvettes (1 cm path length), while a Perkin-Elmer LS 55 spectrofluorimeter was used to measure the photoluminescence properties. Raman spectra for few representative samples were recorded using Horiba Jobinyvon Raman spectrometer using 514.5 nm lasers, at room temperature.

### *2.2.6.7. Powder X-ray diffraction (pXRD)*

Powder diffraction patterns of the films and nanoparticles were recorded at room temperature in the high angle 2$\theta$ range (20 – 80 °) using an Advanced Bruker AXS D8 diffractometer, equipped with nickel-filtered Cu $K_\alpha$ radiation ($\lambda$ = 1.542 Å) at 40 kV and 40 mA. The scan speed and step sizes were 0.05 °/min and 0.00657 ° respectively.

#### *2.2.6.8. Transmission electron microscopy (TEM) and high resolution TEM (HRTEM)*

Samples were prepared by evaporating drops of diluted solution of CdS nanoparticles on Formvar-coated Cu grids (150 mesh) for TEM and holey carbon grids for HRTEM analyses. A JEOL 1400 TEM and JEOL 2100 HRTEM were used for respective analyses, at an accelerating voltage of 120 kV and 200 kV, respectively. For TEM, a Megaview III camera was used and the images were captured using iTEM software. For HRTEM, a Gatan camera and Gatan software were used.

#### *2.2.6.9. Scanning electron microscopy (SEM) and Energy dispersive X-ray analysis (EDX)*

The SEM and EDX measurements of the as-deposited thin films were performed on a Philips XL 30 FEG (at 10 kV) and DX4 detector (at 20 kV), respectively. The films were carbon-coated by using Edward's E306A coating system, prior to the analyses. The analyses were carried out at the School of Material Science, University of Manchester, United Kingdom.

#### *2.2.6.10. Atomic Force Microscopy (AFM)*

Atomic force microscopy (AFM) analyses of the as-deposited CdS thin films were carried out on a Bruker Multimode 8 instrument (School of Chemistry, University of Manchester, United Kingdom), and a Bruker Inova (Chemistry Department, University of Zululand, South Africa).

## 2.3. Results and discussion

### 2.3.1. Single crystal X-ray crystallography structures of complex (1) and (3)

The ORTEP crystal structure of *bis*(piperidinedithiocarbamato)cadmium(II), complex (**1**), is shown in Figure 2.2 while the accompanying crystal data and selected bond parameters are provided in Table 2.1 and Table 2.2, respectively. The complex crystallizes in the triclinic crystal system, with space group Pī and Z=2. The structure exhibits a dimeric compound with each of the Cd centre chelated to two DTC ligands through their S atoms. Two S atoms from

two separate DTC ligands form $\mu_3$-S bridges between the two Cd atoms and a C-atom of each of the ligands, thus forming a square pyramidal geometry, Figure 2. The Cd-S bond lengths range from 2.513 to 2.971 Å. The shorter Cd-S bond distances (2.513 – 2.515 Å) lie in the range consistent to Cd-S bond distances in pentacoordinate complexes (range 2.511-2.518A) [34], shorter than values reported for four-coordinate complexes (2.5274 Å) and for six-coordinate complexes (Cd-S range 2.558-2.810Å), thus supporting the involvement of Cd in electron delocalization [34,35]. The longer Cd-S bond lengths involving the $\mu_3$-S are longer than those observed for six-coordinate complexes. The *bis*(tetrahydroquinolinedithiocarbamato)cadmium(II)complex **(2)** did not give the crystals of good enough quality for X-ray single structure elucidation.

**Table 2.1.** Crystal Data and Structural Refinement Parameters for complex (**1**) and (**3**)

| Complex | (**1**) | (**3**) |
|---|---|---|
| Formula | $C_{24}H_{40}Cd_2N_4S_8$ | $C_{17}H_{25}CdN_3S_4$ |
| $M_r$ | 865.88 | 512.04 |
| Cryst Syst | Triclinic | Monoclinic |
| Space group | $P^{-1}$ | P2(1)/c |
| a (Å) | 8.7196(4) | 8.8114(4) |
| b (Å) | 12.5000(9) | 9.8021(5) |
| c (Å) | 15.9023(8) | 24.4201(11) |
| α (deg) | 80.328(5) | 90 |
| β (deg) | 89.921(4) | 95.928 (2), |
| γ (°) | 72.778(5) | 90 |
| V ($Å^3$) | 1629.86(16) | 2097.89 (17) |
| Z, Calculated density (D) | 2, 1.764 Mg $m^{-3}$ | 4, 1.621 Mg $m^{-3}$ |
| Temperature (K) | 100(2) | 180(2) |
| Refinement method | Full-matrix least-squares on $F^2$ | Full-matrix least-squares on $F^2$ |
| Reflections collected /unique | 9866/5919, [R(int)=0.0566] | 10171/3882 [R(int) = 0.0534], |
| Final R indices [I > 2σ(I)] | R1 = 0.0613, wR2 = | R1 = 0.0349, wR2 = 0.0870 |

| | | |
|---|---|---|
| | 0.1649 | |
| R indices (all data) | R1 = 0.0751, wR2 = 0.1736 | R1 = 0.0365, wR2 = 0.0882 |
| largest diff. peak and hole | 2.189 and −1.473 eÅ$^{-3}$ | 0.830 and −0.571 eÅ$^{3}$ |
| GOF | 1.101 | 1.048 |

**Table 2.2** Selected bond lengths (Å) and angles (deg) for complex **(1)**

| | | | | | |
|---|---|---|---|---|---|
| Cd(1)-S(2) | 2.513 (2) | S(2)-Cd(1)-S(3) | 130.86 (9) | S(7)-Cd(2)-S(5) | 135.70 (9) |
| Cd(1)-S(3) | 2.514 (2) | S(2)-Cd(1)-S(1) #1 | 104.79 (8) | S(7)-Cd(2)-S(8) #2 | 102.53 (8) |
| Cd(1)-S(1) #1 | 2.576 (2) | S(3)-Cd(1)-S(1) #1 | 121.58 (8) | S(5)-Cd(2)-S(8) #2 | 119.90 (8) |
| Cd(1)-S(4) | 2.640 (2) | S(2)-Cd(1)-S(4) | 112.54 (8) | S(7)-Cd(2)-S(6) | 110.91 (8) |
| Cd(1)-S(1) | 2.971 (2) | S(3)-Cd(1)-S(4) | 70.60 (7) | S(5)-Cd(2)-S(6) | 70.00 (7) |
| Cd(2)-S(7) | 2.514 (2) | S(1) #1-Cd(1)-S(4) | 106.96 (7) | S(8) #2-Cd(2)-S(6) | 107.20 (7) |
| Cd(2)-S(5) | 2.515 (2) | S(2)-Cd(1)-S(1) | 65.70 (7) | S(7)-Cd(2)-S(8) | 66.31 (7) |
| Cd(2)-S(8) #2 | 2.568 (2) | S(3)-Cd(1)-S(1) | 97.91 (7) | S(5)-Cd(2)-S(8) | 97.20 (7) |
| Cd(2)-S(6) | 2.677 (2) | S(1) #1-Cd(1)-S(1) | 88.86 (7) | S(8) #2-Cd(2)-S(8) | 93.35 (6) |
| Cd(2)-S(8) | 2.917 (2) | S(4)-Cd(1)-S(1) | 163.67 (7) | S(6)-Cd(2)-S(8) | 159.19 (7) |

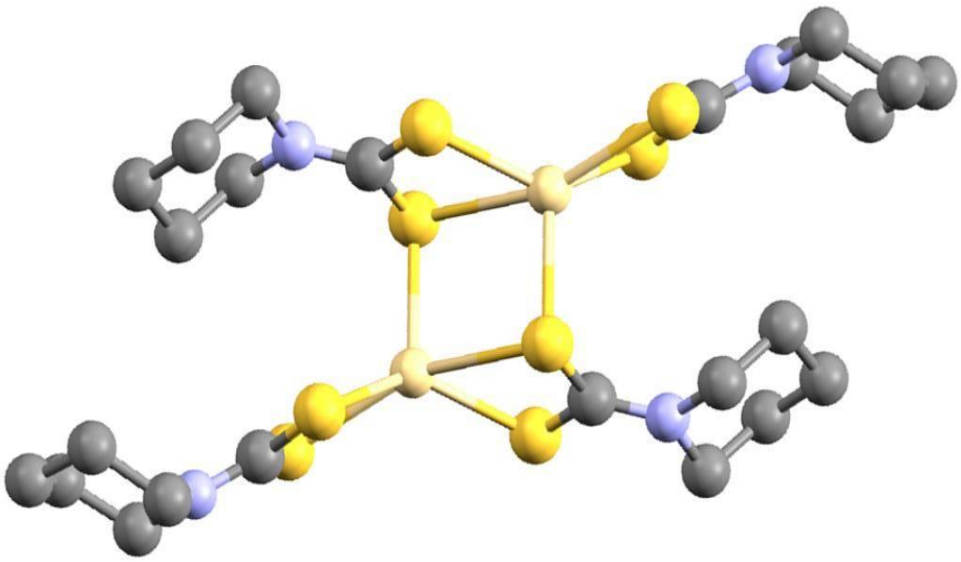

**Figure 2.2.** Single X-ray crystal structure of *bis*(piperidinedithiocarbamato)cadmium(II) complex (**1**). CCDC reference number 1008839.

The single-crystal X-ray structure of *bis*(piperidinedithiocarbamato)pyridinecadmium(II), complex (**3**), is shown in Figure 2.3. There are three coordinating ligands of two different molecules in the symmetric unit of the complex. The pentacoordinated, mixed-ligand complex shows the Cd centre bonded to 4 × S and 1 × N atoms, from two pip-dtc and pyridine ligands, respectively. A square pyramidal geometry is observed. The bond lengths of Cd-S range from 2.5648 to 2.6684 Å, which are longer than that of Cd-N (2.320 Å). Two of the Cd-S bond lengths are relatively longer than the other two in each dithiocarbamato ligand as observed previously [36]. Structural refinement data are given in Table 2.1; selected bond angles and lengths are presented in the caption to Figure 2.3.

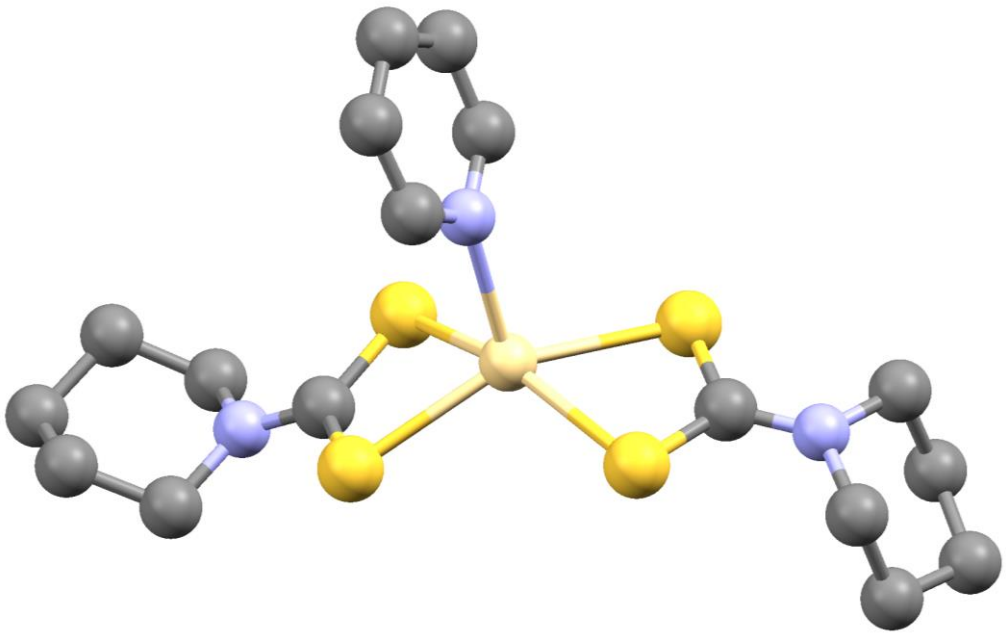

**Figure 2.3.** The X-ray single crystal structure of *bis*(piperidinedithiocarbamato)cadmium(II) complex (**3**). Selected bond lengths (Å) and bond angles (°): Cd(1)-N(3) 2.320(2), Cd(1)-S(3) 2.5648(7), Cd(1)-S(2) 2.5758(7), Cd(1)-S(1) 2.6322(7), Cd(1)-S(4) 2.6684(7), N(3)-Cd(1)-S(3) 107.57(6), N(3)-Cd(1)-S(2) 111.32(6), S(3)-Cd(1)-S(2) 106.77(2), N(3)-Cd(1)-S(1) 102.46(6), S(3)-Cd(1)-S(1) 148.57(2), S(2)-Cd(1)-S(1) 69.65(2), N(3)-Cd(1)-S(4) 94.03(6), S(3)-Cd(1)-S(4) 69.25(2), S(2)-Cd(1)-S(4) 153.95(2), S(1)-Cd(1)-S(4) 99.90(2). CCDC reference number 984434.

### 2.3.2. Thermogravimetric analysis (TGA)

Thermogravimetric analysis (TGA) gives insight into the thermal stability and decomposition pattern undergone by precursors, as well as the product formed after complete decomposition. A single-step decomposition pattern is observed for piperidine (**1**) and tetrahydroquinoline (**2**), displaying a weight loss of 64.9% (decomposed organic matter calc. to afford CdS = 66.6 %) at 331 ˚C and 70.9 % (calc. = 72.7 %) at 320 °C, respectively (Figure 2.4). The final residues 35.1 % and 29.1 % were close to 33.4 and 27.3 %, calculated for the anticipated CdS obtained from complexes (**1**) and (**2**), respectively.

The thermogram of the pyridine adduct (**3**) reveals a two-step decomposition curves between *ca*. 130 °C and 320 °C (Figure 2.4). The first decomposition is attributed to the loss of the pyridine ligand, confirmed by the weight percentage loss of 14.1 %. The remaining residue amounts to 31 %, close to the calculated value of 28 % equivalent to the anticipated CdS. The EDX analysis of the residue suggested a small amount of carbon contamination,

which may explain the higher experimental values obtained. This contamination may be due to the bulky organic moiety of the ligands which does not give a clean decomposition.

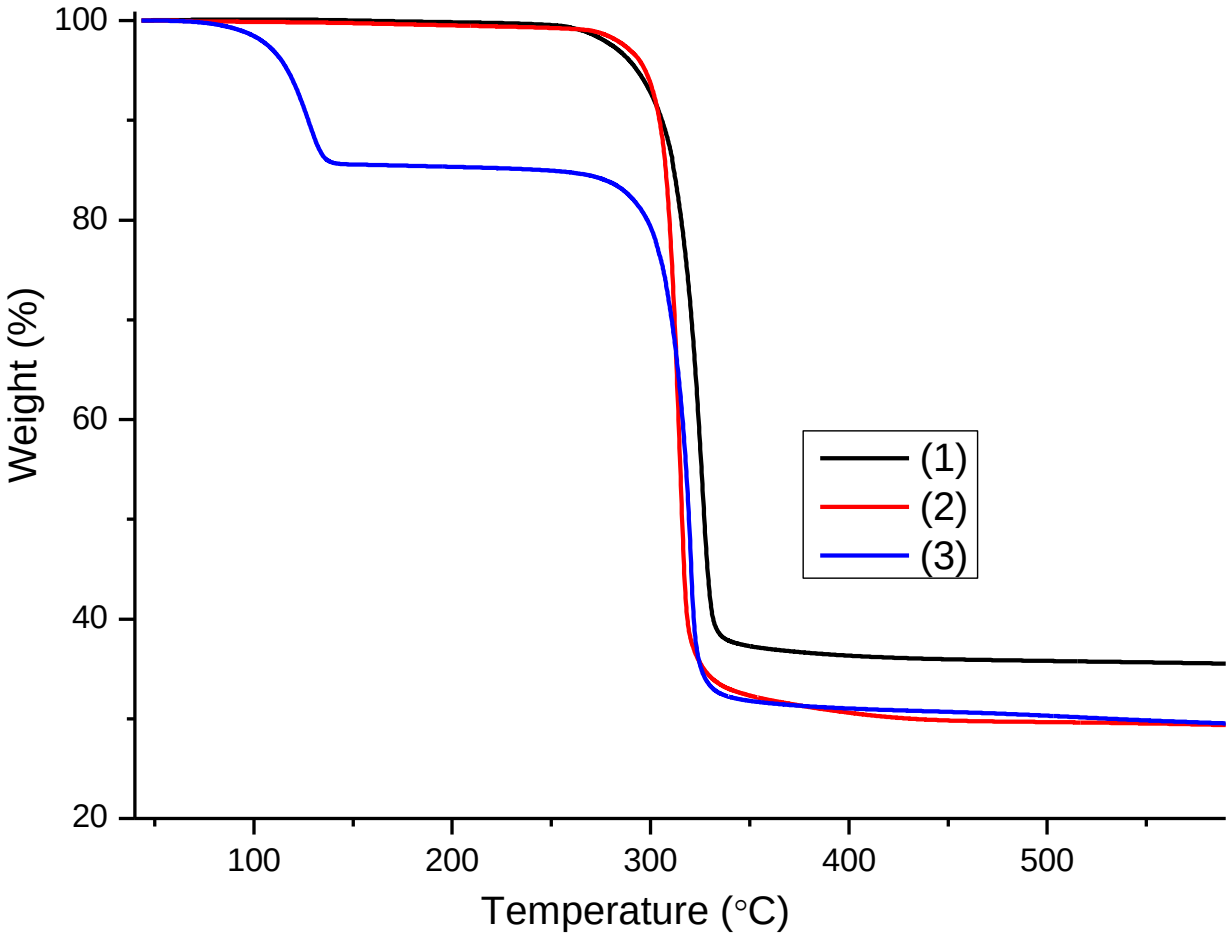


**Figure 2.4.** Thermogravimetric analysis (TGA) plots of complexes (**1**), (**2**) and (**3**) at a heating rate of 10 $^{o}$C/min under inert $N_2$ atmosphere.

### 2.3.3. Optical properties of CdS thin films

The room temperature UV–Vis absorption spectra of the CdS thin films (Figure 2.5) were recorded in the range 320-800 nm, using glass substrate as a reference. The energy band gaps (Eg) were calculated from the corresponding Tauc plots (Inset Figure 2.5). The blue shift in absorption edge is clearly observed from the UV–Vis absorption spectra, when CdS thin films were deposited using complex (**1**). An increase in the deposition temperature from 350 °C to 450 °C influences the band gap of the CdS thin films (Figure 2.6). The average band gap energy of the films was estimated to be 2.38 ± 0.04 eV from the Tauc plots [37]. These observations are similar to those of CdS thin films deposited from complex (**2**),

however the absorption peaks were not as prominent as those from complex (**1)** (Figure 2.6). The photoluminescence (PL) properties of the thin films from complex (**1)** were also investigated at 380 nm excitation wavelength; a blue emission peak at 483 nm with FHWM of 9 nm is observed (Figure 2.7). The broad, red emission peak observed between 520 and 545 nm is due to electron-hole traps (surface defect emission from sulfur vacancies) [38]. It could also be related to microstructure imperfection and lattice defects of the CdS thin films [39].

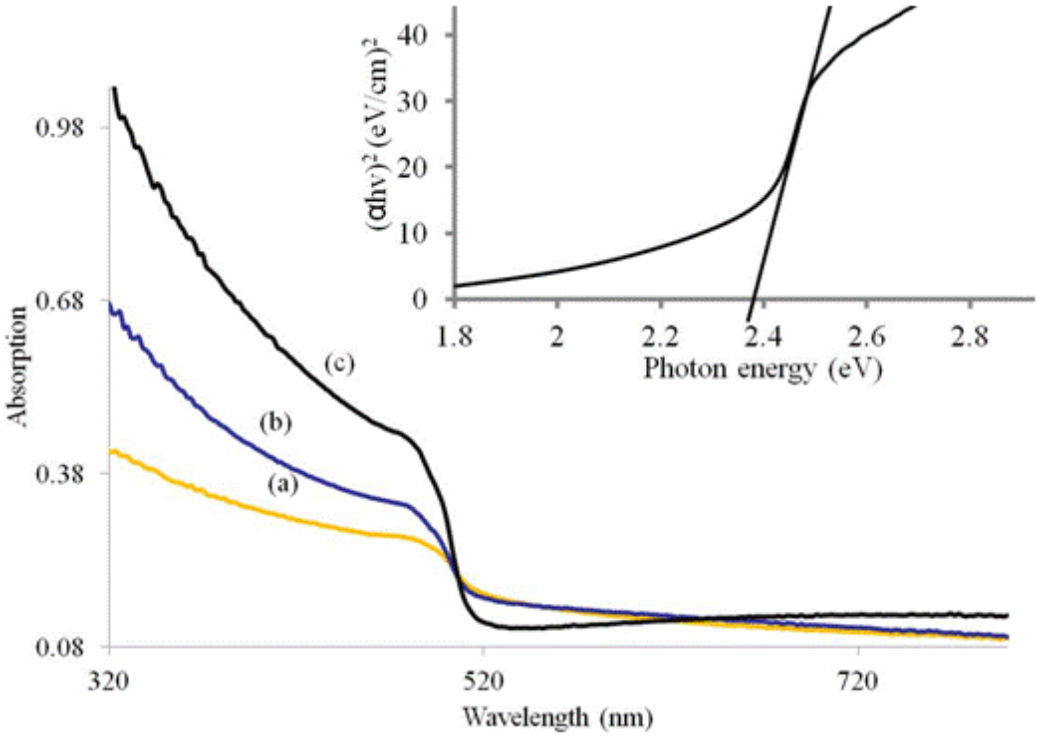


**Figure 2.5.** UV visible absorption spectra of CdS films deposited on glass substrate using complex (**1**) at (a) 350 °C, (b) 400 °C and (c) 450 °C (Inset: Tauc plot showing the estimated optical band gap of 2.38 ± 0.04 eV).

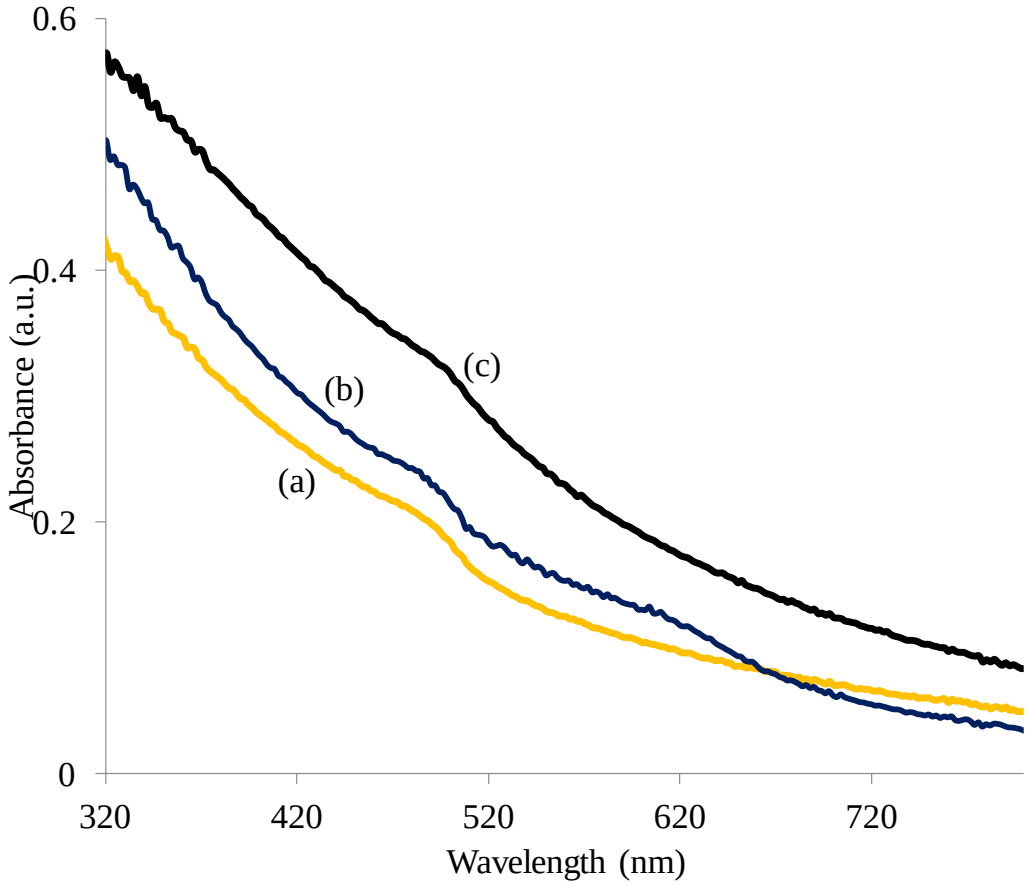


**Figure 2.6.** UV visible absorption spectra of CdS films deposited on glass substrate using complex (**2**) at (a) 350 °C, (b) 400 °C and (c) 450 °C.

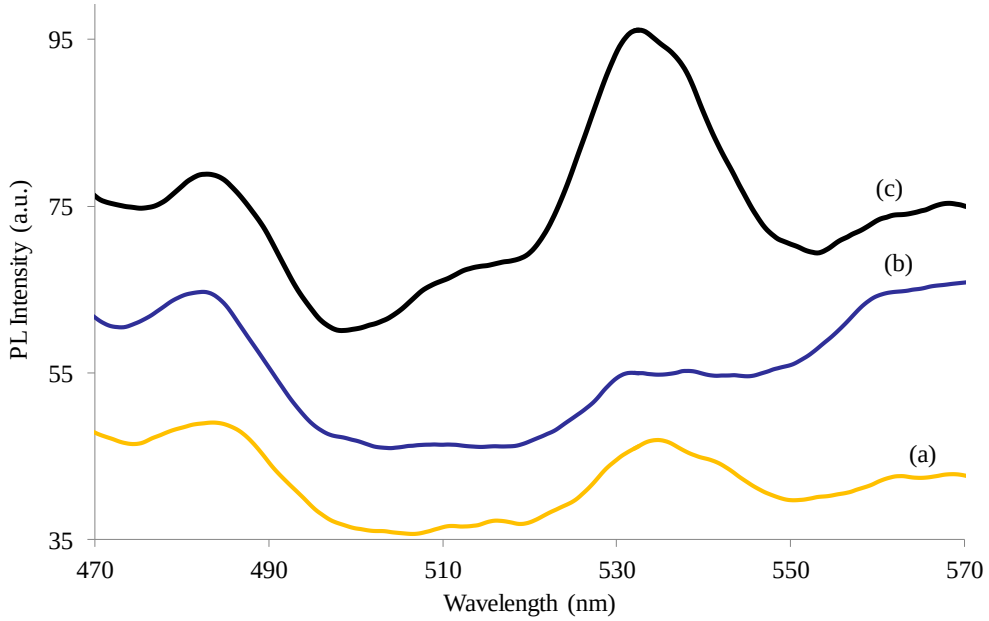


**Figure 2.7.** Photoluminescence emission spectra of CdS thin films deposited from complex (**1**) at (a) 350 °C, (b) 400 °C and (c) 450 °C ($\lambda_{exc}$ = 380 nm).

The UV-Vis absorption spectra of the CdS thin films deposited from an adduct complex (**3**) are shown in Figure 2.8. The sharp absorption edges of the samples at ca. 516 nm confirm the energy of the optical band gap. The optical features of the CdS films were not significantly affected by deposition temperature, with an excitonic peak around 496 nm (2.5 eV); the band gaps estimated from Tauc plot ( inset Figure 2.8) are commensurate with those previously reported for CdS thin films [40,41]. The variation of the fluorescence spectrum of the CdS thin films with reaction temperature is shown in Figure 2.9. There is one narrow, sharp emission peak in the photoluminescence (PL) spectrum due to excitonic emission for the CdS films deposited at 350 °C, which is also located around 510 nm at the deposition temperature of 400 °C. The sharp excitonic emission peaks located near the absorption edge of the films are due to fewer surface trap states [42]. CdS thin films deposited at 450 °C display a much more undefined and broader emission profile.

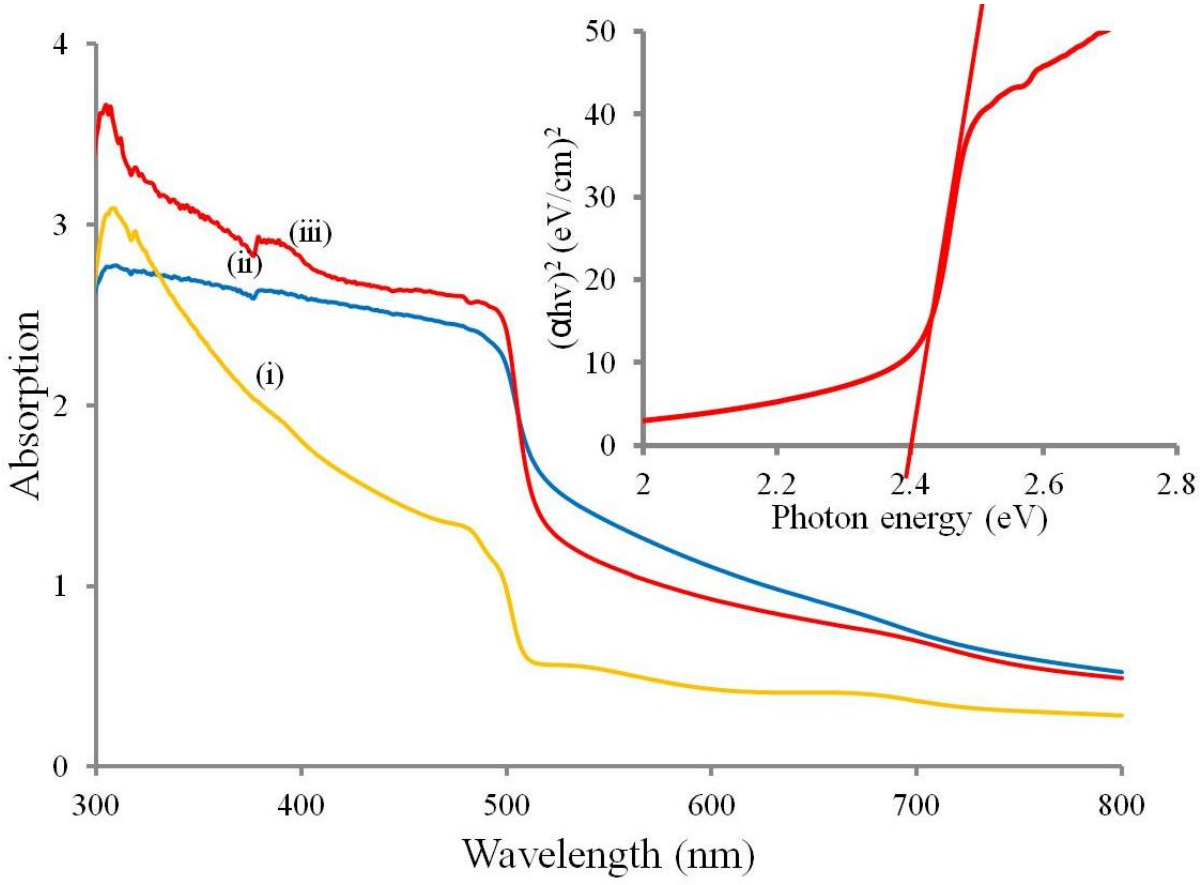


**Figure 2.8.** UV-vis absorption of CdS thin films deposited using an adduct complex (**3**) by AACVD at (i) 350 °C, (ii) 400 °C and (iii) 450 °C. Inset: Tauc plot showing the estimated optical band gap (2.4 ± 0.2 eV).

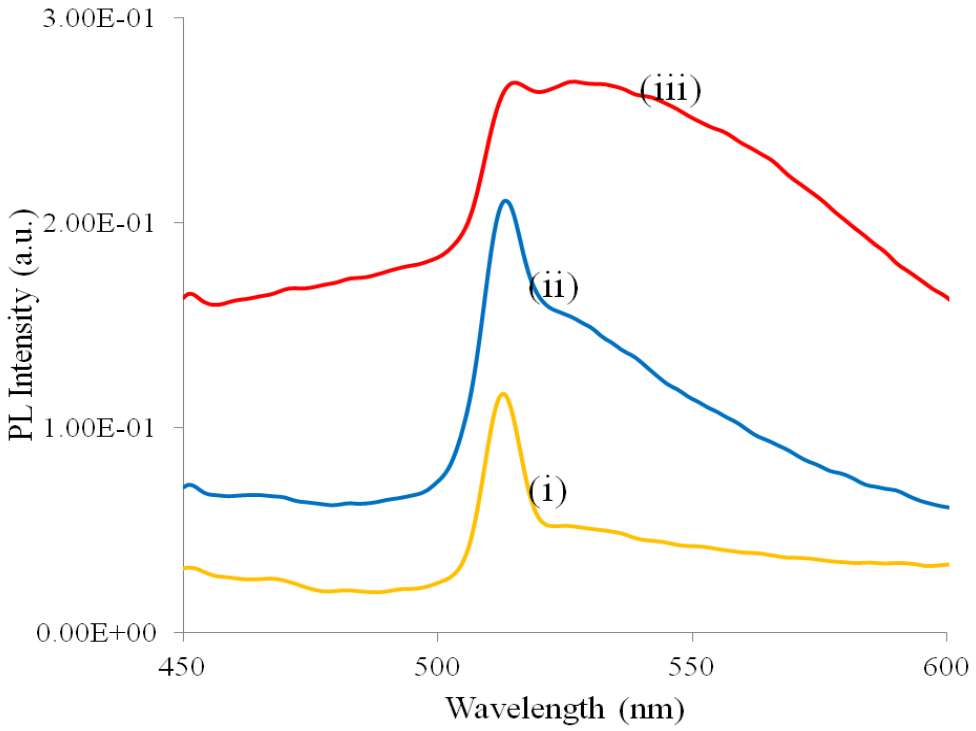


**Figure 2.9.** Photoluminescence emission spectra of CdS thin films deposited using adduct complex (**3**) at (i) 350 °C, (ii) 400 °C, and (iii) 450 °C ($\lambda_{exc}$ = 350 nm). Spectra are corrected for instrument response.

The Raman spectra of CdS thin films of complexes (**1**) and (**2**) are shown in Figure 2.10 and 2.11. The typical peaks of the longitudinal optical (LO) modes of CdS are evident from the Raman spectra. The fundamental frequencies at 297.5 and 599 $cm^{-1}$ correspond to the 1LO and 2LO of the bulk hexagonal CdS system [43,44], while the deposited CdS thin films have 1LO and 2LO at 299 and 603 $cm^{-1}$ respectively. The shift in peak position of CdS thin films towards lower wavelength side was noted. Recently, it has been reported that phonon confinement, strain, defects and broadening associated with the size distribution, were important factors which affect the phonon properties [45]. As a result of the phonon confinement and strain effect, we observed the shift in 1LO and 2LO peak positions of CdS nanoparticles with respect to the bulk CdS.

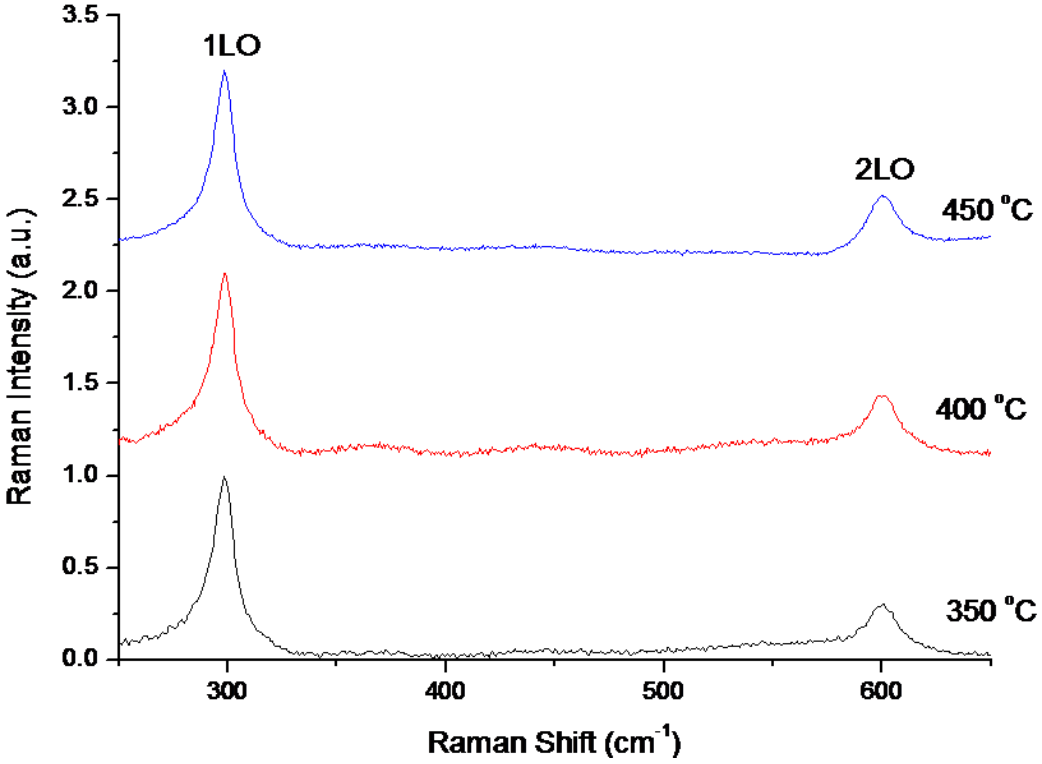


**Figure 2.10.** Raman spectra of CdS thin films deposited by using complex (**1**).

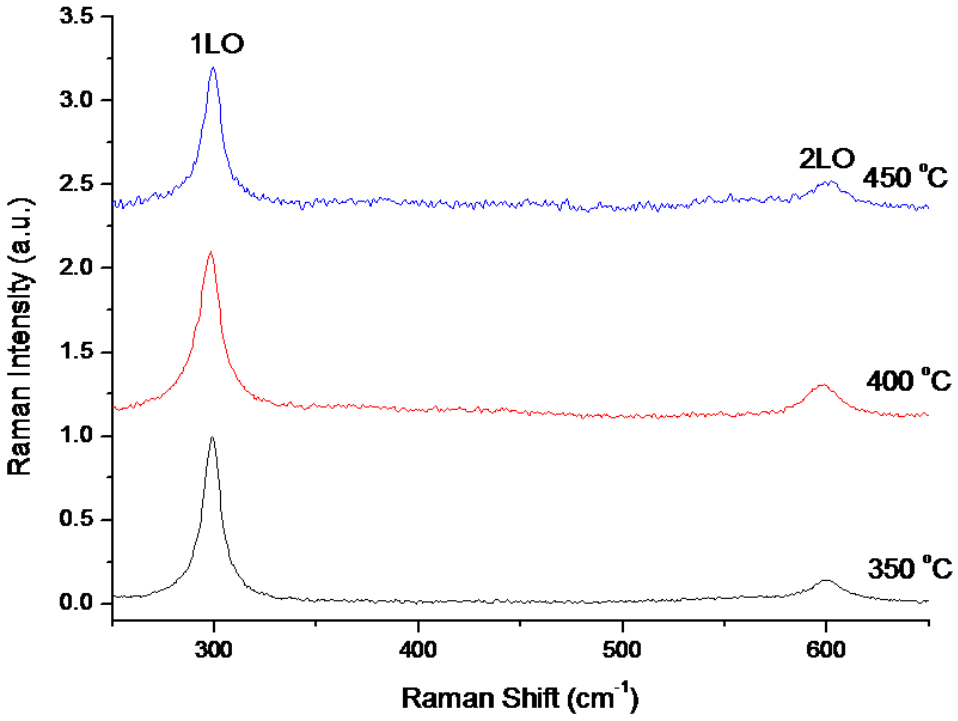


**Figure 2.11.** Raman spectra of CdS thin films deposited by using complex (**2**).

### 2.3.4. Powder X-ray diffraction

The powder X-ray diffraction (p-XRD) patterns of the CdS thin films deposited from complex (**1**), at the three different temperatures, are presented in Figure 2.12. The three dominant peaks in all diffraction patterns can be assigned to the (100), (002), (101) reflections of pure hexagonal CdS phase (card # 01-077-2306). The particle sizes were calculated using Scherrer equation reported elsewhere [46] and were found to be 57.37 nm (350 $^{o}$C), 63.57 nm (400 $^{o}$C) and 72.97 nm (450 $^{o}$C) from the most prominent peak (101). A similar diffraction pattern was observed when complex (**2**) was used, where the hexagonal phase of CdS was dominant (Figure 2.13). Furthermore, the high intensity of (002) peak in p-XRD patterns of CdS thin films deposited from complex (**2**) indicated that the particles preferably grow along the c-axis, while films grown from complex (**1**) prefers (101) plane.

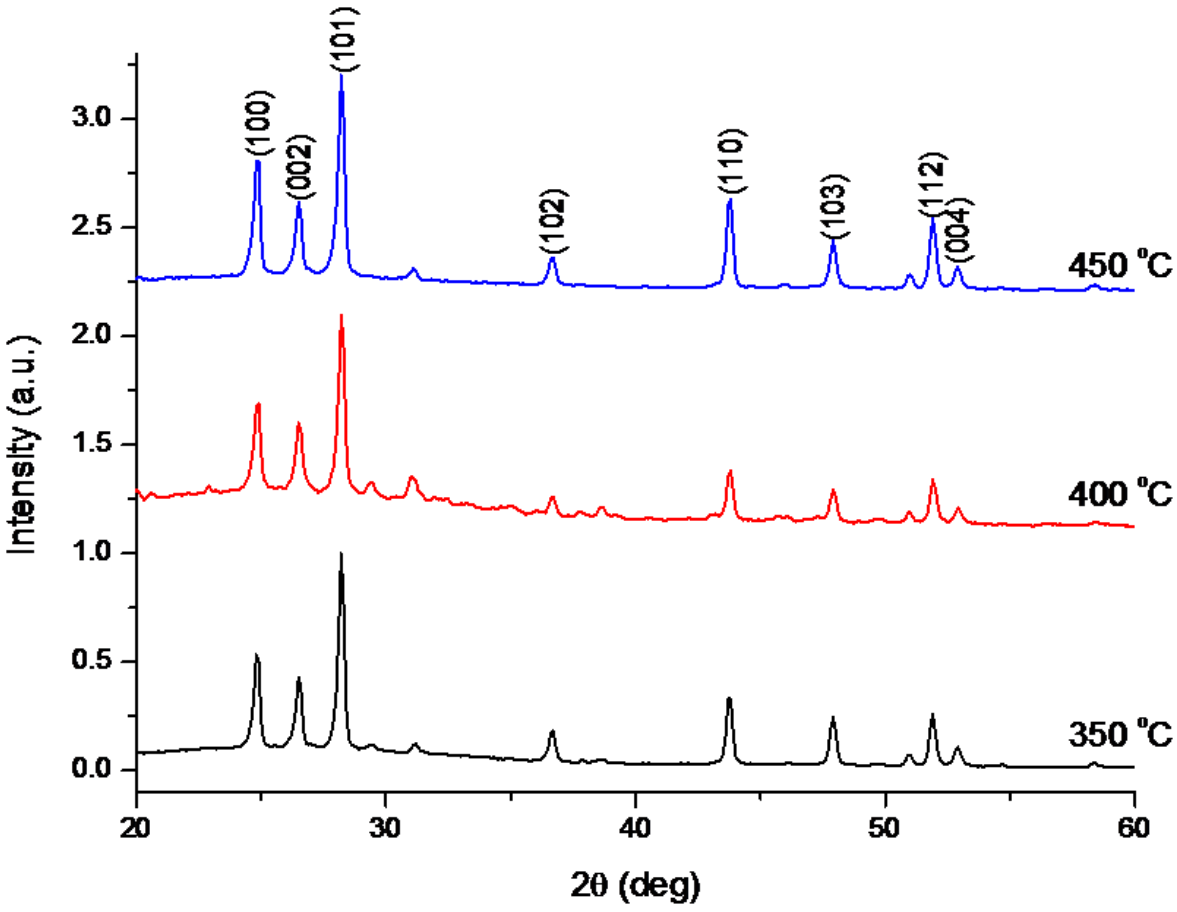


**Figure 2.12.** p-XRD patterns of CdS films deposited on glass substrate using complex (**1**) at (a) 350 $^{o}$C, (b) 400 $^{o}$C and (c) 450 $^{o}$C.

The films deposited from complex (**3**) were analyzed using similar parameters to those from complex (**1**) and (**2**); Cu $K_\alpha$ ($\lambda$ = 1.5406 Å) radiation was used. The diffraction patterns matched the greenockite (hexagonal) CdS structure (JCPDS card no 04-002-3090), Figure 2.14. The seven reflections at 2θ, from 20 to 80°, correspond to the (*hkl*) planes (100), (002), (101), (102), (110), (103) and (112) respectively. There are no signs of any crystalline impurities such as CdO, elemental Cd and S.

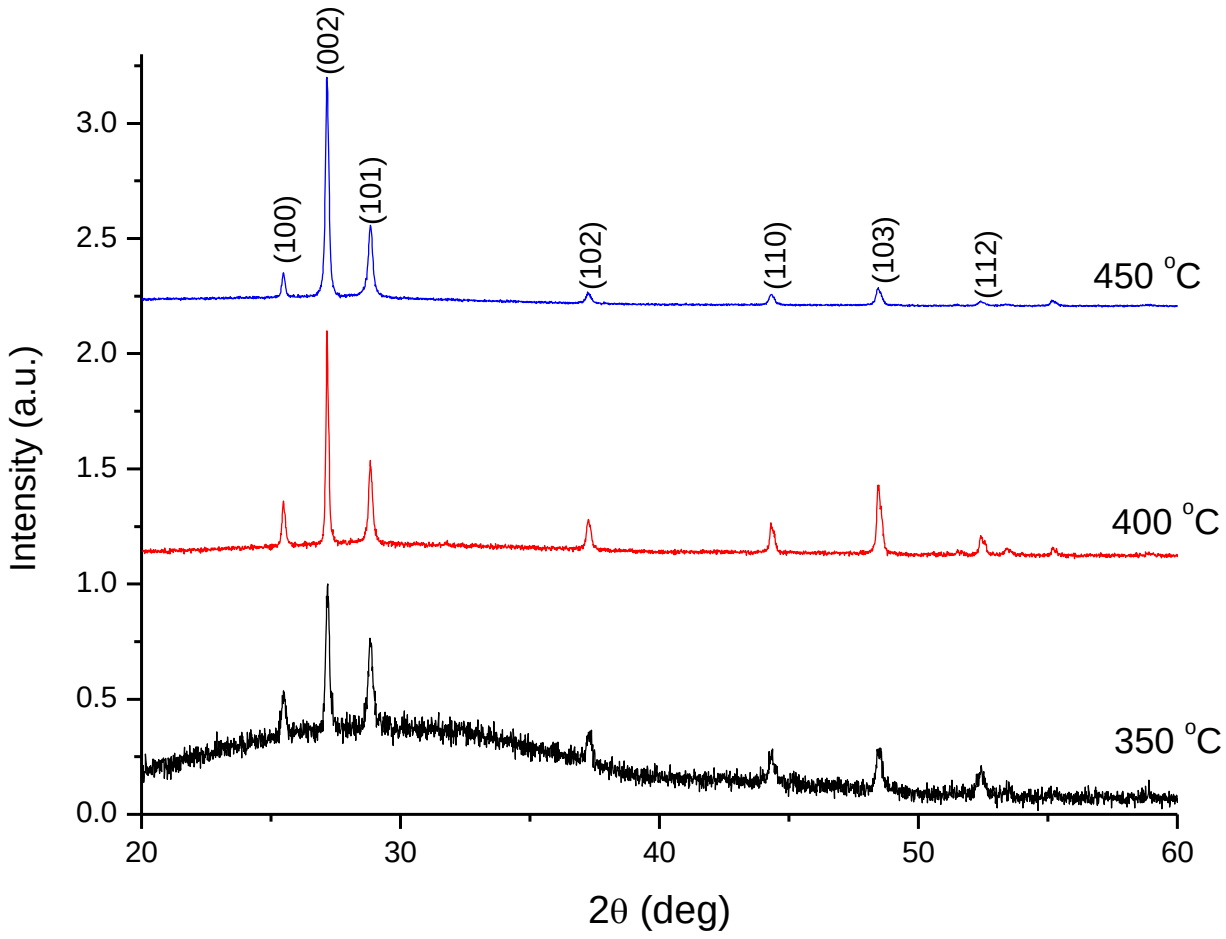


**Figure 2.13.** Powder X-ray patterns of CdS films deposited using complex (**2**).

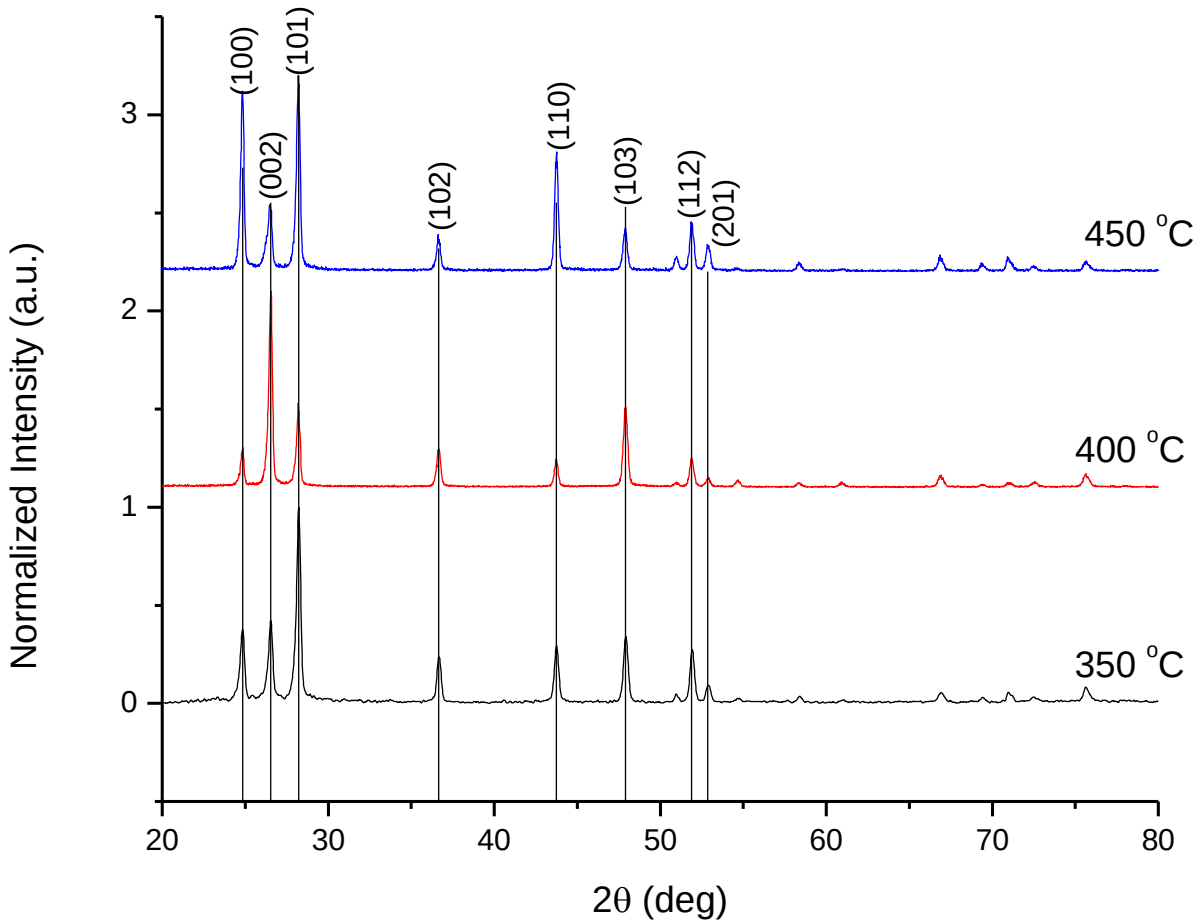


**Figure 2.14.** The p-XRD pattern of greenockite CdS thin films deposited using an adduct complex (**3**) by AACVD.

### 2.3.5. SEM and EDX analyses

The scanning electron microscopy (SEM) micrographs of the CdS films deposited from complex **(1)** exhibit a uniform morphology, Figure 2.15. From the images, it can be seen that the coverage area was approximately 100 % at the substrate temperature of 450 $^{o}$C, while at lower temperature (350 and 400 $^{o}$C) the coverage of the deposited films varied from 80 – 90%. Increasing the deposition temperature resulted in an increase in nucleation and deposition rates; particle sizes range from 55 – 75 nm and 90 – 110 nm for films deposited at 350 °C and 450 °C, respectively. The thickness of the film deposited at 450 °C was estimated to be *ca.* 615 nm (Figure 2.15d).

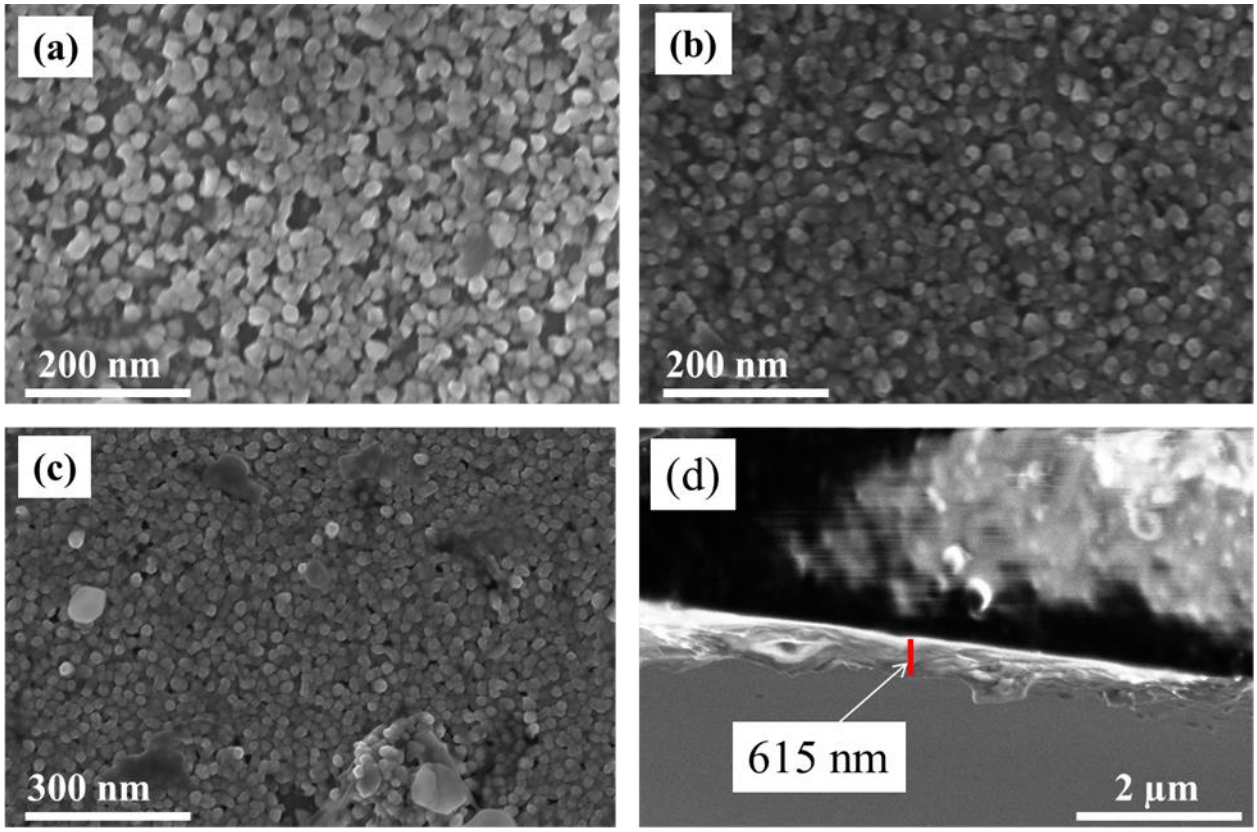


**Figure 2.15.** The SEM images of CdS films deposited on glass substrate using complex (**1**) at deposition temperatures (a) 350 °C, (b) 400 °C and (c) 450 °C, and (d) cross section (thickness) of the CdS films obtained at 450 °C.

The SEM images of the films deposited from complex **(2)** display a remarkable difference in both grain size and uniformity as the temperature was varied from 350 – 450 °C (Figure 2.16). The films deposited at 450 °C show relatively smaller, spherical-like aggregated particles of *ca.* 100 nm average size. At 400 °C and 350 °C deposition temperatures, cubic to spherical-like aggregated particles were obtained, with particle sizes relatively larger, in the 160 – 220 nm range. The EDX microelemental measurements indicated that the average atomic ratio of Cd:S is 1, in all cases. A representative spectrum is provided in Figure 2.16 (d),

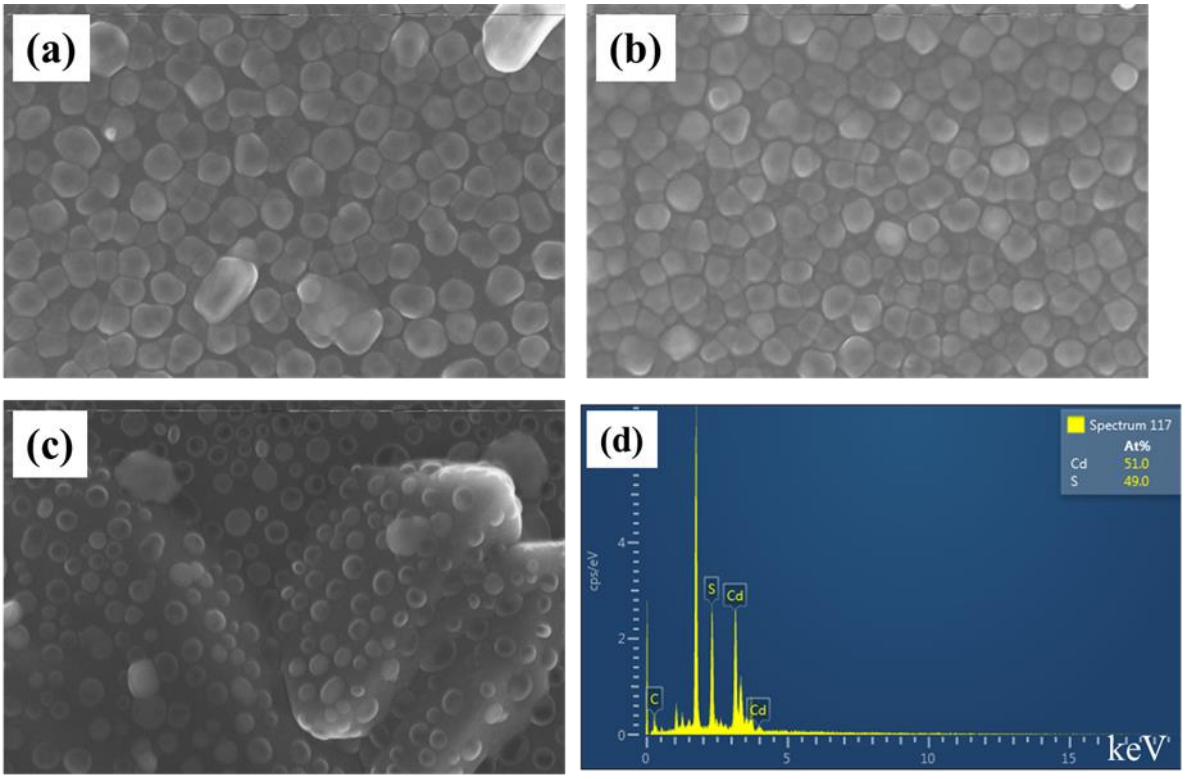


**Figure 2.16.** The SEM images of CdS films deposited on glass substrate by AACVD using complex (2) at deposition temperatures (a) 350 °C , (b) 400 °C, (c) 450 °C, and (d) the representative EDX spectrum of film deposited at 350 °C.

The SEM studies show that the morphology of the as-deposited films from an adduct complex (3) changes with deposition temperature. The films deposited at 350 °C exhibit truncated cube-like particles with an average size of 310 nm (Figure 2.17). The films deposited at 400 °C show different morphological features which range from spherical-like particles to hexagonal-like columns; the feature are averagely sized at 200 nm and 500 nm, respectively. There is a further change of morphology on films deposited at 450 °C; close to spherical granules are obtained. The EDX microanalysis confirmed the stoichiometric ratio Cd:S of 1.0 for films deposited at 350 °C, while Cd-rich films are obtained at 400 °C and 450 °C due to 1.1 stoichiometric ratio obtained (Table 2.3).

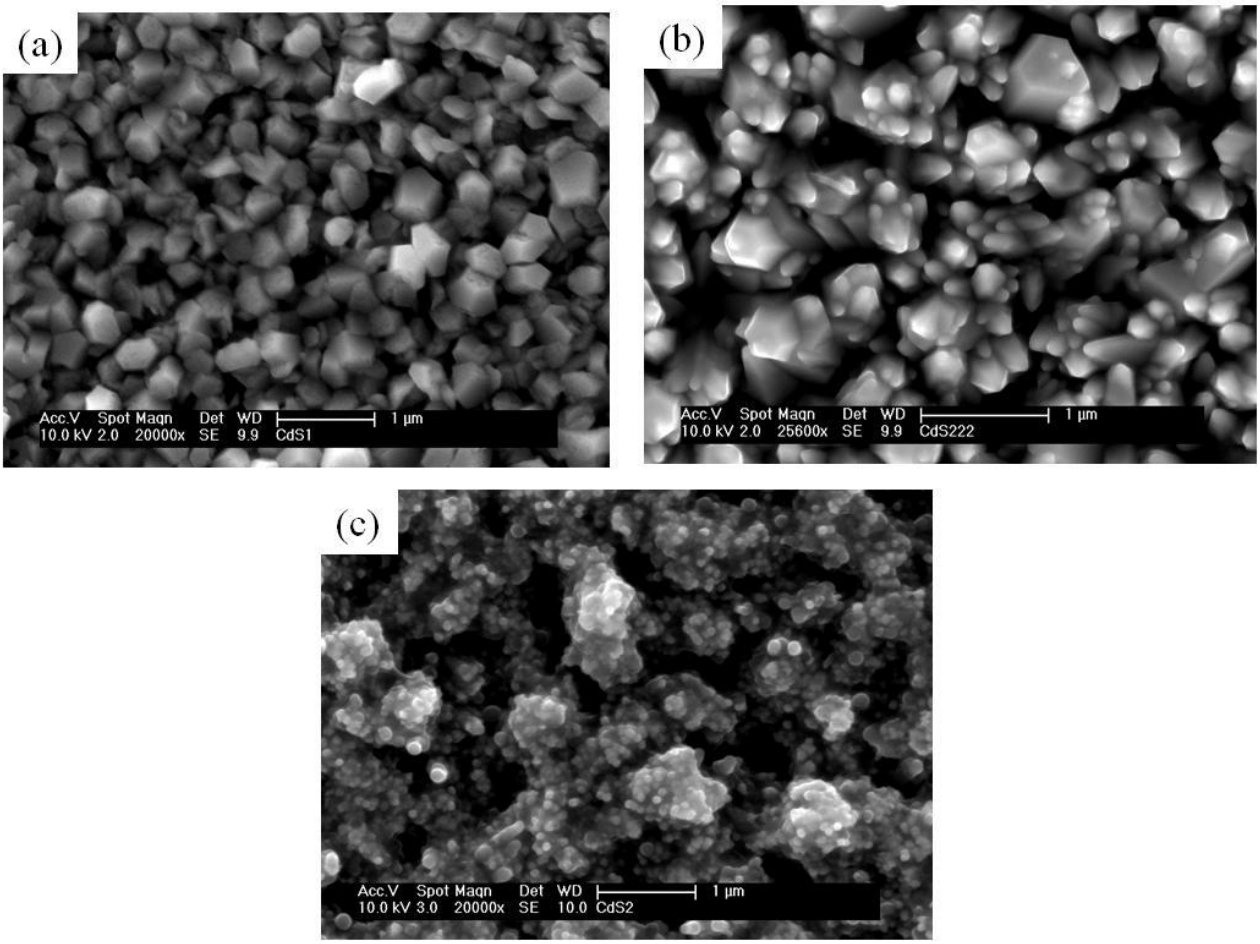


**Figure 2.17.** The SEM images of CdS thin films deposited at (a) 350 °C, (b) 400 °C and (c) 450 °C.

**Table 2.3.** EDX analysis (atomic %) of CdS thin films at three different deposition temperatures.

| Temperature (°C) | Cd at% | S at% | Cd/S ratio |
|---|---|---|---|
| 350 | 50.4 | 49.6 | 1.0 |
| 400 | 51.5 | 48.5 | 1.1 |
| 450 | 53.0 | 47.0 | 1.1 |

### 2.3.6. Atomic Force Microscopy

Representative AFM analyses from the films deposited using precursor (**1**) and (**2**) at different temperatures are shown in Figure 2.18 and 2.19. The film deposited at 350 °C consists of continuous film, composed of columnar and uniform nanosized grains, while the

films deposited at 450 °C are slightly uniform, spherical crystallites with the typical root-mean-square roughness (Rq) of 17.65 and 23.36 nm at deposition temperatures 300 and 450 °C, respectively. The increase in surface roughness with increasing deposition temperature is associated with an increase in grain size. Similarly, well-defined and densely packed isolated nanocrystallites were observed from films deposited at 350 °C when complex (**2**) was used (Figure 2.19), while relatively larger non-uniform crystalline grains were obtained at 450 $^{o}$C with root-mean-square roughness (Rq) of 29.86 nm and 38.70 nm at deposition temperature 300 $^{o}$C and 450 $^{o}$C, respectively.

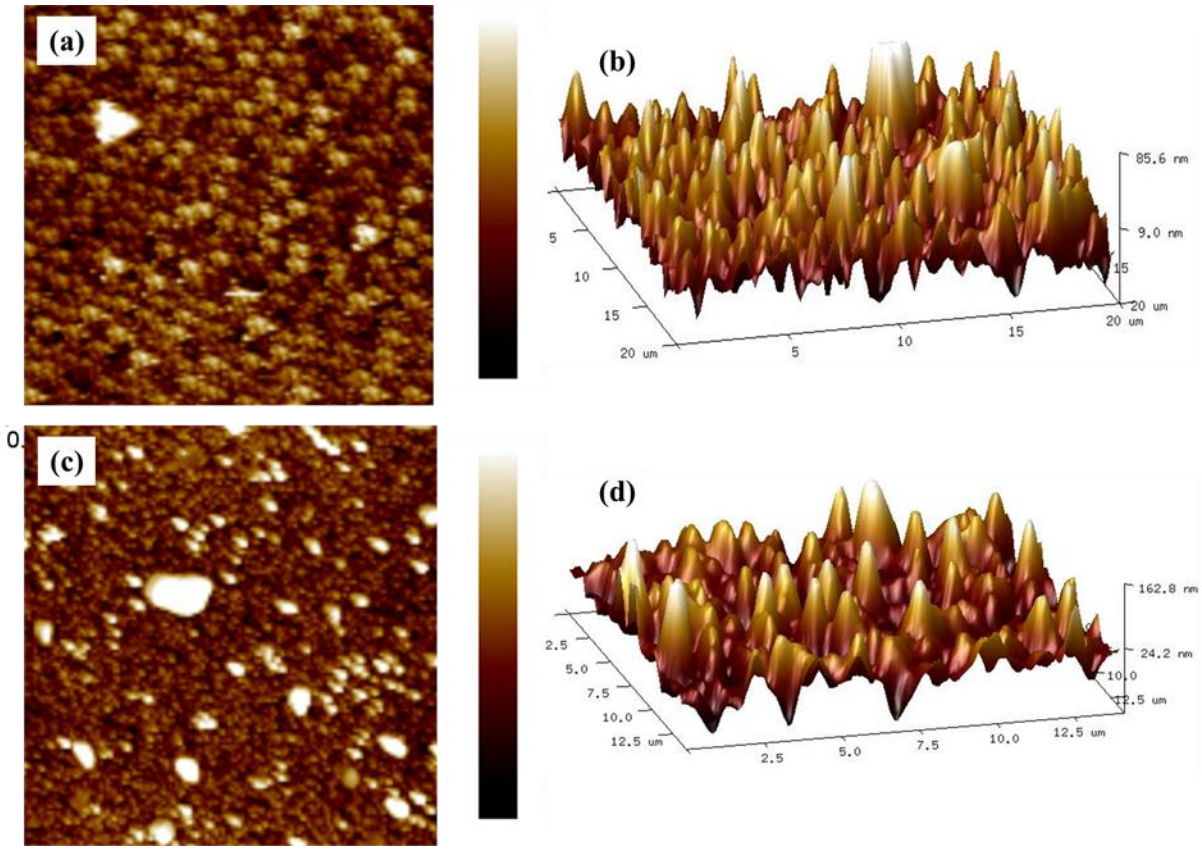


**Figure 2.18.** The 2D and 3D AFM height profiles of CdS thin films deposited by AACVD at (a and b) 350 °C and (c and d) 450 °C using complex (**1**).

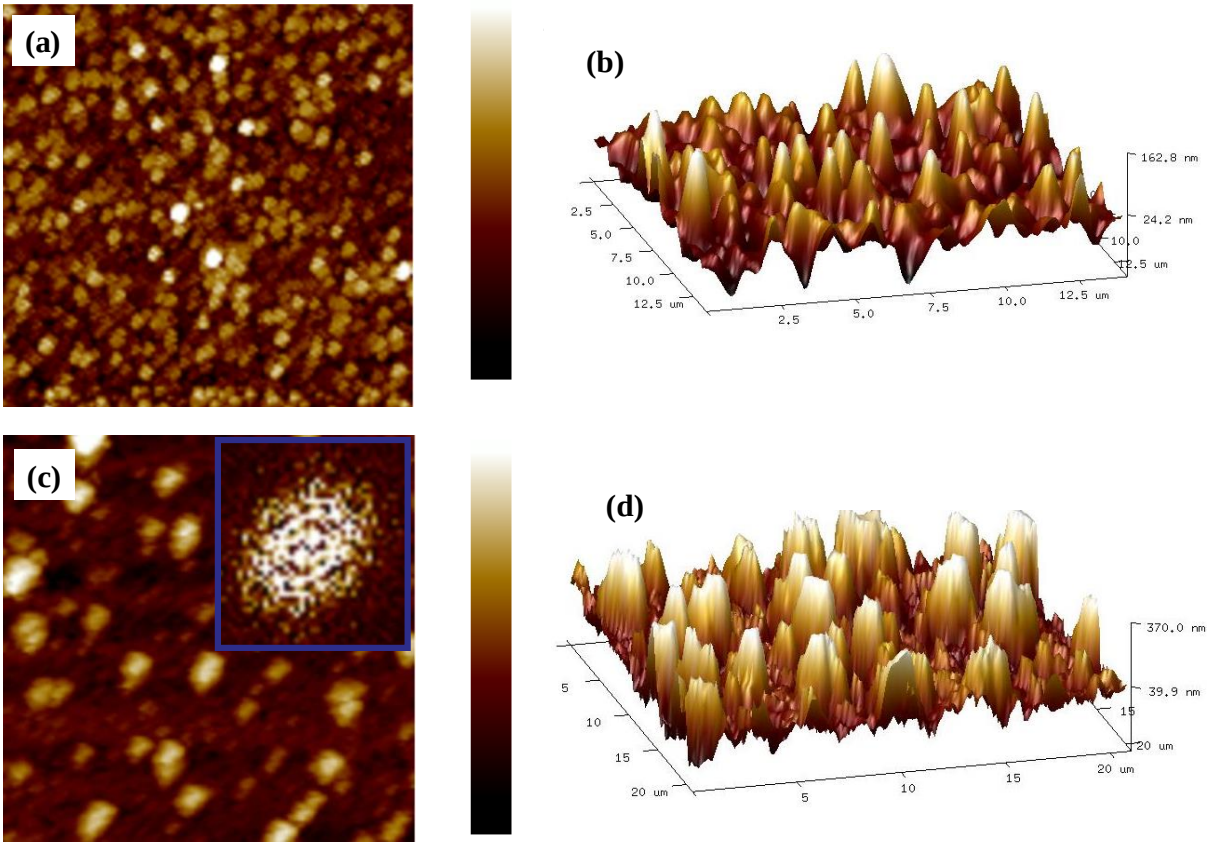


**Figure 2.19.** The 2D and 3D AFM height profiles of CdS thin films deposited by AACVD at (a and b) 350 °C and (c and d) 450 °C using complex (**2**).

The surface topography of the films deposited from complex (3) show the presence of uniform and relatively smoother surface morphologies, characterized by well-interconnected spherical crystallites. The typical root-mean square roughness (*Rq*) was 16.9 nm, 17.8 nm and 22.7 nm at deposition temperatures of (a) 350 °C, (b) 400 °C and (c) 450 °C, respectively. The increase in surface roughness with increasing deposition temperature is associated with an increase in grain size. It is evident that the deposition temperature of the thin film modifies the grain sizes as well as the surface roughness. An even and regular morphology is required for respectable performance in photovoltaic devices [47].

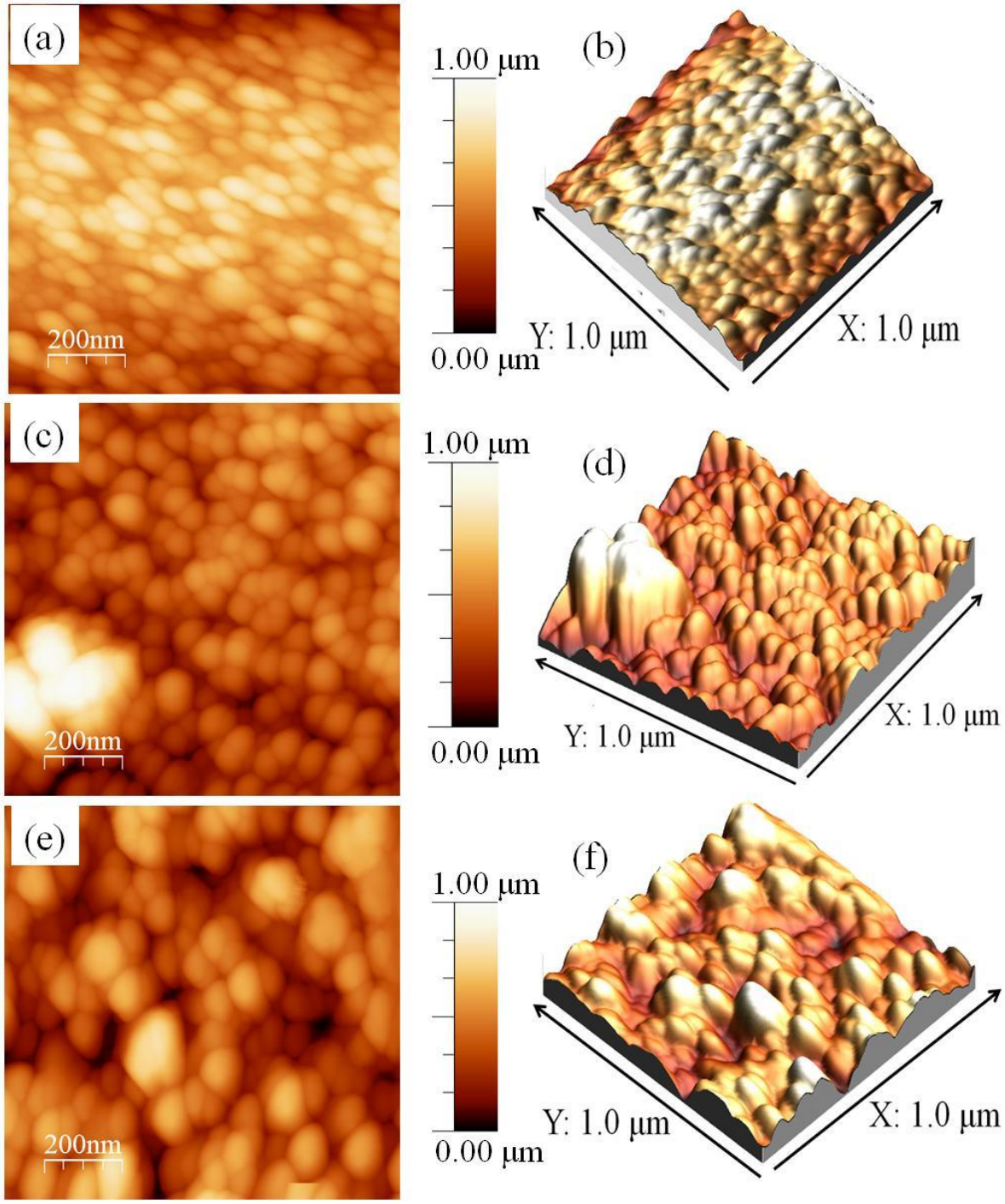


**Figure 2.20.** 2-D and 3-D AFM images of CdS thin films using complex (**3**) deposited by AACVD at (a and b) 350 °C, (c and d) 400 °C and (e and f) 450 °C.

### 2.3.7. CdS nanoparticles from complex (3)

#### 2.3.7.1. Optical properties of CdS nanoparticles

The effect of reaction temperature on the optical absorption of CdS nanoparticles has been investigated. The absorption and photoluminescence (PL) emission spectra for the as-synthesized CdS nanoparticles are shown in Figure 2.21A and B, respectively. Reaction time produced negligible effects in the optical spectra; samples were collected after 1 and 2 hours reaction times.

The UV-Vis absorption spectrum for CdS nanoparticles synthesized at 190 °C reveal a sharp absorption band edge at 468 nm (Figure 2.21A). Generally, semiconductor nanoparticles exhibit two emission peaks. The first sharp peak near the absorption edge of the particle is attributed to excitonic emissions, while the other broad and relatively Stokes-shifted peak is due to deep trap emissions [48,49]. The corresponding PL spectrum of the as-synthesized nanoparticles shows similar features; a narrow band edge emission peak with a maximum at 478 nm was observed (Figure 2.21A). The bathochromic shift observed is typical for nanostructured semiconductors [50,51]. There is also a weaker broad emission peak observed in the 560–670 nm region, which most likely results from electron-hole recombination from surface defects.

The absorption features of nanoparticles synthesized at 230 °C and 270 °C are less prominent than those from 190 °C. The band edge for nanoparticles synthesised at 230 °C is observed at 479 nm, while the red-shifted absorption peak observed at 496 nm is the band edge of nanoparticles synthesised at 270 °C.

The formation of CdS nanocrystals was also monitored with UV–Vis absorption spectroscopy. The growth of the nanoparticles can be tracked through bathochromical shifts in the bandgap absorption edges. Upon increase of the reaction temperature from 190 °C to 270 °C, the growth rate of the CdS nanocrystals is increased. A potential reason for this phenomenon could be that higher reaction temperature results in the formation of irregular nanoparticles with reduced crystallinity due to random, faster nucleation and with the rapid growth affecting the ligand configuration at the nanocrystal surface [48].

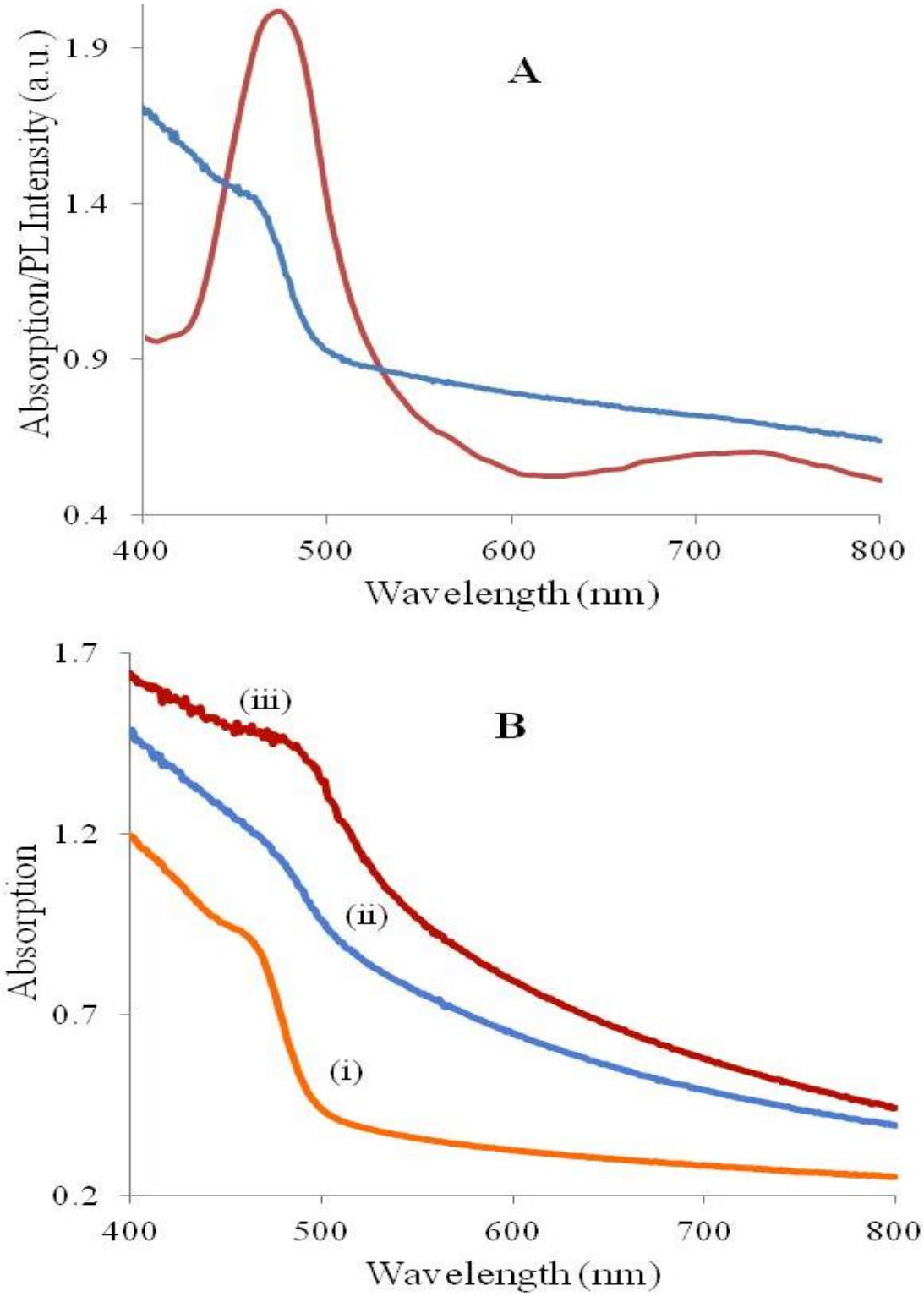


**Figure 2.21.** (A) UV-vis absorption (blue) and PL (red) spectra of HDA capped CdS nanoparticles at 190 °C and (B) combined UV-vis absorption spectra for CdS nanoparticles synthesized at (i) 190 °C, (ii) 230 °C and (iii) 270 °C reaction temperatures. PL spectra are corrected for instrument response.

### 2.3.7.2. Transmission electron microscopy and High Resolution TEM

The TEM and HRTEM images of the CdS nanoparticles are shown in Figure 2.22(a)-(f). Rod-shaped nanoparticles were obtained at 190 °C growth temperature, with length of 64.38 ± 4.62 nm, width of 5.20 ± 0.98 nm and an aspect ratio of 12.38, Figure 2.22(a). Similar morphologies were obtained when $[Cd(S_2CNC_5H_{10})_2]$ is used as a single source precursor, formation of multiple-armed rods are observed [9-11]. When the reaction temperature was increased to 230 °C (Figure 2.22c), rods with a reduced average length of 24.84 ± 4.42 nm and width of 6.58 ± 1.02 nm were obtained. The particles synthesized at 230 °C have lattice fringes with a *d*-spacing of 3.15 Å, corresponding to the (002) plane of hexagonal CdS (Figure 2.22d). The nanoparticles evolved from rods to an oval-shaped morphology when growth temperature is increased to 270 °C; particle size diameters range from 16.8 to 23.3 nm (Figure 2.22e). Thus, the aspect ratio of the nanorods decrease with increase in growth temperature [48]. The oval-shaped particles exhibit lattice fringes with a *d*-spacing of 3.13 Å, corresponding to the (002) basal plane of hexagonal CdS (Figure 2.22f). In summary, CdS nanoparticles synthesized at higher temperature, favour the thermodynamic growth regime resulting in isotropic particles (spherical and cubes) while CdS nanoparticles synthesized at lower temperatures favour non-equilibrium kinetic growth regime and yields anisotropic particles (rods) [49].

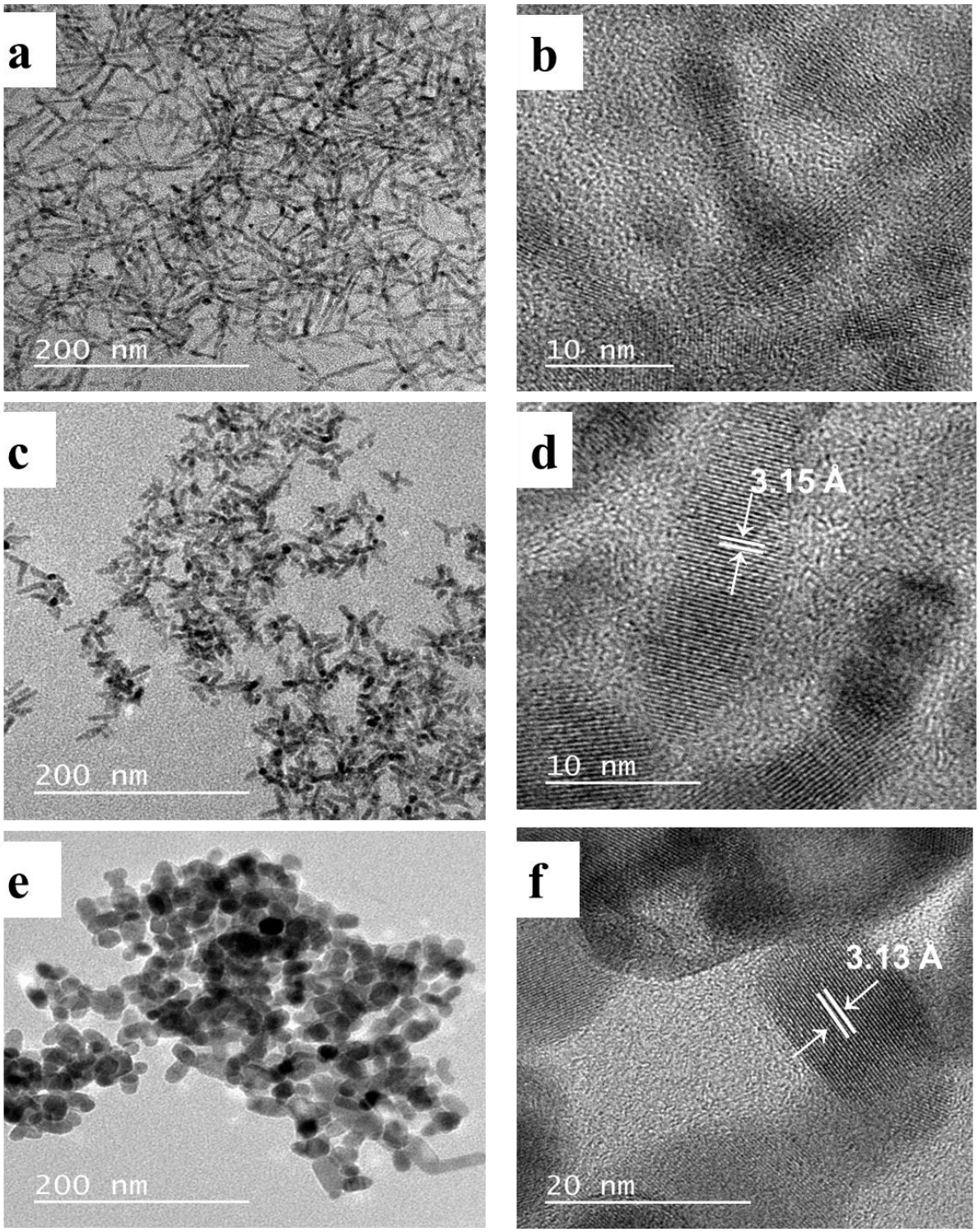


**Figure 2.22.** The TEM and HRTEM images of HDA-capped CdS nanoparticles synthesized by thermolysis of $[Cd(S_2C(NC_5H_{10}))_2(NC_5H_5)]$ at temperatures of (a-b) 190 °C, (c-d) 230 °C and (e-f) 270 °C.

### 2.3.7.3. Powder X-ray diffraction

The p-XRD patterns of the CdS nanoparticles are shown in Figure 2.23, and could all be indexed to the hexagonal phase of hexagonal CdS (Card number: 03-065-3414). Diffraction peaks at 2θ = 24.80°, 26.32°, 28.12°, 43.70°, 47.82° and 51.82° are indexed to (100), (002), (101), (110), (103) and (112) planes of hexagonal CdS, respectively. The narrow peak (002) of high intensity indicate that the nanoparticles were elongated along the *c*-axis [21].

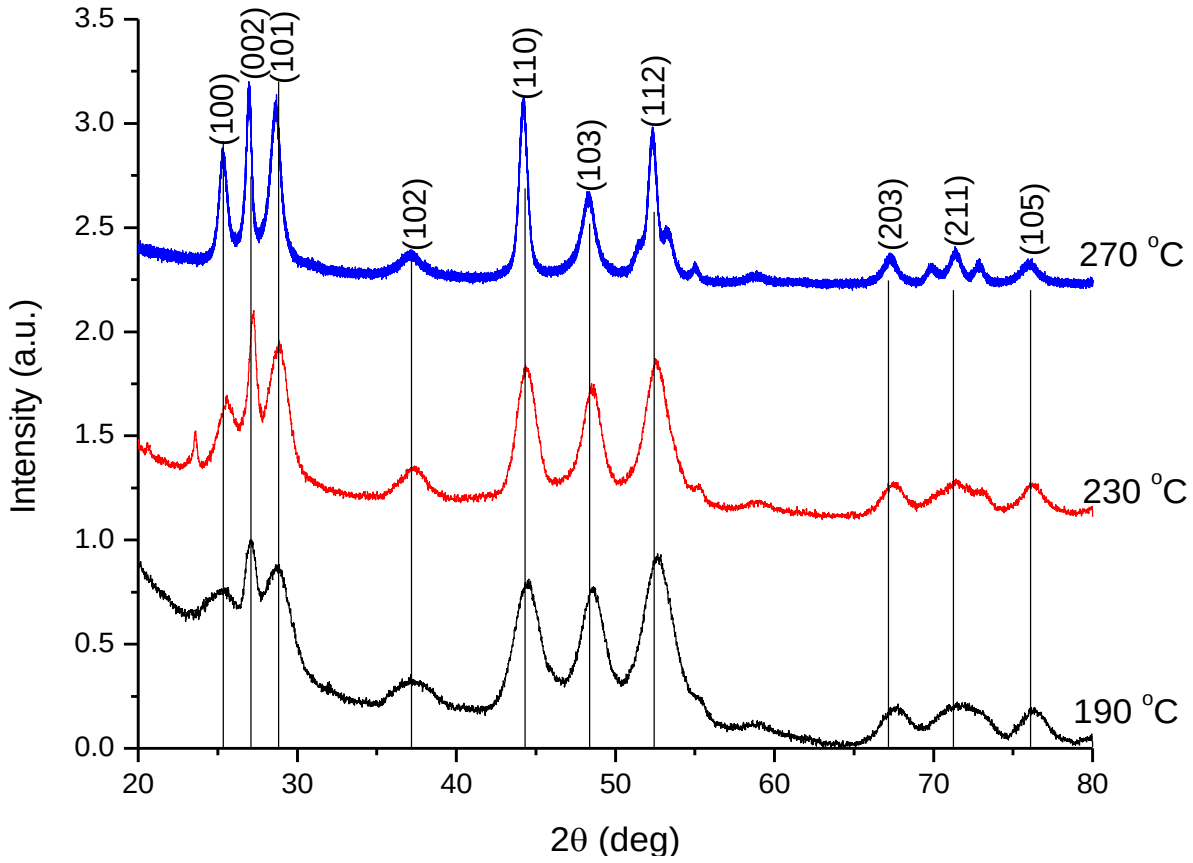


**Figure 2.23.** The pXRD patterns of the hexagonal CdS nanoparticles using an adduct complex (**3**). Patterns are offset in *y* for clarity.

## 2.4. Conclusion

In this chapter, the Cd-DTC single source precursors of piperidine (**1**) and tetrahydroquinoline (**2**), as well as pyridine adduct of piperidine (**3**), have been synthesized and fully characterised; single crystal X-ray structures for complex (**1**) and (**3**) were elucidated. Deposition of cadmium sulfide thin films by aerosol assisted chemical vapour deposition using these complexes, at different deposition temperatures, showed that the growth of the corresponding thin films were temperature-dependant. The morphologies of the as-deposited films showed that the thin films become increasingly dense with increase in temperature. The p-XRD studies confirm the formation of hexagonal CdS thin films, while morphological studies have suggested well-defined morphologies and adequate Cd:S elemental ratios.

The HDA-capped nanoparticles synthesized from an adduct complex (**3**) at temperatures of 190 – 270 °C, predominantly gave rod-shaped morphology at lower reaction temperatures, whereas oval-shaped particles were observed at higher reaction temperatures. The effect of temperature further showed a bathochromical shifts in the band gap absorption edges. The band gaps were observed to vary between 2.54 eV and 2.43 eV.

## 2.5. References


1. G. Hogarth. Mini Rev Med Chem. 2007, 12(12), 1202.
2. T. Trindade and P. O'Brien, J. Mater. Chem. 1996, 6, 343.
3. M. Lazell and P. O'Brien, Chem. Commun. 1999, 2041.
4. M.A. Malik, N. Revaprasadu and P. O'Brien. Chem. Mater. 2001, 13, 913.
5. P. S. Nair, T. Radhakrishnan, N. Revaprasadu, G. A. Kolawole and P. O'Brien, Chem. Commun. 2002, 6, 564.
6. P. S. Nair, T. Radhakrishnan, N. Revaprasadu and P. O'Brien, Mater. Sci. Technol. 2005, 21, 237.
7. A. A. Memon, M. Afzaal, M. A. Malik, C. Q. Nguyen, P. O'Brien and J. Raftery, Dalton Trans. 2006, 4499.
8. A. L. Abdelhady, M. Afzaal, M. A. Malik and P. O'Brien, J. Mater. Chem. 2011, 21, 18768.
9. T. P. Mthethwa, V. S. R. Rajasekhar Pullabhotla, P. S. Mdluli, J. Wesley Smith and N. Revaprasadu, Polyhedron. 2009, 28, 2977.
10. L. D. Nyamen, V. S. R. Rajasekhar Pullabhotla, A. A. Nejo, P. Ndifon and N. Revaprasadu, New J. Chem. 2011, 35, 1133.
11. L. D. Nyamen, N. Revaprasadu, V. S. R. Rajasekhar Pullabhotla, A. A. Nejo, P. T. Ndifon, M. A. Malik and P. O'Brien, Polyhedron. 2013, 56, 62.
12. G. Hogarth, Prog. Inorg. Chem. 2005, 53, 71.
13. E. R. T. Tiekink and I. Haiduc, Prog. Inorg. Chem. 2005, 54, 127.
14. P. Popluakhin and E. R. T. Tiekink, Acta Cryst. 2008, E64, m1176.
15. P. A. Ajibade and D. C. Onwudiwe, J. Mol. Struct. 2013, 1034, 249.
16. N. Srinivasan, P. J. Rani and S. Thirumaran, J. Coord. Chem. 2009, 62, 1271.
17. P. V. Subha, P. Valarmathi, N. Srinivasan, S. Thirumaran and K. Saminathan, Polyhedron. 2010, 29, 1078.
18. M. Chunggaze, M. A. Malik and P. O'Brien, Adv. Mater. Opt. Electron. 1997, 7, 311.
19. N. Srinivasan and S. Thirumaran, Superlattice Microst. 2012, 51, 912.
20. C. D. Onwudiwe, C. A. Strydom and O. S. Oluwafemi, New J. Chem. 2013, 37, 834.

21. P. Yan, Y. Xie, Y. Qian and X. Liu, Chem. Commun. 1999, 1293.
22. D. Barreca, A. Gasparotto, C. Maragno, R. Seraglia, E. Tondello, A. Venzo, V. Krishnan and H. Bertagnolli, Appl. Organometal. Chem. 2005, 19, 59.
23. K. S. Youn, K. H. Yu, J. S. Song and I. H. Choi, J. Korean Phys. Soc. 2005, 47(1), 89.
24. S. H. Yoon, S. S. Lee, K. W. Seo and I-W. Shim, Bull. Korean Chem. Soc. 2006, 27, 2071.
25. A. S. R. Chesman, N. W. Duffy, A. Martucci, L. De Oliveira Tozi, Th. Birendra Singha and J. J. Jasieniak, J. Mater. Chem. C. 2014, 2, 3247.
26. D. M. Frigo, O. F. Z. Khan and P. O'Brien, J. Cryst. Growth, 1989, 96, 989.
27. M. A. Malik, M. Afzaal, , P. O'Brien, Chem. Rev. 2010, 110, 4417.
28. K. Ramasamy, M. A. Malik, M. Helliwell, J. Raftery and P. O'Brien, Chem. Mater. 2011, 23, 1471.
29. D. Oyetunde, M. Afzaal, M. A. Vincent, I. H. Hillier and P. O'Brien, Inorg. Chem. 2011, 50, 2052.
30. M. A. Ehsan, H. N. Ming, M. Misran, Z. Arifin, E. R. T. Tiekink, A. P. Safwan, M. Ebadi, W. J. Basirun and M. Mazhar, Chem. Vap. Deposition. 2012, 18, 191.
31. I. D. Rojas-Montoya, A. Santana-Silva, V. García-Montalvo, M-Á. Muñoz-Hernández and M. Rivera. New J. Chem. 2014, 38, 4702.
32. D. Barreca, A. Gasparotto, C. Maragno, R. Seraglia, E. Tondello, A. Venzo, V. Krishnan and H. Bertagnolli, Appl. Organometal. Chem. 2005, 19, 129.
33. SHELXTL, version 6.12, Bruker AXS, Inc.: Madison, WI, (2001).
34. T. Mandal, V. Stavila, I. Rusakova, S. Gosh and K. H. Whitmire, Chem. Mater. 2009, 21, 5617.
35. K. Ramasamy, M. A. Malik, M. Hilliwell, J. Raftery and P. O'Brien, Chem. Mater. 2011, 23, 1471.
36. S. Thirumaran, K. Ramalingam, G. Bocelli and L. Righi, Polyhedron. 2009, 28, 263.
37. A. Rakhshani, J. Phys. Condens. Matter. 2000, 12, 4391.
38. J. Dilag, H. Kobus, A.V. Ellis, Forensic Sci. Int. 2009, 187, 97.
39. X. Yang, Z. G. Jin, Y. Chai, H. Du, T. Liu and T. Wang, Thin Solid Films 2009, 517, 6617.

40. Y. Li, X. Li, C. Yang and Y. Li, J. Mater. Chem. 2003, 13, 2641.
41. K-T. Yong, Y. Sahoo, M. T. Swihart and P. N. Prasad, J. Phys. Chem. C. 2007, 111, 2447.
42. S. A. Vanalakar, S. S. Mali, R. C. Pawar, N. L. Tarwal, A. V. Moholkar, J. A. Kim, Y. Kwon, J. H. Kim and P. S. Patil, Electrochim. Acta. 2011, 56, 2762.
43. V. Singh, P. K. Sharma, P. Chauhan, Mater. Chem. Phys. 2010, 121, 202.
44. A. Pan, R. Liu, Q. Yang, Y. Zhu, G. Yang, B. Zou, J. Phys. Chem. B. 2005, 109, 24268.
45. J. E. Spanier, R. D. Robinson, F. Zhang, S. W. Chan, I. P. Heraman, Phys. Rev. B. 2001, 64, 245407.
46. R. J. Bandaranayake, G. W. Wen, J. Y. Lin, H. X. Jiang, C. M. Sorensen, Appl. Phys. Lett. 1995, 67(6). 831.
47. M. Tsuji, T. Aramoto, H. Ohyama, T. Hibino and K. Omura, Jpn. J. Appl. Phys. Part 1. 2000, 39, 3902.
48. M. Nell, J. Marohn and G. Mclendon, J. Phys. Chem. B. 1990, 94, 4359.
49. L. Spanhel, M. Haase, H. Weller and A. Henglein, J. Am. Chem. Soc. 1987, 109, 5649.
50. M. A. Malik, P. O' Brien and N. Revaprasadu, S. Afr. J. Sci. 2000, 96, 55.
51. M. Green and P. O' Brien, Chem. Commun. 1999, 2235.

# CHAPTER THREE

# HETEROCYCLIC DITHIOCARBAMATO-LEAD(II) COMPLEXES: SINGLE-SOURCE PRECURSORS FOR LEAD SULFIDE THIN FILMS

## 3.1. Introduction

Lead sulfide (PbS) is among the group IV-VI semiconducting materials which have received considerable attention over the past decades, owing to their tuneable electronic and morphological properties [1-3]. Because of its small effective mass, PbS shows unique quantization effect properties which are accompanied by a direct band gap of 0.41 eV at 300 K, and a large excitonic Bohr radius of 18 nm [4-6]. Studies mainly involved improvement of these features, and this could be achieved by simply reducing the particle sizes down to the nanometre scale. [7-9]. The resulting crystalline PbS semiconducting nanomaterials are found to exhibit interesting physical and chemical properties as the particle size decreases.

The ability to tune its broad band edge which is found within Near Infrared (NIR) to Ultra Violet visible (UV-Vis) range through particle size and morphology manipulations is an important feature for optoelectronic devices which allow them to harness energy within this broad range [10,11]. As a result, PbS nanomaterials may be useful in fields such as solar cells [12], NIR communication [11,13], thermal and biological imaging [14], tunable near infrared detectors [15] and electroluminescent devices such as light-emitting diodes (LEDs) [16]. In addition, lead sulfide nanomaterials are expected to have exceptional third-order nonlinear optical properties [17] and may thus be useful in optical devices such as optical switches.

Apart from particle size manipulations, PbS nanomaterials have been found to exist in different morphologies which include cubes [18], octahedrons [19], dendrites [20] and star-hierarchical shapes [21]. These have been achieved through fabrication protocols such as gas phase syntheses [22], sonochemical approach [23], solvothermal decomposition [24], ultrasonic irradiation [25] and hydrothermal methods [26-28]. The fabrication protocols can utilize either multiple or single source molecular precursors (SSPs) [28-30]. The latter has been preferred for size and shape-controlled fabrication, due to high quality materials obtained [26,27,31]. This is easily achieved through the decomposition or disintegration of the SSPs, which is usually an organometallic compound bearing preformed metal-chalcogen bonds.

Dithiocarbamates [5], xanthates [31] and thiourea [28] are among known SSPs which have been used to prepare high quality PbS nanomaterials. Furthermore, several studies on

the deposition of lead sulfide thin films using single source precursors have also been reported. O'Brien group has extensively studied the deposition of PbS thin films by aerosol assisted chemical vapour deposition (AACVD) using alkyldithiocarbamato and dichalcogenoimidodiphosphinato lead complexes [32-34]. In one of the studies [32], it was found that the length of alkyl chain had an effect on the crystallinity of the deposited PbS thin films. Clark *et al.* also generated PbS nanocubes by AACVD using a series of xanthate lead(II) complexes on different substrates (glass, Mo-coated glass and Si) when decomposed under an autogenerated pressure at 350 °C [35].

The design and development of a simple technique that is able to fabricate very pure, high quality and tunable morphology thin films is therefore important and pressing. Therefore, in this chapter, the synthesis of two complexes namely; *bis*-(piperidinedithiocarbamato)lead(II) (**4**) and *bis*-(tetrahydroquinolinedithiocarbamato)lead(II) (**5**) complexes is presented. These complexes have been used as single-source precursors (SSPs) for the deposition of lead sulfide (PbS) thin films by aerosol-assisted chemical vapour deposition (AACVD) and spin coating methods. Various parameters such as temperature have also been varied and studied.

## 3.2. Experimental

### 3.2.1 Materials and method

Lead(II) acetate trihydrate 99.999 %, acetone and chloroform were purchased from Sigma-Aldrich and all chemicals were used without further purification.

### 3.2.2. Synthesis of ligands and complexes

Organic salts of sodium piperidine and/tetrahydroquinolinedithiocarbamato ligands were prepared according to procedures reported in literature [5] and were then converted to the corresponding lead(II) complexes by salt metathesis. A brief description of the synthesis of complexes is given below.

This preparation was carried out under an inert atmosphere of dry nitrogen using a standard Schlenk line. To an aqueous solution of $Pb(CH_3COO_2)_2.3H_2O$ (1.897 g, 5.0 mmol) (25 mL), was added drop-wise in an aqueous solution of the ligand, $NaC_6NS_2H_{10}$ or $NaC_{10}NS_2H_{10}$ (1.833 g or 2.313 g, 10.0 mmol) dissolved in a minimal amount of water, under

vigorous stirring. The reaction mixture was stirred for a further 1 h before the solution was filtered. The remaining black coloured solids were washed with deionized water and dried under vacuum overnight.

### 3.2.3. AACVD of lead sulfide thin films

Lead sulfide thin films were deposited on glass substrates by AACVD using precursor (**4**). The AACVD assembly is similar to that described in chapter two with few modifications. The glass substrates were ultrasonically cleaned in distilled water and acetone and then stored in ethanol prior to use. In a typical deposition procedure, aerosols of the desired complex from its 15 mL solution (chloroform) are generated at room temperature using an ultrasonic humidifier operating at a frequency of 50 Hz. Argon was used as a carrier gas to transport the aerosols to the reactor chamber at a flow rate of 160 mL $min^{-1}$. Deposition processes were conducted for 30 minutes.

### 3.2.4. Spin coated deposition of lead sulfide thin films

In a typical deposition of PbS thin films, 0.25 mM of (**4**) or (**5**) was dissolved in chloroform (1.5 mL). The glass slides were cleaned by sonication in acetone and allowed to dry at room temperature. The solution was carefully spin coated onto a glass slide (20 x 15 mm) to fit the spin coater. The coated glass substrates were then spun at a speed of 1000 rpm for 120 seconds. Brewer Science spin coater (Model 200X) was used. The resulting films were allowed to dry and then loaded into a quartz tube for heating. The coated slides were then annealed at 350 to 500 °C under argon gas for 60 minutes. The furnace was held at the chosen temperature for the specified time, and once this time had elapsed the furnace was turned off and the tube allowed to return to room temperature.

### 3.2.5. Characterization techniques

#### *3.2.5.1. Scanning electron microscopy (SEM) and Energy dispersive X-ray spectroscopy (EDX)*

A Zeiss Ultra Plus FEG SEM was used for the surface morphology analysis at 10 kV, equipped with an Oxford detector EDX at 20 kV which uses Aztec software for elemental analysis. Samples were carbon coated using Quorum coater (Model Q150TE) prior to SEM

characterization. All other analytical techniques were similar to those detailed in chapter two of this thesis.

## 3.3. Results and discussion

### 3.3.1. Single source precursors

The purity of all compounds was checked by elemental analysis, infra-red and proton NMR analyses. All the complexes were air and moisture stable at room temperature for long periods. Attempts to grow good quality crystals for single crystal X-ray structure studies of both complexes (**4**) and (**5**) were unsuccessful, partly due to poor solubility of the complexes in most of the organic solvents. The compounds were found to be soluble in DMSO and partially soluble in organic solvents such as chloroform and dichloromethane.

Complex (**4**): Yield 78.5 %. $^1$H NMR (400 MHz, $CDCl_3$): δ 2.07 (m, 8H, 3-$CH_2$), 2.71 (t, 4H, 4-$CH_2$), 4.50 (t, 8H, 2-$CH_2$). Elemental analysis for $Pb(C_6\ H_{10}NS_2)_2$: obs. (Calc): C 27.31 (26.41), H 3.82 (4.06), N 5.31 (5.13). IR υ(O–H): 2937 $cm^{-1}$, υ(C=S): 974 $cm^{-1}$, υ(C=N): 1465 $cm^{-1}$, υ(Pb–S): 408 $cm^{-1}$.

Complex (**5**): Yield 83.6 %. $^1$H NMR (400 MHz, $CDCl_3$): δ 2.10 (m, 4H, 3-$CH_2$), 2.80 (t, 4H, 4-$CH_2$), 4.30 (t, 4H, 2-$CH_2$), 7.26-7.92 (m, 8H, Ar-H). Elemental analysis for $Pb(C_{10}\ H_{10}NS_2)_2$: obs. (Calc): C 38.77 (38.51), H 3.39 (3.23), N 4.47 (4.49). IR υ(O–H): 3038 $cm^{-1}$, υ(C=S): 964 $cm^{-1}$, υ(C=N): 1485 $cm^{-1}$, υ(Pb–S): 367 $cm^{-1}$.

The thermal gravimetric analysis (TGA) curves of complexes (**4**) and (**5**) are shown in Figure 3.1. TGA curve of complex (**4**) showed one-step decomposition behaviour at 338 °C whereas complex (**5**) showed a two-step decomposition pattern. Complex (**4**) displays a weight loss of approximately 52.4 %, the residue weighing approx. 47.6 % is higher than the theoretical value (45.3 %), which could be due to carbonaceous deposition. The first stage decomposition (249 °C) in the TGA thermogram of complex (**5**) could be a result of the detachment of one bulk ligand (-$C_9NH_{10}$). The second weight loss (51.4 %) is due to partial decomposition of the organic moiety resulting in a residue amounting to 48.6 %, higher than the calculated value (38.4 %) of PbS, and this could be due to formation of carbonaceous matter or $Pb(SCN)_2$.

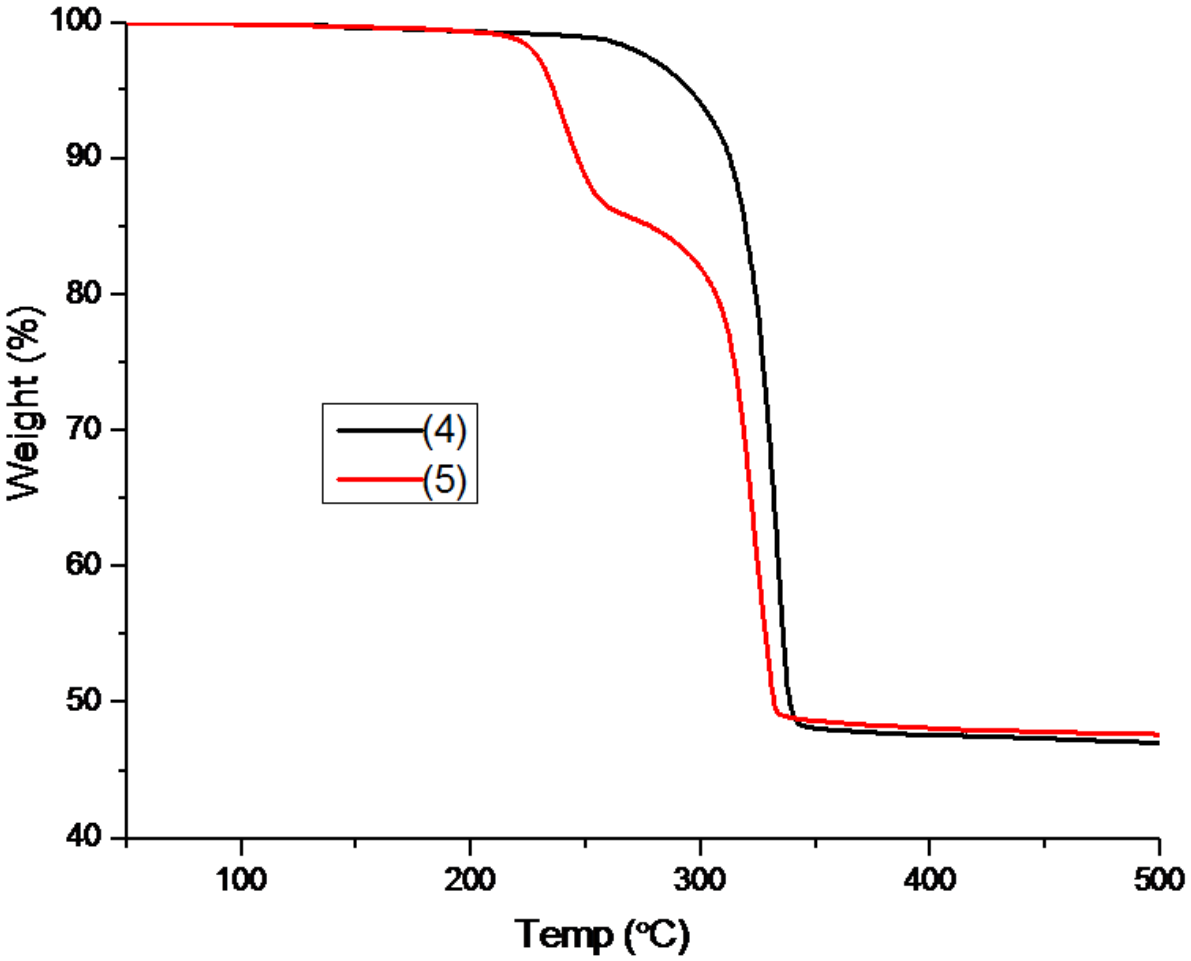


**Figure 3.1.** Thermogravimetric analysis (TGA) of complexes **(4)** and **(5)** at a heating rate of 10 °C/min under nitrogen with a flow rate of 10 $cm^3$/min.

### 3.4.2. AACVD of PbS thin films

Thin films of lead sulfide were deposited on glass substrates by AACVD at 350, 400 and 450 °C using chloroform as solvents. The films produced were characterized by scanning electron microscopy (SEM), energy dispersive X-ray (EDX) spectroscopy, powder X-ray diffraction (p-XRD) and optical absorbance spectroscopy. Only complex (**4**) was used to deposit thin films by AACVD, as complex (**5**) could not dissolve in most of the organic solvents.

The UV-vis NIR absorption spectrum of the PbS thin film deposited at 350, 400 and 450 °C is shown in Figure 3.2. The as-deposited thin films absorb light in the visible and near-infrared spectral regions. The deposition at 350 and 400 °C displays a sharp absorption peak which is typical of material exhibiting quantum confinement effect; a band gap of 1.55 eV was estimated from Tauc's plots [36] (Inset: Figure 3.2). The films deposited at 450 °C

exhibited red shifted absorption properties (~1.32 eV) compared to that of 350 and 400 ˚C. The blue shift was observed for the absorption spectra as compared to the bulk counterpart (0.41 eV) [37], revealing high optical performance of the films in the visible and infrared region. The significant blue shift of band gap observed from the bulk value reveals that the films exhibit quantum size effects, however the sizes of the films are larger than the Bohr radius (18 nm) of PbS. Lead sulfide has the rock salt crystal structure and its band structure is complicated by large relativistic splitting. The optical behaviour of the deposited films reveals that the absorption properties are temperature and size dependant.

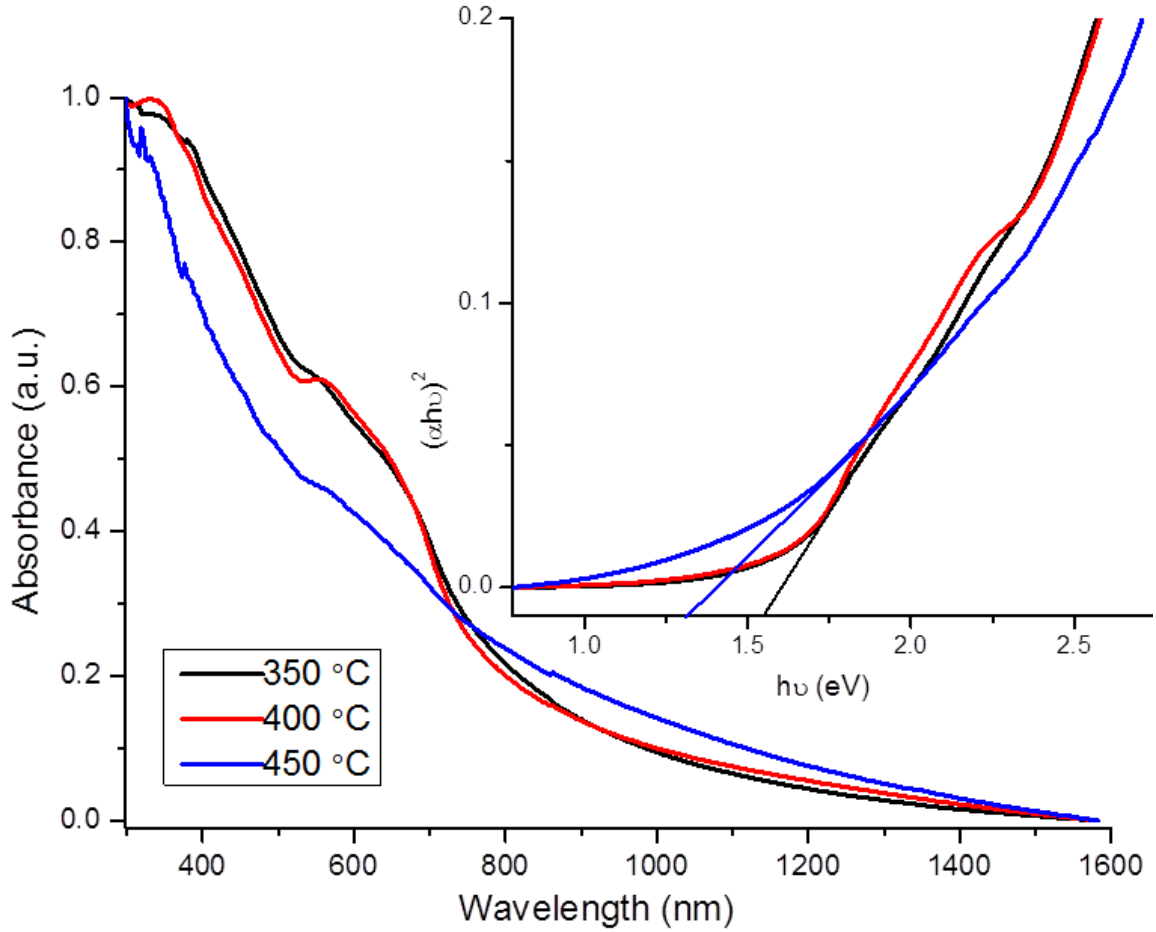


**Figure 3.2.** UV-Vis-NIR absorption spectra of PbS thin films deposited at 350, 400 and 450 °C using complex (**4**). Inset: Tauc plot showing the estimated optical band gap of the deposited PbS films.

The surface morphology of the as-prepared thin films was investigated by field emission gun scanning electron microscopy (FEGSEM). The images of PbS films in Figure 3.3 deposited using complex (**4**), show the growth of randomly oriented nanorod-structures, bipods or T-shaped features in a zigzag fashion at 350 ˚C. The formation of nanorod PbS

films is unusual phenomenon and few or no data documented on the formation of nanorod PbS thin films. The films deposited at 400 ˚C (Figure 3.3b) indicate formation of much larger nanorods to cubes, growing upward/radially oriented. The results are similar to literature data [33], where $[Pb((SPiPr_2)_2N)_2]$ was used as single-source precursors to grow lead sulfide thin films by LP-MOCVD on glass substrates. The films deposited at 450 ˚C exhibit completely different morphologies as shown in Figure 3.3(c). The films deposited at 450 ˚C are compact cube like nanostructured with sizes ranging from 150 to 220 nm. The films size increased with an increase in deposition temperature. The morphologies obtained from this study are different to those of a recent report on PbS thin films which were deposited using symmetrical and unsymmetrical alkyldithiocarbamato complexes [32]. Thus these findings suggest that, the structure of the starting material influences the structure of the final deposited thin films. Table 3.1 shows the elemental composition of several areas of the deposited films measured using the EDX spectroscopy. The typical compositions of PbS nanomaterials are observed whilst increasing the temperatures produced slightly sulfur deficient PbS films. Other elements were due to the glass substrate used to deposit the films.

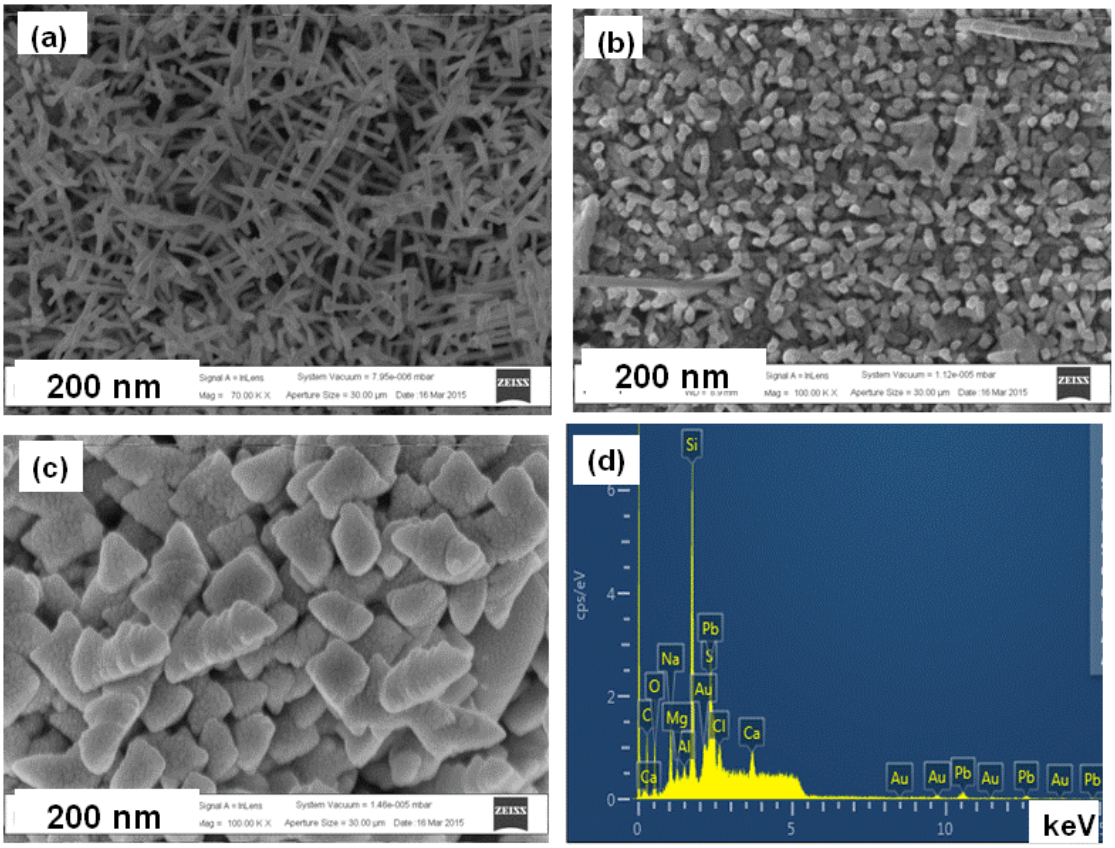


**Figure 3.3.** Secondary electron SEM images of the lead sulfide thin films deposited using complex (**4**) at (a) 350, (b) 400, (c) 450 °C and a representative EDX spectrum (d).

**Table 3.1.** Elemental composition of Pb and S in the thin films deposited using complex (**4**).

| Temp (°C) | Pb (%) | S (%) | Pb:S |
|---|---|---|---|
| 350 | 50.2 | 49.8 | 1.01:1 |
| 400 | 53.2 | 46.8 | 1.14:1 |
| 450 | 54.1 | 45.9 | 1.18:1 |

The p-XRD patterns confirmed that the deposited films are exclusively made of PbS with patterns corresponding to the face centered cubic (FCC) rock-salt structure (ICDD: 5-592). There was no phase change observed when the temperature was varied from 350 – 450 °C. Preferred growth along the (200) plane was observed as the temperature was increased. The relative intensities of the peaks also increased as the temperature increased, such that the crystallinity of the deposited films increased as a consequence of temperature increase. The average crystallite size of PbS in the film was also determined from the (200) plane by using Scherrer formula (Equation 3.1) [38], and the sizes were 45.5 nm (350 °C), 46.1 nm (400 °C) and 51.2 nm (450 °C). The increase in crystallite sizes as a result of increase in temperature is observed.

$$Ps = k\lambda/\beta cos\theta \quad \text{..... 3.1}$$

where *K* is a constant (0.94) (constant K, a shape factor, that varies from 0.89 for spherical to 0.94 for cubic particles), λ is the wavelength of the XRD, and $\beta$ is the full width at half maximum of the diffraction peak corresponding to a particular plane crystal, which is obtained from the diffraction pattern in a direction perpendicular to the (200) plane.

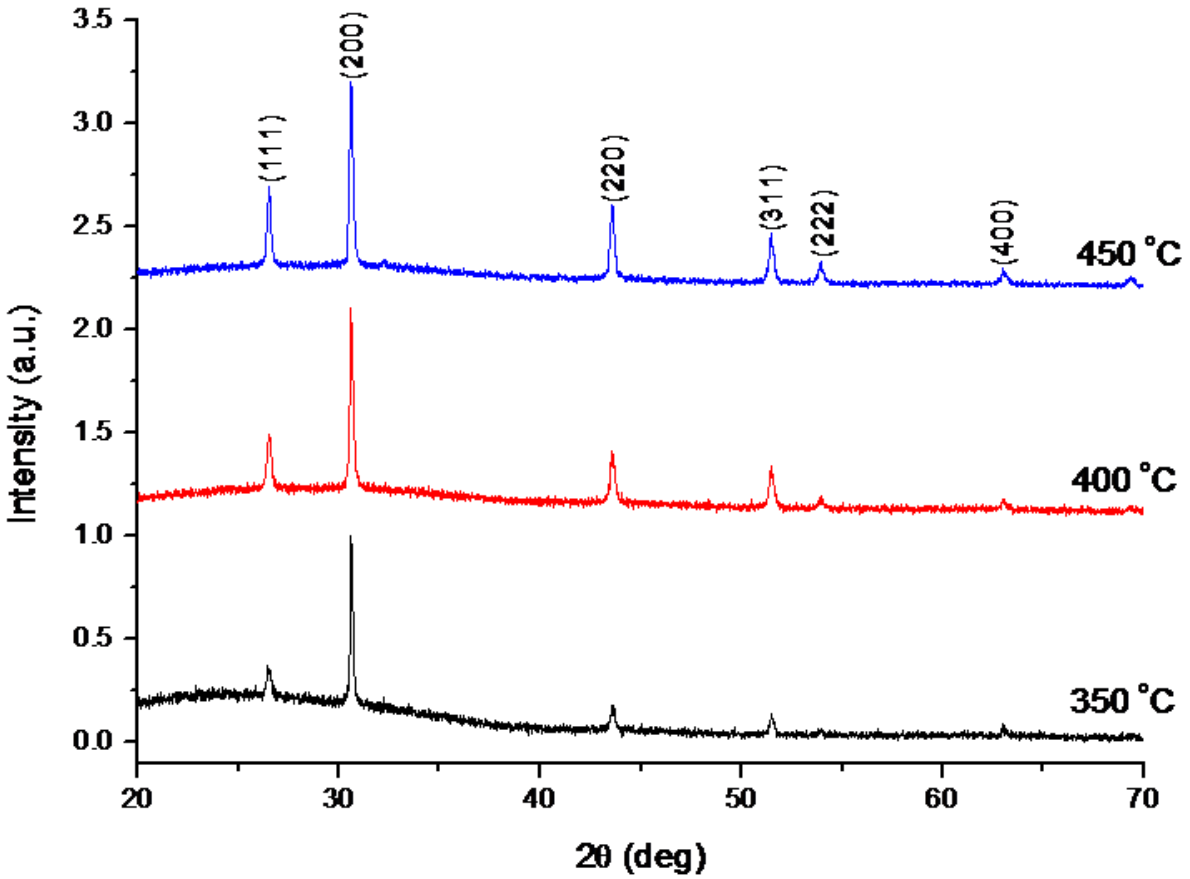


**Figure 3.4.** p-XRD patterns of PbS thin films deposited using complex (**4**).

### 3.3.3. Deposition of PbS thin films by spin coating

An attempt to fabricate thin films was also made by a simple deposition of PbS on glass substrate by an approach that features multiple cycles of spin coating with a single-source precursor solution and thermal decomposition at different temperatures. These cycles of spin coating and thermal decomposition were repeated, allowing for an accurate control over the shape of the deposited PbS deposition. The samples were annealed at 350–450 °C for one hour in Ar atmosphere. Very few reports have used spin coating techniques to deposit PbS thin films using single source precursors. Choi *et al.* have used multiple cycles of spin coating to deposit $Sb_2Se_3$ from single source precursors [39]. O'Brien and co-workers have also used lead(II) dithiocarbamates and xanthates complexes of varying alkyl chains to deposit lead sulfide within a polymer matrix to form networks of PbS nanocrystals by spin coating and annealing at high temperatures [40].The morphology, elemental composition and structure of the PbS that was formed via this approach were investigated by field emission

scanning electron microscopy (FESEM), energy dispersive X-ray (EDX) spectroscopy, and X-ray diffraction (XRD), respectively.

The SEM images of PbS thin films prepared using complex (**4**) at different annealing temperatures by spin coating are shown in Figure 3.5. Thin films deposited at 350 °C show typical growth of close packed perfect PbS cubes of the sizes ranging from 0.5 – 1.2 μm (Figure 3.5a and b). Thin films deposited at 400 and 450 °C (Figure 3.5c-f) also contain the same loading of PbS nanocubes, but the coverage of PbS nanocubes observed in the SEM images appear more loose than those samples deposited at 350 °C. The samples displayed less size uniformity ranging from 0.7 – 1.1 μm for both temperatures. Similar morphology has been reported, where cubic shaped PbS thin films were deposited by LP-MOCVD when $[Pb((SPiPr_2)_2N)_2]$ was used as single-source precursors [33]. A nonclassical growth mechanism involving the coalescence of smaller nanocrystals to form large nanocubes may be expected at higher temperature [41] but this phenomenon was not observed.

The morphology of the PbS films differs dramatically when the annealing temperature was increased to 500 °C for complex (**4**). A mixture of dendritic structures along with some interlinked quasi-cube/rod shaped crystals was obtained (Figure 3.6). At this temperature, the oscillatory growth between the faceted growth and dissolution growth is observed. The growth mechanism of dendritic and star-shaped PbS nanoarchitectures has been investigated and reported [42-44]. However, we identified an interesting growth regime (Figure 3.6d), that oscillates between faceting and dissolution growth leading to shapes close to regular nanoarchitectures with extended length scale (rods). The suggestion that growth of these particles occurs via oriented attachment between building block's facets can be a complex growth mechanism to be explained at this stage. It is also well-known that for fcc structure, the cube is the thermodynamically stable morphology, while branched morphologies have been shown to be characteristic of growth in a kinetically controlled growth regime [45]. The influence of the temperature on the formation of the PbS structures has been investigated by many authors [46,47]. In this study, the morphology of the films was significantly affected by the temperature. Higher temperature caused more branching in the structure of the deposited PbS.

The SEM images of PbS thin films deposited using complex (**5**) are shown in Figure 3.7. Thin films deposited at 350 °C (Figure 3.7a) and 400 °C (Figure 3.7b) showed

formations of compact thick and agglomerated spherical granules of the sizes ranging from 140 – 180 nm are observed. As the temperature was increased to 450 °C (Figure 3.7c), a mixture of spherical and cubic shaped PbS were formed. A significant change in morphology was observed when the temperature was raised to 500 °C (Figure 3.7d and 3.7e), where mixed shapes of cubes, spherical and branched/flower like structures were formed.

Table 3.2 summarizes the findings of the elemental composition from the energy dispersive X-ray spectroscopy (EDX) at 20 kV. All PbS thin films were in a stoichiometric composition of Pb to S of nearly 1:1. The extra elements in the EDX spectrum (C and Si) are due to carbon coating and glass substrate.

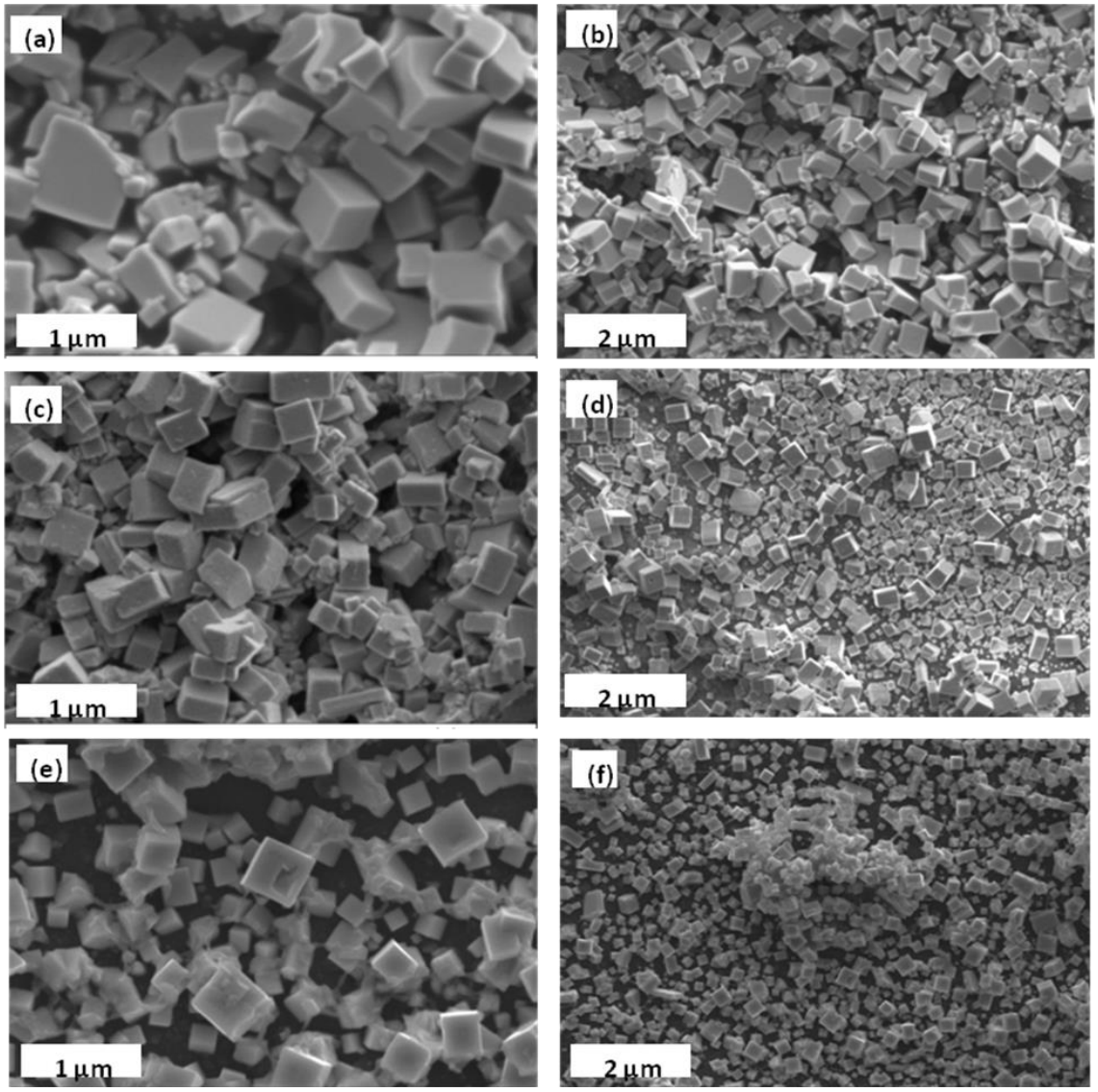


**Figure 3.5.** Secondary electron SEM images of the lead sulfide thin films deposited by spin coating using complex (**4**) at 350 (a) and (b), 400 (c) and (d) and 450 °C (e) and (f).

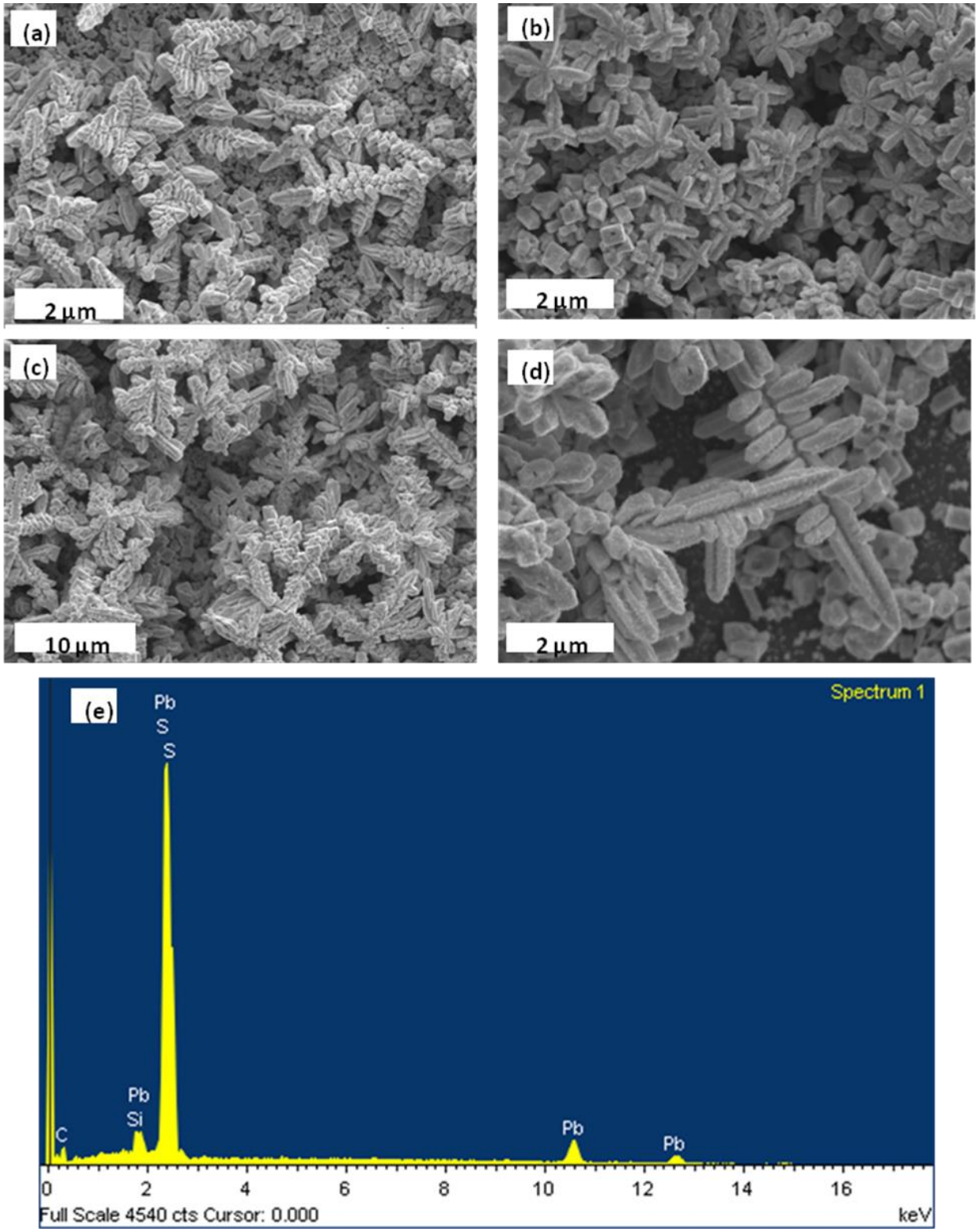


**Figure 3.6.** Secondary electron SEM images of the lead sulfide thin films deposited by spin coating using complex (**4**) at 500 °C (a-d) and a representative EDX (e).

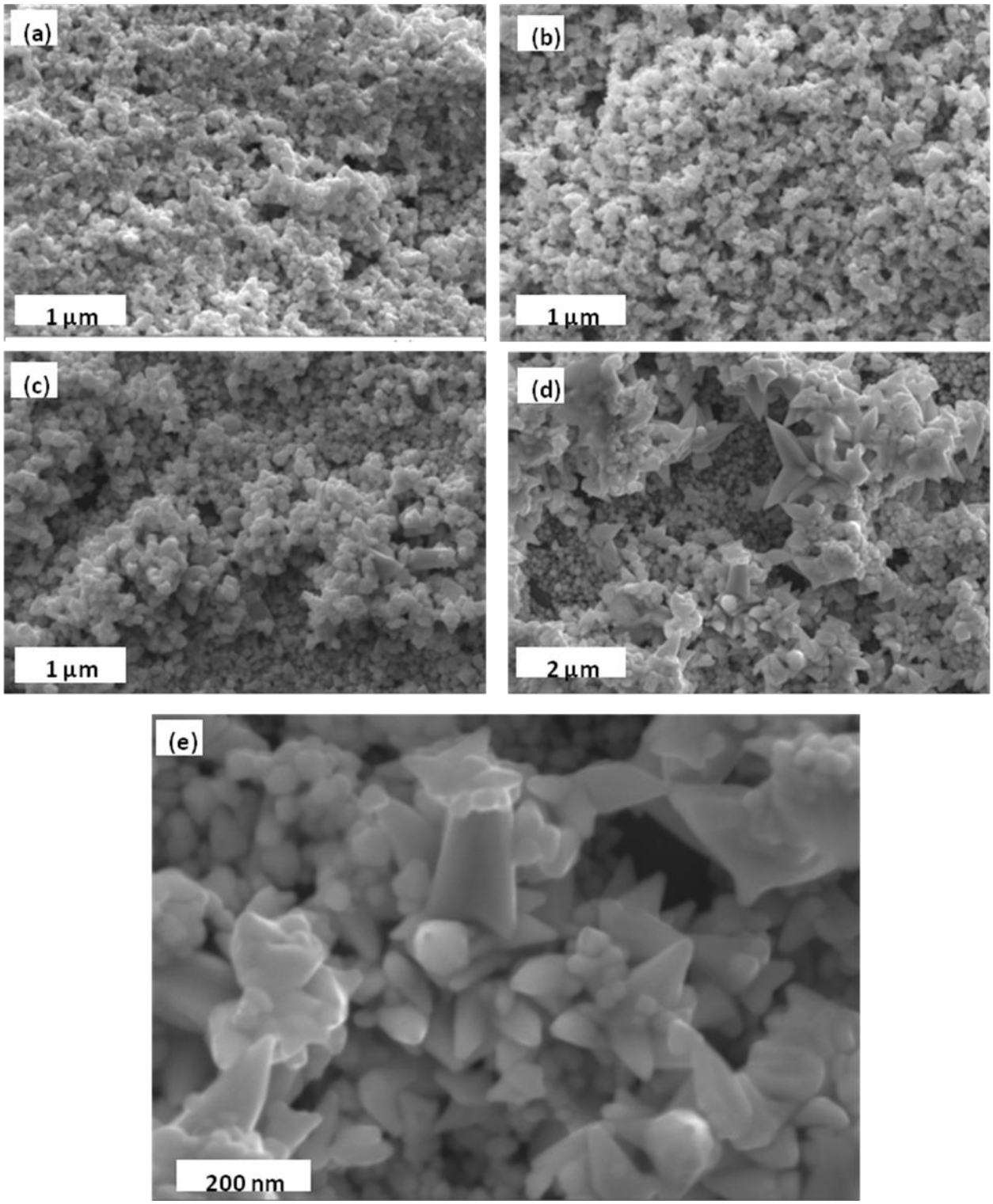


**Figure 3.7.** Secondary electron SEM images of the lead sulfide thin films deposited by spin coating using complex (**5**) at 350 °C (a), 400 °C (b), 450 °C (c) and 500 °C (d and e).

**Table 3.2.** Elemental composition of Pb and S in the thin films deposited by spin coating using complex (**4**) and (**5**).

| Complex | Temp (°C) | Pb (%) | S (%) |
|---|---|---|---|
| **(4)** | 350 | 48.01 | 51.99 |
| | 400 | 49.08 | 50.92 |
| | 450 | 49.23 | 50.77 |
| | 500 | 48.63 | 51.37 |
| **(5)** | 350 | 48.04 | 51.96 |
| | 400 | 47.29 | 52.71 |
| | 450 | 51.25 | 48.75 |
| | 500 | 47.75 | 52.25 |

The p-XRD patterns of the as-deposited PbS thin films after annealing at temperatures between 350–500 °C (Figure 3.8) were consistent with the face-centered cubic (halite) structure of PbS (ICDD 00-005-0592). Preferred growth along (200) plane was observed in all crystalline thin films. The p-XRD pattern of the as-prepared thin films grown on glass substrate showed sharp and narrow peaks. The estimated crystallite sizes from the (200) plane using Scherrer equation are presented in Table 3.3. Similarly, complex (5) gave face-centered cubic (halite) structure of PbS (ICDD 00-005-0592) (Figure 3.10).

The lattice constant of the PbS thin films were calculated by the relation for the cubic phase structure using the following relation [48]:

$$a = d(h^2 + k^2 + l^2)^{1/2} \quad \text{.....3.2}$$

where *h*, *k*, and *l* are the Miller indices, and *d* is the interplanar spacing. The lattice constant and plane spacing (200) for the PbS films are as shown in Table 3.3. Increasing temperature results in a general increase of lattice constant and d-spacing, clearly indicating that the crystal is influenced by stress, which leads to the compression of the lattice constants [49,50]. Figure 3.9 further reveals some micron and sub-micro-transformations as temperature increases. The observed lattice constant and d-spacing values are larger than the bulk values. Similarly, thin films deposited using complex (**5**) displayed similar crystal properties. Sizes

calculated from the Scherrer equation, lattice constants and d-spacings are summarized in Table 3.3.

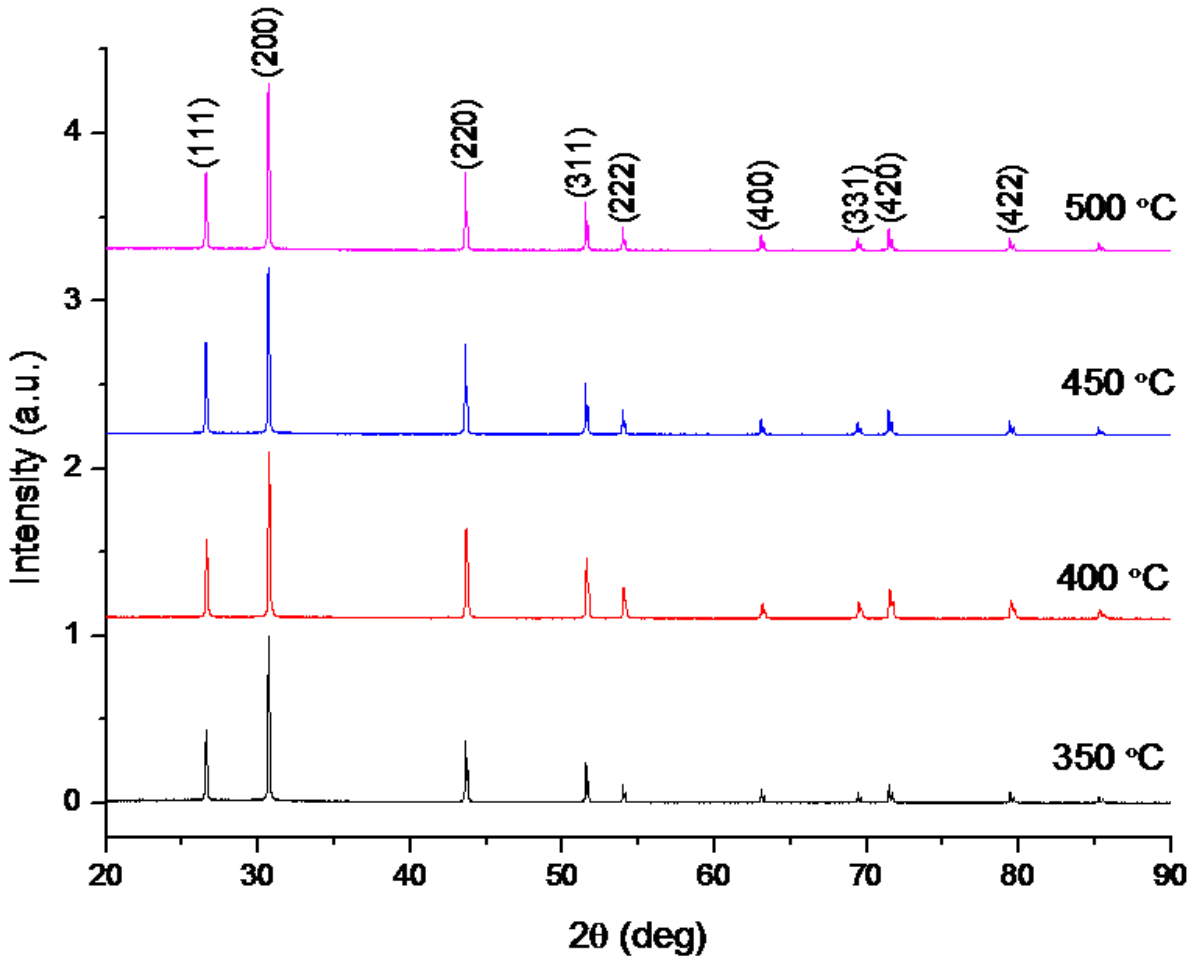


**Figure 3.8.** p-XRD patterns of PbS thin films deposited using complex (**4**).

**Table 3.3.** The structural properties of PbS thin films deposited by spin coating (Theoretical lattice constant a = 5.938 Å).

| **Complex** | **Temp (°C)** | **a (Å)** | **Obs d (Å)** | **Theor d (Å)** | **Size (nm)** |
|---|---|---|---|---|---|
| (**4**) | 350 | 5.7908 | 2.8954 | 2.969 | 56.44 |
| | 400 | 5.79446 | 2.8972 | | 56.45 |
| | 450 | 5.79580 | 2.8979 | | 63.30 |
| | 500 | 5.79920 | 2.8996 | | 59.08 |
| (**5**) | 350 | 5.7888 | 2.8944 | 2.969 | 44.34 |
| | 400 | 5.79404 | 2.8970 | | 47.76 |
| | 450 | 5.79460 | 2.8973 | | 50.06 |
| | 500 | 5.79484 | 2.8974 | | 51.72 |

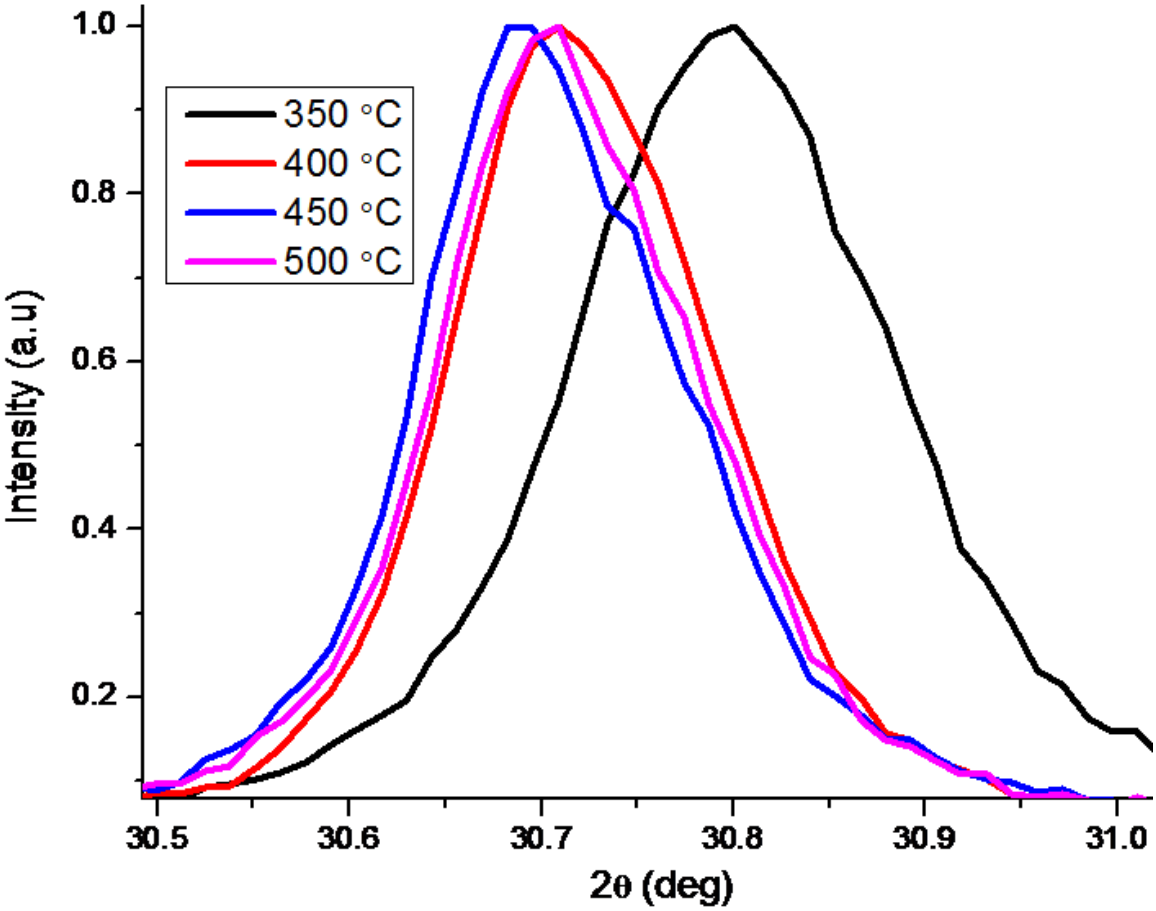


**Figure 3.9.** p-XRD pattern of the expanded form of PbS thin films deposited using complex (**4**) along the (200) plane.

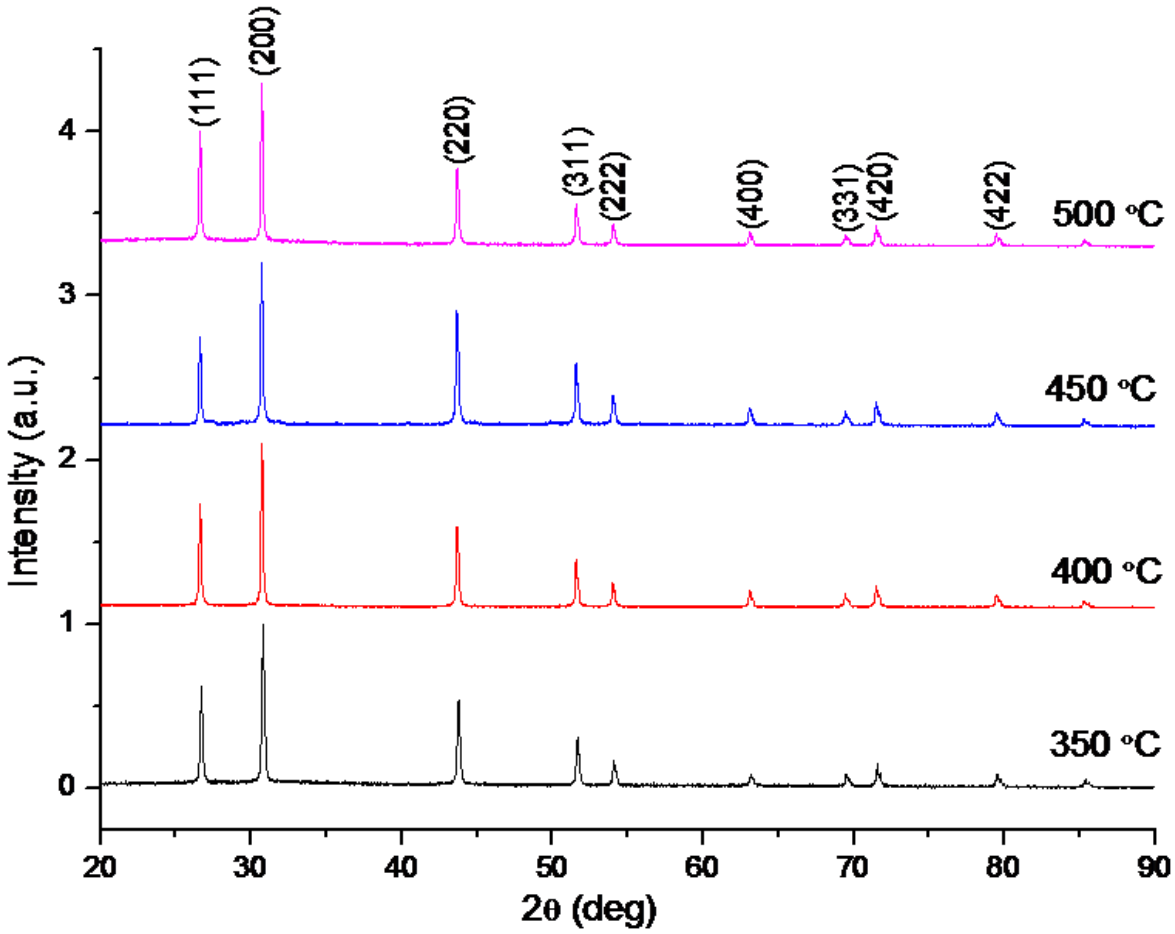


**Figure 3.10.** p-XRD patterns of PbS thin films deposited using complex (**5**).

Effects of synthesis factors have been shown to affect the crystalline structure of the nanomaterials [51]. Figure 3.11 presents the effect of temperature on the lattice cell parameters of the deposited PbS thin films at varying temperatures. As the temperature increases, the lattice constant parameter is observed to increase non-linearly, suggesting an increase in the lattice parameters as a result of thermal stress [51]. It is also observed that, there is no significant deviation of the trend on PbS films deposited from both complexes (**4**) and (**5**).

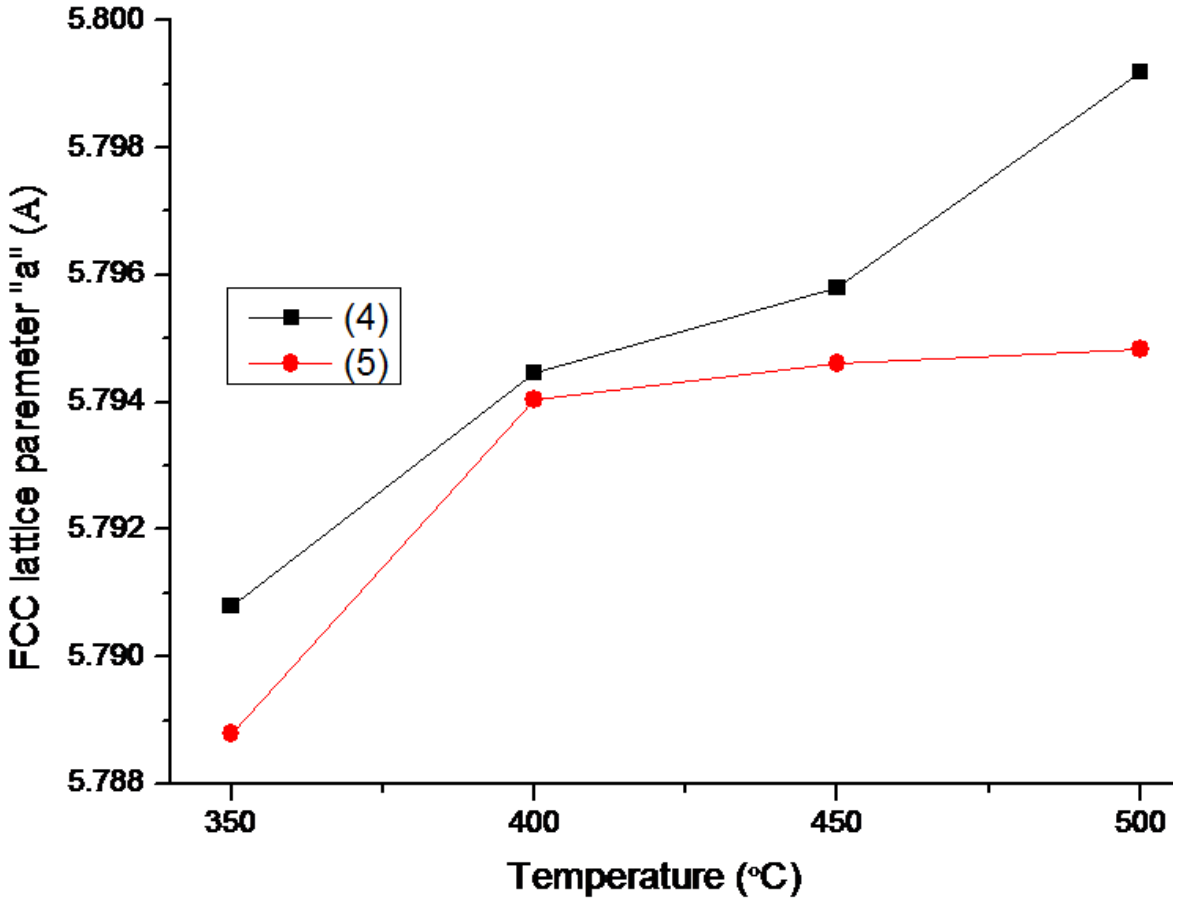


**Figure 3.11.** Plot of temperature (°C) against a-lattice parameters (Å) for PbS thin films deposited by spin coating of complexes (**4**) and (**5**) at temperatures 350, 400, 450 and 500 °C.

## 3.4. Conclusion

We intended to develop facile methods to synthesize PbS thin films by employing high temperature solid state techniques. Thus, in this chapter, single source precursors or complexes of piperidine (**4**) and tetrahydroquinoline (**5**) lead(II) dithiocarbamato complexes have been synthesized and characterized. Deposition of PbS thin films by aerosol assisted chemical vapour deposition (AACVD) using these complexes at different temperatures showed that the growth of PbS films was influenced by deposition temperature and method. The adoption of spin coated technique has also provided best morphologies, typical of PbS thin films. The UV–Vis NIR spectra of the films showed blue shift in absorption edge compared to bulk PbS. The powder X-ray diffraction (p-XRD) studies confirmed the formation of face-centred cubic PbS thin films. The variation of PbS thin films have well been investigated, varying from spherical, cubes, star and dendritic shaped microcrystals. The findings shown in this chapter have proven that the developed deposition approaches have a high potential as simple and effective routes for the fabrication of high quality nanomaterials. These approaches may provide a useful route to the shape control in the synthesis of other hierarchical, superstructured metal chalcogenides.

## 3.5. References


1. M. Salavati-Niasari, A. Sobhani and F. Davar, J. Alloys Compd. 2010, 507, 77.
2. N. Reilly, M. Wehrung, R. Andrew, O. Dell, and L. Sun, Mater. Chem. Phys. 2014, 147, 1.
3. K. T. Yong, Y. Sahoo, K. R. Choudhury, M. T. Swihart, J. R. Minter and P. N. Prasad, Chem. Mater. 2006, 18, 5965.
4. I. Chakraborty and S. P. Moulik, J. Nanoparticle Res. 2005, 7, 237.
5. L. D. Nyamen, V. S. R. Rajasekhar Pullabhotla, A. a. Nejo, P. T. Ndifon, J. H. Warner and N. Revaprasadu, Dalt. Trans. 2012, 41, 8297.
6. H. Karami, M. Ghasemi and S. Matini, Int. J. Electrochem. Sci. 2013, 8, 11661.
7. Y. K. Jung, J. Kim and J. Lee, J. Am. Chem. Soc. 2010, 132, 178.
8. K. C. Preetha and T. L. Remadevi, Mater. Sci. Semicond. Process. 2013, 16, 605.
9. M. Corricelli, D. Altamura, L. De Caro, A. Guagliardi, A. Falqui, A. Genovese, A. Agostiano, C. Giannini, M. Striccoli and M. L. Curri, CrystEngComm. 2011, 13, 3988.
10. K. N. Bourdakos, D. M. N. M. Dissanayake, T. Lutz, S. R. P. Silva and R. J. Curry, Appl. Phys. Lett. 2008, 92, 2008.
11. D. S. Gregory and R. Garry, Nat. Mater. 2006, 5, 683.
12. S. Günes, K. P. Fritz, H. Neugebauer, N. S. Sariciftci, S. Kumar and G. D. Scholes, Sol. Energy Mater. Sol. Cells, 2007, 91, 420.
13. F. C. J. M. Van Veggel, Chem. Mater. 2014, 26, 111.
14. J. D. Patel, Mater. Sci. Appl. 2012, 03, 125.
15. M. Asad, M. Fathipour, M. H. Sheikhi and M. Pourfath, Sensors Actuators A Phys. 2014, 220, 213.
16. L. Sun, J. J. Choi, D. Stachnik, A. C. Bartnik, B.-R. Hyun, G. G. Malliaras, T. Hanrath and F. W. Wise, Nat. Nanotechnol. 2012, 7, 369.
17. Y. Wang, Acc. Chem. Res. 1991, 24, 133.
18. S. S. Sun, Q. F. Han, X. D. Wu, J. W. Zhu and X. Wang, Mater. Lett. 2011, 65, 3344.
19. Z. Peng, Y. Jiang, Y. Song, C. Wang and H. Zhang, Chem. Mater. 2008, 20, 3153.
20. D. Wang, D. Yu, M. Shao, X. Liu, W. Yu and Y. Qian, J. Cryst. Growth 2003, 257, 384.

21. G. Pandey, S. Shrivastav and H. K. Sharma, Phys. E Low-Dimensional Syst. Nanostructures. 2014, 56, 386.
22. S. Axnanda, M. Scheele, E. Crumlin, B. H. Mao, R. Chang, S. Rani, M. Faiz, S. D. Wang, A. P. Alivisatos and Z. Liu, Nano Lett. 2013, 13, 6176.
23. Y. Zhao, X. H. Liao, J. M. Hong and J. J. Zhu, Mater. Chem. Phys. 2004, 87, 149.
24. M. R. Karim, M. D. Aktaruzzaman, M. Ashrafuzzaman and M. D. B. Zaman, 2014, 11, 531.
25. M. Behboudnia, M. Behboudnia, A. Habibi-Yangjeh, A. Khodayari, A. Khodayari and Y. Jafari-Tarzanag, Bull. Korean Chem. Soc. 2008, 29, 53.
26. D. Berhanu, K. Govender, D. Smyth-Boyle, M. Archbold, D. P. Halliday and P. O'Brien, Chem. Commun. 2006, 4709.
27. I. Jen-La Plante, T. W. Zeid, P. Yang and T. Mokari, J. Mater. Chem. 2010, 20, 6612.
28. S. Ye, Y. Ye, Y. Ni and Z. Wu, J. Cryst. Growth 2005, 284, 172.
29. T. Trindade, P. O'Brien, X. Zhang and M. Motevalli, J. Mater. Chem. 1997, 7, 1011.
30. F. Gerdes, M. Volkmann, C. Schliehe, T. Bielewicz and C. Klinke, Zeitschrift Für Phys. Chemie 2015, 229, 139.
31. N. O. Boadi, M. A. Malik, P. O'Brien and J. A. M. Awudza, Dalt. Trans. 2012, 41, 10497.
32. J. Akhtar, M. A. Malik, P. O'Brien and M. Helliwell. J. Mater. Chem, 2010, 20, 6116.
33. M Afzaal, K. Ellwood, N. L. Pickett, P. O'Brien, J. Raftery and J. Waters. J. Mater. Chem. 2004, 14, 1310.
34. J. Akhtar, M. Afzaal, M. A. Vincent, N. A. Burton, I. H. Hillier and P. O'Brien, Chem. Commun., 2011, 47, 1991.
35. J. M. Clark, G. Kociok-Köhn, N. J. Harnett, M. S. Hill, R. Hill, K. C. Molloy, H. Saponia, D. Stanton and A. Sudlow. Dalton Trans., 2011, 40, 6893.
36. J. Tauc, (1966) Optical Properties of Solids. Academic Press, New York, USA
37. Y. Wang, A. Suna, W. Mahler and R. Kasowski. J.Chem. Phys. 1987, 87, 7315.
38. A. L. Patterson, The Scherrer formula for X-Ray particle size determination. Phys. Rev. 1939, 56, 978.
39. Y. C. Choi, T. N. Mandal, W. S. Yang, Y. H. Lee, S. H. Im, J. H. Noh and S. I. Seok, Angew. Chem. Int. Ed. 2014, 53, 1329.

40. E. A. Lewis, P. D. McNaughter, Z. Yin, Y. Chen, J. R. Brent, S. A. Saah, J. Raftery, J. A. M. Awudza, M. A. Malik, P. O'Brien and S. J. Haigh, 2015, 27 (6), 2127. DOI: 10.1021/cm504765z.
41. C. H. Jo, J. H. Kim, J. Kim, J. Kim, M. S. Oh, M. S. Kang, M.-G. Kim, Y.-H. Kim, B-K. Ju and S. K. Park, J. Mater. Chem. C 2014, 2, 10305.
42 M. A. Lovette, A. B. Robben, D. W. Griffin, J. P. Sizemore, R. C. Snyder and M. F. Doherty, Ind. Eng. Chem. Res. 2008, 47, 9812.
43. S. Guenes, K. P. Fritz, H. Neugebauer, N. S. Sariciftci, S. Kumar and G. D. Scholes, Sol. Energy Mater. Sol. Cells 2007, 91, 420.
44. Z. Peng, Y. Jiang, Y. Song, C. Wang and H. Zhang, Chem. Mater. 2008, 20, 3153.
45. X. Duan, J. Ma, Y. Shen and W. Zheng, Inorg. Chem. 2012, 51, 914.
46. Y. Ma, L. Qi, J. Ma and H. Cheng, Crystal Growth & Design, 2004, 4( 2), 351.
47. A-J, Wang, Q-C. Liao, J-J. Feng, P-P. Zhang, Z-M. Zhang and J-R. Chen, Cryst. Growth Des. 2012, 12, 832.
48. S. Kumar, T. P. Sharma, M. Zulfequar and M. Husain, Physica B. 2003, 325, 8.
49. P. K. Basu, T. K. Chauduri, K. C. Nandi, R. S. Saraswat and H. N. Acharya, J. Mater. Sci. 1990, 25, 4014.
50. E. Pentia, L. Pintilie, I. Matei, T. Botila, and E. Ozbay, J. Optoelectro. Adv. Mater. 2001, 2, 525.
51. A. J. Saldivar-Garcia and H. F. Lopez, Mettall. Mater Trans. 2004, 35A, 2517.

# CHAPTER FOUR

# HETEROCYCLIC DITHIOCARBAMATO-IRON(II/III) COMPLEXES: SINGLE-SOURCE PRECURSORS FOR AEROSOL-ASSISTED CHEMICAL VAPOUR DEPOSITION (AACVD) OF IRON SULFIDE THIN FILMS

## 4.1. Introduction

Iron sulfide (Fe-S), the most abundant transition metal chalcogenide in the earth's crust, is potentially significant in several applications, these include biomedical and catalytic processes [1,2], hydrogen generation [3,4], environmental remediation [5], batteries and solar cells [6-8]. Furthermore, it has a number of advantages over other materials, such as low toxicity and cost, vacancy-dependent crystalline structures which could be useful in bandgap tuning across quantum confinement regimes, as well as interesting magnetic and electric properties [9]. It exists in several phases, such as pyrite (cubic-$FeS_2$), marcasite (orthorhombic-$FeS_2$), pyrrhotite ($Fe_{1-X}S$), greigite (cubic spinel-$Fe_3S_4$), smythite ($Fe_3S_4$), troilite-2H (FeS) and mackinawite ($Fe_{1+X}S$), amongst others [10,11]. The phase diagram of iron-sulfur compounds is complex, and a small variation in stoichiometry often leads to drastic changes in the structural, magnetic, electronic and physical properties of the chalcogenide formed [9,12].

Iron sulfide compounds exhibit a wide range of properties, from the semiconducting $FeS_2$ to ferromagnetic $Fe_3S_4$ [13]. In contrast to the properties of their bulk counterparts, iron sulfide thin films and nanoparticles can exist in magnetic structures with enhanced surface contributions. Amongst the iron sulfide phases, cubic-$FeS_2$ (pyrite) has attracted most interest, in particular in the development of thin-film solar cells and solid-state batteries, owing to its properties which include strong light absorption (~ $5 \times 10^5$ $cm^{-1}$) and a direct band gap of 0.95 eV [14-17].

Several studies on the deposition of iron sulfide thin films using single source precursors have been reported [18-20]. Aerosol-assisted chemical vapour deposition (AACVD) is a versatile route for the deposition of iron sulfide thin films. The morphology, particle size and crystal structure of the films deposited by this route can be closely controlled by the choice of a suitable solvent, deposition temperature and the nature of the precursor. The O'Brien group has been using single source precursors for the deposition of corresponding metal chalcogenide thin films and/or solution growth of nanoparticles; the group has recently utilised iron complexes of dithiocarbamates [21-24], thiosemicarbazone [25] and thiobiurets [26] for the deposition of Fe-S thin films by AACVD.

Presented in this chapter is the synthesis and characterisation of new iron(III) dithiocarbamate complexes, namely: *tris*-(piperidinedithiocarbamato)iron(III) (**6**) and *tris*-(tetrahydroquinolinedithiocarbamato)iron(III) (**7**). These complexes have been used as single-source precursors for the deposition of iron sulfide thin films using AACVD. Powder X-ray diffraction (p-XRD), scanning electron microscopy and optical measurements reveal that the structural and electronic properties of the as-deposited nanostructured iron sulfide films are strongly dependent on the deposition parameters such as temperature and solvent used. Structural and morphological transformations in the deposited films were also observed as a result of the change in the chemical structure of the starting materials, allowing the fabrication of rare phases of iron sulfide that have not been accessed before by AACVD. The decomposition mechanism of complex (**6**) is also proposed, based upon thermal analysis, gas chromatography mass spectroscopy (GC MS) and powder X-ray diffraction studies. For comparison purposes, the Fe(II) analogues (**8**) and (**9**) were prepared and used to deposit iron sulfide thin films under the same deposition conditions.

## 4.2. Experimental

### 4.2.1. Materials and method

*Tert*-butylthiol, toluene, hexane, Iron(II) chloride 98 %, Iron(III) chloride 97 % and chloroform were purchased from Sigma-Aldrich. Chemicals were used without further purification.

### 4.2.2. Synthesis of ligands and complexes

Sodium salts of piperidine and tetrahydroquinolinedithiocarbamato ligands were prepared according to procedures reported in literature [28] and were then converted to the corresponding iron(II/III) complexes by salt metathesis. A brief description of the synthesis of complexes is given below.

An aqueous solution of $FeCl_3$ (0.82 g, 5.0 mmol) in degassed deionised water (25.0 mL) was prepared under an inert atmosphere of dry nitrogen using a standard Schlenk line. To the resulting-coloured solution was added drop-wise a colourless aqueous solution of the ligand, sodium piperidine dithiocarbamate ($NaC_{10}NS_2H_{10}$) (3.482 g, 15.0 mmol) dissolved in a minimal amount of water, under vigorous stirring. The reaction mixture was stirred for a

further 1 h before the solution was filtered. The retained black coloured solids were washed with deionized water and dried under vacuum overnight. The solubility test of the resulting complex (**6**) found effortless solubility in chloroform and dichloromethane; solubility in toluene is enhanced at elevated temperatures. The solids were recrystallized from the chloroform and hexane (1:1) by diffusion method, to obtain black-coloured crystals. Complexes (**7**), (**8**) and (**9**) were prepared in a similar manner.

### 4.2.3. AACVD deposition of iron sulfide thin films

The AACVD technique was used to deposit iron sulfide thin films on glass substrates, from precursors (**6**) and (**7**). The AACVD assembly is similar to that described in chapter two, with few modifications. The glass substrates were ultrasonically cleaned in distilled water and acetone and then, finally stored in ethanol, prior to use.

In a typical deposition procedure, the 46.0 mM solution (8.0 mL) of the desired complex is used to generate aerosols at room temperature, on an ultrasonic humidifier operating at 50 Hz frequency. Argon was used as a carrier gas at a flow rate of 160 mL/min. Deposition experiments were conducted for 30 min and 2 hours for chloroform and toluene solutions, respectively.

### 4.2.4. Characterization techniques

#### *4.2.4.1. Carlo Erba EA 1108 elemental analyser*

The elemental analysis of C, H, N, S and Fe was carried out on a Carlo Erba EA 1108 elemental analyser which had been calibrated with standard reference materials.

#### *4.2.4.2. Spray gas chromatography mass spectroscopy*

Electrospray gas chromatography mass spectroscopy (GC-MS) analyses were recorded on a Kratos concept 1S instrument. Samples were dissolved in dichloromethane.
Other analyses tools were similar to those explained in Chapters 3.

## 4.3. Results and discussion

The iron complexes were isolated pure from water in good yields. The purity of the iron(III/II) dithiocarbamato complexes were established by microanalyses and infra-red

analysis and the results are summarized below. Both piperidine and tetrahydroquinoline dithiocarbamates complexes of iron(III) were black, where as those of iron(II) were brown, changing to black after a long time of exposure in air or moisture.

Yield 79.7 %. Elemental analysis for $C_{18}H_{30}FeN_3S_6$: Calc: C, 40.28; H, 5.63; N, 7.83; S, 35.85; Fe, 10.41. Found: C, 40.32; H, 5.73; N, 7.94; S, 35.34; Fe, 9.55. IR ($cm^{-1}$): 1422 (C=N), 965 (C=S), 365 (Fe-S).

Complex (**7**): Yield 62.4 %. Elemental analysis for $C_{30}H_{30}FeN_3S_6$: Calc: C, 52.93; H, 4.54; N, 6.17; S, 28.26; Fe, 8.20. Found: C, 53.19; H, 4.99; N, 6.42; S, 27.76; Fe, 7.81. IR ($cm^{-1}$): 1440 (C=N), 978 (C=S), 383 (Fe-S).

Complex (**8**): Yield 63.4 %. Elemental analysis for $C_{12}H_{20}FeN_2S_4$: Calc: C, 38.29; H, 5.36; N, 7.44; S, 34.08; Fe, 14.84. Found: C, 36.88; H, 5.53; N, 7.12; S, 32.57; Fe, 13.80. IR ($cm^{-1}$): 1498 (C=N), 989 (C=S), 369 (Fe-S).

Complex (**9**): Yield 59.7 %. Elemental analysis for $C_{20}H_{20}FeN_2S_4$: Calc: C, 50.84; H, 4.27; N, 5.93; S, 27.15; Fe, 11.82. Found: C, 47.21; H, 4.24; N, 5.53; S, 24.64; Fe, 11.06. IR ($cm^{-1}$): 1477 (C=N), 965 (C=S), 373 (Fe-S).

### 4.3.1. Single crystal X-ray crystallography structures of complex (6) and (7)

The single crystal X-ray structure of *tris*-(piperidinedithiocarbamato)iron(III) (**6**), is shown in Figure 4.1a. The X-ray structure has an octahedral iron cation coordinated by six sulfur atoms from the three bidentate piperidinedithiocarbamato ligands. The bond distances of Fe-S range from 2.2920 to 2.3067 Å. Structural refinement data are given in Table 4.1; selected bond angles and lengths are presented in the caption to Figure 4.1.

The single crystal X-ray structure of *tris*-(tetrahydroisoquinolinedithiocarbamato)iron(III) (**7**) is shown in Figure 4.1b. The structure also shows a distorted octahedral ($O_h$) environment with the Fe-S distances from 2.293 to 2.316 Å, relatively longer than those of complex (**6**). The Fe-S bond lengths from both complex (**6**) and (**7**) are relatively closer to those observed in previous work [29]. The bite angles 75.20°, 75.78° and 75.86° of S1-Fe1-S2, S3-Fe1-S4 and S5-Fe1-S6, respectively further reveal the distorted octahedral geometry on iron(III). Structural refinement data are

given in Table 4.1; selected bond angles and lengths are presented in the caption to Figure 4.1.

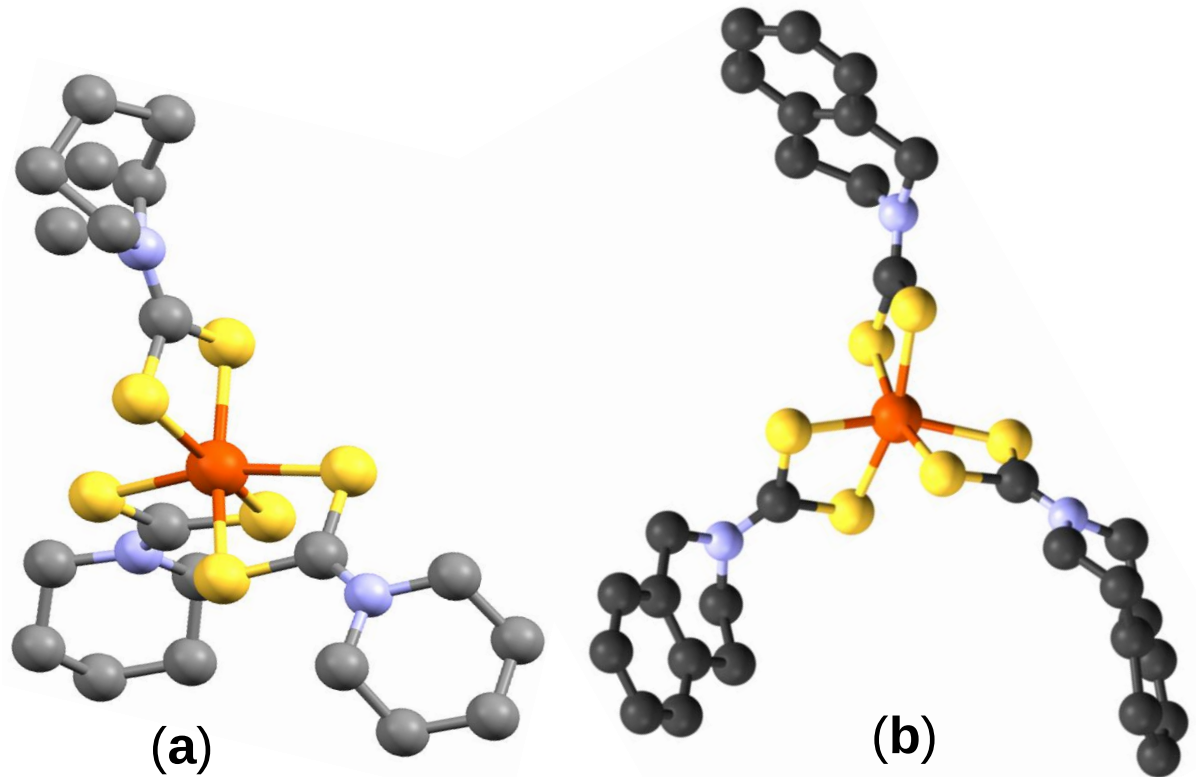


**Figure 4.1. (a)** The X-ray single crystal structure of $C_{18}H_{30}FeN_3S_6$ (**6**) (CCDC 984433) (Red = Fe, Yellow = S, Blue = N and Black = C). Selected bond lengths (Å) and bond angles (°); Fe(1)-S(1) 2.2920 (13), Fe(1)-S(1) #1 2.2920 (13), Fe(1)-S(3) #1 2.3003 (13), Fe(1)-S(3) 2.3003 (13), Fe(1)-S(2) 2.3067 (13), Fe(1)-S(2) #1 2.3067 (13), S(1)-Fe(1)-S(1) #1 99.40 (7), S(1)-Fe(1)-S(3) #1 93.87 (4), S(1) #1-Fe(1)-S(3) #1 162.84 (5), S(1)-Fe(1)-S(3) 162.84 (5), S(1) #1-Fe(1)-S(3) 93.88 (4), S(3) #1-Fe(1)-S(3) 75.46 (6), S(1)-Fe(1)-S(2) 75.81 (5), S(1) #1-Fe(1)-S(2) 94.62 (5), S(3) #1-Fe(1)-S(2) 99.17 (5), S(3)-Fe(1)-S(2) 92.41 (5), S(1)-Fe(1)-S(2) #1 94.62 (5), S(1) #1-Fe(1)-S(2) #1 75.81 (5), S(3) #1-Fe(1)-S(2) #1 92.41 (5), S(3)-Fe(1)-S(2) #1 99.17 (5), S(2)-Fe(1)-S(2) #1 165.37 (8). **(b)** The X-ray single crystal structure of $C_{30}H_{30}FeN_3S_6$ (**7**) (CCDC 1008838) (Red = Fe, Yellow = S, Blue = N and Black = C). Selected bond lengths (Å) and bond angles (°);Fe(1)-S(6) 2.293 (3), Fe(1)-S(2) 2.299 (3), Fe(1)-S(3) 2.307 (3), Fe(1)-S(5) 2.308 (3), Fe(1)-S(4) 2.309 (3), Fe(1)-S(1) 2.316 (3), S(6)-Fe(1)-S(2) 95.56 (11), S(6)-Fe(1)-S(3) 163.17 (12), S(2)-Fe(1)-S(3) 96.38 (11), S(6)-Fe(1)-S(5) 75.86 (10), S(2)-Fe(1)-S(5) 163.44 (12), S(3)-Fe(1)-S(5) 95.21 (11), S(6)-Fe(1)-S(4) 91.27 (11), S(2)-Fe(1)-S(4) 95.70 (11), S(3)-Fe(1)-S(4) 75.78 (10), S(5)-Fe(1)-S(4) 98.59 (10), S(6)-Fe(1)-S(1) 99.53 (11), S(2)-Fe(1)-S(1) 75.20 (10), S(3)-Fe(1)-S(1) 94.97 (11), S(5)-Fe(1)-S(1) 92.06 (10), S(4)-Fe(1)-S(1) 166.42 (12).

**Table 4.1.** Crystal Data and Structural Refinement Parameters for complexes (**6**) and (**7**)

| Complex | (**6**) | (**7**) |
|---|---|---|
| Formula | $C_{18}H_{30}FeN_3S_6$ | $C_{30}H_{30}FeN_3S_6$ |
| $M_r$ | 536.66 | 680.78 |
| Cryst Syst | Monoclinic | Orthorhombic |
| Space group | C2/c | Pca2(1) |
| a (Å) | 13.0387(9) | 21.9551(8) |
| b (Å) | 11.8818(9) | 18.8423(6) |
| c (Å) | 15.9260(15) | 14.7741(4) |
| α (deg) | 90 | 90 |
| β (deg) | 101.292(6) | 90 |
| γ (°) | 90 | 90 |
| V ($Å^3$) | 2419.5(3) | 6111.8 (3) |
| Z, Calculated density (D) | 4, 1.473 Mg $m^{-3}$ | 4, 1.480 Mg $m^{-3}$ |
| Temperature (K) | 100(2) | 100(2) |
| Refinement method | Full-matrix least-squares on $F^2$ | Full-matrix least-squares on $F^2$ |
| Reflections collected /unique | 8309/2300, [R(int)=0.0695] | 24173/8695 [R(int) = 0.0991], |
| Final R indices [I > 2σ(I)] | R1 = 0.0541, wR2 = 0.1176 | R1 = 0.0670, wR2 = 0.1576 |
| R indices (all data) | R1 = 0.0707, wR2 = 0.1336 | R1 = 0.1083, wR2 = 0.1784 |
| largest diff. peak and hole | 0.707 and −0.935 $eÅ^{-3}$ | 1.034 and −0.614 $eÅ^3$ |
| GOF | 1.068 | 1.027 |

### 4.3.2. Thermogravimetric analysis (TGA)

The thermogravimetric analysis (TGA) of complex **(6)** shows a two step decomposition pattern with a rapid weight loss of 15.6 % and 65.5 % at 210 °C and 304 °C,

respectively (Figure 4.2). The weight of the remaining residue after complete decomposition is 15.7%, which corresponds to the material bearing an empirical formula of FeS. On the other hand, the thermogram of complex (**7**) shows an undefined three-step decomposition pattern with weight loss of 28.0%, 44.3% and 7.1% at 207 °C, 257 °C and 351 °C, respectively; the final weight of 11.8% is assumed to be a residue of iron sulfide material, which is sulfur deficient (Figure 4.2). Decomposition seems to continue when approaching 700 °C, probably due to the presence of residual carbonaceous species in the films, or sublimation of the iron sulfide product, perhaps leading to sulfur deficient phases.

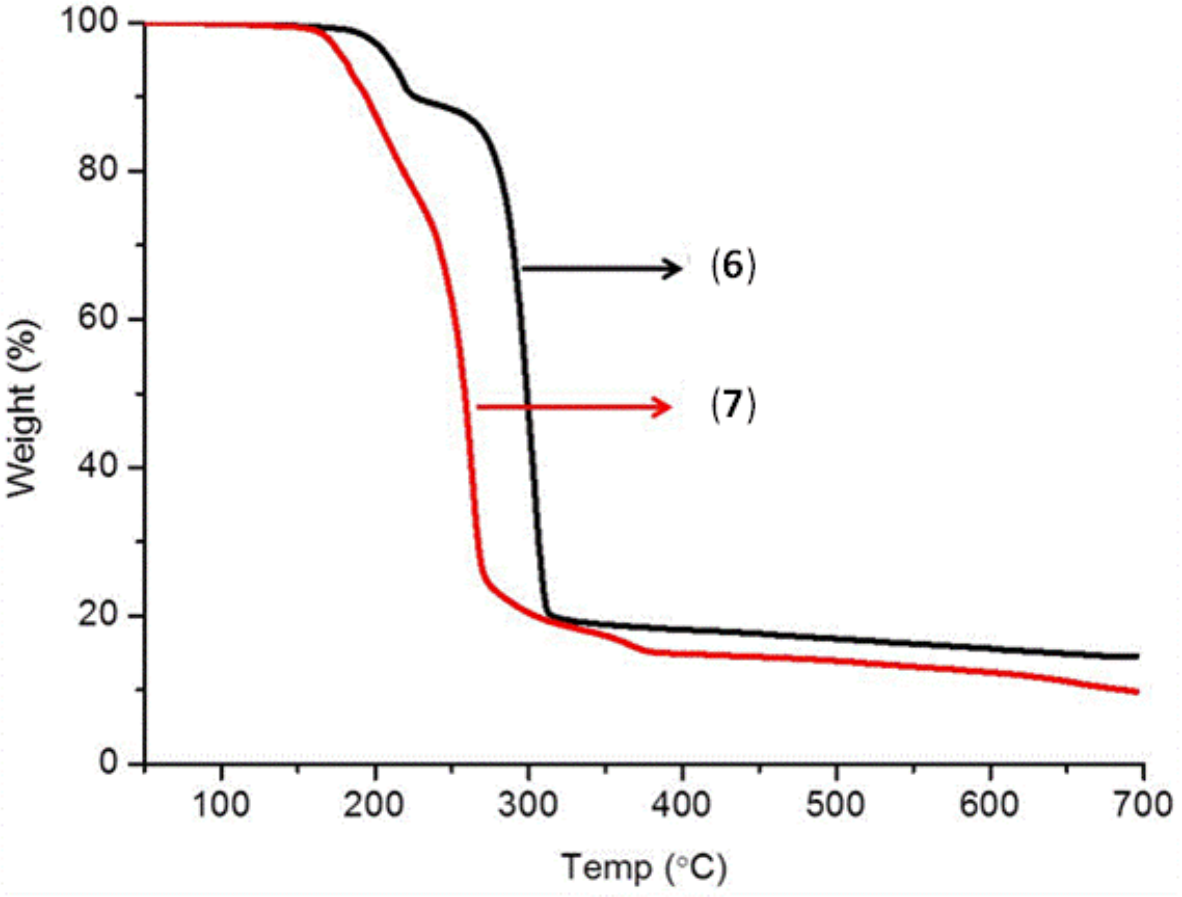


**Figure 4.2.** Thermogravimetric analysis (TGA) of complexes **(6)** and **(7)** at a heating rate of 10 °C/min under nitrogen with a flow rate of 10 $cm^3$/min.

### 4.3.3. Decomposition mechanism of complex (6)

The decomposition mechanism of complex (**6**) (Figure 4.3) was investigated using thermogravimetric analysis (TGA), gas chromatography mass spectroscopy (GC-MS) and

powder X-ray diffraction (p-XRD) analytic techniques. Thermal studies discussed in section 4.4.2 showed that the decomposition of the complex proceeds through two major steps which may probably follow the following pattern: (i) detachment of one of the three dithiocarbamate ligands in the six coordinated *tris*-(piperidinedithiocarbamato)iron(III) complex, thus forming an intermediate four-coordinated complex, and lastly (ii) final decomposition/detachment (304 °C) of the four coordinated dithiocarbamato complex of iron to afford materials of either FeS or indefinite Fe-S composition (Figure 4.2). The first weight loss of 15.6 % is smaller than the weight of the anticipated release of only one piperidine dithiocarbamate ligand (~29 %). Thus, the first step may involve partial decomposition, rearrangement of the complex and/or reduction to Fe(II) complex. GC mass spectrum also confirmed complete decomposition of the complex via two steps (Figure 4.4): (i) elimination of one piperidinyl dithiocarbamato ligand (*m/z* 160), followed by (ii) complete removal of the remaining organic components (*m/z* 290) thus affording FeS as the final product (*m/z* 86).

A separate study which aimed at identifying the existence of temperature-dependent phase transformation in the iron sulfide materials was carried out. The progress of this experiment was monitored using powder X-ray diffractometry. Diffraction studies (Figure 4.5) were carried out at a heating rate of 2.5 °C/$h^{-1}$, where complex (**6**) was the starting material pyrolized and annealed from 180 °C to 310 °C under $N_2$ flow. A total of 27 diffraction patterns were collected. Hexagonal phase (card number 01-080-1032) of iron sulfide and mackinawite (card number 04-003-6935) became prominent with an increase in temperature, with few peaks unassigned. The observed temperatures for the occurrence of Fe-S phases are lower than those established from phase diagrams, probably due to the prolonged time of the diffraction analysis and heating.

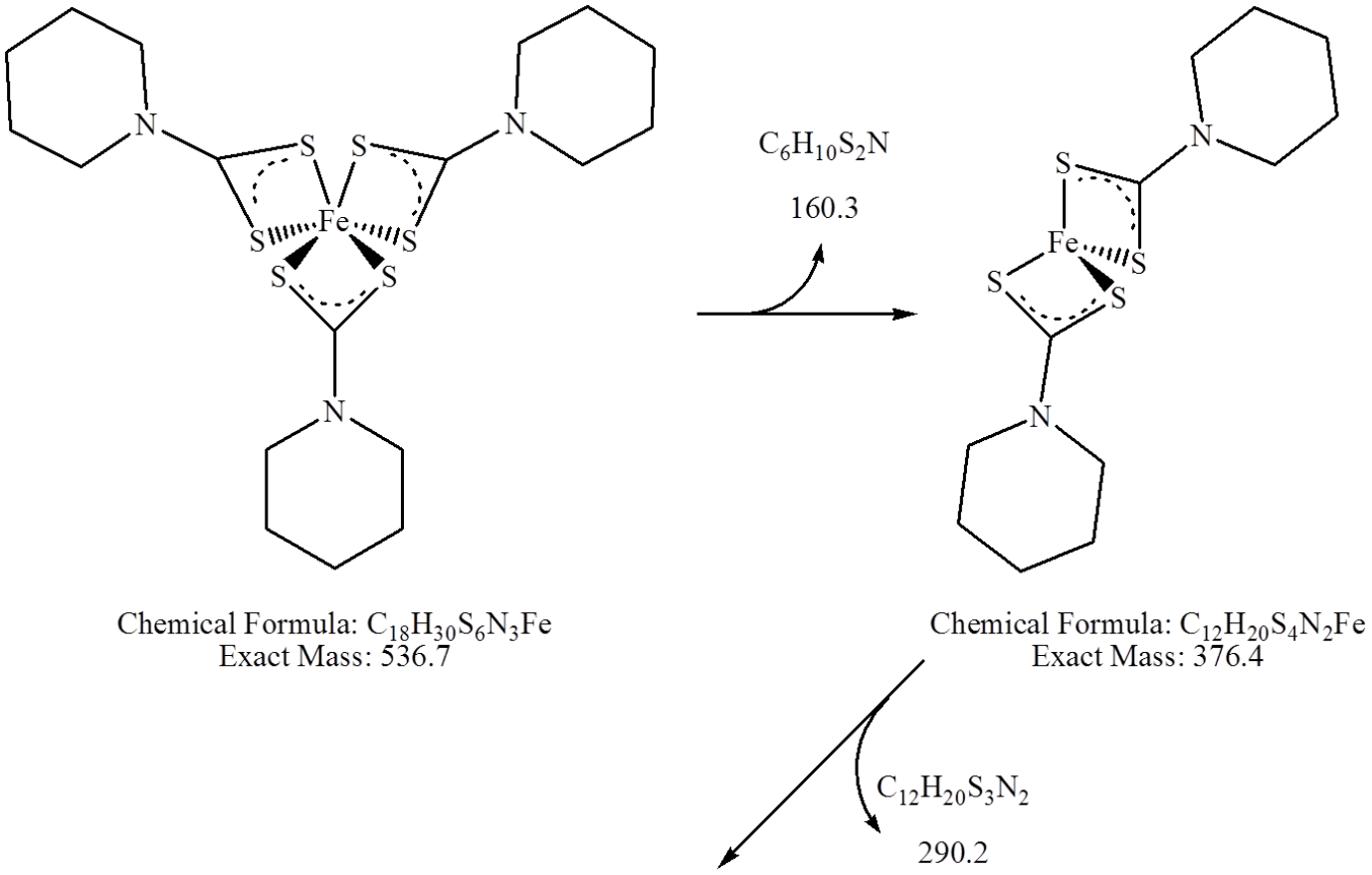


**Figure 4.3.** Proposed decomposition mechanism of complex (**6**).

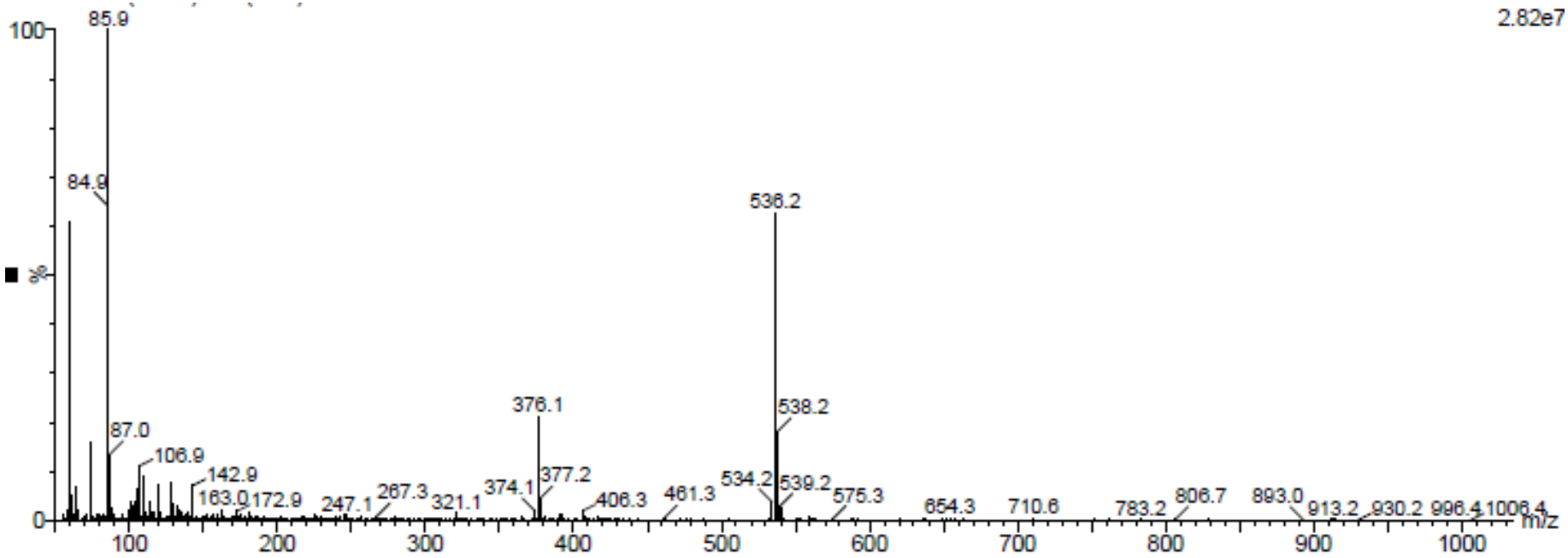


**Figure 4.4.** GC MS spectrum of complex (**6**).

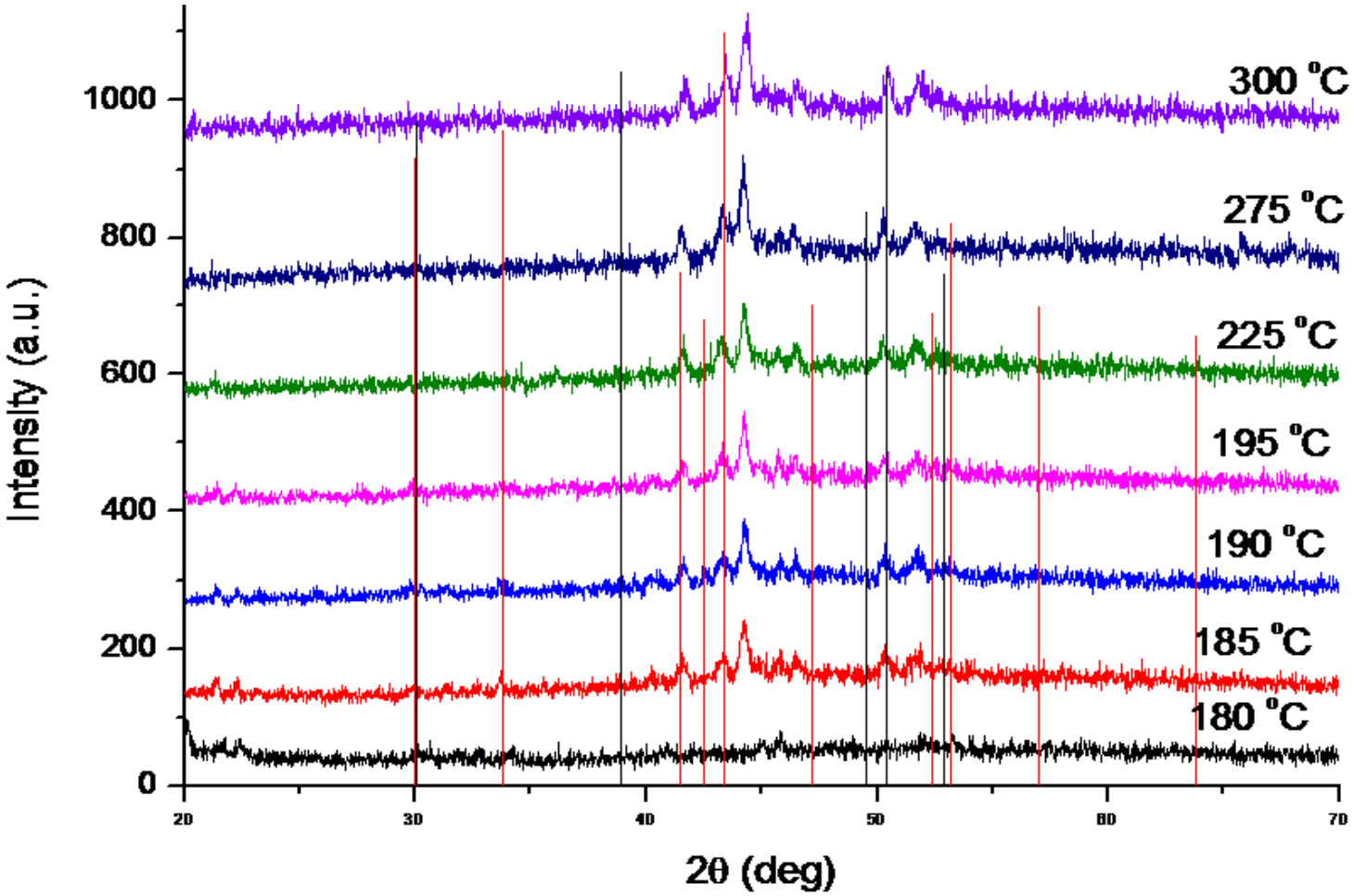


**Figure 4.5.** p-XRD pattern of the decomposed product of complex (**6**) under $N_2$ flow studied from 180 to 310 °C. Only few patterns were chosen to represent in this study. (A red stick represents hexagonal $Fe_{0.975}S$, card number 01-080-1032 and black for mackinawite phase FeS, card number 04-003-6935).

### 4.3.4. Deposition of iron sulfide thin films using toluene solution

Thin films of iron sulfide were deposited on glass substrates by AACVD at three different temperatures: 350, 400 and 450 °C using either chloroform or toluene (sonicated at 70 °C) as solvents. The films produced were characterized by scanning electron microscopy (SEM), energy dispersive X-ray (EDX) spectroscopy, powder X-ray diffraction (p-XRD), optical absorbance spectroscopy and atomic force microscopy (AFM). Table 4.2 provides a summary of results obtained from deposition of iron sulfide films using complexes (**6**) and (**7**).

The SEM images of iron sulfide films in Figure 4.6 deposited using complex (**6**) in toluene solvent, show the growth of sheet-like structures at 350 °C and nano-leaf/flake like crystallites at 400 °C and 450 °C. The film sizes increased with an increase in deposition temperature; an increase in film size of 0.6 - 1.0 μm was observed when the temperature was increased to 400 °C and 450 °C. Some microstructures on the surfaces were also observed. The morphology obtained from this study is reasonably similar to those recently reported on iron sulfide thin films deposited using iron thiobiuret and diethyldithiocarbamate complexes [21,27]. The EDX spectroscopy on five different areas of the films showed that the compositions are slightly sulfur deficient, a trend that increased at elevated temperature (Table 4.3).

**Table 4.2.** Summary of iron sulfide thin films obtained from complex (**6**) and (**7**) under different reaction conditions

| Precursor | Reaction conditions | Morphology | Phase |
|---|---|---|---|
| Complex (**6**) marcasite | Toluene, 350-450 °C, 2 hrs | Leaf, flake, sheet | Hexagonal ($Fe_{0.975}S$), ($FeS_2$) |
| | Chloroform, 350-450 °C, 30 minutes | Fiber | Hexagonal ($Fe_{0.975}S$), smythite ($Fe_3S_4$) |
| | *Tert*-butyl thiol, 450 °C, 2 hrs | Flower, spherical-globular | Greigite ($Fe_3S_4$) |
| Complex (**7**) | Toluene, 350-450 °C, 2 hrs | Leaf, flake, Sheet | Pyrrhotite ($Fe_{0.95}S_{1.05}$), hexagonal ($Fe_{0.975}S$) |
| | Chloroform, 350-450 °C, 30 minutes | Fiber | Hexagonal ($Fe_{0.975}S$) |
| | *Tert*-butyl thiol, 450 °C, 2 hrs | Spherical and flake | Greigite ($Fe_3S_4$) |

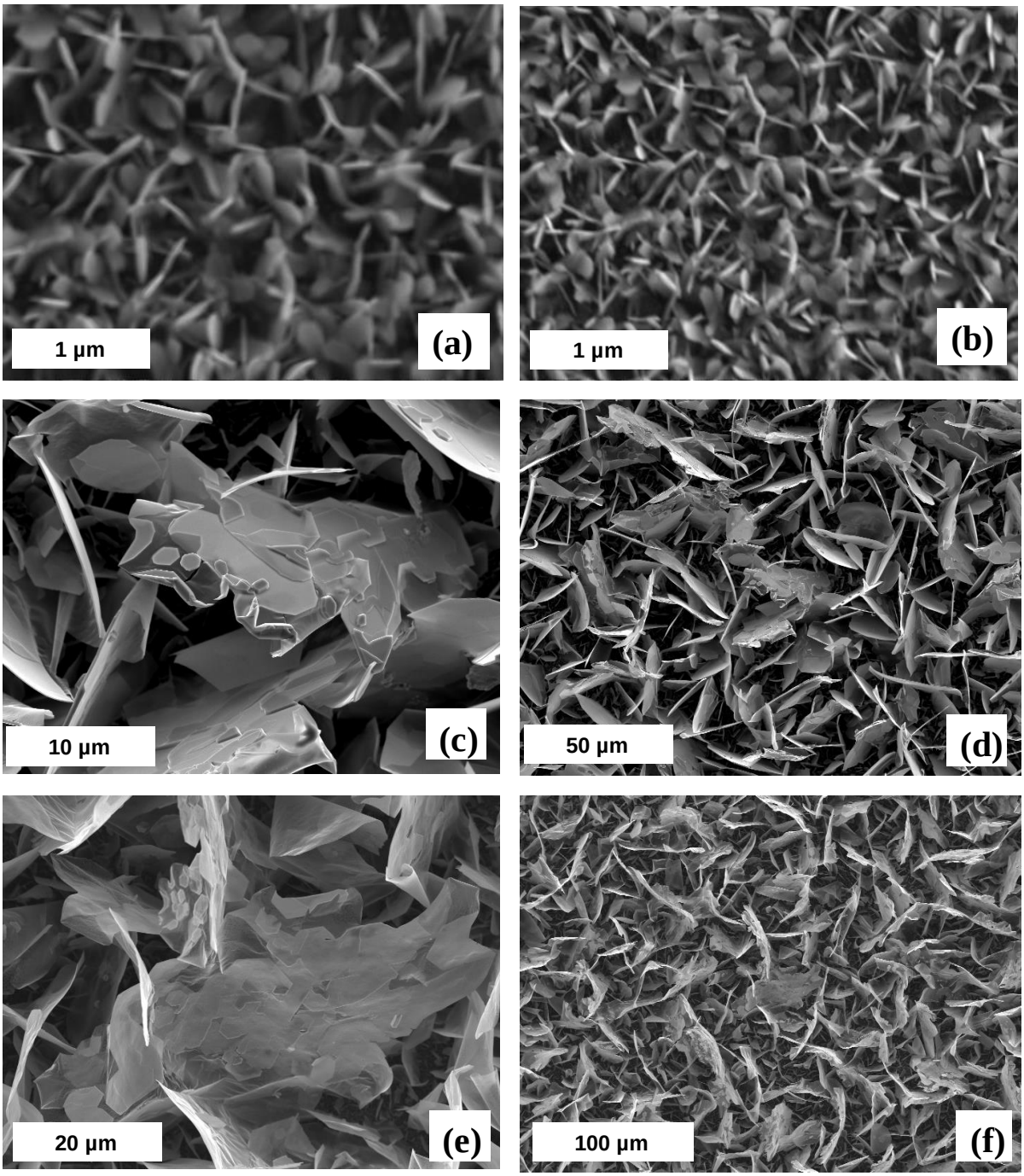


**Figure 4.6.** Secondary electron SEM images of the iron sulfide thin films deposited at (a and b) 350 °C, 400 °C (c and d) and (e and f) 450 °C using complex (**6**).

A similar trend was observed when complex (**7**) was used as single source precursor to deposit a pyrrhotite film (Figure 4.7a and b). The images illustrate formation of typical nanosheet-like structures. A slight morphological transformation is observed, as a result of the change in the chemical structure of the starting materials.

**Table 4.3.** Elemental composition of Fe and S in the thin films deposited using complex (**6**).

| **Temp (°C)** | **Fe (%)** | **S (%)** | **Ratio (Fe:S)** |
|---|---|---|---|
| 350 | 57.3 | 42.7 | $Fe_{(1+x)}S$, $x$=0.3 |
| 400 | 60.8 | 39.2 | $Fe_{(1+x)}S$, $x$=0.5 |
| 450 | 66.3 | 33.7 | $Fe_2S$ |

The back-scattered electron (BSE) SEM image (which provide *Z* contrast) of iron sulfide films, show small particles with bright contrast embedded into darker flakes. EDX revealed that the white spots (chunks) were S-rich (Fe 53.7% and S 46.3%), while the opposite is observed for the black spots (flakes) which are Fe-rich (Fe 66.9% and S 33.1%) (Figure 4.7c). This phenomenon validates that Fe and S atoms in an iron sulfide thin film are unevenly distributed on a substrate, strongly suggestive of the formation of an overall S-deficient film. The darkness of the iron rich area suggests that there is a lighter element such as carbon in this area of the film that tends to darken the contrast compared to the small crystallites observed which appear white.

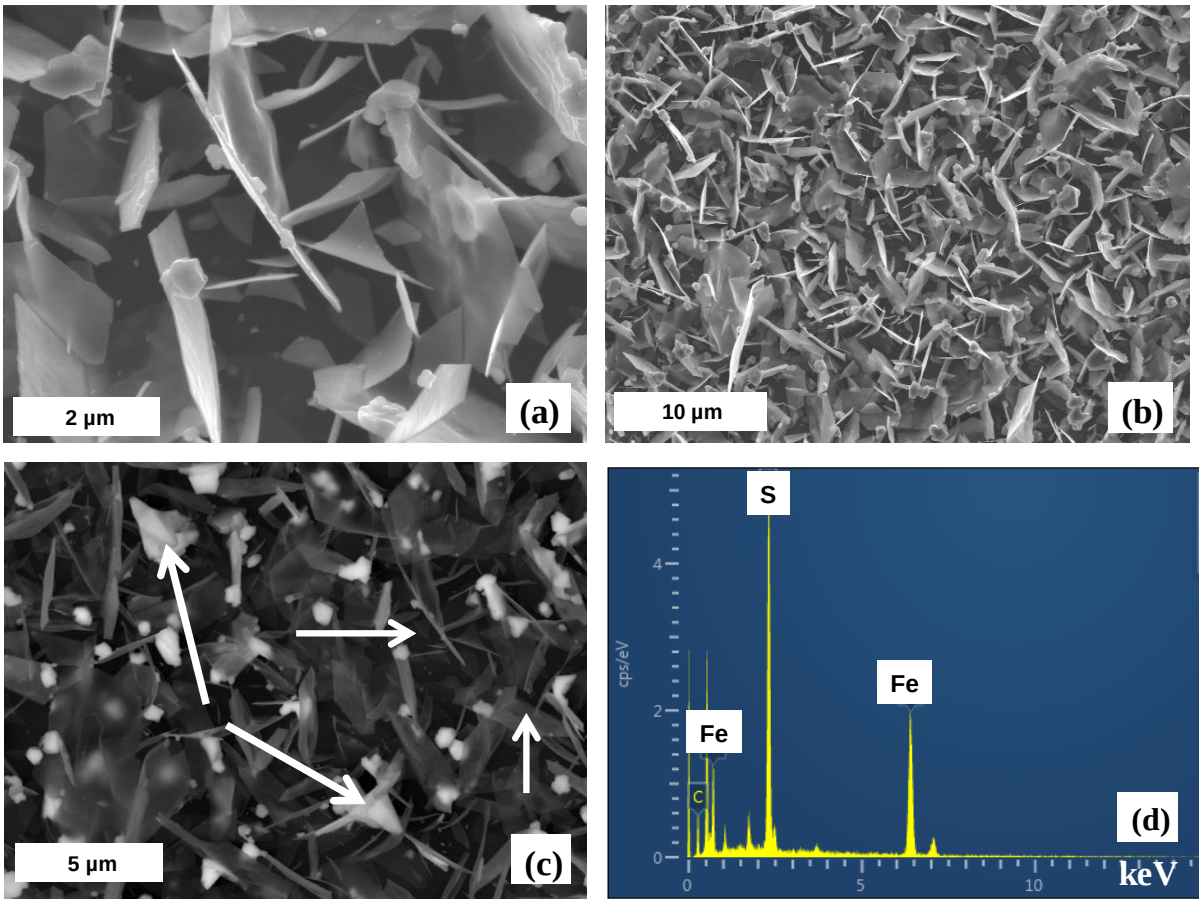


**Figure 4.7.** Representative secondary electron SEM images of the iron sulfide thin films deposited at (a and b) 450 °C and its corresponding backscattered electron SEM image (c) and a representative EDX spectrum (d) when complex (**7**) was used {white spots (chunks) and black spots (flakes)}.

The *p*-XRD patterns of the as-deposited films from complex (**6**) show hexagonal-phase iron sulfide ($Fe_{0.975}S$) (card number: 01-080-1032), dominating at the higher temperature of 450 °C (Figure 4.8). The reflection (*hkl*) planes of (110), (201) (114) (214) and (220) corresponding to the $Fe_{0.975}S$ phase were observed at 450 °C. At the deposition temperatures of 350 °C and 400 °C, the XRD patterns showed mixed phases of marcasite ($FeS_2$) and iron sulfide ($Fe_{0.975}S$) phases. The reflections at 25.97°, 37.38°, 38.89° and 40.59° were indexed to the (110), (111), (120) and (200) planes of marcasite $FeS_2$ (card number: 03-065-2567), respectively. Mixed phases of marcasite ($FeS_2$) and hexagonal iron sulfide ($Fe_{0.975}S$) coexist at 350 °C and 400 °C, while the latter are predominantly obtained in its pure phase at 450 °C. The transformation of iron sulfide compounds into different phases is possible under certain conditions such as high temperature or pressure [30-32].

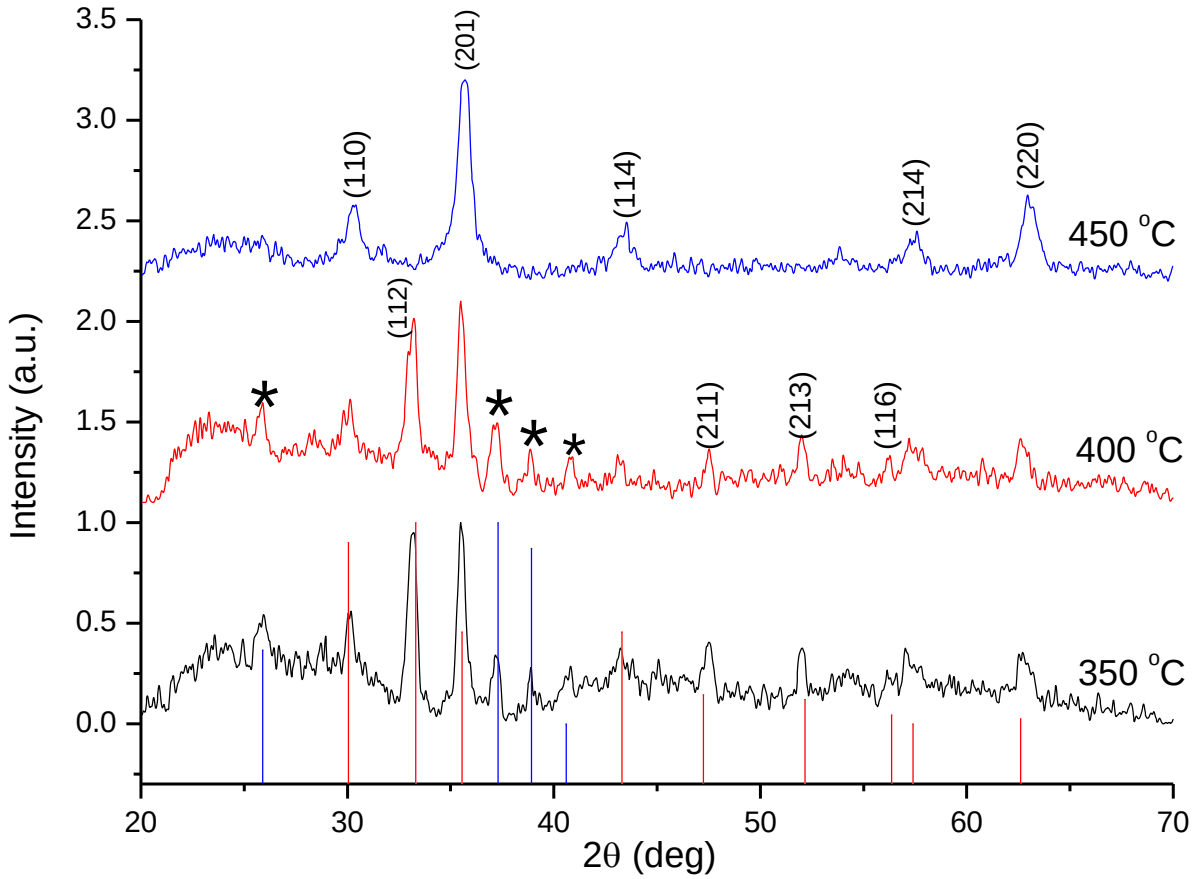


**Figure 4.8.** p-XRD of predominantly iron sulfide ($Fe_{0.975}S$, red sticks) thin films deposited from toluene solution of complex (**6**). The asterisk symbol (*) denotes the marcasite phase ($FeS_2$ represented by blue sticks).

A comparison *p*-XRD pattern for the iron sulfide film deposited from complex (**7**) by AACVD at 350, 400 and 450 °C is presented in Figure 4.9. A pure hexagonal-pyrrhotite 1T ($Fe_{0.95}S_{1.05}$) phase is formed at 450 °C (card number: 01-075-0600), while at 350 and 400 °C some additional peaks are observed (denoted by a symbol #) which matched a hexagonal iron sulfide phase ($Fe_{0.975}S$) (card number 01-080-1032). These results suggest that the mechanism at which the complexes decompose are different. Intergrowth involving different pyrrhotite types are known [33-35], and the degree of such intergrowths (micron to submicron) makes analysis difficult and therefore information on accurate Fe:S ratios and concentration of impurity are relatively incomplete for the pyrrhotite in this study. These results are similar to recent reports [21], where formation of pyrrhotite phase were observed at 400 and 450 °C when alkylldithiocarbamatoiron(III) complexes were used as single source precursors to deposit films by AACVD.

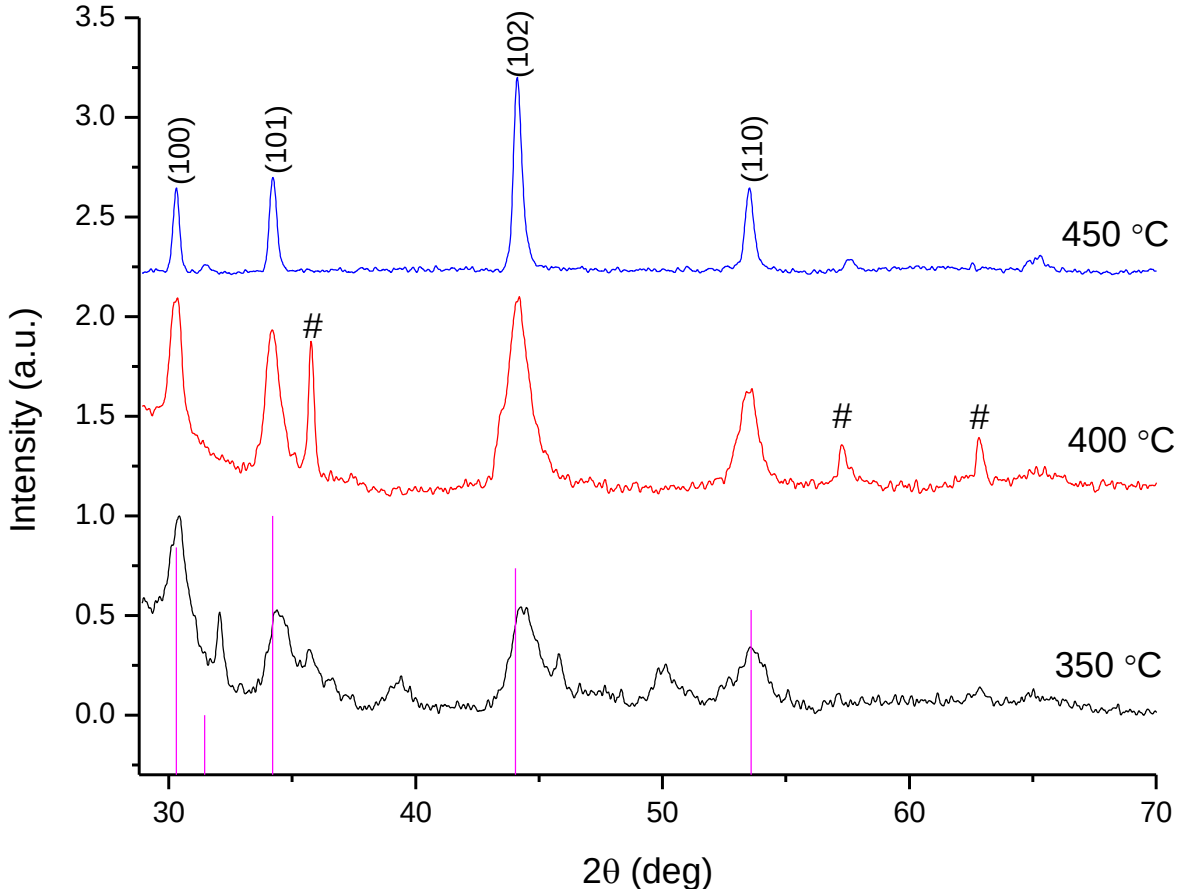


**Figure 4.9.** p-XRD of Fe-S thin films deposited from toluene solution of complex (**7**). (Purple sticks represent standard card for hexagonal-pyrrhotite 1T ($Fe_{0.95}S_{1.05}$) phase) The symbol # denotes the iron sulfide ($Fe_{0.975}S$) phase (card number: 01-080-1032).

The UV-Vis-NIR absorption spectra of the iron sulfide thin films deposited from complex (**6**) at 350, 400 and 450 °C are shown in Figure 4.10. The as-deposited iron sulfide thin films absorb light in the visible and near-infrared spectral regions. Deposition at 350 °C displays a sharp absorption band gap of 1.63 eV, estimated from Tauc's plots (Inset Figure 4.10) [36]. The films deposited at 400 and 450 °C exhibited red shifted absorption properties (~1.25 - 1.34 eV) compared to that of 350 °C. The blue shift observed for the absorption spectra, reveals formation of surface defects free [37] and hence high optical performance activeness of the films in the visible and infrared region. The optical behaviour of the deposited films reveals that the absorption properties are temperature, size and structure

dependant.

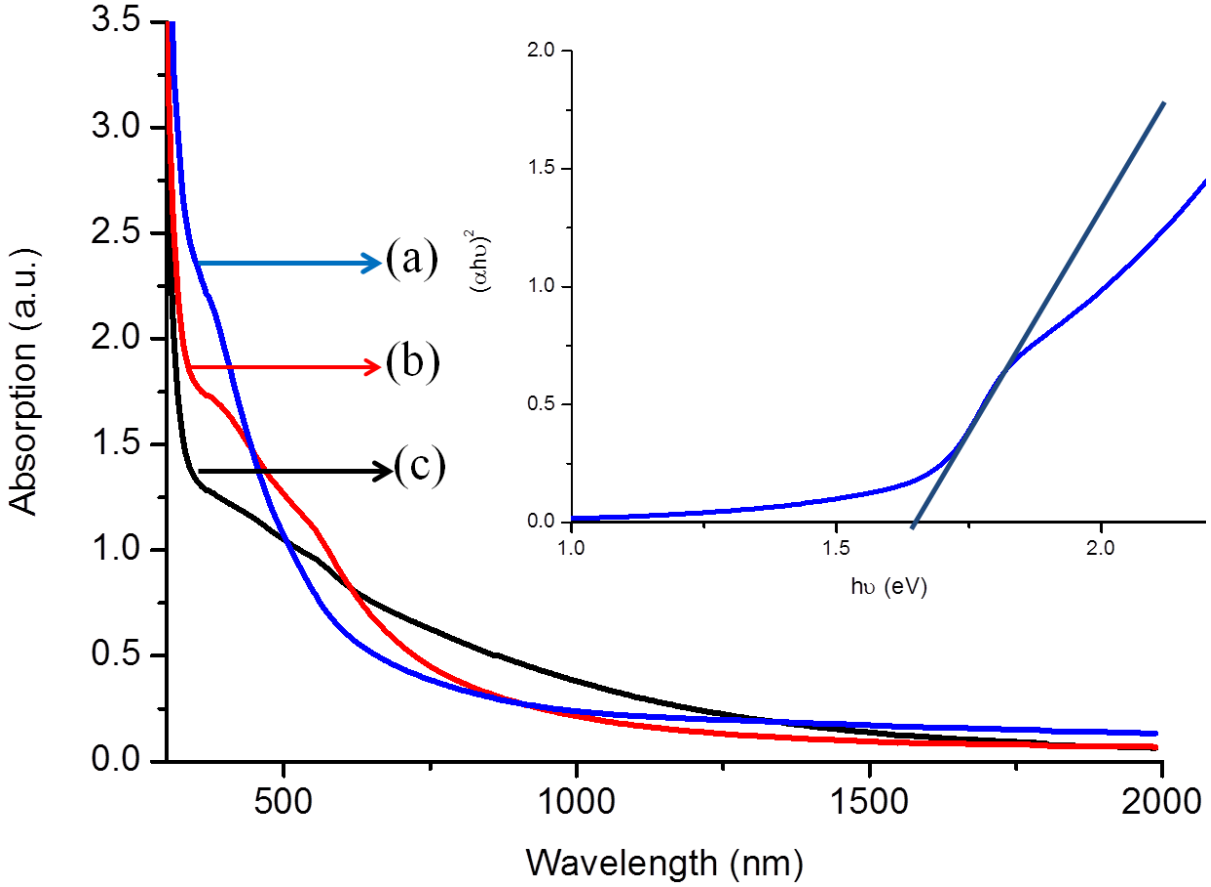


**Figure 4.10.** UV-Vis-NIR absorption spectra of Fe-S thin films deposited at (a) 350 (b) 400 and (c) 450 °C from toluene solution of complex (**6**). Inset: A representative Tauc plot showing the estimated optical band gap of Fe-S film deposited at 350 °C.

### 4.3.5. Deposition of iron sulfide thin films from solution in chloroform

The role of a solvent in the formation of thin films by AACVD can be significant and has been described on the physical basis of the enthalpy of combustion and vaporization, nature of bonding between precursor and solvent molecules in aerosol droplets as well as the coordinating ability of the solvent, which in one way or another may influence the nucleation by changing the enthalpy of the system [38,39]. Chloroform has lower heat of combustion and vaporization (473.2 and 31.4 kJ $mol^{-1}$, respectively), thus evaporates faster, causing homogeneous nucleation. On the other hand, the higher heat of combustion and vaporization (3910.3 and 38.06 kJ $mol^{-1}$, respectively) of toluene facilitates both homogeneous and heterogeneous nucleation growth of the particles. Indeed, the iron sulfide films deposited from chloroform aerosols were observed to be significantly different from those deposited from the toluene aerosols. The representative SEM images of iron sulfide thin films deposited

at various temperatures are shown in Figure 4.11. Irregular, bundles of nanofibers structures are observed when complex (**6**) was deposited at 350 °C with particle sizes ranging between 400 – 450 nm. No significant morphological changes were observed when the temperature was increased (Figure 4.11a&b). However, a considerable increase in particle sizes to 530 – 580 nm and 600 – 650 nm are observed at 400 and 450 °C, respectively. A similar morphological trend was observed for complex (**7**); Figure 4.11(c&d) showing a representative bundle of nanofiber-like structures obtained at 450 °C with sizes between 525 – 575 nm.

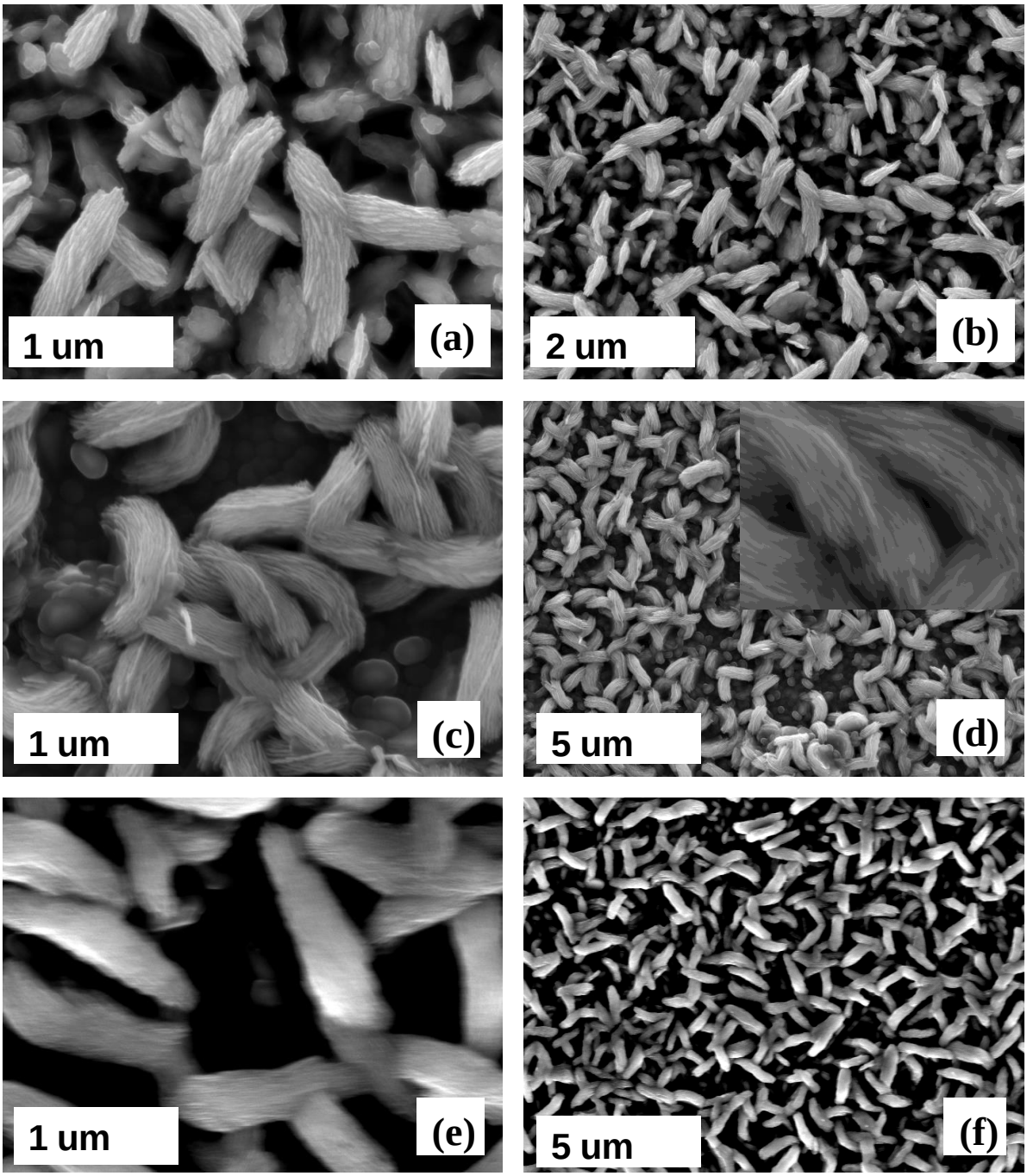


**Figure 4.11.** Representative SEM images of the iron sulfide thin films deposited at (a and b) 350 °C and 450 °C (c and d) for complex (**6**) and (e and f) 450 °C using complex (**7**) using chloroform solvent. Inset (d): a zoomed in high magnification image showing more structural features of the bundle of fibrous.

The *p*-XRD patterns of iron sulfide films grown from chloroform solutions of complex (**6**) at all temperatures (Figure 4.12) showed (112), (201), (203), (320), (220) and (222) reflections which correspond to hexagonal-phase iron sulfide ($Fe_{0.975}S$) (card number: 01-080-1032). Some minor peaks which can be attributed to smythite phase ($Fe_3S_4$) (Card

number 04-007-2189) are observed at 350 °C, while a pure hexagonal phase is observed at temperatures 400 °C and 450 °C. Furthermore, the intensity of the (112) reflection increases as a function of temperature. The growth of a hexagonal phase-iron sulfide ($Fe_{0.975}S$) from complex (**7**) dominates at all deposition temperatures (Figure 4.13).

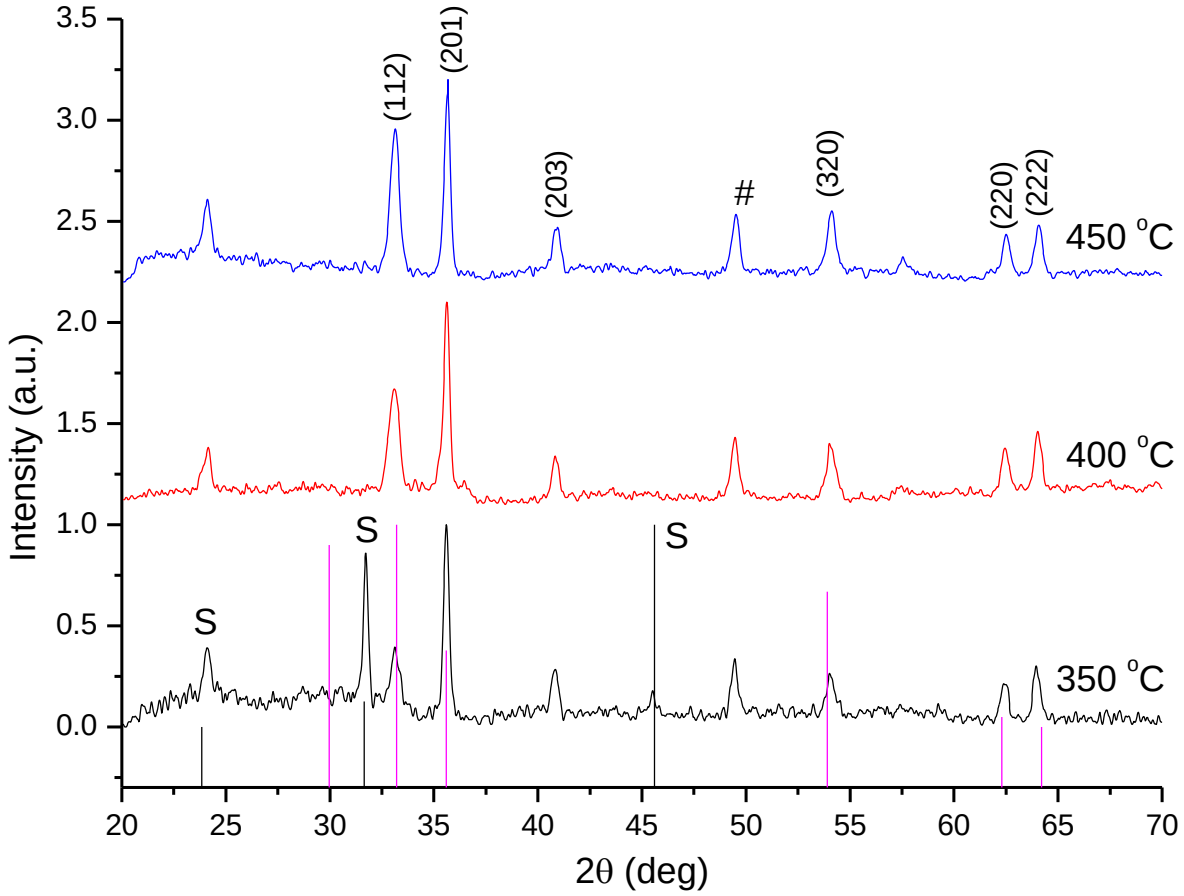


**Figure 4.12.** p-XRD of Fe-S thin films deposited from complex (**6**) using chloroform as the solvent. ((Purple and black sticks represent standard card for hexagonal phase ($Fe_{0.975}S$). smythite (S = $Fe_3S_4$) and # = Mackinawite (FeS).

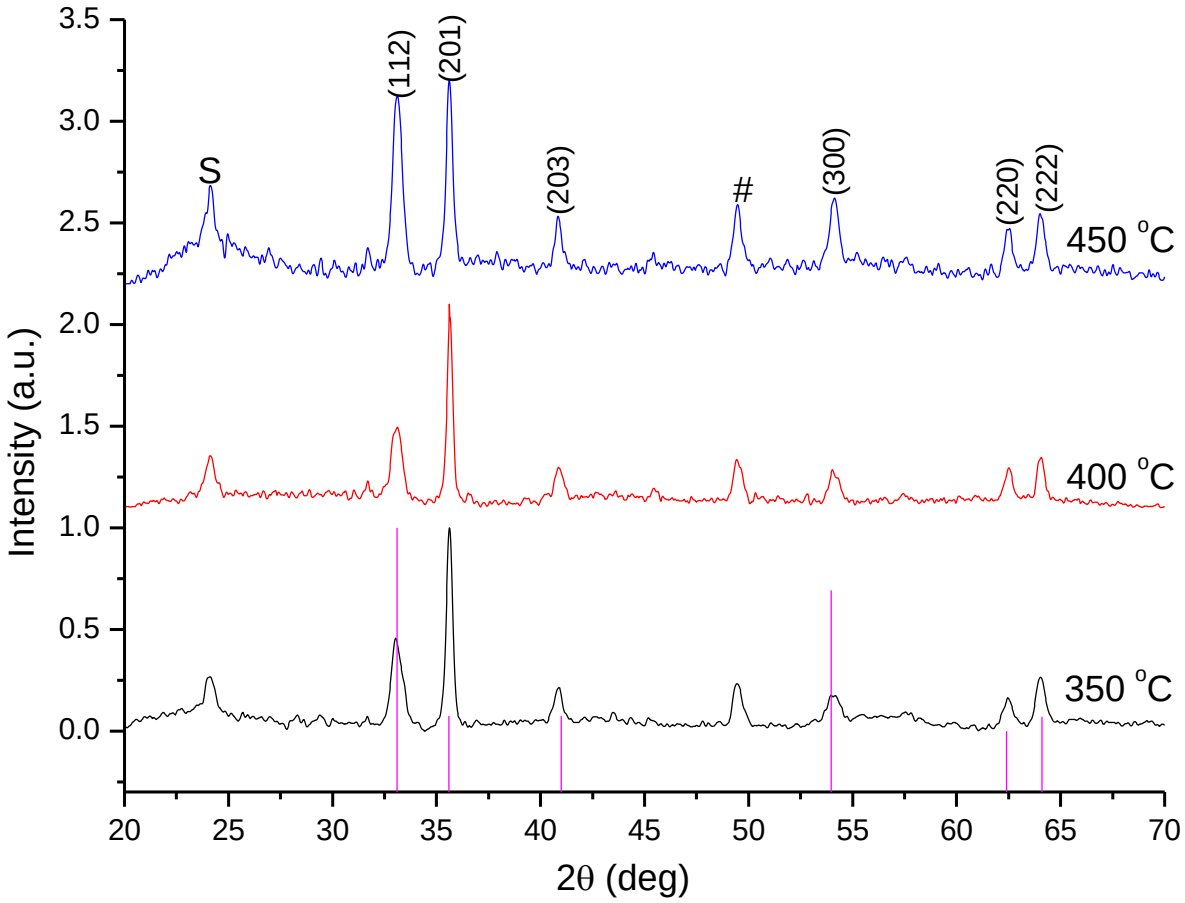


**Figure 4.13.** p-XRD of Fe-S thin films deposited from complex (**7**) using chloroform as the solvent. (Purple sticks represent standard card for hexagonal phase ($Fe_{0.975}S$) {S = smythite ($Fe_3S_4$) and # = Mackinawite (FeS)}.

The UV-Vis-NIR absorbance spectroscopy of a representative sample {350 °C for complex (**6**)} showed a broad absorption with the absorption maxima at around 1300 nm (0.95 eV) at 350 °C (Figure 4.14), bathochromically shifted compared with films produced using toluene solvent. These results reveal that the role of the solvent significantly determines the path of the reaction than just acting as a medium of transport.

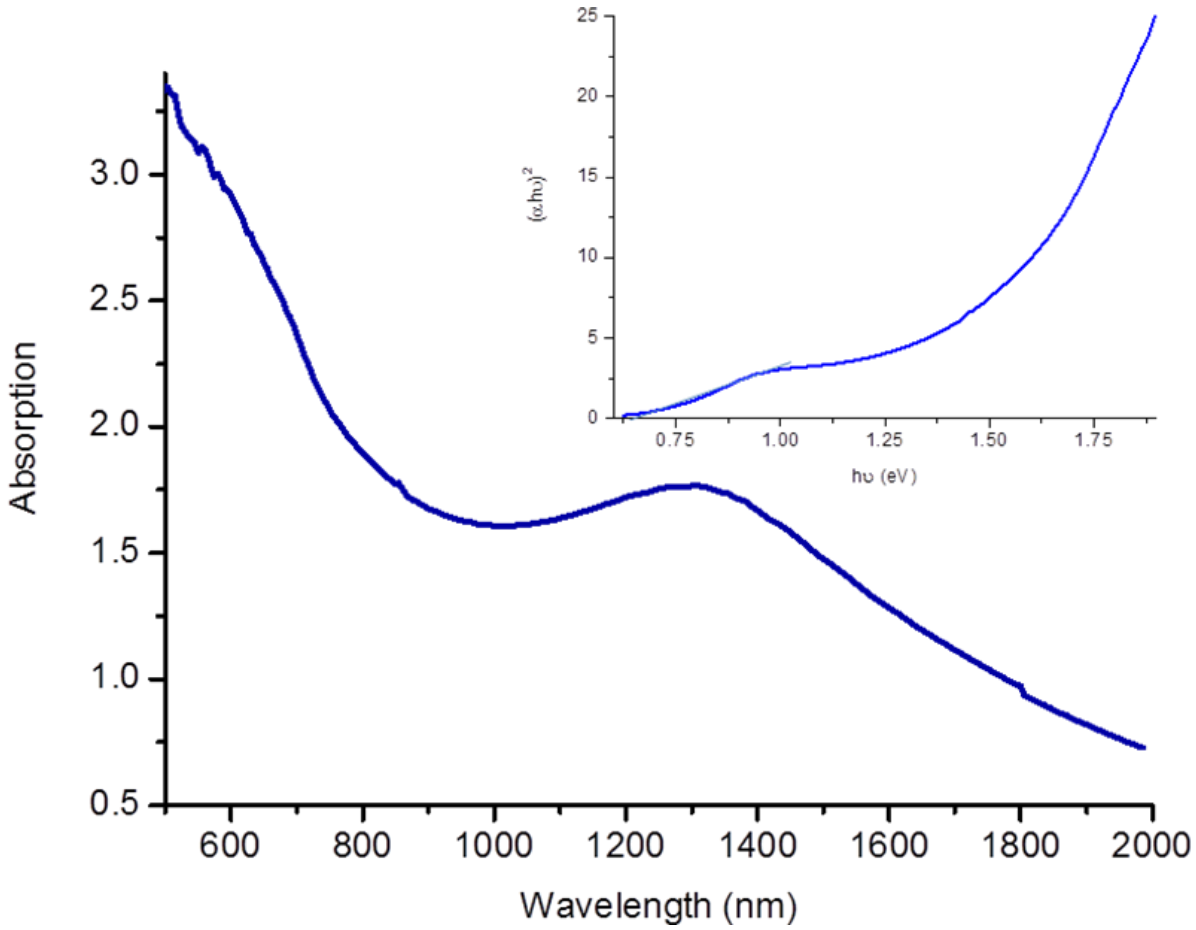


**Figure 4.14.** UV-Vis-NIR absorption spectra of Fe-S thin films deposited at 350 ºC from complex (**6**) with chloroform used as a solvent. Inset: Tauc plot showing the estimated optical band gap of Fe-S film.

### 4.3.6. Effect of *tert*-butyl thiol (*t*-BuSH)

The composition and structure of Fe-S films have been described in terms of $Fe_XS_Y$ phases which are mainly temperature-dependent [30,31]. There exists six sulfur atoms for each iron atom in compounds (**6**) and (**7**), seemingly sufficient to produce sulfur-rich phases such as pyrite. It is also known that higher temperature syntheses result in the formation of sulfur-deficient films. Therefore, an attempt was made out to increase the sulfur content during the deposition experiments. A series of AACVD experiments were carried out by adding 1 mL (8.87 mmol) of *tert*-butyl thiol (*t*-BuSH). In this regard, toluene solutions of both complexes were used and depositions were conducted at 350, 400 and 450 °C. High quality representative results for the deposition temperature of 450 °C are described.

Addition of *t*-BuSH had a strong influence on the morphologies of the deposited iron sulfide films. SEM images (Figure 4.15a&b) of iron sulfide films deposited using complex (**6**) at 450 °C, showed formation of flower-like bundles of spherical-to-globular shaped crystallites with particle sizes ranging between 500 - 600 nm. Complex (**7**) deposited double-layered films: the bottom relatively compact layer is composed of spherical shaped particles (~500 nm), and a loose top layer is composed of mainly flake shaped crystallites (900 nm) (Figure 4.15c&d). A significant increase of sulfur composition (S 53.8 % and Fe 46.2 %) was observed as a result of sulfurization using *t*-BuSH. The p-XRD patterns of deposited iron sulfide samples reveals two sharp reflections at 32° and 45.8° which we could not assign (Figure 4.16).

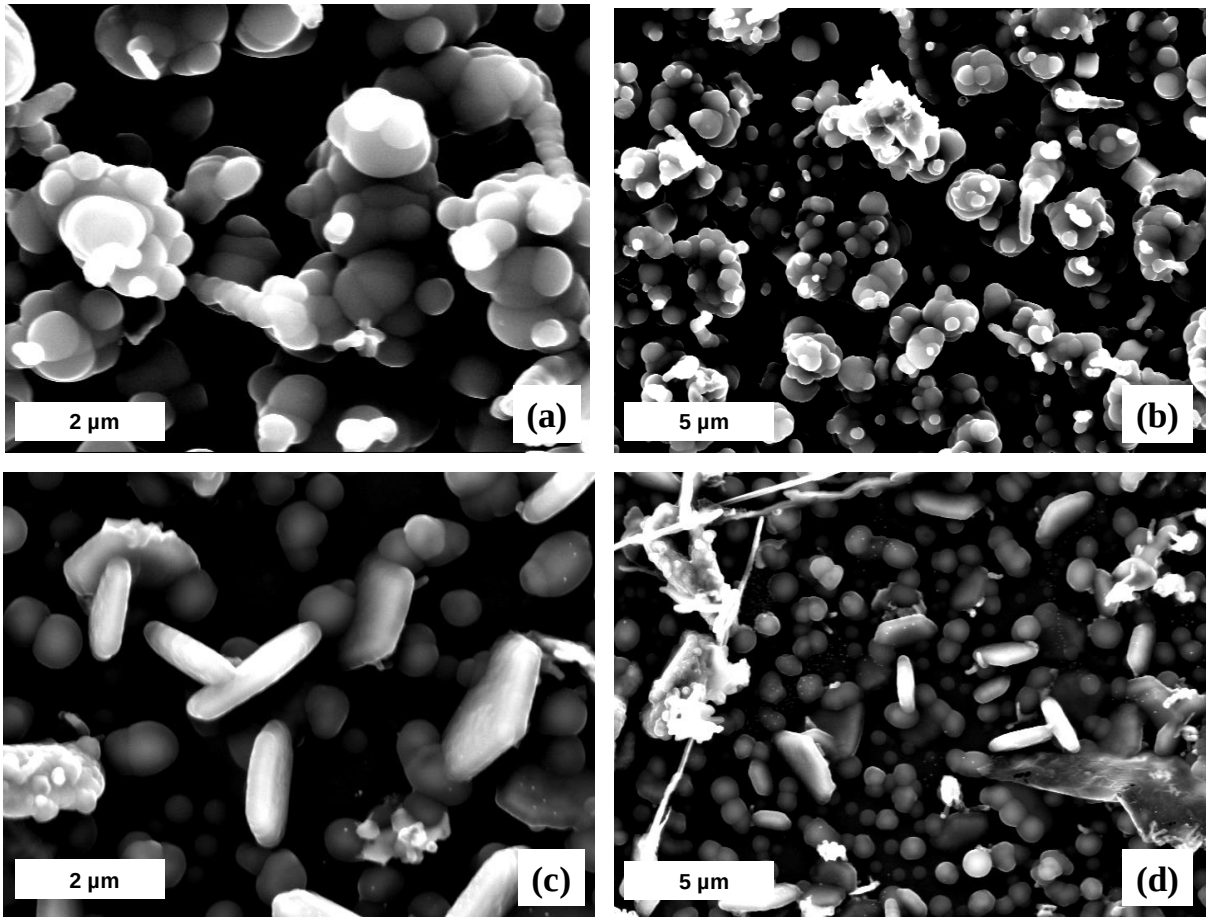


**Figure 4.15.** SEM images of the iron sulfide thin films deposited at 450 °C using (a and b) complex (**6**) and (c and d) complex (**7**).

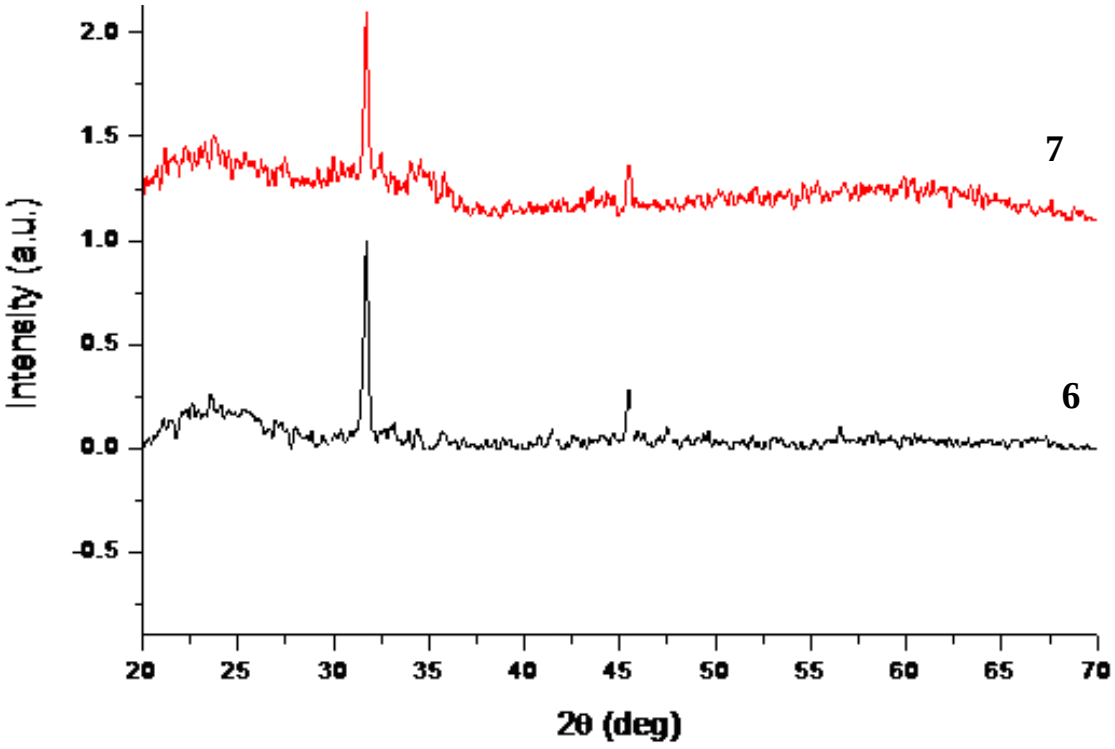


**Figure 4.16.** p- XRD of the thin films deposited using toluene solvent and 1 mL of *tert*-butyl thiol.

Topological analysis of the films was performed using atomic force microscopy (AFM), which revealed the formation of uniform films (Figure 4.17). The room temperature UV-Vis NIR absorption spectra in Figure 4.18 of iron sulfide thin films deposited using complex (**6**) and (**7**) both showed absorption edge approx. 1.7 – 2.0 eV, a hypsochromic shift as compared with reported values of iron sulfide [40,41]. This blue shift phenomenon confirms the enrichment of the Fe-S film by sulfur, as a result of *t*-BuSH addition. It has been reported that sulfur vacancies and impurities are potentially responsible in lowering the band gap of iron sulfide particles [37,42]. Additionally, bulk sulfur vacancies are also responsible for nonconstant charge distribution resulting in poor optical properties and photo conversion efficiency.

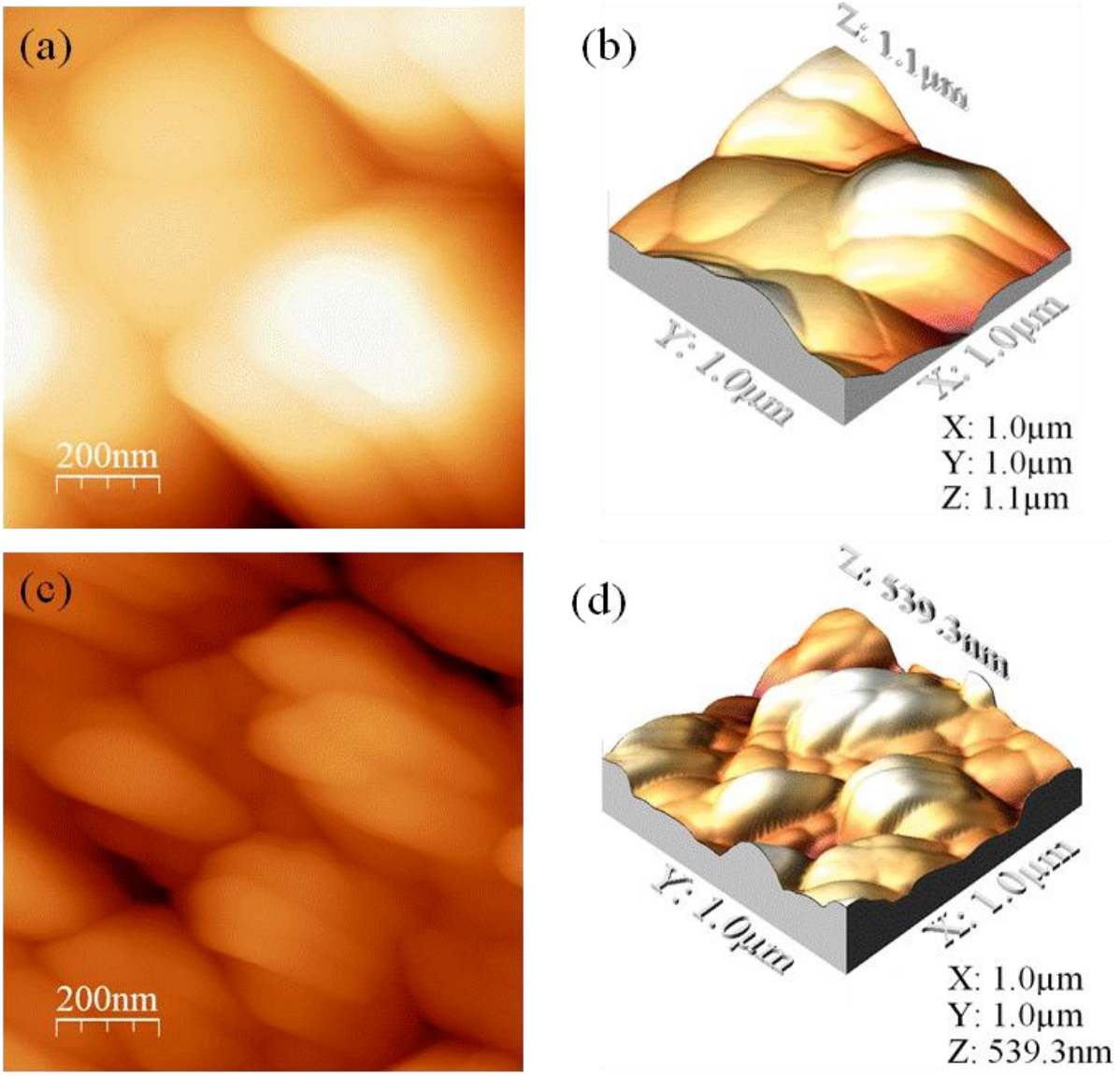


**Figure 4.17.** 2-D and 3-D AFM height profiles of Fe-S thin films deposited by AACVD at 450 ºC for 2 hrs using toluene solvent and added amount of 1 mL *tert*-butyl thiol when complexes (**6**) (a & b) and (**7**) (c & d) were used as precursors.

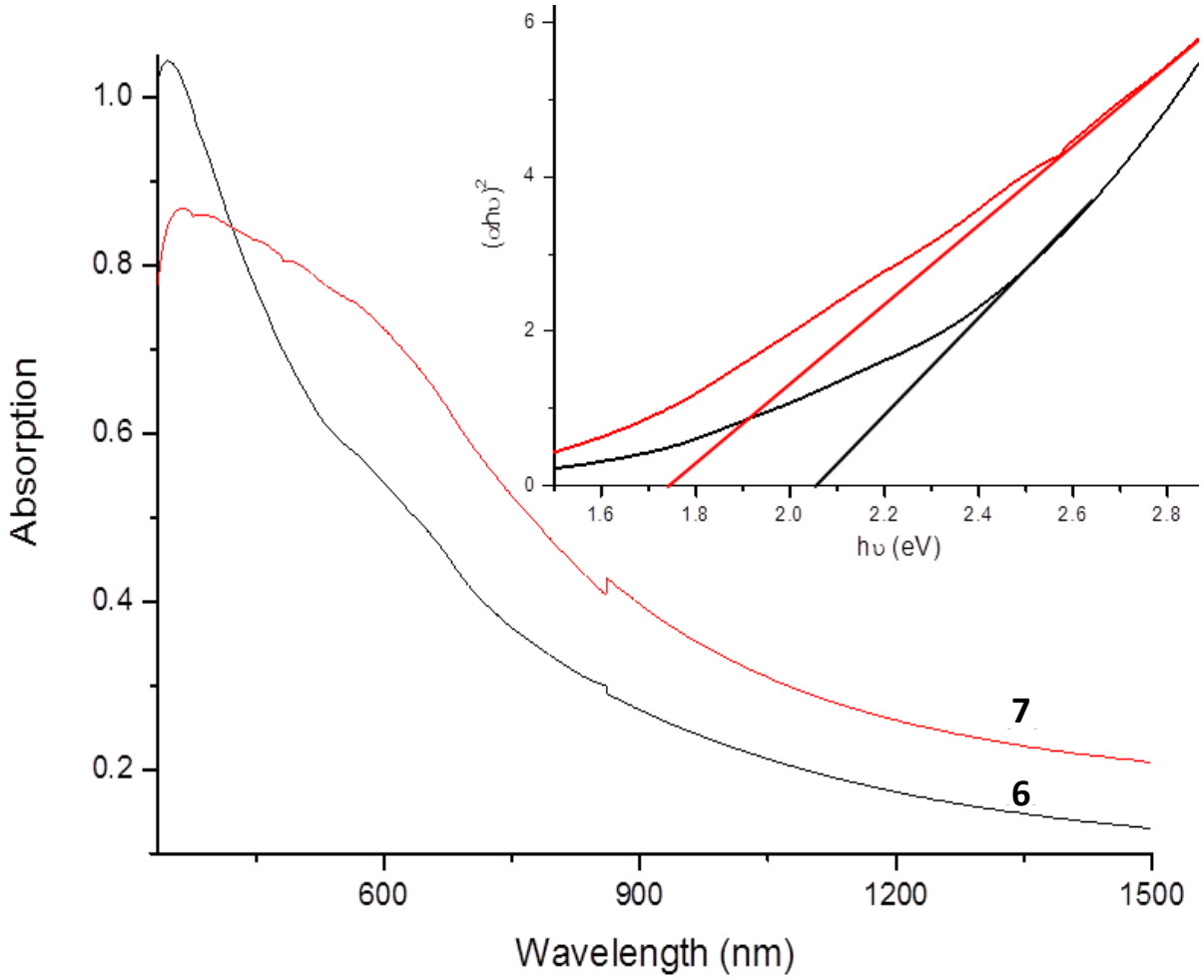


**Figure 4.18.** UV-Vis-NIR absorption spectra of Fe-S thin films deposited 450 °C using toluene solvent and *tert*-butyl thiol. Inset: Tauc plot showing the estimated optical band gap of the film.

## 4.4. Deposition of iron sulfide thin films using Fe(II) dithiocarbamate complexes

An attempt to prepare Fe(II) analogues and their subsequent use as single source precursors for the deposition of iron sulfide thin films is outlined here. The *bis*-(piperidinedithiocarbamato)iron(II) (**8**) and *bis*-(tetrahydroquinolinedithiocarbamato)iron(II) (**9**) complexes were synthesized and characterized by elemental analysis, infra red and thermal gravimetric analysis. Complex (**9**) and it's crystal structure is already known in the literature, it has also been used to deposit iron sulfide thin films through AACVD technique, using THF solvent at 400 and 450 °C [23]. In this study, chloroform was chosen as a suitable solvent and depositions are conducted at 350 and 450 °C.

The thermogravimetric analysis (TGA) of both precursors showed a single step decomposition pattern at around 286 and 241 °C for complex (**8**) and (**9**), respectively. The weights of the remaining residue after decomposition of both complexes were 20.7 % (calc. 23.4 %) and 22.3 % (calc. 18.6 %), respectively. The lower value of the remaining residue from complex (**8**) compared to the theoretical value could be due to carbonaceous contaminants, while the higher value for the complex (**9**) could be due to either volatility of S in the form of $H_2S$ or formation of sulfur deficient Fe-S.

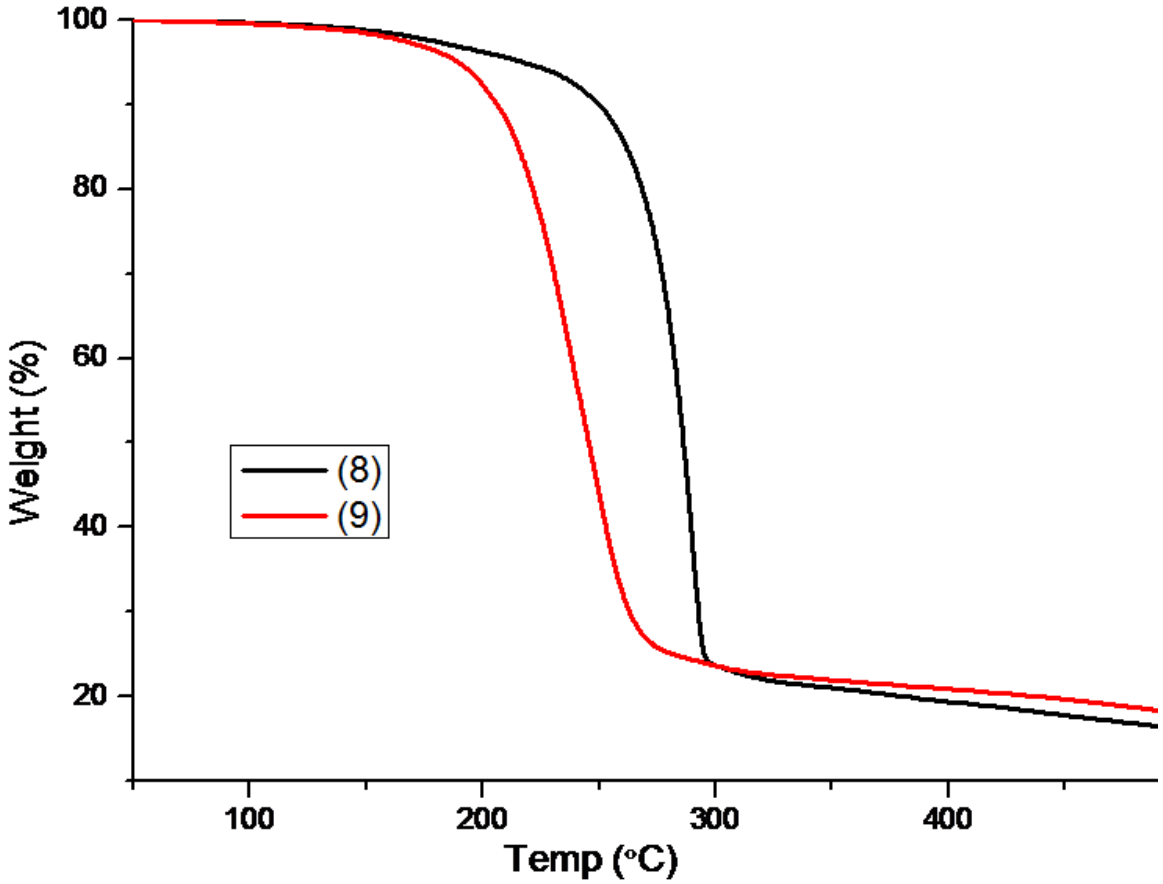


**Figure 4.19.** Thermogravimetric analysis (TGA) of complexes **(8)** and **(9)** at a heating rate of 10 °C/min under nitrogen with a flow rate of 10 $cm^3$/min.

Iron sulfide thin films were deposited as described in section 4.3.3 above; all deposition experiments in this temperature range produced uniform, black-coloured films. The SEM analysis of the films deposited from complex (**8**) showed growth of films consisting of spherical-like crystallites with particle sizes ranging from 90 – 115 nm, at 350 °C decomposition temperature (Figure 4.20). As the temperature was increased to 450 °C, formation of elongated structures with particle sizes ranging from 0.67 – 1.05 µm, were obtained. Some microstructures were also observed in films deposited at 450 °C. A similar

trend was also observed in films deposited from complex (**9**) (Figure 4.21). The images illustrate formation of typical uniform spherical, granule-like structures at 350 °C, with particle sizes ranging from 250 – 360 nm. An increase in temperature to 450 °C, resulted in the formation of elongated crystallites with particle sizes ranging from 1.13 – 1.57 µm. Saeed *et al*. [23] obtained flower-like structures of sizes in the range of 5 – 10 µm, from a THF solution of complex (**9**). This further reveals the influence of solvent in the deposition of thin films. In both cases, complex (**9**) produced larger particle sizes than those obtained from complex (**8**).

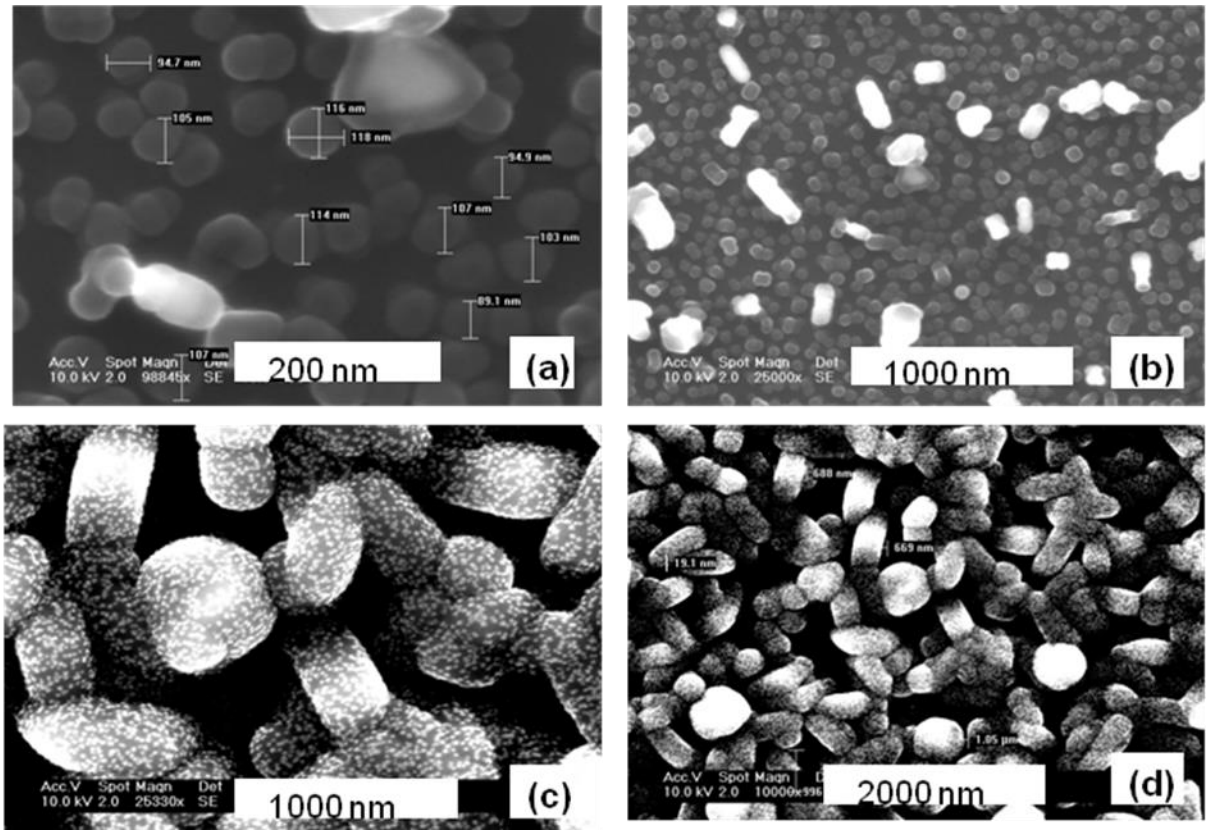


**Figure 4.20.** SEM images of the iron sulfide thin films deposited using complex (**8**) at 350 °C (a and b) and 450 °C (c and d).

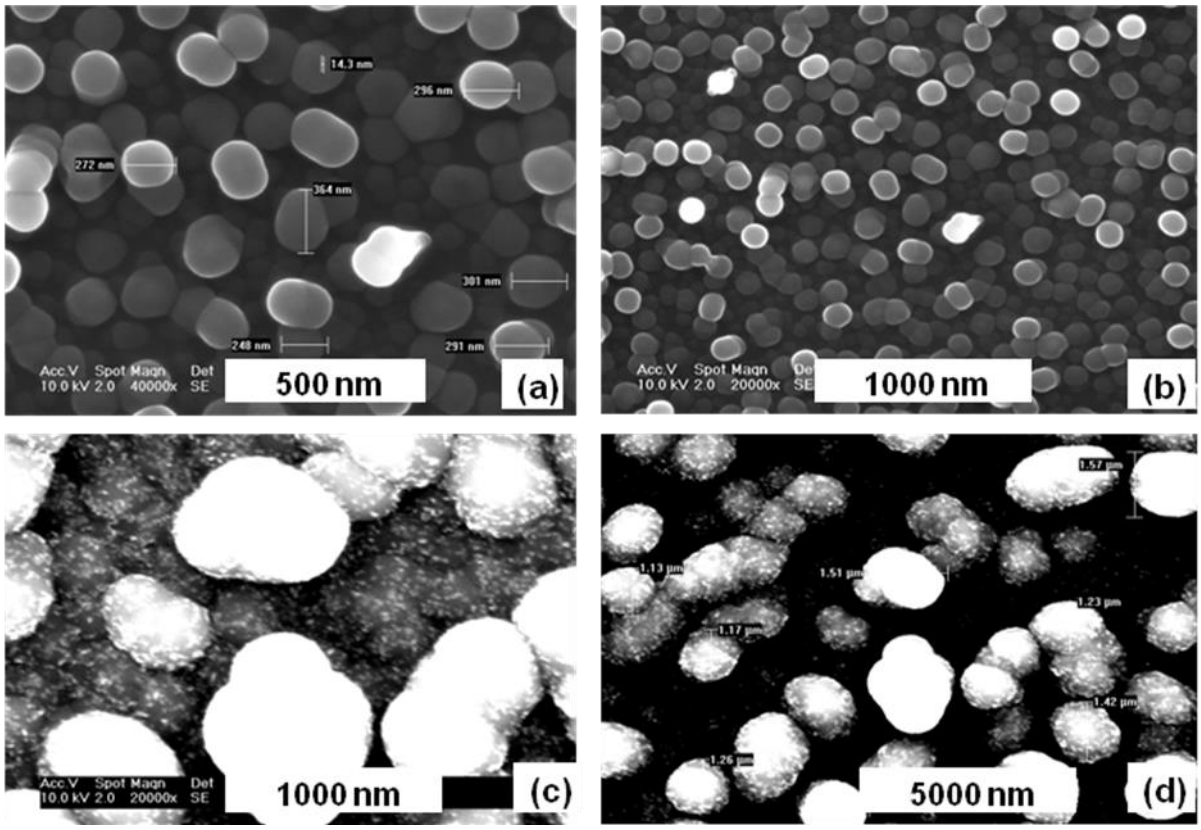


**Figure 4.21.** SEM images of the iron sulfide thin films deposited using complex (**9**) at 350 °C (a and b) and 450 °C (c and d).

The X-ray diffraction studies of the as-deposited iron sulfide films grown from chloroform solutions of complex (**8**) at temperatures 350 and 450 °C are shown in Figure 4.22. The diffraction planes (112), (201), (203), (320), (220) and (222) were observed, which correspond to hexagonal $Fe_{0.975}S$ (card number: 01-080-1032). Some minor peaks which can be attributed to smythite ($Fe_3S_4$) phase (Card number 04-007-2189) are observed at 450 °C, while ill-crystalline film can be observed at 350 °C. The diffraction patterns of complex (**9**) were not well-defined.

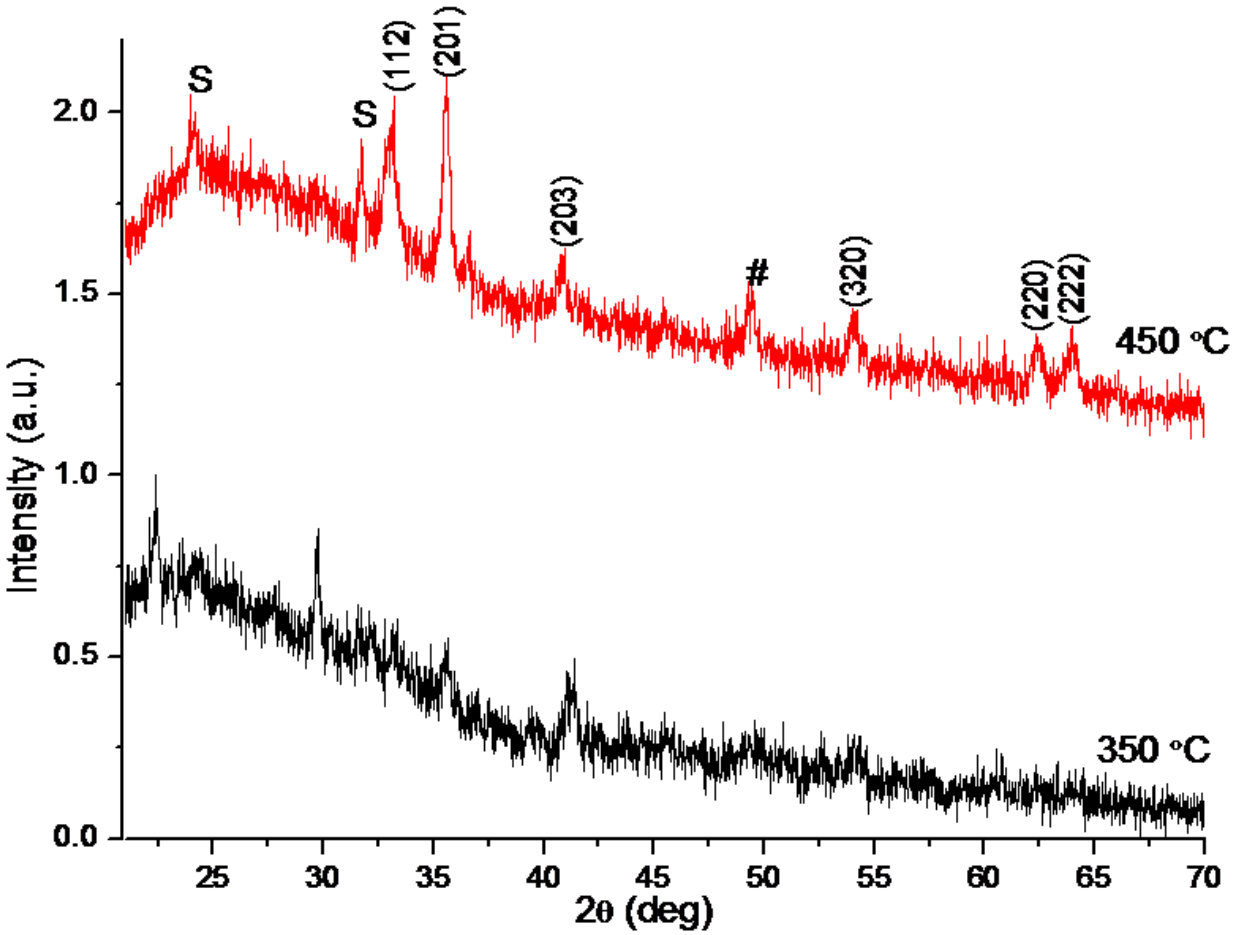


**Figure 4.22.** p-XRD of Fe-S thin films deposited from complex (**8**) using chloroform as the solvent. {Smythite (S = $Fe_3S_4$) and # = Mackinawite (FeS)}.

## 4.5. Conclusions

The single source precursors- *tris*-(piperidinedithiocarbamato)iron(III/II) (**6**/**8**) and *tris-(*tetrahydroquinolinedithiocarbamato)iron(III/II) (**7**/**9**) complexes have been synthesized and fully characterized. They were then used to deposit thin films of iron sulfide thin films on glass substrates, by aerosol assisted chemical vapor deposition technique. Thermogravimetric and powder X-ray diffraction studies revealed the formation of iron sulfide(s). A mechanism for the decomposition of complex (**6**) was studied using thermogravimetric analysis, X-ray diffraction and gas chromatography mass spectroscopy. The mechanism revealed the decomposition of complex (**6**) through two steps; firstly detachment of one piperidinyl dithiocarbamato ligand, followed by complete removal of the remaining organic moiety.

Different deposition parameters such as temperature and solvent were used and correlated with the morphological, structural and optical properties of the resultant deposited films. The morphology of the iron sulfide films were found to be strongly dependent on the nature/structure of the complex, solvent and the amount of *tert*-butyl thiol added to the precursor mixture. The X-ray diffraction studies revealed the formation of mixed phase and/or pure phase iron sulfide films, an effect which was found to be temperature dependent. Toluene and chloroform precursor solutions mainly formed pyrrhotite and hexagonal phases of iron sulfide thin films at elevated temperatures from complex (**6**) and (**7**). Optical measurements revealed the formation of blue shifted (0.95 – 2.0 eV) Fe-S films which were solely influenced by the structure and morphologies. The experimental conditions that were used allowed access to a range of new iron sulfide phases by AACVD, using dithiocarbamate precursors.

## 4.6. References


1. P. A. Janick and L. M. Siegel, Biochem., 1982, 21, 3538.
2. W. O. Gillum, L. E. Mortenson, J. S. Chen and R. H. Holm, J. Am. Chem. Soc., 1977, 99, 584.
3. C. Di Giovanni, W-A. Wang, S. Nowak, J-M. Grenèche, H. Lecoq, L. Mouton, M. Giraud and C. Tard, ACS Catal., 2014, 4, 681.
4. D. Kong, J. J. Cha, H. Wang, H. R. Lee and Y. Cui, Energy Environ. Sci., 2013, 6, 3553.
5. E-J. Kim, J-H. Kim, A-M. Azad and Y-S, Chang, ACS Appl. Mater. Interfaces, 2011, 3, 1457.
6. G. L. Henriksen and D. R. Vissers, J. Power Sources, 1994, 51, 115.
7. H. Geng, L. Zhu, W. Li, H. Liu, L. Quan, F. Xi and X. Su, J. Power Sources, 2015, 281, 204.
8. H. Chen, L. Zhu, H. Liu and W. Li, J. Power Sources, 2014, 245, 406.
9. H. Wang and I. Salveson, Phase Transform, 2005, 78, 547.
10. S. A. Kissin and S. D. Scott, Econ. Geol., 1982, 77, 1739.
11. D. J. Vaughan and J. R. Craig, (1978) Minerals Chemistry of Metal Sulfides. Cambridge University Press. Cambridge.
12. X. F. Qian, X. M. Zhang, C. Wang, Y. Xie, W. Z. Wang and Y. T. Qian, Mater. Sci. Eng., 1999, B64, 170.
13. D. Hobbs and J. Hafner, J. Phys: Condens Matter, 1999, 11, 8197.
14. S. Shukla, N. H. Loc, P. P. Boix, T. M. Koh, R. R. Prabhakar, H. K. Mulmudi, J. Zhang, S. Chen, C. Fan Ng, C. H. A. Huan, N. Mathews, T. Sritharan and Q. Xiong, ACS Nano, 2014, 8, 10597.
15. J. Xia, J. Jiao, B. Dai, W. Qiu, S. He, W. Qiu, P. Shen and L. Chen, RSC Adv., 2013, 3, 6132.
16. L. Li, M. Cabán-Acevedo, S. N. Girard and S. Jin, Nanoscale, 2014, 6, 2112.
17. D. Liang, M. Cabán-Acevedo, N. S. Kaiser and S. Jin, Nano Lett., 2014, 14, 6754.
18. R. Morrish, R. Silverstein and C. A. Wolden, J. Am. Chem. Soc., 2012, 134, 17854.
19. V. G. Bessergenev, R. J. F. Pereira and A. M. B. do Rego, Surf. Coat. Technol., 2007, 201, 9141.
20. M. J. Almond, H. Redman and D. A. Rice, J. Mater. Chem., 2000, 10, 2842.

21. M. Akhtar, A. L. Abdelhady, M. A. Malik and P. O'Brien, J. Cryst. Growth, 2012, 346, 106.
22. S. Khalid, E. Ahmed, M. A. Malik, D. J. Lewis, S. A. Bakar, Y. Khan and P. O'Brien, New J. Chem., 2015, 39, 1013.
23. S. Saeed, R. Hussain and R. J. Butcher. J. Coord. Chem., 2014, 67, 1693.
24. P. O'Brien, D. J. Otway and J-H Park, Mat. Res. Soc. Symp. Proc., 2000, 606, 133.
25. S. D. Disale and S. S. Garje, Appl. Organometal. Chem., 2010, 24, 734.
26. K. Ramasamy, M. A. Malik, M. Helliwell, F. Tuna and P. O'Brien, Inorg. Chem., 2010, 49, 8495.
27. G. M. Sheldrick, A short history of SHELX, Acta Crystallographica, Section A, Foundations of Crystallography, International Union of Crystallography, 2008, 64, 112.
28. L. D. Nyamen, V. S. R. Pullabhotla, A. A. Nejo, P. Ndifon and N. Revaprasadu, New J. Chem., 2011, 35, 1133.
29. M. Akhtar, J. Akhter, M. A. Malik, P. O'Brien, F. Tuna, J. Raftery and M. Helliwell, J. Mater. Chem., 2011, 21, 9737.
30. O. Kubaschewski, (1982) "Iron-Sulfur", Iron-Binary Phase Diagrams, Springer-Verlag, Berlin, 125.
31. D. J. Vaughan and A. R. Lennie, Scientific Progress (Edinburgh), 1991, 75, 371.
32. R. A. Berner, Science, 1962, 137, 669.
33. C. A. Francis and J. R. Craig, Amer. Mineral., 1976, 61, 21.
34. D. F. Shriver, P. W. Atkins, T. L. Overton, J. P. Rourke, M. T. Weller and F. A. Armstrong, (2006) "Inorganic Chemistry" W. H. Freeman, New York, USA.
35. W. W. Barker and T. C. Parks, Geochimica et Cosmochimica Acta, 1986, 50, 2185.
36. J. Tauc, (1966) Optical Properties of Solids. Academic Press, New York, USA.
37. M. Cabán-Acevedo, N. S. Kaiser, C. R. English, D. Ling, B. J. Thompson, H-E. Chen, K. J. Czech, J. C. Wright, R. J. Hamers and S. Jin, J. Am. Chem. Soc., 2014, 136, 17163.
38. A. A Tahir and K. G. U. Wijayantha, J. Photochem. Photobiol. A-Chem., 2010, 216, 119.
39. C. Piccirillo, R. Binions and I. P. Parkin, Chem. Vap. Depos., 2007, 13, 145.

40. J. P. Wilcoxon, P. P. Newcomer and G. A. Samara, Solid State Commun., 1996, 98, 581.
41. A. M. Karguppikar and A. G. Vedeshwar, Phys. Status Solidi A, 1988, 109, 549.
42. C. Wadia, Y. Wu, S. Gul, S.K. Volkman, J. Guo and A. P. Alivisatos, Chem. Mater., 2009, 21, 2568.

# CHAPTER FIVE

# SYNTHESIS OF IRON SULFIDE NANOPARTICLES AND GAS SENSING APPLICATIONS

## 5.1. Introduction

Iron sulfide nanocrystals are considered as of the more attractive semiconductor materials for the second generation of electronic devices. Iron sulfide has extensively been adopted as a promising material for photocatalysis [1], sensor devices [2,3], solar cells [4-6], and ultra high-density magnetic storage devices [7,8]. Iron sulfide materials contain complex solid phase structures and various properties that play a crucial role in recent investigations [9,10]. Their surpassing benefits such as high abundances, low cost and low toxicity, make them competitive candidates in various applications. Although the iron-sulfur system is a binary system, its phase relationships are complicated due to the different valency states taken by sulfur (disulfide, mono sulfide) and iron (ferric, ferrous) [11]. Because of the complex structure of iron sulfide compound, a small variation in stoichiometry can lead to huge changes in their properties. This indicates that the synthesis of pure phase, monocrystalline and small size of these iron sulfide nanocrystals is still challenging.

Among the iron sulfide materials, pyrrhotite ($Fe_{1-X}S$) and nanosized greigite ($Fe_3S_4$) an analogue of magnetite) are of interest in modern material science. In particular, greigite iron sulfide reveals its potential applicability in the fabrication of lithium-ion batteries [12-14], hydrogen generation and/or storage [15-17], cancer hyperthermia and biomedicine [18], environmental decontamination of heavy metals [13,19-21] and paleomagnetic indicator [22]. On the other hand, antiferromagnetic pyrrhotite ($Fe_{1-X}S$) phase, which is found between FeS and $FeS_2$, has also recently revealed its potential application in lithium storage [23] and paleomagnetic indicator [22].

Greigite and pyrrhotite iron sulfide nanocrystals have alreadybeen successfully synthesized by several solution chemical methods [12,23-25]. Currently, several studies on the use of single source precursors (SSPs) have gained attention. Zhang *et al*, used $Fe(Ddtc)_3$ and $Fe(Ddtc)_2(Phen)$ complexes as single source precursors in the mixture of oleic acid/oleylamine/1-octadecene, pure greigite and pyrrhotite phases were obtained [26]. Han and Gao (2005) also prepared $Fe_7S_8$ and $Fe_3S_4$ iron sulfide nanocrystals by thermolysing iron(III)diethyldithiocarbamate complexes as single source precursors in oleylamine and/or in octadecene as non-coordinating solvent [27].

In this chapter, iron sulfide nanoparticles have been synthesized by hot injection thermal decomposition and pyrolysis methods. The hot injection method employed oleylamine and ethylene glycol as coordinating solvents and the temperatures were varied from 230 and 300 $^{o}$C for oleylamine and 190 $^{o}$C for ethylene glycol. Pyrolysis method involved the solid state decomposition of the single source precursors at relatively high temperatures of 350, 400 and 450 $^{o}$C. The same single source precursors reported in chapter four were used in this case. The structural, magnetic and optic-electronic measurements strongly revealed that the properties of the as-prepared nanostructured nanocrystals are dependent on the synthesis conditions such as temperature. The reaction temperature played a critical role in controlling the chemical composition, crystalline structure and magnetic properties of the as-synthesized iron sulfide nanocrystals. Oleylamine capped iron sulfide nanoparticles were further studied for gas sensing applications.

## 5.2. Experimental details

### 5.2.1. Materials

Oleylamine, ethylene glycol and ethanol were purchased from Sigma-Aldrich, and were used without further purification. Iron(III) piperidine (**6**) and tetrahydroquinoline (**7**) dithiocarbamate precursors were prepared as reported in chapter four and as per our recent report [28].

### 5.2.2. Characterization of iron sulfide nanoparticles

#### *5.2.2.1. X-ray photoelectron spectrometry (XPS)*

The X-ray photoelectron spectrometry measurements were carried out using Kratos Axis Ultra-DLD spectrometer with a monochromatic Al Kα radiation source ($h\upsilon$ = 1486.6 eV), supplied by Kratos Analytical (UK).

#### *5.2.2.2. Magnetic measurements*

The variation of room temperature hysteresis loops were investigated by using a Lakeshore model 735 vibrating sample magnetometer (VSM). In this case, the hysteresis loops were obtained in external applied magnetic fields of only up to 14 kOe.

#### *5.2.2.3. Gas sensing measurements*

Samples for gas sensing were spin coated on aluminium strip substrates at room temperature. The sensing tests were performed in a KSGA565 Kenosistec (Italy) gas sensor comprising of Keithley voltage and current sources as well as source meters. Ammonia ($NH_3$), nitrogen dioxide ($NO_2$), hydrogen ($H_2$), methane ($CH_4$) and humidity were the gases used in this study.

### 5.2.3. Synthesis of iron sulfide nanoparticles

#### 5.2.3.1 Synthesis of ethylene glycol capped iron sulfide nanoparticles

In a two-necked flask, equipped with a reflux condenser, 0.5 g complexes (**6**) and (**7**) were introduced in a hot ethylene glycol (EG) (~ 190 °C) under $N_2$ gas flow. The reaction mixture was stirred for 2 hours and samples were cooled to about 70 °C. The extracted samples were first washed with methanol then centrifuged; the supernatant was discarded. The washing process was repeated thrice and the product vacuum dried.

#### 5.2.3.2. Synthesis of oleylamine capped iron sulfide nanoparticles.

Using Schlenk line system, 6.00 g of oleylamine was heated to an appropriate temperature (230 °C or 300 °C). Into the heated oleylamine, a suspension of a complex (**6**) or (**7**) (0.5 g) was injected using a glass syringe. After 2 h of reaction, the system was cooled to about 70 °C, then washed with methanol several times. The synthesized greigite and pyrrhotite iron sulfide nanoparticles were then well dispersed in ethanol solvent, the suspensions were later carefully spin coated on the alumina strips for gas sensing measurements. The alumina strips were then spin coated at a speed of 1000 rpm for 120 seconds using Brewer Science spin coater (Model 200X).

#### 5.2.3.3. Pyrolysis method

Approximately, 0.5 g iron(III) pip/thqdtc complex was loaded in a quartz boat container. The boat was kept at the centre of a horizontal furnace. $N_2$ gas was kept flowing throughout the experiment to maintain an inert atmosphere. The furnace was then heated at the rate of 25 °C/min to 350 °C and then held at 350 °C for 1 h. After this hour, the sample quartz boat was removed from the furnace and cooled to room temperature. The black

coloured residue of iron sulfide obtained in the boat was used for further characterizations. The reaction protocol was repeated for 400 and 450 $^{o}$C reaction temperatures for both complexes.

## 5.3. Results and discussions

### 5.3.1. Ethylene glycol capped iron sulfide nanoparticles

Complexes (**6**) and (**7**) were thermally decomposed in ethylene glycol (EG) as coordinating solvent at 190 °C for 2 hr. The synthetic approach was set in an inert system. The black nanoparticles collected were further analysed by optical measurements, X-ray diffraction and electron microscopy (TEM, HRTEM and SEM/EDX). Figure 5.1 shows the room temperature UV-vis NIR absorbance spectra of greigite nanocrystals. The particles absorb light in the visible and near-infrared spectral regions. Absorption band gap of 2.65 eV estimated from Tauc's plot [29] (inset Figure 5.1) reveals the particles exhibiting quantum confinement effects. This large blue shift (compared to the bulk band gap of 0.9 eV) displays electronic properties of the nanocrystalline materials and which is quite different from the other iron sulfide NCs [30].

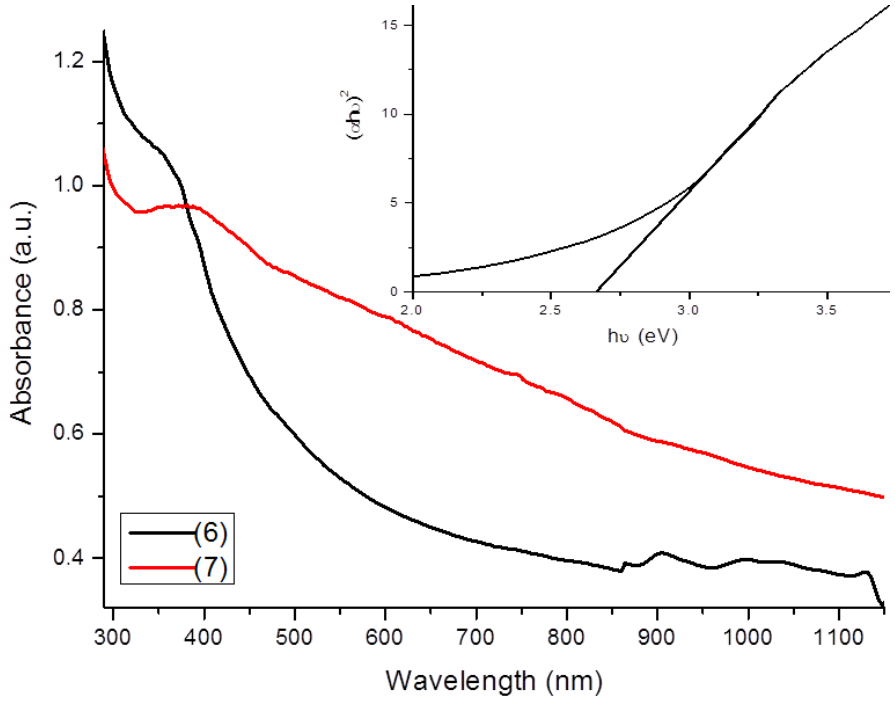


**Figure 5.1.** UV-Vis-NIR absorption spectra of $Fe_3S_4$ nanoparticles in ethylene glycol. Inset: Tauc plot showing the estimated optical band gap of the $Fe_3S_4$ nanoparticles.

Figure 5.2 is the typical p-XRD patterns obtained when complex (**6**) and (**7**) were thermally decomposed in the presence of ethylene glycol at 190 °C (this was chosen as the boiling point of ethylene glycol is 195 – 198 °C). Iron sulfide nanoparticles obtained from complex (**7**) gave highly crystalline pure $Fe_3S_4$ as greigite phase (card no: 016-0713), no other phases or other peaks belonging to sulfur or Fe were observed. The diffraction peaks observed could be indexed to (220), (311), (400), (511) and (440) Miller indices of cubic greigite phase ($Fe_3S_4$) with spinel structure. Similarly, complex (**6**) also gave greigite phase of poor crystallinity.

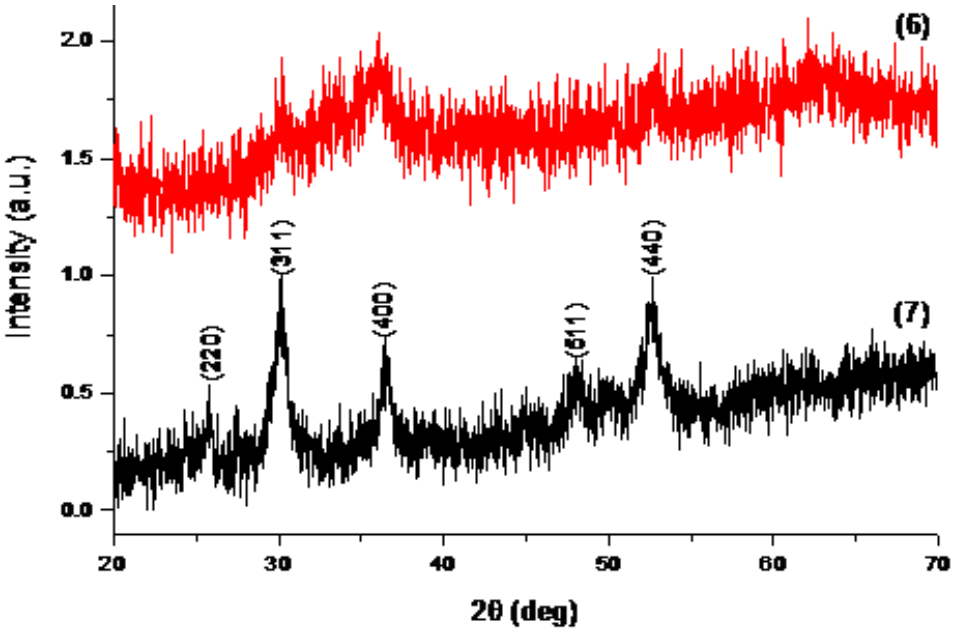


**Figure 5.2.** p-XRD pattern of a greigite phase ($Fe_3S_4$) nanoparticles synthesized using complex (**6**) and (**7**) as a single source precursor in ethylene glycol.

With the quality of the samples confirmed, scanning electron microscopy (SEM) was used to investigate the surface morphology of the representative samples which were spin coated on the glass substrate prior to analysis. Figures 5.3 (a) and (b) illustrate the formation of $Fe_3S_4$ microflower bundles, consisting of nanoflake-like structures. The energy dispersive X-ray (EDX) spectroscopy confirmed the elemental composition of a stoichiometric $Fe_3S_4$ phase (Figure 5.3 c). The rest of the elements are due the glass substrate and carbon coating of the spin coated films. The crystalline structure of greigite can be further observed by selective area electron diffraction (SAED) (Figure 3d) and HRTEM images (Figure 5.3 e and f). The lattice distance of 3.18 Å in the HRTEM image are in good agreement with the value of the lattice spacings of the (311) planes of the greigite phase (card no: 016-0713).

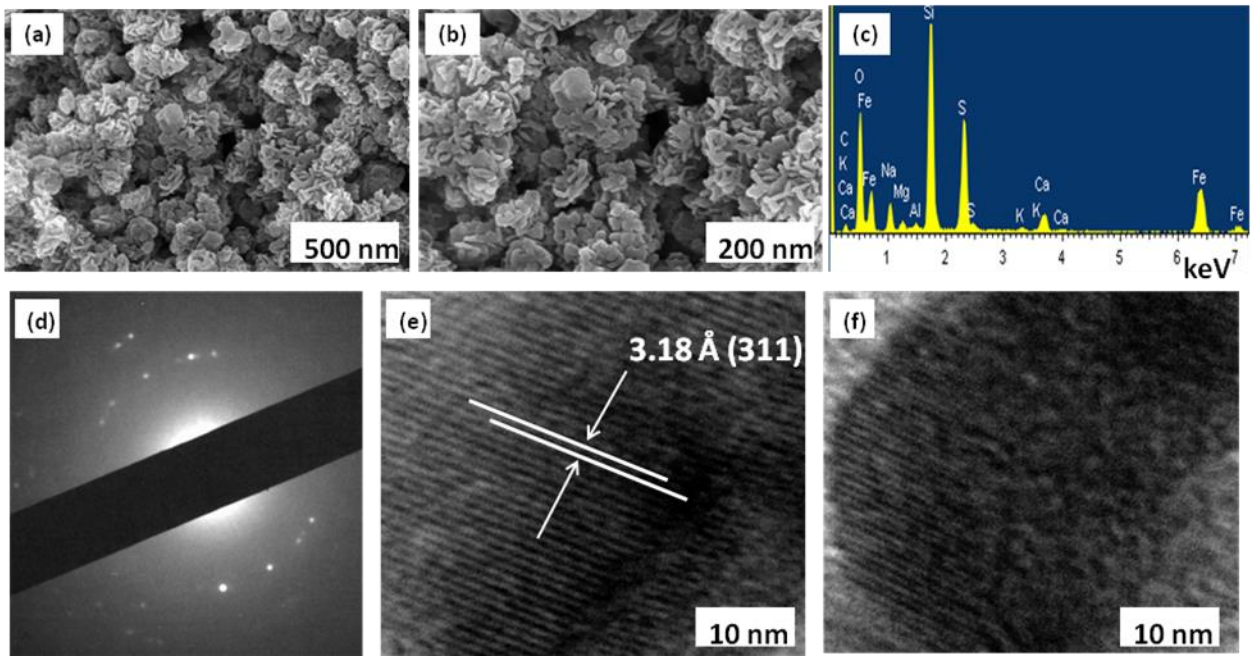


**Figure 5.3.** SEM images of iron sulfide ($Fe_3S_4$) nanoparticles obtained by solvothermal synthesis of complex (**6**) (a) and (**7**) (b) in ethylene glycol. (c) A representative EDX spectrum; (d) SAED pattern and HRTEM images (e) and (f) of nanoparticles obtained by solvothermal method of precursor (**6**) and (**7**) respectively.

### 5.3.2. Oleylamine capped iron sulfide nanoparticles

Iron sulfides have very interesting optical properties, ranging from visible region to infra-red region of the spectrum. Absorption properties of the as-synthesized oleylamine capped iron sulfide nanoparticles from complex (**6**) at temperatures 230 and 300 °C are presented in Figure 5.4. The as-synthesized nanocrystals absorb light in the visible and near-infrared spectral regions. The band gaps of iron sulfide nanoparticles were estimated by the Tauc's plot (Figure 5.4 inset) [29]. The samples absorption band gaps of 2.60 eV (230 °C, greigite) and 2.12 eV (300 °C, pyrrhotite) shows a blue shift absorption as compared to the bulk counterpart (0.9 eV) [34,35]. The optical behaviour of the nanocrystals further reveals that the absorption properties are temperature and structure dependant. The absorption features of iron sulfide nanocrystals obtained from complex (**7**) showed poor optical characteristics and are not included.

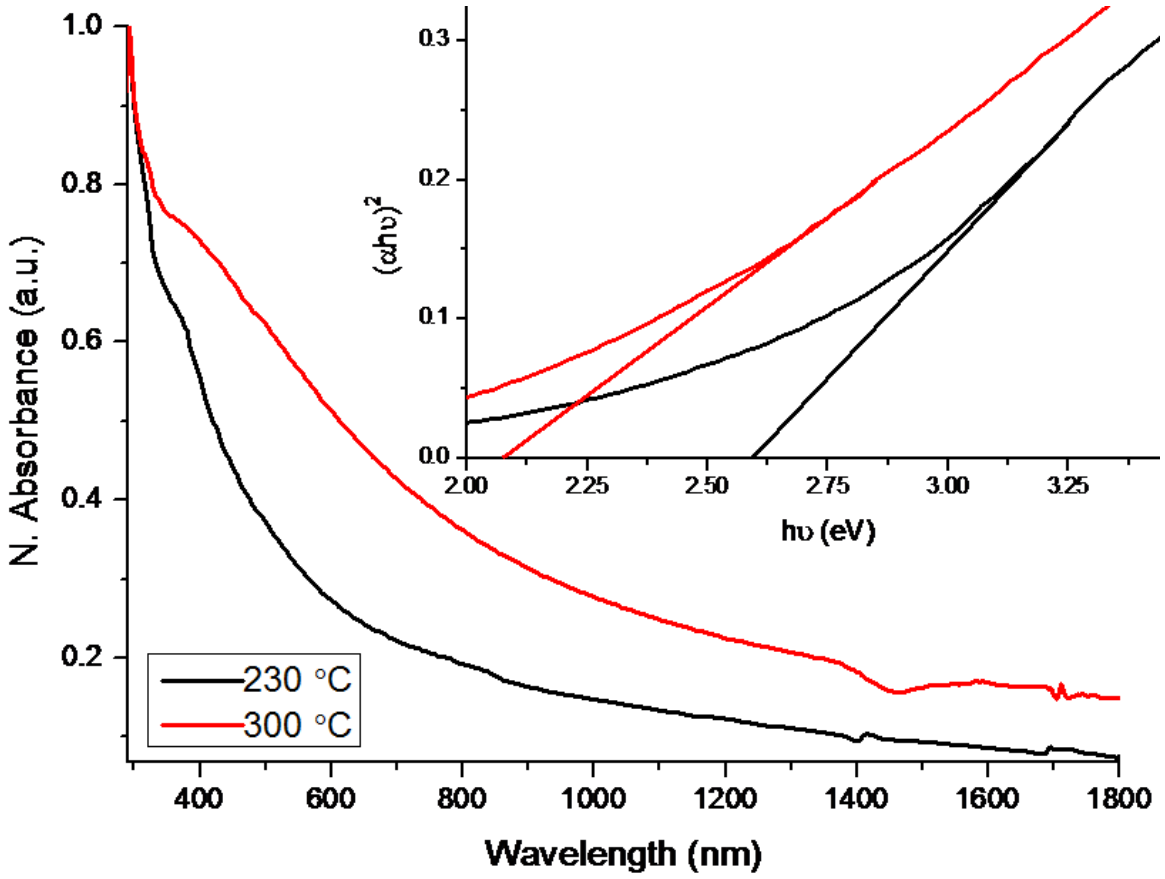


**Figure 5.4.** UV-Vis-NIR absorption spectra of iron sulfide nanoparticles from complex (**6**) in oleylamine obtained at 230 °C ($Fe_3S_4$) and 300 °C ($Fe_{1-X}S$). Inset: the estimated optical band gaps of the as-synthesized nanoparticles using the Tauc plot.

The crystalline structure of the samples synthesized from complex (**6**) and (**7**) were analyzed by p-XRD. The results are shown in Figure 5.5 and 5.6. It is seen that when the reaction is carried out at 230 °C, both complexes gave cubic greigite ($Fe_3S_4$) phase. The diffraction patterns can be indexed to (200), (311), (400), (422), (511) and (440) mirror planes of a typical greigite phase (JCPDS card number: 89-1998). When the reaction temperature was increased to 300 °C, both complexes gave hexagonal pyrrhotite phase ($Fe_{1-x}S$). The diffraction peaks can be indexed as pyrrhotite - $Fe_{1-x}S$ (X ~ 0.125; card No. 29–0724), with major diffractions peaks assigned to (100), (101), (102) and (110) mirror indices. Based on the XRD analysis, the reaction temperature plays an important role in phase transformation. O'Brien *et al.* obtained $Fe_3S_4$ and $Fe_7S_8$ from the precursor of $[N^nBu_4]_2$-$[Fe_4S_4(SPh)_4]$ and considered that the composition of nanocrystals is considerably dependent on the temperature as well as the alkylamines employed in the reaction [24].

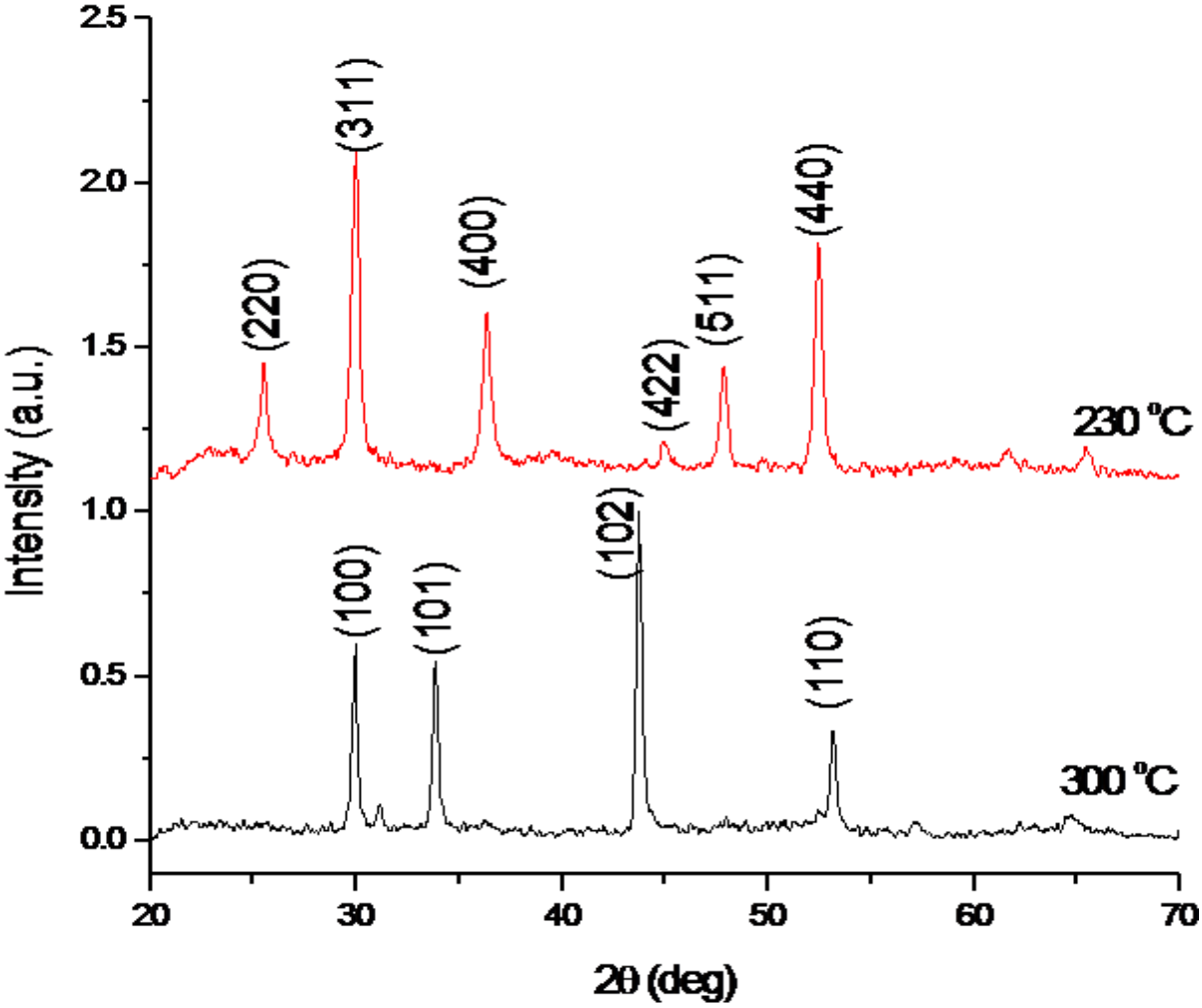


**Figure 5.5.** p-XRD pattern of iron sulfide nanoparticles synthesized using complex (**6**) as a single source precursor in oleylamine.

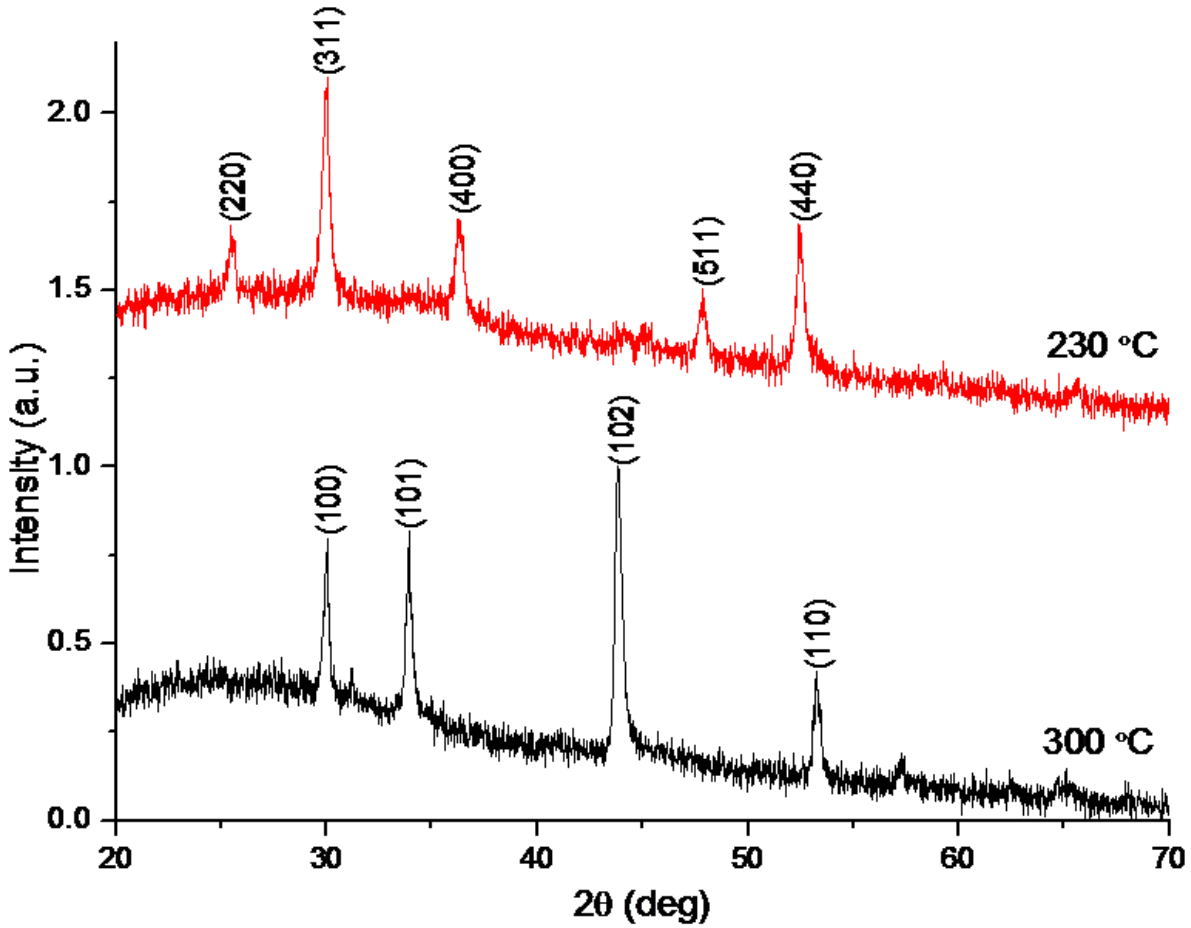


**Figure 5.6.** p-XRD pattern of iron sulfide nanoparticles synthesized using complex (**7**) as a single source precursor in oleylamine.

Iron sulfide compounds are featured with significant temperature induced composition and phase transformations. In our study, different thermolysis temperatures of 230 and 300 °C were used during solvothermal synthesis of iron sulfide nanoparticles in oleylamine. The results show that at relatively low temperature (230 °C), a metastable greigite phase is formed, whereas with increasing temperature (300 °C), the pyrrhotite phase is preferred. These results are consistent with the pyrrhotite phase being more stable at high temperature (Figure 5.7). The relative stabilities of various iron sulfide phases are shown in Figure 5.13 using a plot adopted from Vaughan and Lennie and others [36-39]. The line represents the thermodynamic stability and connects the stable phases FeS (troilite) and $FeS_2$ (pyrite). It is also known that the formation of iron-sulfur compounds is affected by the d-electron configuration of Fe, thus in a more complex range of structures than expected. The mechanisms of formation, particularly in solution with relationships to other iron sulfides are determined by the kinetics and mechanisms of transformations [36-38]. Figure 5.7

summarizes the gain in free energy ($kJmol^{-1}$) of Fe obtained from forming the various sulfides from the elements. The free energies of formation of these complex superstructures of Fe-S systems are predominantly inhibited by kinetic factors [36-38].

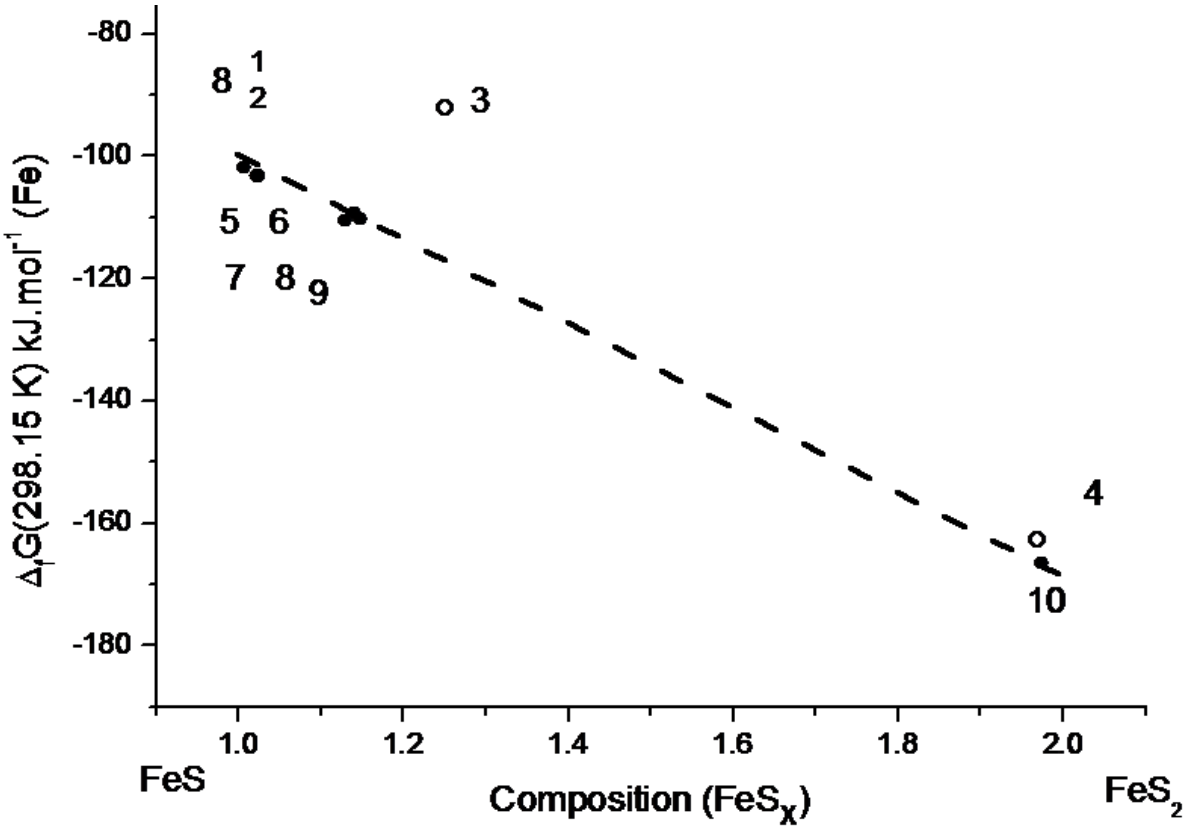


**Figure 5.7.** Schematic free energy-composition diagram for the iron sulfide materials. Open circles: amorphous FeS (1), mackinawite (2), greigite (3) and marcasite (4), filled circles are pyrrhotite forms (5-9) and pyrite (10) [36-39]. Free energy values for phases 1-4 lie above the line of those for 5-10 suggesting metastability at this temperature (298.15 K).

The morphologies and structures of the greigite and pyrrhotite nanocrystals were investigated using field-emission scanning electron (FESEM) and transmission electron microscopy (TEM). The TEM images (Figure 5.8a and d) show that the nanoparticles are well dispersed in a hexagonal, cube-shaped morphology. The increase of temperature did not show any significant morphological transformation. The selected area electron diffraction (SAED) (Figure 5.8b) presents a crystalline structure of the greigite particle. The HRTEM image of a hexagonal $Fe_3S_4$ NP (Figure 5.8c) indicates that the NPs possess well defined crystal lattices which exhibit an interplanar distance of 3.12 Å. This corresponds to the (311) plane of the $Fe_3S_4$ crystal with a spinel structure. The SEM image of a 300 °C sample (pyrrhotite) (Figure 5.8e), showing the majority of the $Fe_{1-X}S$ particles were densely packed and uniformly distributed in the shape of hexagonal to cubes with smooth surfaces. The

coalesced property of the sample on the substrate might be beneficial for various applications such as assembly of electronic devices. The EDX analysis data showed formation of S-rich $Fe_3S_4$ and $Fe_{1-X}S$ nanocrystals as summarized in Table 5.1 below.

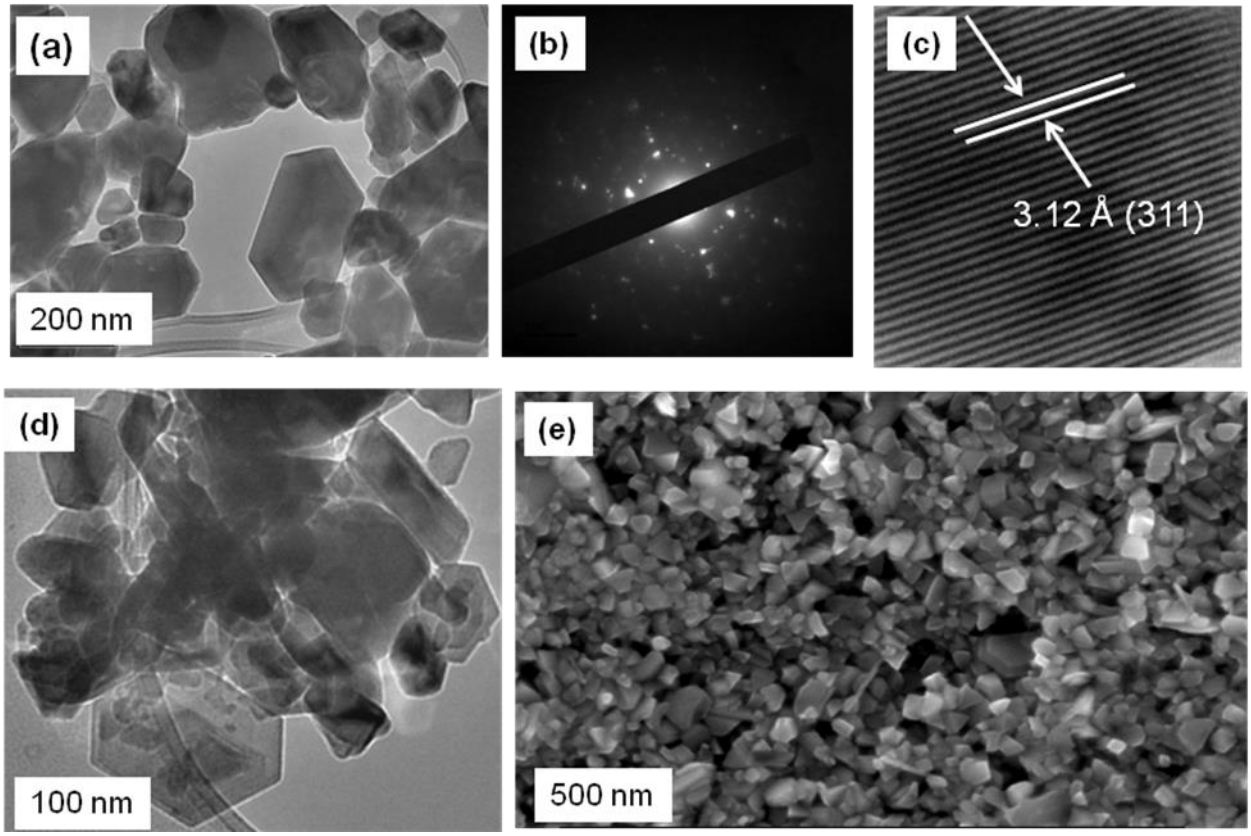


**Figure 5.8.** TEM images of greigite (a) and pyrrhotite (d) nanocrystals synthesized at 230 and 300 °C respectively. The SAED (b) and HRTEM (c) of a crystalline $Fe_3S_4$ and an SEM (e) image obtained from sample (d), when complex (**6**) was used.

**Table 5.1.** Elemental composition of iron sulfide nanocrystals obtained by solvothermal method in oleylamine.

| Complex | Temp (°C) | Fe (%) | S (%) |
|---|---|---|---|
| **(6)** | 230 | 46.4 | 53.6 |
| | 300 | 47.02 | 53.08 |
| **(7)** | 230 | 46.6 | 53.4 |
| | 300 | 47.1 | 52.9 |

The products obtained by thermolysis of precursor (**7**) in pure oleylamine were also analyzed by TEM. Figure 5.9 (a and c) presents TEM results on an iron sulfide sample obtained at reaction temperature of 230 and 300 °C. The resultant iron sulfide particles present hexagonal and sheet-like structures. A representative HRTEM image of the edge area of the hexagonal particle in Figure 5.9b exhibits well-resolved lattice fringes, further confirming the single-crystal nature of the particles. In Figure 5.9d, the SAED pattern taken from the edge of the particle shows that the structure is well crystallized, and these diffraction spots can readily be indexed to cubic iron sulfide crystal ($Fe_{1-X}S$) recorded from the (100) zone axis.

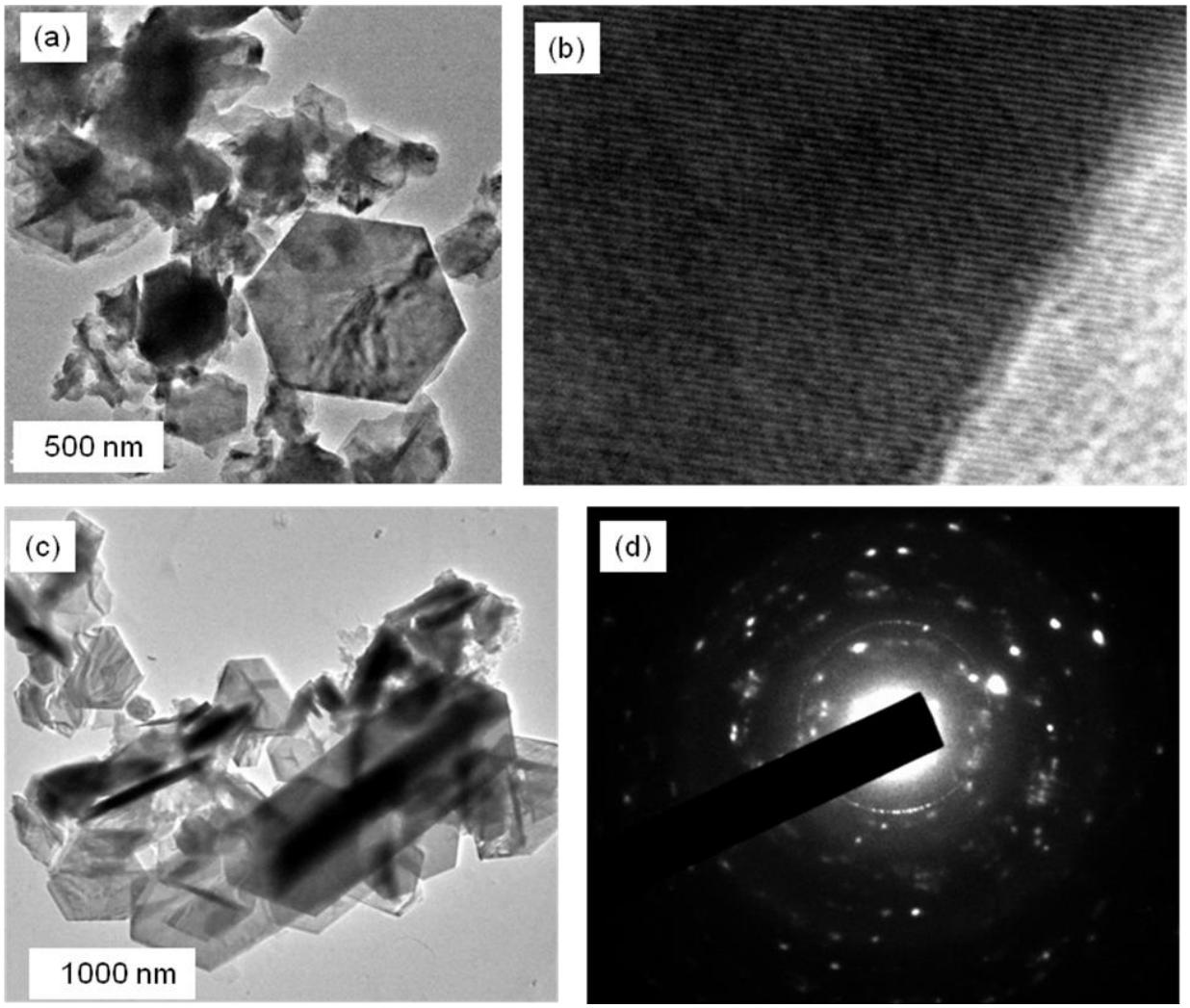


**Figure 5.9.** TEM images of greigite (a) and pyrrhotite (c) nanocrystals synthesized at 230 and 300 °C respectively. The HRTEM of a greigite NP (b) and SAED of a pyrrhotite NP (d) obtained from complex (**7**).

X-ray photoelectron spectroscopy (XPS) was employed to further investigate the purity and microstructure of the as-synthesized $Fe_3S_4$ and $Fe_{1-x}S$ nanoparticles. As shown in the full range scan (Figure 5.10a), the appearance of Fe and S species confirmed formation of pure forms of iron sulfide nanocrystals. A more detailed structure of Fe and S species could be obtained in the high resolution XPS spectra in the region of Fe 2p and S 2p (Figure 5.10 b and c). As shown in Figure 5.10b, Fe $2p_{3/2}$ resolved peaks at 710.1 and 710.6 eV for $Fe_3S_4$ and $Fe_{1-x}S$ nanoparticles, respectively confirming the formation of Fe(III)-S systems. The peaks at 161.4 eV and 161.8 eV (Figure 5.10c) can be assigned to S 2p and the results are consistent with the literature [40]. The peaks at ~ 168 eV can be assigned to an oxidized form of $SO_4^{2-}$ [41].

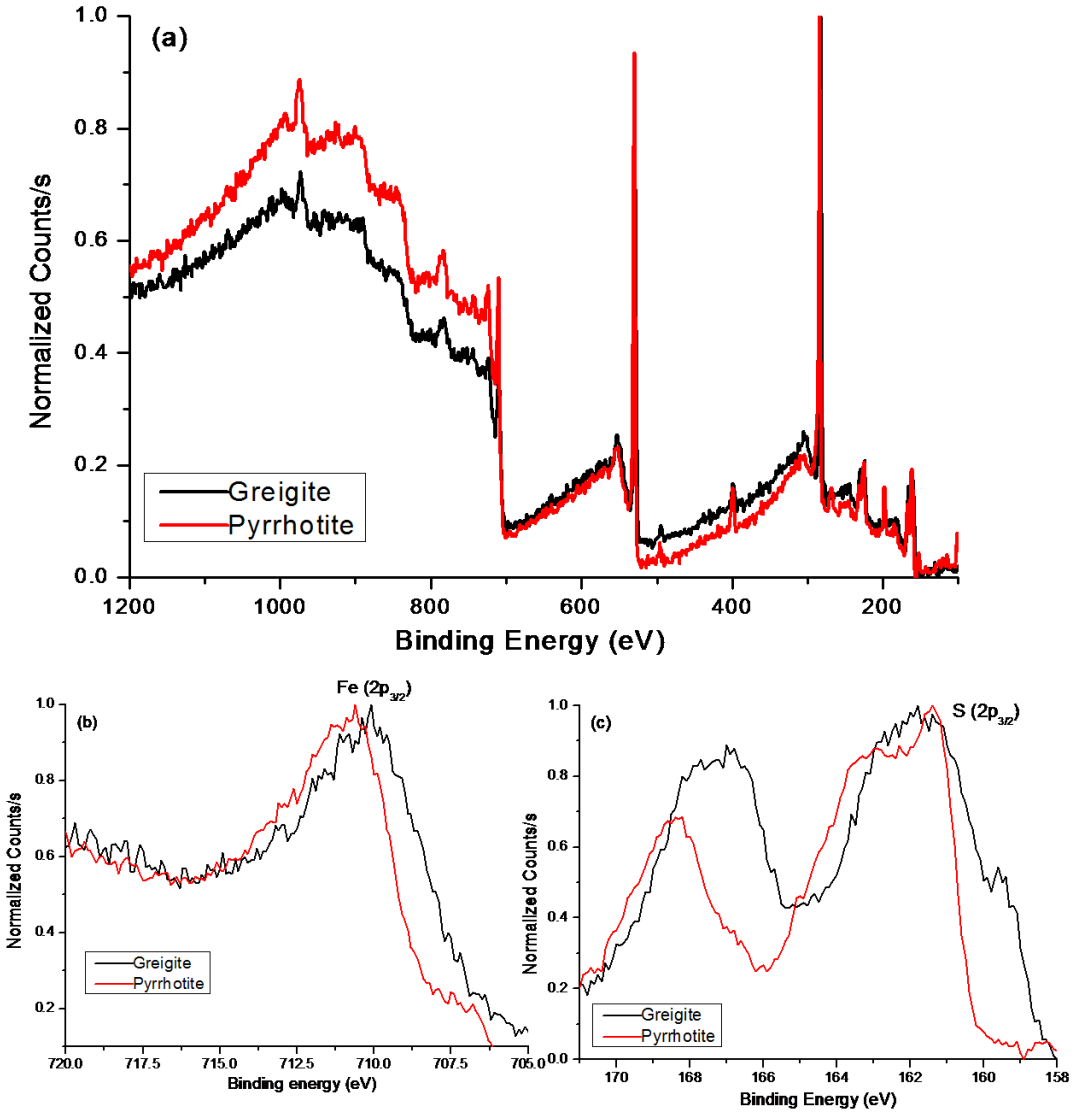


**Figure 5.10.** (a) Full range XPS spectra of Fe-S prepared from complex (**6**), (b) Fe 2p and (c) S 2p XPS spectra of greigite (black) and pyrrhotite (red) samples.

The room temperature magnetic properties of the samples obtained at 230 and 300 °C from complex (**6**) were recorded by a vibrating sample magnetometer. The sample prepared at 230 °C (greigite-$Fe_3S_4$) presents weak ferrimagnetic properties; whereas hexagonal pyrrhotite (300 °C) is antiferromagnetic (Figure 5.11). The magnetic hysteresis of the greigite sample prepared shows the saturation magnetization and coercive force of 3.27 emu/g and 26.81 Oe, respectively. Pyrrhotite ($Fe_{1-X}S$) also shows magnetic saturation of 1.66 emu/g and coercive force of 408.17 Oe. The coercive force of the sample prepared at 300 °C is higher than that of greigite phase prepared at 230 °C. The saturation susceptibility of greigite phase is a little higher than that of pyrrhotite, concluding that the crystal structure of the Fe-S system is an important factor determining the magnetic properties.

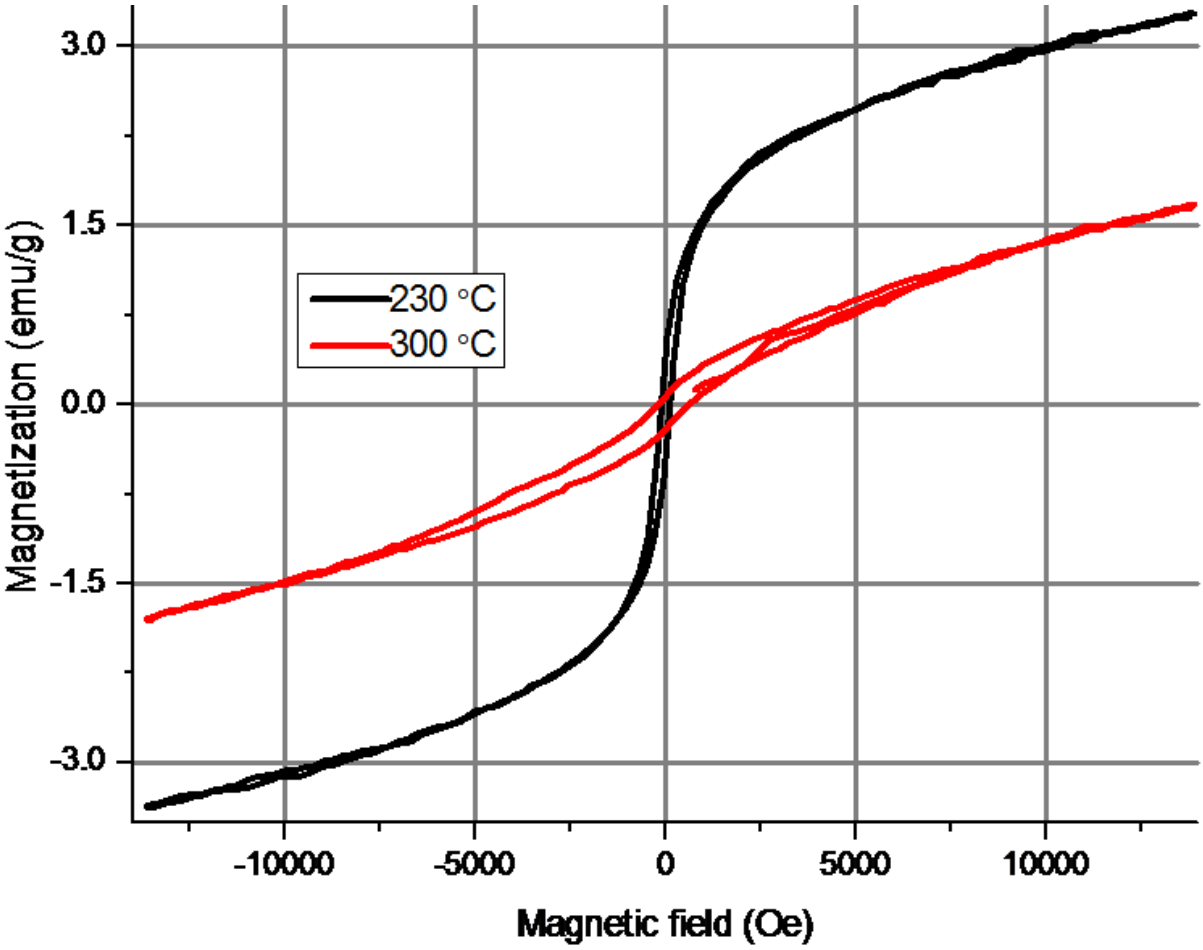


**Figure 5.11.** Magnetic hysteresis curves of the iron sulfide samples obtained by the hot injection thermal decomposition of complex (**6**) in oleylamine at 230 °C (greigite) and 300 °C (pyrrhotite).

### 5.3.3. Synthesis of iron sulfide by pyrolysis method

In view of inherent advantages of single source precursors, such as low toxicity, control over stoichiometries, limited pre-reactions, the designed solid state thermal decomposition (pyrolysis) of single source precursors was intended for the preparation of iron sulfide nanocrystals. Thermal properties of complexes (**6**) and (**7**) (Figure 4.2, chapter 4) showed decomposition in the temperature range 260 – 320 $^{o}$C, thus, the pyrolysis of both complexes was carried out in the temperature range of 350 – 450 $^{o}$C. Magnetically active black powders of iron sulfide were obtained. These samples were characterized by scanning electron microscope (SEM), energy dispersive X-ray spectroscopy (EDX), X-ray diffraction (XRD), X-ray photoelectron spectroscopy (XPS) and magnetic measurements.

Pyrolysis of complex (**6**) resulted in the formation of pure pyrrhotite phase of the formula $Fe_7S_8$ (T3) at all three temperatures (card no: 00-025-0411) (Figure 5.12). The diffraction was indexed to (200), (203), (206) and (220) which are mirror planes of pyrrhotite phase. Powder X-ray diffraction (XRD) of iron sulfide nanoparticles obtained from complex (**7**) resulted in the formation of pyrite ($FeS_2$) phase (card number: 01-071-0053) at 350 °C (Figure 5.13). When pyrolysis was carried out at 400 and 450 $^{o}$C, the iron sulfide nanoparticles tended to form pyrrhotite phase (#) of the formula $Fe_7S_8$ (T3) with few peaks of pyrite. The pyrrhotite phase could be indexed to (200), (203), (206) and (220) mirror planes (card no: 00-025-0411). These results reveal that the complexes decompose differently. The results show that the structure of the starting material plays a significant role in determining the crystalline structure of the as-synthesized nanocrystals. It is also observed that, the temperature affects the mechanism of the formation of these complex structures of iron sulfide nanocrystals. Gao *et al.* reported the composition– and phase-transformation of iron sulfide compounds as being significantly dependent on the temperature [27]. The sizes of the crystals calculated from Scherrer equation, lattice constants and d-spacings are summarized in Table 5.2. Increasing temperature resulted in a general increase of lattice constant, d-spacing and Scherrer sizes.

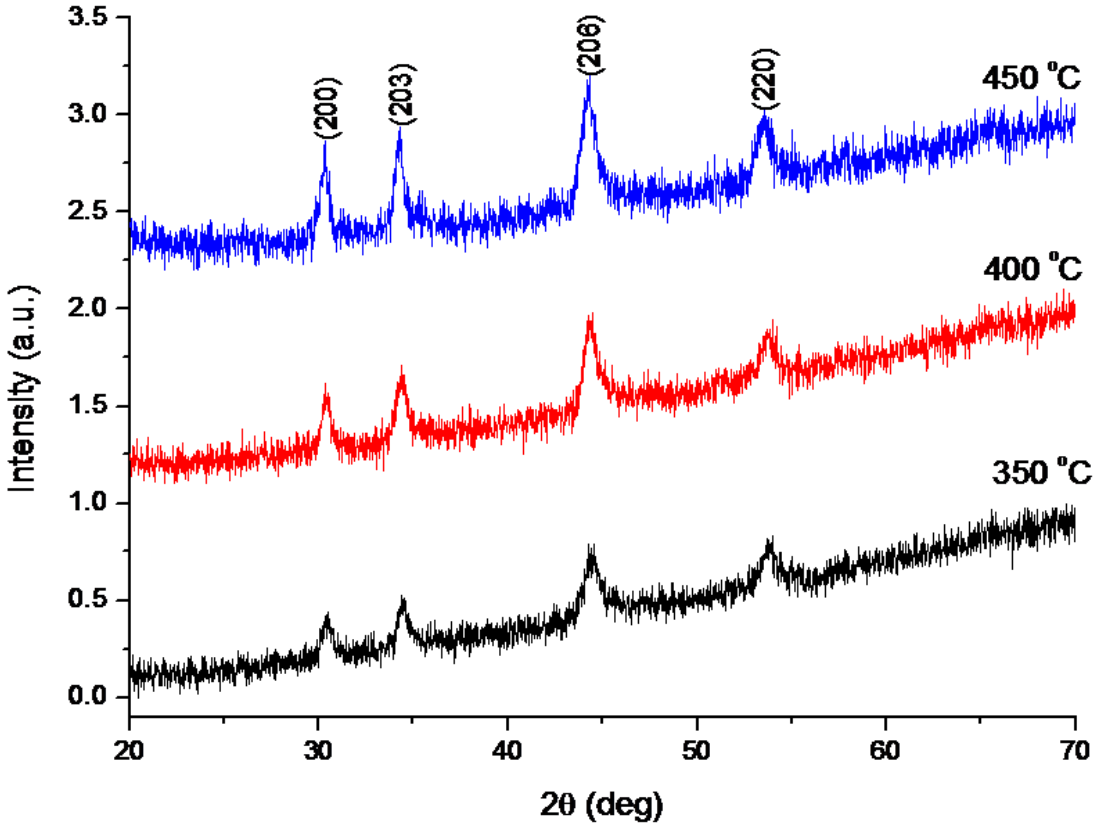


**Figure 5.12.** p-XRD pattern of a pyrrhotite phase of $Fe_7S_8$ nanoparticles synthesized using complex (**6**) as a single source precursor.

**Table 5.2.** The structural properties and particles sizes of iron sulfide obtained by pyrolysis of complexes (**6**) and (**7**) (values are obtained from (206) plane).

| **Complex** | **Temp (°C)** | **a (Å)** | **Obs. d (Å)** | **Size (nm)** |
|---|---|---|---|---|
| (**6**) | 350 | 12.8915 | 2.03833 | 8.39 |
| | 400 | 12.9105 | 2.04133 | 8.45 |
| | 450 | 12.9425 | 2.04639 | 8.96 |
| (**7**) | 350 | 12.8982 | 2.03939 | 19.92 |
| | 400 | 12.9012 | 2.03985 | 20.84 |
| | 450 | 12.9137 | 2.04183 | 23.64 |

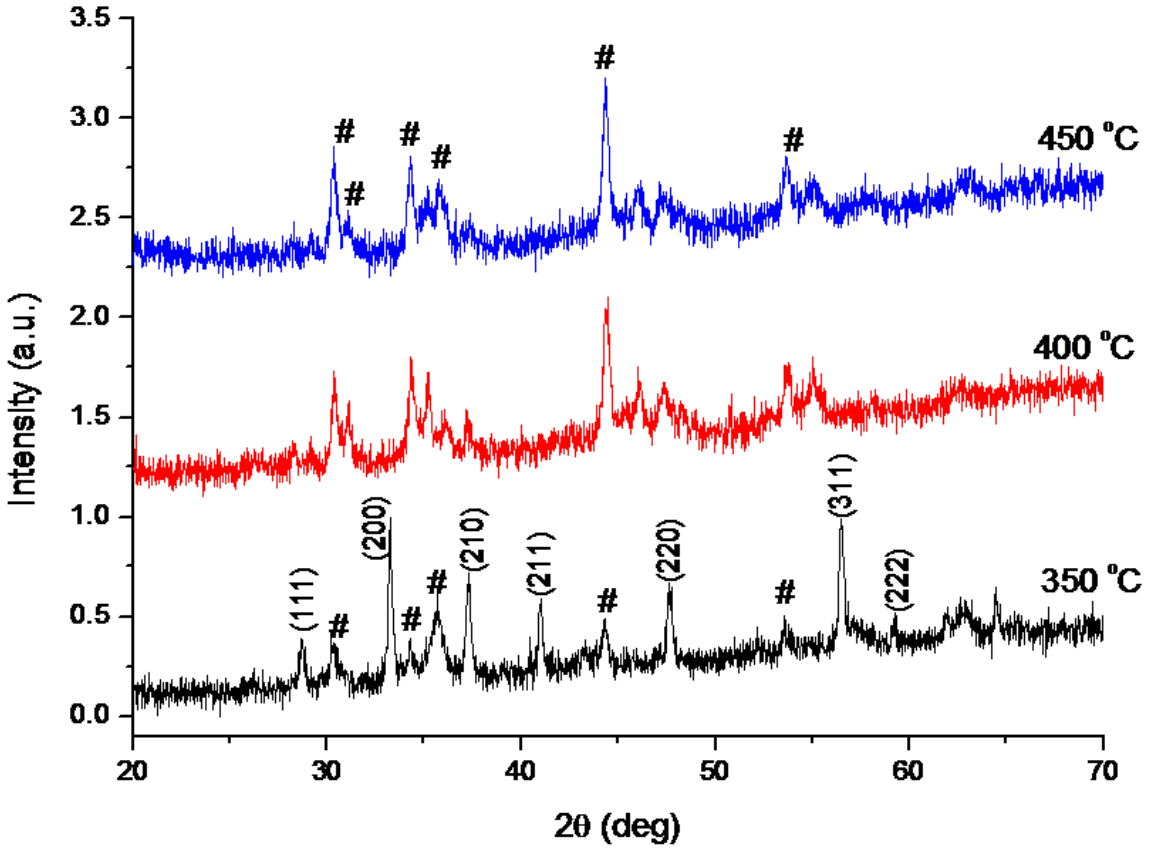


**Figure 5.13.** p-XRD pattern of iron sulfide nanoparticles synthesized using complex (**7**) as a single source precursor (# pyrrhotite phase).

The morphology of the as-synthesized iron sulfide nanoparticles from complex (6) was investigated by SEM and the images are shown in Figure 5.14. Nanoflake-like structures with sizes between 200 – 400 nm were obtained at all temperatures. The temperature change did not show any morphological transformation. The energy dispersive X-ray spectroscopy (EDX) was performed on the samples and the results are summarized in Table 5.3. The stoichiometric composition showed the formation of iron-rich nanocrystals as the temperature was increased.

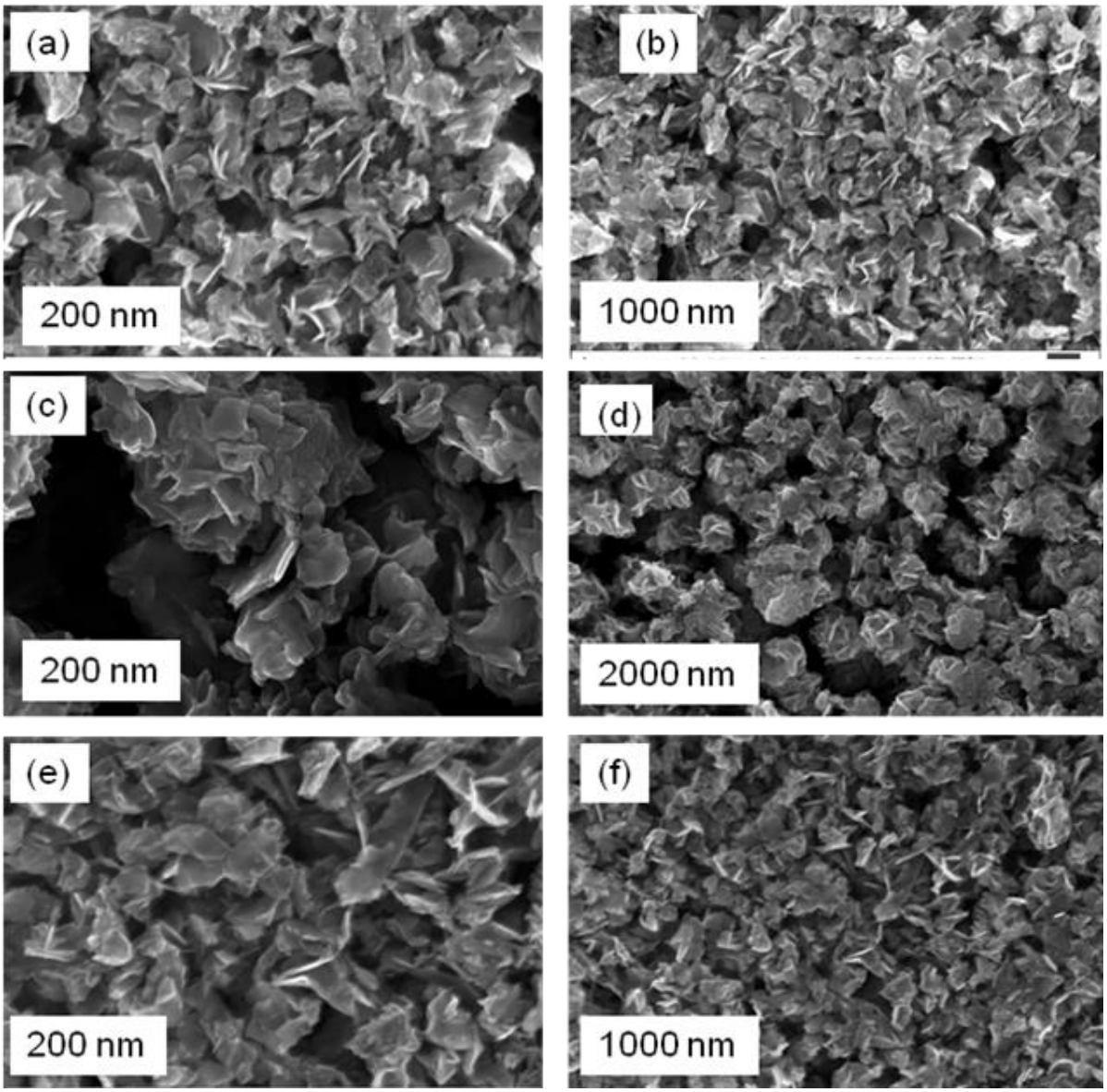


**Figure 5.14.** SEM images of iron sulfide nanocrystals obtained by pyrolysis of complex (**6**) at 350 °C (a and b), 400 °C (c and d) and 450 °C (e and f).

The surface morphology of the samples pyrolized from complex (**7**) is shown in Figure 5.15. SEM image of the samples reveals formation of well interconnected spherical microstructures at 350 °C (Figure 5.15a and b). When the temperature was increased to 400 and 450 °C, a clear transformed morphology was observed, where stacks of oval to cubic or plate-shaped nanocrystals with some small flake like structures were observed (Figure 5.15c-f). These results further manifests that the different sorts of precursors (**6**) and (**7**), resulted in different shapes of iron sulfide nanocrystals. Similarly, EDX measurements showed formation of iron-rich nanocrystals and the results are assembled in Table 5.3.

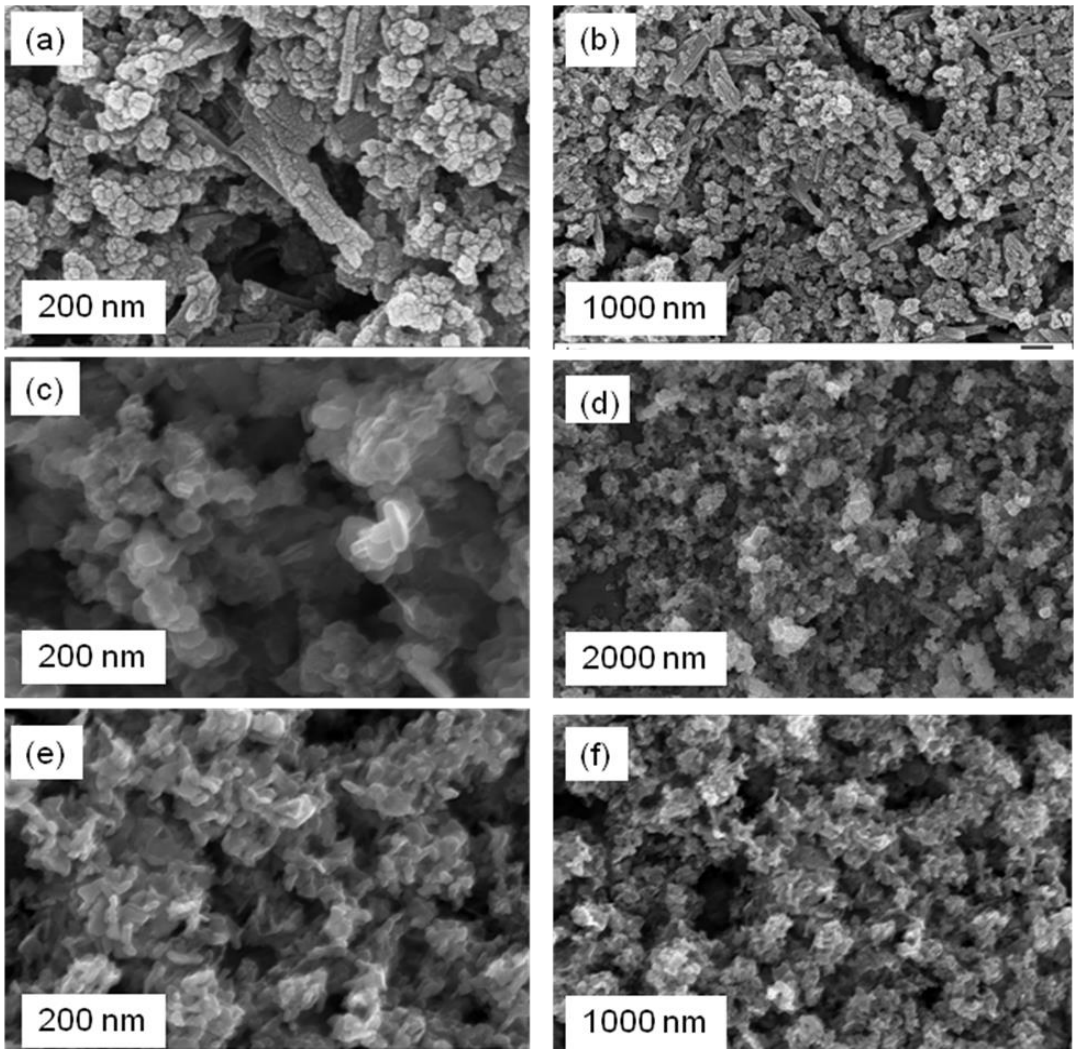


**Figure 5.15.** SEM images of iron sulfide nanocrystals obtained by pyrolysis of complex (**7**) at 350 °C (a and b), 400 °C (c and d) and 450 °C (e and f).

**Table 5.3.** Elemental composition of iron sulfide nanocrystals obtained by pyrolysis method using complex (**6**) and (**7**).

| **Complex** | **Temp (°C)** | **Fe (%)** | **S (%)** |
|---|---|---|---|
| **(6)** | 350 | 59.92 | 40.08 |
| | 400 | 60.17 | 39.83 |
| | 450 | 61.56 | 38.44 |
| **(7)** | 350 | 59.86 | 40.14 |
| | 400 | 61.03 | 38.97 |
| | 450 | 61.66 | 38.34 |

X-ray photoelectron spectrometry (XPS) was used to determine the surface chemical composition of the as-synthesized iron sulfide nanostructures. Representative samples prepared from complex (**6**) and (**7**) at 350 °C were chosen for analysis. The binding energy of Fe ($2p_{3/2}$) was carefully fitted (Figure 5.16a). Complex (**6**) gave iron sulfide with Fe 2p peak located at 710.8 eV, whereas the peak at 709.2 eV for complex (**7**) can be assigned to the major peak of Fe(III) bonded with S. These assignments are in good agreement with the literature results [31]. Figure 5.16b shows the S 2p spectrum of iron sulfide nanocrystals synthesized from complex (**7**) and the peaks at 161.7 eV and 166.8 eV are attributed to $S_2$ and possible oxidation of S to $SO_4^{2-}$ respectively [32,33]. Similarly, complex (**6**) peaks at 161.4 and 169.4 eV were attributed to S 2p, typical of Fe-S systems and an obvious oxidized form of S, respectively.

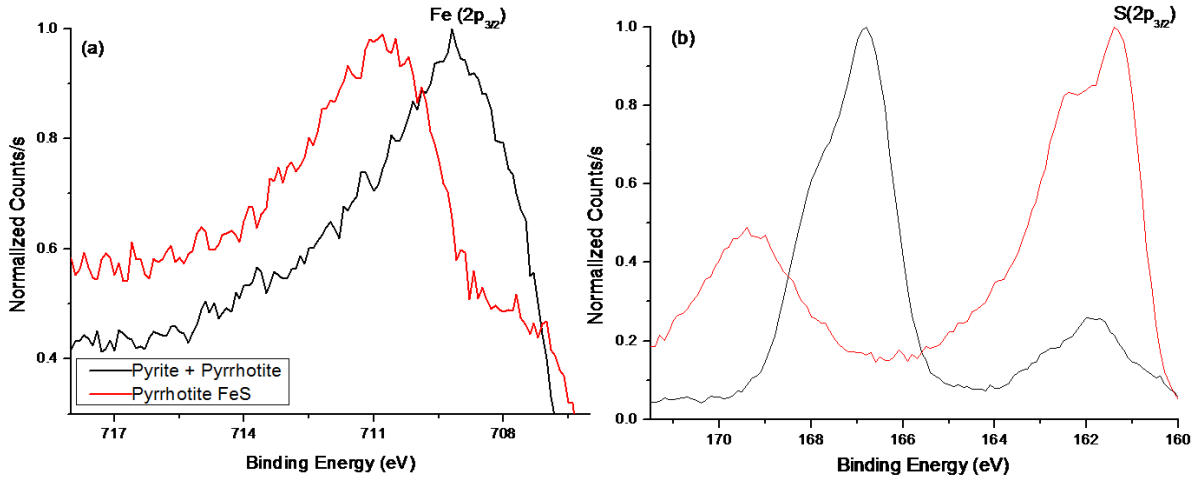


**Figure 5.16.** XPS spectra for the as synthesized iron sulfide nanocrystals from complex (**6**) and (**7**) (black) 350 °C.

The magnetization of the representative samples of iron sulfide nanoparticles measured by the vibrating sample magnetometer are shown in Figure 5.17. The magnetic properties reveal that all crystalline iron sulfide nanomaterials prepared from pyrolysis treatment of complex (**6**) and (**7**) show room temperature magnetic hysteresis loops with magnetization well saturated under the applied magnetic fields of 10-15 kOe (1 Oe = $10^{-4}$ T). The saturation susceptibility and the coercive forces of iron sulfide nanocrystals obtained from complex (**6**) and (**7**) are 7.13 and 5.52 emu/g and 135.5 and 121 Oe, respectively. The saturation susceptibility and coercive force of samples from complex (**6**) are a little higher than those from complex (**7**).

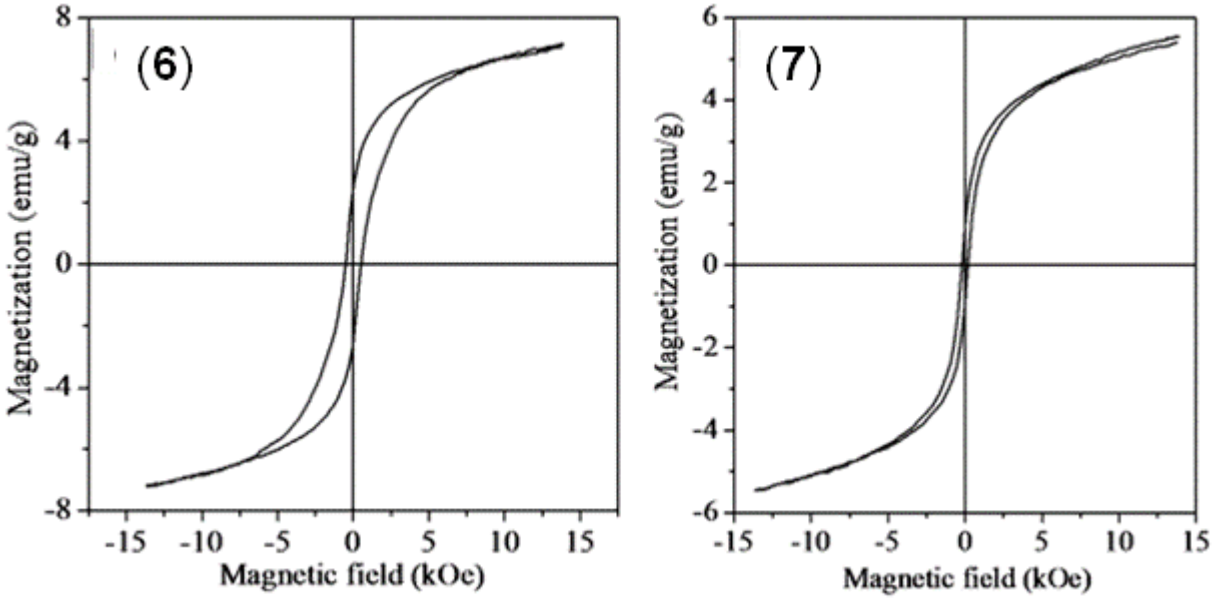


**Figure 5.17.** Magnetic hysteresis curves of the iron sulfide samples obtained from the pyrolysis of complex (**6**) (pyrrhotite) and (**7**) (pyrite and pyrrhotite) at 350 °C.

### 5.3.4. Gas sensing application

Recently, gas sensors have become key technology in several commercial, domestic and industrial gas sensing systems. Gas sensors based on semiconducting metal oxide nanostructures show high responses to various gases, however they require external heater to operate [42,43]. The use of external heater however, increases the power consumption. Considerable efforts have so far been made to overcome the problem of using external heaters. One of the option has been the use of a two-dimensional (2D) carbon monolayer crystal (graphene), which can operate at room temperature [44,45]. The main drawback of graphene based sensor is its poor recovery and sluggish response. Many gases emitted from industrial and several human activities pose threat to human and other living organism's health problems. Thus gas sensing technology is suitable to detect hazardous gases in the environment [46,47].

Metal sulfide semiconductor nanomaterials have rarely been used for gas sensing technology. In this paper, we show the application of iron sulfide nanocrystals (greigite and pyrrhotite phases) for gas sensing. The gas sensing tests were performed using a Kinosistec gas sensor capable of measuring resistance of the iron sulfide thin films, while automatically changing the concentrations of the gases and the gas type. We have also subjected the samples to humidity sensing and all measurements were carried out at room temperature. In

this work, iron sulfide nanoparticles obtained by solvothermal method in oleylamine from complex (**6**) were used. Both samples obtained at 230 °C (greigite-$Fe_3S_4$) and 300 °C (pyrrhotite-$Fe_{1-x}S$) have been used for this purpose. A typical diagram of KSGA565 Kenosistec sensing station illustrating how the gas sensing measurement was performed is shown in Figure 5.18.

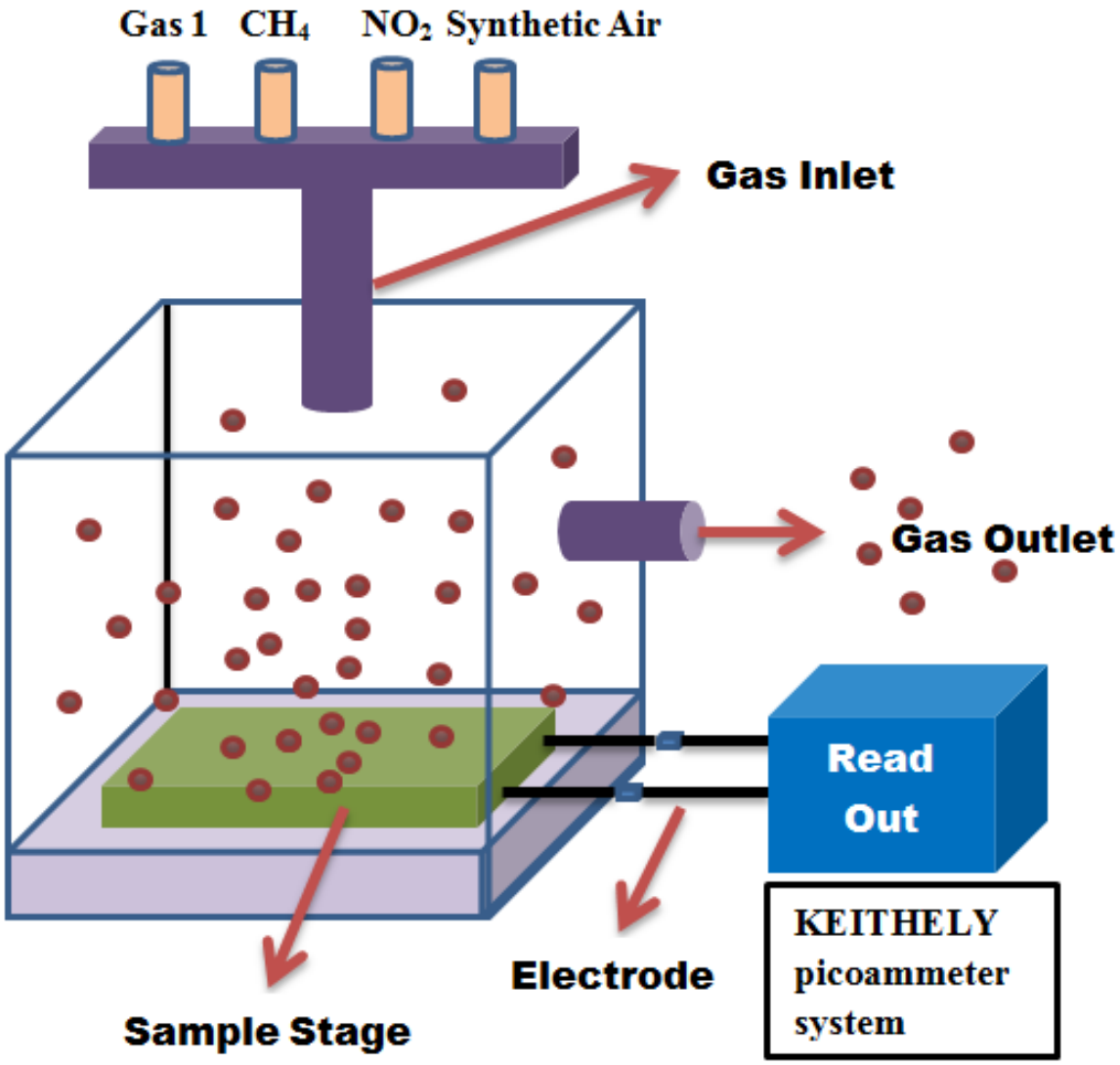


**Figure 5.18.** Schematic diagram of KSGA565 KENOSISTEC sensing station illustrating how the gas sensing measurement was performed.

Both greigite-$Fe_3S_4$ (230 °C) and pyrrhotite-$Fe_{1-x}S$ (300 °C) samples were employed in humidity sensing at room temperature. The greigite and the pyrrhotite-$Fe_{1-x}S$ were active towards humidity sensing and the results are shown in Figure 5.19. The resistive response of the greigite and the pyrrhotite sensor to varying humidity levels was measured at room

temperature (21 °C). The sensor resistances decrease (currents increase) with decreasing the humidity level in the chamber and vice versa. It can also be noted that, although the greigite displays a higher response to humidity than the pyrrhotite in all humidity level, the greigite saturates at a lower humidity level than the pyrhotite. It is also noteworthy that the pyrhotite sensor exhibits faster response and recovery than the greigite. The obvious gain in resistance of the sensors upon interaction with water vapour reveals the adsorption-desorption isotherms of water molecules to both the greigite and the pyrrhotite-$Fe_{1-x}S$-sensors.

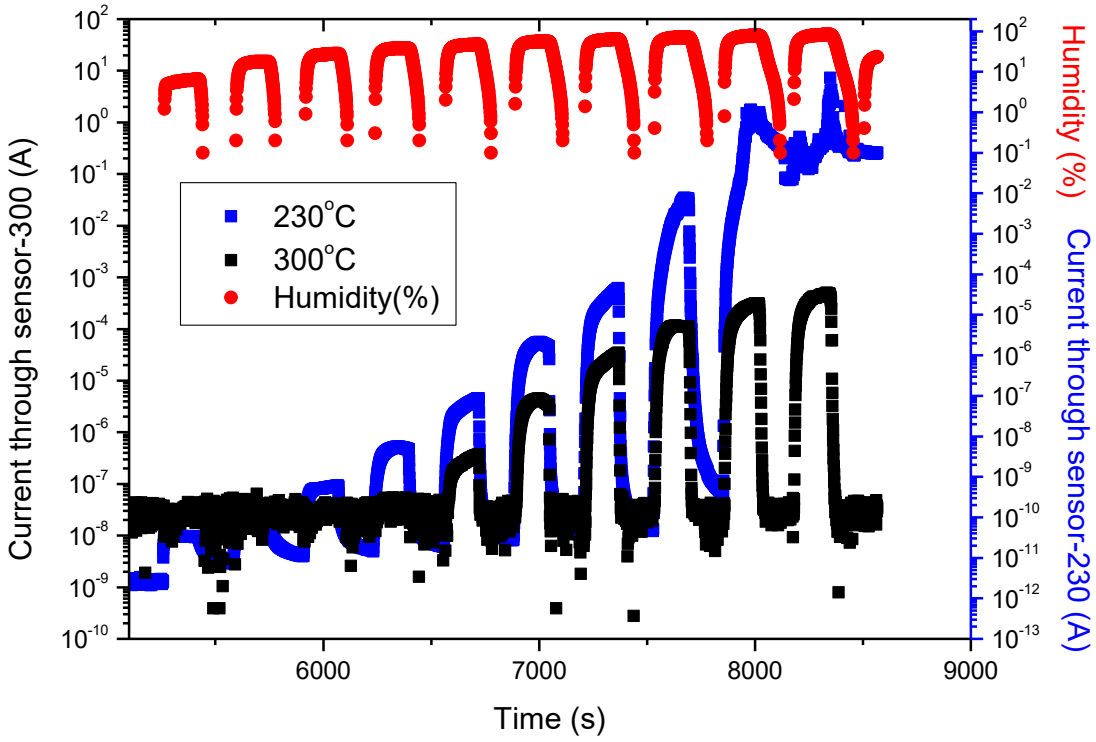


**Figure 5.19.** Resistance-time profiles of the iron sulfide based sensor when exposed to varying concentrations of humidity at room temperature. This figure shows that the greigite sample (annealed at 200 °C) response better to humidity than the pyrrhotite sample (annealed at 300 °C) although the greigite saturates at lower humidity level (about 80%) than its competitor which hardly saturates.

Gas sensing response profiles for the greigite (230 °C) and the pyrrhotite-$Fe_{1-x}S$ (300 C) sensors responding to $H_2$, $CH_4$, $NO_2$ and $NH_3$ at room temperature are shown in Figures 5.20. There is very little discernible response of the greigite to all the gases considered but the pyrhotite sensor showed to respond to both nitrogenous gases $NO_2$ and $NH_3$ and the $H_2$ and $CH_4$ gases. Between the two nitrogenous gases, the pyrhotite shows higher response to $NO_2$

than $NH_3$ while it shows more response to $CH_4$ than $H_2$. As opposed to its response to humidity, the pyrrhotite's resistances increased (currents decreased) as a consequence of increase in amounts of gases in the sensor chamber. The mechanism of metal oxides-based sensor is well established [48,49], where by reduction-oxidation processes occur on the sensor surfaces resulting in the exchange of electrons with the target gas molecules thus affecting the sensor's resistance. We assume similar electron-exchange mechanism occurs in metal sulfide sensors. It can thus be concluded that nitrogenous-sites showed sensor responses, possibly because of the availability of lone pairs on the $NO_2$ and $NH_3$ molecules. The mechanism of response of the pyrrhotite to $H_2$ and $CH_4$ which show similar profiles to those of $NH_3$ and $NO_2$ shows that the pyrhotite does not distinguish between reducing and oxidizing classes of gases and may point to the fact that this materials has both n-type and p-type phases. The fact that the greigite shows poorer sensing properties than the pyrrhotite suggests that the ferrimagnetic material is poorer sensor than the anti-ferromagnetic one.

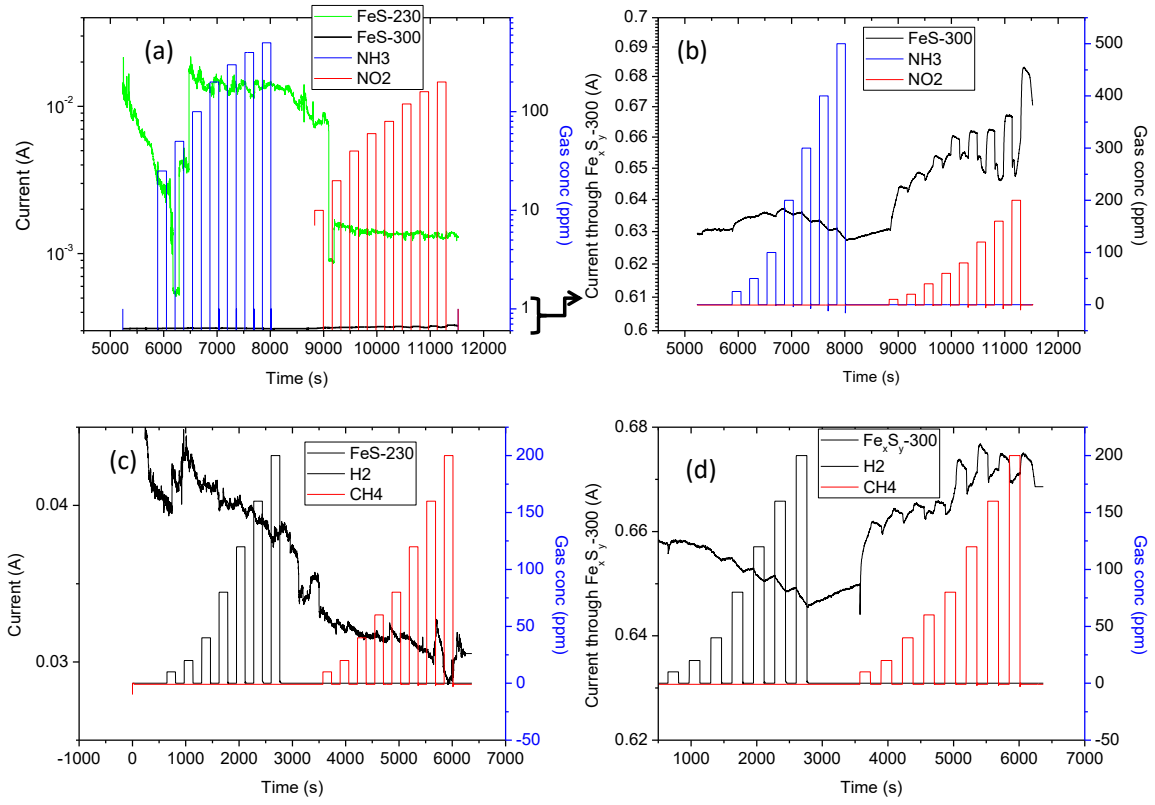


**Figure 5.20.** Resistance-time profiles of the greigite- $Fe_3S_4$ and the pyrrhotite-$Fe_{1-x}S$ based sensor when exposed to varying concentrations of $NO_2$ and $NH_3$ gases at room temperature.

The actual order of responses of the pyrrhotite to the four gases at a constant concentration of 40 ppm is presented in Figure 5.21. For a slightly large proportion of Fe in the pyrrhotite than in the greigite, its magnetic properties are much better and its band optical band energy gap slightly lower than the greigite. It appears these properties make the pyrrhotite a more stable gas sensor doing much better in $H_2$, $CH_4$ and $NO_2$ than the greigite does. The greigite tries to compete with the pyrrhotite on $NH_3$ but still its response to $NH_3$ is lower than that of the pyrrhotite.

The responses of the greigite are not as poor as they seem bearing in mind that all these measurements were done at room temperature. There are indications that this sample has high responses at ultra-low gas concentrations, say less than 10 ppm, but it quickly saturates at more than 30 ppm. This is an indication that at higher temperature, the greigite may compete or possible do better than the pyrrhotite. These insights form part of our on-going search.

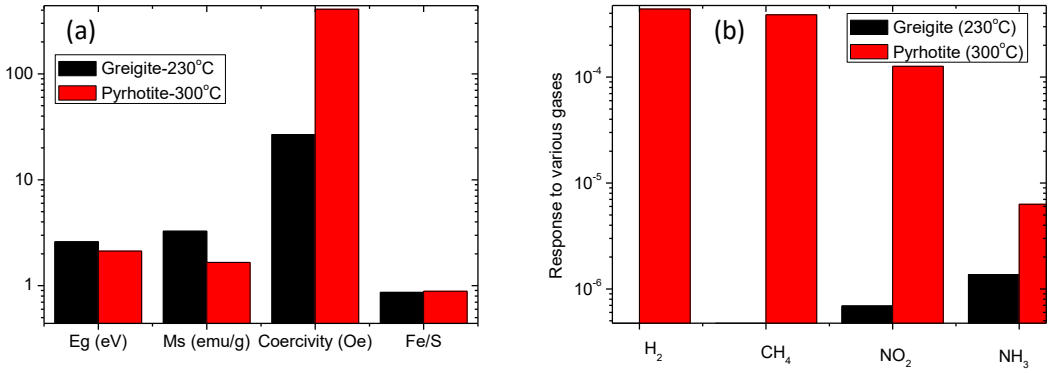


**Figure 5.21**. Summary of data (a) optical band gap, magnetic propertied and composition of the greigite and pyrrhotite (b) the responses of the greigite and the pyrrhotite to $H_2$, $CH_4$, $NO_2$ and $NH_3$ gases.

## 5.4. Conclusions

Heterocyclic iron(III) dithiocarbamate complexes were used as single source precursors to synthesize high quality iron sulfide nanoparticles via solvothermal and pyrolysis methods. Solvothermal route using ethylene glycol as coordinating solvent afforded the formation of only cubic greigite $Fe_3S_4$ phase, whereas oleylamine produced greigite phase at 230 °C and pyrrhotite phase at 300 °C. Pyrrhotite phase ($Fe_{1-X}S$) and a mixture of pyrrhotite and pyrite ($FeS_2$) phases could be obtained via pyrolysis route. Significant differences were noticed in the phase of iron sulfide nanocrystals by changing the complexes during pyrolysis of the single source precursors. Furthermore, the $Fe_3S_4$ and $Fe_{1-X}S$ nanoparticles displayed magnetic properties at room temperature. This study has provided a relatively reliable single precursor route for preparing stoichiometric iron sulfides nanocrystals with well-defined crystalline structures, compositions and morphologies. Moreover, the reaction temperature showed to play a critical role in controlling the chemical compositions, morphologies, crystalline structures and even the magnetic properties of the resultant iron sulfide nanocrystals.

We further developed the self-activated iron sulfide gas and humidity sensors without external heating. The reliable room-temperature operation guarantees the stability of iron sulfide sensing layer. Moreover, the sensor composed of single binary material, which is iron sulfide. The sensor measurement reveals satisfactory performance of the assembled device without external heating, thus ensuring low power consumption for practical applications of the sensor. Although the greigite show better response to humidity than does the pyrrhotite, is completely outrun by the pyrhotite when exposed to industrial gases $H_2$, $CH_4$, $NO_2$ and $NH_3$. The pyrrhotite shows much better response especially to $H_2$, $CH_4$ and $NO_2$. This suggests the pyrrhotite to be a useful material, perhaps utilizing its magnetic properties for other applications such as catalysis or corrosion alleviation.

## 5.5. References


1. A. K. Dutta, S. K. Maji, D. N. Srivastava, A. Mondal, P. Biswas, P. Paul and B. Adhikary. ACS Appl. Mater. Interfaces 2012, 4, 1919.
2. K. Isaac and J. Lee, Sensors, 2009, 9, 8130.
3. L. Wang. Y. Zhao and Y. Tian, J. Nanopart. Res. 2015, 17, 393.
4. Y. Y. Lin, D. Y. Wang, H. C. Yen, H. L. Chen, C. C. Chen, C. M. Chen, C. Y. Tang and C. W. Chen, Nanotechnology 2009, 20, 405207.
5. H. Geng, L. Zhu, W. Li, H. Liu, L. Quan, F. Xi and X. Su, J. Power Sources 2015, 281, 204.
6. H. Chen, L. Zhu, H. Liu and W. Li, J. Power Sources 2014, 245, 406.
7. H. Zheng, J. Li, J. P. Liu, Z. L. Wang and S. H. Sun, Nature. 2002, 420, 395
8. T. Hyeon, Chem. Commun., 2003, 927.
9. S. A. Kissin and S. D. Scott, Econ. Geol. 1982, 77, 1739
10. D. J. Vaughan and J. R. Craig. (1978) Mineral Chemistry of Metal Sulfides. Cambridge University Press. Cambridge.
11. R. E. Krupp, Eur. J. Mineral. 1994, 6, 265.
12. T. Li, H. Li, Z. Wu, H. Hao, J. Liu, T. Huang, H. Sun, J. Zhang, H. Zhang and Z. Guo, Nanoscale. 2015, 7, 4171.
13. J. Zheng, Y. Cao, C. Cheng, C. Chen, R-W. Yan, H-X. Huai, Q-F. Dong, M.-S. Zheng and C-C. Wang, J. Mater. Chem. A, 2014, 2, 19882.
14. G. Li, B. Zhang, F. Yu, A. A. Novakova, M. S. Krivenkov, T. Y. Kiseleva, L. Chang, J. Rao, A. O. Polyakov, G. R. Blake, R. A. De Groot and T. T. M. Palstra. Chem. Mater. 2014, 26, 5821.
15. F. Cao, W. Hu, L. Zhou, W. Shi, S. Song, Y. Lei, S. Wang and H. Zhang. Dalton Trans. 2009, 9246.
16. J. H. P. Watson, B. A. Cressey, A. P. Roberts, D. C. Ellwood, J. M. Charnock and A. K. Soper, J. Magn. Magn. Mater. 2000, 214, 13.
17. Y. Shim, R. M. Young, A. P. Douvalis, S. M. Dyar, B. D. Yuhas, T. Bakas, M. R. Wasielewski, and M. G. Kanatzidis. J. Am. Chem. Soc. 2014, 136 (38), 13371.
18. Y-S. C S. Savitha, S. S. C-K Hsu, F-H. Lin, J. Colloid Interface Sci. 2011, 363. 314–319.

19. L. Kong, L. Yan, Z. Qu, N. Yan and L. Li, J. Mater. Chem. A. 2015, 3, 15755.
20. Xianbiao Wang, Weiping Cai, Guozhong Wang, Zhikun Wu and Huijun Zhao. CrystEngComm. 2013, 15, 2956.
21. E-J. Kim, J-H. Kim, A-M. Azad and Y-S, Chang, ACS Appl. Mater. Interfaces 2011, 3, 1457.
22. C. J. Rowan and A. P. Roberts. Earth and Planetary Science Letters. 2006, 241, 119.
23. K. Zhang, T. Zhang, J. Liang, Y. Zhu, N. Lin and Y. Qian, RSC Adv. 2015, 5, 14828.
24. P. V. Vanitha and P. O'Brien, J. Am. Chem. Soc. 2008, 130, 17256.
25. X. Chen, X. Zhang, J. Wan, Z. Wang and Y. Qian, Chem. Phys. Lett. 2005, 403, 396.
26. Y. Zhang, Y. Du, H. Xu and Q. Wang, CrysEngComm. 2010, 12, 3658.
27. W. Han and M. Y. Gao, Cryst. Growth Des. 2008, 8, 1023.
28. S. Mlowe, D. J. Lewis, M. A. Malik, J. Raftery, E. B. Mubofu, P. O'Brien and N. Revaprasadu, Daltons. Trans. 2016. DOI: 10.1039/C5DT03881B.
29. J. Tauc, (1966) Optical Properties of Solids. Academic Press, New York, USA
30. A. Paolella, C. George, M. Povia and L. Manna, Chem. Mater. 2011, 23, 3762.
31. A. R. Pratt, I. J. Muir and H. W. Nesbitt, Geochim. Cosmochim. Ac. 1994, 58 827.
32. R. Murphy and D. R. Strongin, Surf. Sci. Rep. 2009, 64, 1.
33. J. E. Thomas, W. M. Skinner and R. S. T. C. Smart, Geochim. Cosmochim. Ac. 67 (2003) 831.
34. C. Wadia, Y. Wu, S. Gul, S.K. Volkman, J. Guo and A. P. Alivisatos, Chem. Mater. 2009, 21, 2568.
35. A. M. Karguppikar and A. G. Vedeshwar, Phys. Status Solidi A 1988, 109, 549.
36. M. W. Jr. Chase, C. A. Davies, J. R. Jr. Downey, D. J. Frurip, R. A. McDonald and A. N. Syverud, J. Phys. Chem. 1984, 14, 1198.
37. W. Davison, Aquatic Sciences. 1991, 53/4, 309.
38. F. Gronvold and S. Stolen, J. Chem. Thermodyn. 1992, 24, 913.
39. D. J. Vaughan and A. R. Lennie, Sci. Prog. (Edinburgh), 1991, 75, 371.
40. C. D. Wagner, W. W. Riggs, L. E. Davis, J. F. Moulder and G. E. Muilenberg. (1978) Handbook of X-ray Photoelectron Spectroscopy, Perkin-Elmer, Eden Prairie, MN.
41. R. B. Jr, Herbert, S. G. Benner, A. R. Pratt and D. W. Blowes, Chem. Geol. 1998, 144, 87.

42. S. Capone, A. Forleo, L. Francioso, R. Rella, P. Siciliano, J. Spadavecchia, D. Presicce and A. Taurino, J. Optoelectron. Adv. Mater. Devices 2003, 5, 1335.
43. G. Eranna, B. Joshi, D. Runthala and R. Gupta, Crit. Rev. Solid State Mater. Sci. 2004, 29, 111.
44. Y. Dan, Y. Lu, N. J. Kybert, Z. Luo and A. C. Johnson, Nano Lett. 2009, 9, 1472.
45. G. Lu, L. E. Ocola and J. Chen, Appl. Phys. Lett. 2009, 94, 083111.
46. Y. Tanaka, M. Furuta, H. Matsura, A. Fujisima and K. Honda, ECS Tans. 2008, 16(11), 387.
47. Q. Xiao, B-H. Yang and S-S. Zhu, J. Optoelectron. Laser, 2010, 21(9), 1332.
48. W. H. Brittain and J. Bardeen, Bell. Syst. Tech. J. 1953, 1, 1.
49. G. H. Heiland, Zeit. Phys. 1954, 138, 459.

# CHAPTER SIX

# SUMMARY, CONCLUSION AND FUTURE WORK

## 6.1. Summary

Semiconductor metal sulfide nanomaterials are important due to their extensively promising applications in optoelectronic and magnetic devices. The well aligned nanostructure arrays are attractive due to their improved properties and applications. In the 21st century, energy scarcity and global warming are among the challenges the world and human beings are facing. Thus the development of high-performance and clean alternative energies is the interest of the current scientists.

Described in this work is the synthesis of single source precursors or complexes of piperidine and tetrahydroquinoline of cadmium, lead and iron dithiocarbamato complexes and a pyridine adduct of *bis*(piperidine dithiocarbamato)cadmium(II) and their use for the synthesis of metal sulfide nanoparticles and thin films. Chapter one details general introduction of materials science and comprehensive literature review underling the interest and the aims of this work. Deposition of cadmium sulfide thin films by aerosol assisted chemical vapour deposition (AACVD) and nanoparticles by hot injection methods is described in chapter two, where by complexes of piperidine (**1**) and tetrahydroquinoline (**2**) of cadmium-dithiocarbamato complexes and a pyridine adduct of *bis*(piperidine dithiocarbamato)cadmium(II) (**3**) were used as single source precursors.

Chapter three presents the synthesis of single source precursors or complexes of piperidine (**4**) and tetrahydroquinoline (**5**) lead(II) dithiocarbamato complexes. These complexes have been used for the deposition of PbS thin films by aerosol assisted chemical vapour deposition (AACVD) and spin coating methods at different temperatures. In chapter four, four single source precursors- *tris*-(piperidinedithiocarbamato)iron(III/II) (**6/8**) and *tris*-*(*tetrahydroquinolinedithiocarbamato)iron(III/II) (**7/9**) complexes have been synthesized and fully characterized. The precursors were then used to deposit thin films of iron sulfide thin films by aerosol assisted chemical vapor deposition technique. A mechanism for the decomposition of complex (**6**) is also described in this chapter. The mechanism revealed the decomposition of complex (**6**) through two steps; firstly detachment of one piperidinyl dithiocarbamato ligand, followed by complete removal of the remaining organic moiety.

Chapter five describes synthesis of high quality iron sulfide nanocrystals via solvothermal and pyrolysis methods using complexes (**6**) and (**7**) reported in chapter four.

The solvothermal route involved the use of ethylene glycol and oleylamine as coordinating solvents whereas the pyrolysis route involved the heating of complexes at different temperatures. Iron sulfide nanocrystals obtained via solvothermal route in oleylamine were further used to assemble iron sulfide gas and humidity sensor. Gases $H_2$, $CH_4$, $NH_3$, $NO_2$ and humidity were tested at room temperature.

## 6.2. Conclusion

A number of cadmium, lead and iron complexes of the type heterocyclic dithiocarbamates have been synthesized and characterized. Single crystal structures of four single source precursors have been elucidated namely:

- *bis*-(piperidinedithiocarbamato)cadmium(II) (**1**),
- *bis*-(piperidinedithiocarbamato)pyridinecadmium(II) (**3**),
- *tris*-(piperidinedithiocarbamato)iron(III) (**6**) and
- *tris-(*tetrahydroquinolinedithiocarbamato)iron(III) (**7**).

These precursors have been used for the fabrication of CdS, PbS and Fe-S thin films by AACVD and in some cases spin coating method. Also solvothermal method has been employed to synthesize high quality nanoparticles. In addition, pyrolysis method was used to synthesize iron sulfide nanoparticles.

Different parameters were varied during the deposition of these metal sulfide thin films including temperature and solvents. The morphological, structural, composition and optical properties of the deposited materials were found to depend on the reaction conditions used during the synthesis such as temperature. High quality synthesis of nanoparticles showed to be influenced by the temperature of the injection. The as-synthesized CdS thin films and nanoparticles were shown to exhibit blue shifted optical properties, which were size and morphological dependent. Their morphologies and structural properties were investigated using different electron microscopic and diffraction techniques.

Similarly, PbS thin films deposited were studied and their optical and structural properties showed formation of high quality nanomaterials which were temperature dependent. Optical properties of the deposited PbS thin films revealed blue shift compared to

the bulk PbS. Best morphologies of PbS films deposited by spin coating method highlighted the usefulness of this route. Iron sulfide thin films deposited by AACVD method showed that variation of parameters could result in the formation of high quality structures. Furthermore, optically active greigite and pyrrhotite-iron sulfide nanoparticles were obtained by simply varying the temperature of the hot solvent. Pyrrhotite-$Fe_{1-X}S$ sensor device showed interesting performance when tested for humidity and different N-site gases such $NO_2$ and $NH_3$. The gas sensors further revealed that stoichiometric structure of iron sulfide nanostructures have significant effect on the end-user device performance.

## 6.3. Future work

Recent research work regarding different metal sulfide nanostructures and their applications have gained interest. Synthetic methods, tremendous properties and wide applications are also of great importance in many areas. Thus, in order to satisfy today's demands of the world and society; distinctive assembling of well-aligned nanostructures is important to ensure high quality properties and best performance of the devices. The followings are perspectives envisaged to improve quality of nanostructures fabrication and/or device performances. To synthesize alloyed sulfides such as bismuth iron sulfide or bismuth lead sulfide nanostructures to improve electronic properties of the materials. Secondly, employing UV-irradiation or external heating could enhance better performance of the gas sensor used.

**Appendices: List of selected publications, conferences, structures and papers**

**List of publications**

1. **Sixberth Mlowe,** Shivram Sopan Garje, Thomas Moyo and Neerish Revaprasadu, **Magnetic Iron Sulfide Nanoparticles for Potential Applications in Gas Sensing.** MRS Advances, 2016, **DOI: 10.1557/adv.2016.12.**
2. **Sixberth Mlowe,** David J. Lewis, Mohammad Azad Malik, James Raftery, Egid B. Mubofu, Paul O'Brien and Neerish Revaprasadu, **Heterocyclic dithiocarbamato-iron(III) complexes: single-source precursors for aerosol-assisted chemical vapour deposition (AACVD) of iron sulfide thin films.** Daltons Trans. 2016, *DOI: 10.1039/c5dt03881b*
3. **S. Mlowe**, E. B. Mubofu, F. N. Ngassapa and N. Revaprasadu Anacardic acid capped Metal Chalcogenide nanoparticles, **In Transferring Nanotechnology Concept towards Business Perspectives,** (Edited by Shogo Shimazu and Silvester Tursiloadi), Daya publishing House, India 2016, 197-211.
4. **Sixberth Mlowe**, Linda D. Nyamen, Peter T. Ndifon, M. Azad Malik, James Raftery, Paul O'Brien and Neerish Revaprasadu. **Aerosol assisted chemical vapor deposition (AACVD) of CdS thin films from heterocyclic cadmium(II) complexes.** Inorganica Chimica Acta 434 (2015) 181–187.
5. **Sixberth Mlowe,** David J. Lewis, Azad M. Malik,,James Raftery, Egid B. Mubofu, Paul O'Brien and Neerish Revaprasadu, **Bis(piperidinedithiocarbamato)pyridinecadmium(II) as a single-source precursor for the synthesis of CdS nanoparticles and aerosol-assisted chemical vapour deposition (AACVD) of CdS thin films.** New J. Chem. 2014, 38, 6073-6080.
6. **S. Mlowe**, A. A. Nejoa, V. S. R. Rajasekhar Pullabhotla, E. B. Mubofu, F. N. Ngassapa, P. O'Brien, N. Revaprasadua. **Lead chalcogenides stabilized by anacardic acid,** Mater Sci. Semicond. Processing. (2013) 16, 263.
7. **S. Mlowe**, V. S. R. Rajasekhar Pullabhotla, Egid B. Mubofu, Faustine N. Ngassapa and N. Revaprasadu, **Low temperature synthesis of anacardic acid capped cadmium chalcogenide nanoparticles,** Int. Nano Lett. (2014). 4, 106.

**Conferences**

1. Oral presenter: Magnetic Iron Sulfide Nanoparticles for Potential Applications in Gas Sensing.2015 MRS Fall Meeting and Exhibition, Hynes Convention Centre and Sheraton Hotel, Boston, USA.
2. Oral presenter: 7th International Symposium On Macro- and Supramolecular Architectures and Materials, Emperors Palace Hotel Casino, Johannesburg, South Africa.
3. Oral presenter: 5th International Conference on Nanoscience and Nanotechnology (SANI), NANOAFRICA 2014, Quest Conference Estate- Curie Boulevard-Vanderbijlpark, Vaal, South Africa.

**Structures**

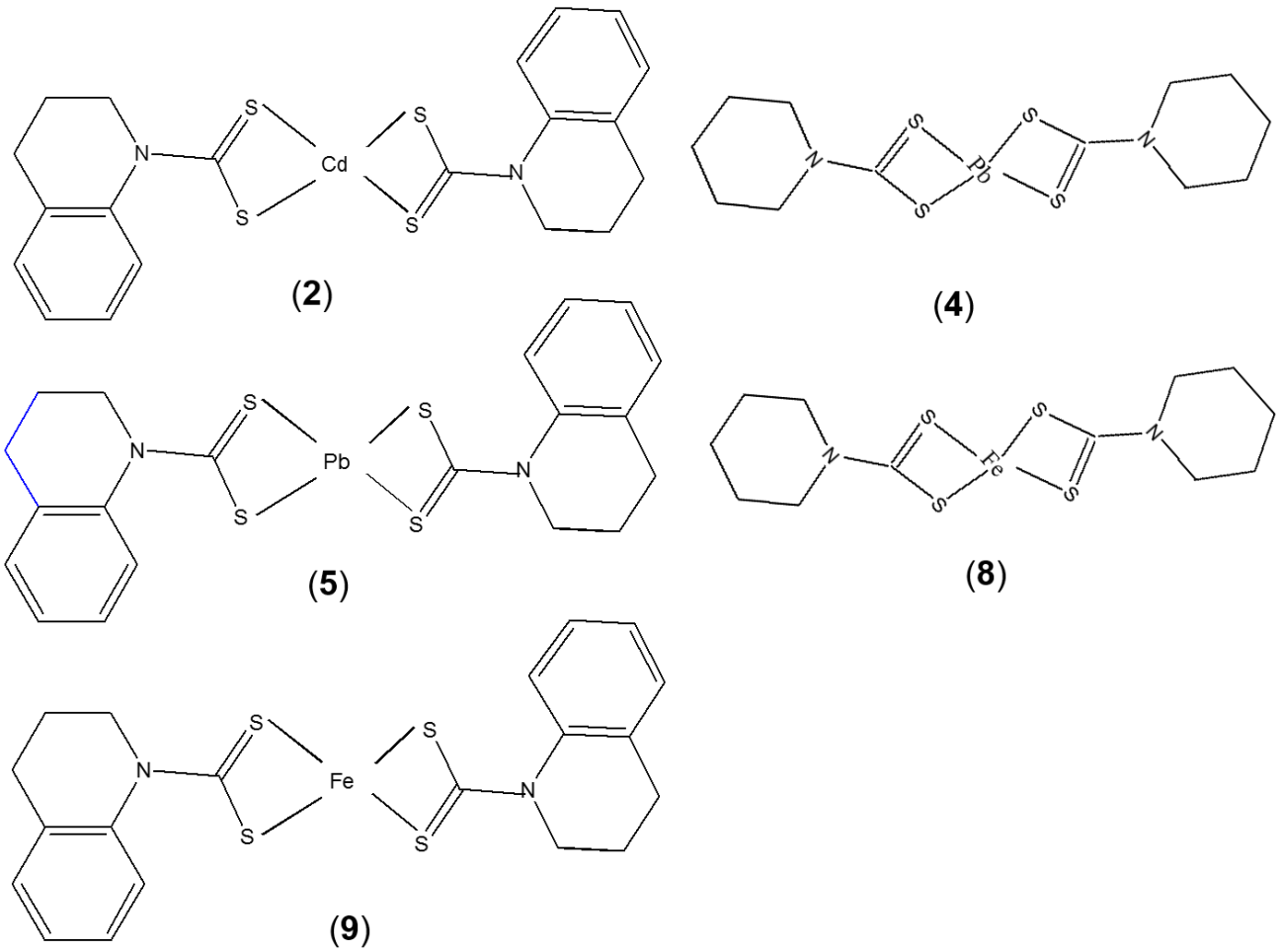


**Figure 1A.** Proposed structures of complexes (**2**), (**4**), (**5**), (**8**) and (**9**).